New Electronic and Multifunctional Polymer Thin Films Enabled by Initiated Chemical Vapor Deposition

Dissertation

zur Erlangung des akademischen Grades
Doktor der Ingenieurwissenschaften
(Dr.-Ing.)
der Technischen Fakultät
der Christian-Albrechts-Universität zu Kiel

Stefan Schröder
Kiel
2020

1. Gutachter: Prof. Dr. Franz Faupel
Lehrstuhl für Materialverbunde
Technische Fakultät - Institut für Materialwissenschaft
Christian-Albrechts-Universität zu Kiel, Germany

2. Gutachter: Prof. Dr. Rainer Adelung
Lehrstuhl Funktionale Nanomaterialien
Technische Fakultät - Institut für Materialwissenschaft
Christian-Albrechts-Universität zu Kiel, Germany

3. Gutachter: Prof. Dr. Karen K. Gleason
Department of Chemical Engineering
Massachusetts Institute of Technology, USA

Datum der Disputation: 28.05.2021

Erklärung

Hiermit versichere ich, dass diese Dissertation, abgesehen von der Beratung durch die Betreuer, nach Inhalt und Form meine eigenständige Arbeit ist und nur mit den angegebenen Hilfsmitteln verfasst wurde. Zudem versichere ich, dass diese Dissertation weder ganz noch in Teilen einer anderen Stelle im Rahmen eines Prüfungsverfahrens vorgelegen hat. Der Inhalt der Arbeit wurde teilweise bereits in meinen wissenschaftlichen Publikationen veröffentlicht. Dies ist in der Arbeit entsprechend vermerkt. Außerdem ist die Arbeit unter Einhaltung der Regeln guter wissenschaftlicher Praxis der Deutschen Forschungsgemeinschaft entstanden. Es wurde noch kein akademischer Grad entzogen.

Ort, Datum

Unterschrift

Zusammenfassung

Ziel dieser Arbeit war die Etablierung der initiierten chemischen Gasphasenabscheidung (engl. initiated chemical vapor deposition, iCVD) am Lehrstuhl für Materialverbunde (Prof. Dr. Franz Faupel) und die Entwicklung von iCVD Elektretschichten für biomagnetische Sensoren. Der von Gleason et al. entwickelte iCVD Prozess ermöglicht durch die CVD-typischen Wachstumscharaktaristika, sowie der lösungsmittelfreien radikalischen Polymerisation aus der Gasphase eine hochpräzise Schichtwachstumskontrolle und Einstellmöglichkeit für die resultierende Filmfunktionalität der Polymerdünnschichten.

Basierend auf den Arbeiten von Gleason et al. wird im Rahmen dieser Arbeit als erste Zielsetzung der iCVD Prozess am Lehrstuhl für Materialverbunde neu etabliert und weiterentwickelt. Um ein genaueres Verständnis der zugrundeliegenden Reaktionsprozesse sowie verbesserte Prozesskontrolle zu erlangen wird zusätzlich eine im Verlauf dieser Arbeit neu entwickelte in-situ Massenspektrometrieerweiterung für den iCVD Prozess vorgestellt.

Ausgehend von einfachen Isolatoren, die gegenwärtig mit iCVD abgeschieden werden können, wird in der nächsten Zielsetzung der Frage nachgegangen, ob sich sogenannte Elektretschichten mit iCVD herstellen lassen. Elektrete sind funktionale Dielektrika, die eine Ladung über einen sehr langen Zeitraum speichern können und somit über lange Zeit ein (quasi)permanentes elektrisches Feld bereitstellen, ganz ähnlich wie ein Permanentmagnet ein magnetisches Feld über lange Zeiträume bereitstellt. Ihr vielseitiger Einsatzbereich reicht von Elektretmikrofonen über Energiegeneratoren bis hin zu elektrostatischen Luftfiltern. Im Rahmen dieser Arbeit sind die Elektrete für neue elektrostatische Magnetfeldsensoren, die in enger Zusammenarbeit mit dem Lehrstuhl für Funktionale Nanomaterialien (Prof. Dr. Rainer Adelung) als Projekt A2 im Rahmen des Sonderforschungsbereiches (SFB) 1261 entwickelt werden, vorgesehen. Hierfür wird auf die langjährige Erfahrung im Bereich des thermischen Aufdampfens von Teflon AF Dünnschichtelektreten am Lehrstuhl für Materialverbunde zurückgegriffen und unter anderem untersucht ob die iCVD Fluorpolymere eine weitere Verbesserung der Ladungsträgerstabilität sowie bessere Schichtkontrolle durch das CVD-typische Wachstum ermöglichen.

Die darauffolgende Zielsetzung beschäftigt sich mit der Frage, wie die iCVD Schichten für die Anwendung in den Sensoren weiterentwickelt und maßgeschneidert werden können. Dies findet nur über ein besseres Verständnis der zugrun-

deliegenden Ladungsspeichermechanismen statt. Daher wird zunächst untersucht wie sich, ermöglicht durch die individuelle Einstellbarkeit der Filmfunktionalität im iCVD Prozess, unterschiedliche Endgruppen auf die Ladungsspeichereigenschaften auswirken. Außerdem werden neue organische iCVD Elektretmultilagen demonstriert, um gezielt Herausforderungen zu adressieren, die im Zusammenhang mit der Elektretkomponente in Sensoren auftreten können. Zudem wird ein Ansatz gezeigt mit dem sich durch eine Phasenseparation während der Abscheidung mikroporöse Polymerfilme bilden, die so die effektive Oberflächenladung vergrößern können. Um den Bereich abzuschließen wird schließlich untersucht, ob es im Gegensatz zu den typischen isolierenden iCVD Schichten auch möglich ist konjugierte Schichten durch die Verwendung von neuen acetylen-artigen Monomeren abzuscheiden.

Adhäsionsprobleme, die während der Abscheidung besonders bei Fluoropolymerschichten auftreten, werden schließlich durch neuartige, von der Natur inspirierte, Gradientcopolymerschichten gelöst. Bei diesen Schichten ändert sich die chemische Zusammensetzung von Polymer Typ A zu Polymer Typ B entlang der Schichtdicke. Mit Hilfe der neu entwickelten in-situ Massenspektrometrieerweiterung wird schließlich die Abscheidung dieser neuen nanoskaligen Gradientcopolymerschichten mit Schichtdicken unter 30 nm ermöglicht. Eine Kombination von zwei Materialien in einem Material stellen in den physikalischen und chemischen Eigenschaften eine völlig neue Art von Material dar. Es ermöglicht nicht nur eine verbesserte Adhäsion, sondern kann unter anderem neue Pfade für die organische Elektronik, zukünftige sub-wavelength Geräte und das Nachbilden von natürlichen Gradientstrukturen zum Beispiel für molekulare Maschinen auf der unteren Nanoskala ebnen.

Abstract

The aim of this work was the establishment of initiated chemical vapor deposition (iCVD) at the Chair for Multicomponent Materials (Prof. Dr. Franz Faupel) and the development of iCVD thin film electrets for biomagnetic sensors. The iCVD process developed by Gleason et al. enables a high-precision film growth control and control of the resulting film functionality of the polymer thin films due to the CVD-typical growth characteristics and the solvent-free radical polymerization from the vapor phase.

Based on the work of Gleason et al., the iCVD process is newly established and further developed as the first objective of this work at the Chair for Multicomponent Materials. In order to obtain a more detailed understanding of the underlying reaction processes and to improve the process control, an in-situ mass spectrometry extension for the iCVD process, which is newly developed in the course of this work, is also presented.

Starting from simple insulators, which can currently be deposited by iCVD, the next objective is to investigate whether it is possible to produce so-called thin film electrets by iCVD. Electrets are functional dielectrics that can store a charge over a very long period of time and thus provide a (quasi)permanent electric field over a long period of time, much like a permanent magnet provides a magnetic field for a long period of time. Their versatile field of application ranges from electret microphones to energy generators and electrostatic air filters. Within the scope of this work, the electrets are intended for new electrostatic magnetic field sensors, which are developed in close cooperation with the Chair for Functional Nanomaterials (Prof. Dr. Rainer Adelung) as project A2 within the Collaborative Research Center (CRC) 1261. For this purpose, the long-standing experience in the field of thermal evaporation of Teflon AF thin film electrets at the Chair for Multicomponent is used and, among other things, it is investigated whether the iCVD fluoropolymers enable a further improvement of the charge carrier stability as well as better film control by the CVD-typical growth conditions.

The subsequent objective is dedicated to the question of how iCVD electrets can be further developed and tailored for the application in sensors. This can only be achieved by a better understanding of the underlying charge storage mechanisms. Therefore, the influence of different end groups on the charge storage properties, enabled by the individual tunability of the film functionality in the iCVD process, is investigated first. In addition, new organic iCVD electret multilayers are

demonstrated to specifically address challenges that may arise in connection with the electret component in sensors. Furthermore, an approach is demonstrated that allows the formation of microporous polymer films by phase separation during deposition, which can increase the effective surface charge. Finally, to complete the field, it is investigated whether it is possible to deposit conjugated thin films by iCVD via new acetylene-like monomers in contrast to the typical insulating iCVD films.

Adhesion problems that occur during deposition, especially with fluoropolymer films, are finally solved by novel gradient copolymer films inspired by nature. The chemical composition of these films changes from polymer type A to polymer type B along the film thickness. With the help of the newly developed in-situ mass spectrometry extension, the deposition of the new nanoscale gradient copolymer films with film thicknesses below 30 nm is finally made possible. A combination of two materials in one material represents a completely new type of material in terms of physical and chemical properties. It not only enables improved adhesion, but can also pave new paths for organic electronics, future sub-wavelength devices and the replication of natural gradient structures, for example for molecular machines on the lower nanoscale.

Contents

List of Abbreviations and Units

18N	1,8-nonadiyne
1E3F	1-ethynyl-3-fluorobenzene
1N	1-nonyne
ALD	Atomic layer deposition
amu	Atomic mass unit (unit)
APCVD	Atmospheric pressure chemical vapor deposition
a-Si	Amorphous silicon
B3LYP	Becke, 3-parameter, Lee-Yang-Parr
cc-pVDZ	Correlation-consistent polarized (valence-only) double-zeta
D3	Hexamethylcyclotrisiloxane
D4	Tetramethylcyclotetrasiloxane
DEAEA	Diethylaminoethyl acrylate
DFT	Density functional theory
C6PFA	1H,1H,2H,2H-perfluorooctyl acrylate
CATCVD	Catalytic chemical vapor deposition
°C	Degree Celsius (unit)
CVD	Chemical vapor deposition
e^-	Electron
e^+	Positron
EG	Ethylene glycol
EGDMA	Ethylene glycol dimethylacrylate
eV	Electronvolt (unit)
FEP	Fluorinated ethylene propylene
FTIR	Fourier-transform infrared spectroscopy
GMA	Glycidyl methacrylate
GRIN	Gradient refractive index
HEMA	Hydroxyethyl methacrylate
HFCVD	Hot filament chemical vapor deposition

HFPO	Hexafluoropropylene oxide
HOMO	Highest occupied molecular orbital
HWCVD	Hot wire chemical vapor deposition
Hz	Hertz (unit)
iCVD	Initiated chemical vapor deposition
IUPAC	International union or pure and applied chemistry
K	Kelvin (unit)
LCVD	Laser chemical vapor deposition
LOD	Limit of detection
LPCVD	Low pressure chemical vapor deposition
LUMO	Lowest unoccupied molecular orbital
MFC	Mass flow controller
mg	Milligram (unit)
MIM	Metal-Insulator-Metal
min	Minute (unit)
MLD	Molecular layer deposition
mm	Millimeter (unit)
MMFF94s	Merck molecular force field
MO	Molceular orbital
MOCVD	Metalorganic chemical vapor deposition
MOF	Metal-organic framework
MP2	Second order Møller–Plesset perturbation theory
MS	Mass spectrometry
ms	Millisecond (unit)
m/z	Mass charge ratio
nBA	n-butyl acrylate
nHA	n-hexyl acrylate
nm	Nanometer (unit)
ns	Nanosecond (unit)
NWChem	Northwest Computational Chemistry Package
oCVD	Oxidative chemical vapor deposition
OLED	Organic light-emitting diode
o-Ps	Ortho-positronium
OSC	Organic solar cell
OTFT	Organic thin film transistor
P3HT	Poly(3-hexylthiophene-2,5-diyl)
PA	Polyacetylene
Pa	Pascal (unit)

PALS	Positron annihilation lifetime spectroscopy
PANI	Poly(3,4-ethylenedioxythiophene)
PECVD	Plasma-enhanced chemical vapor deposition
PEDOT	Polyaniline
PEGDMA	Poly(ethylene glycol dimethylacrylate)
PFDA	1H,1H,2H,2H-perfluorodecyl acrylate
PFBSF	Perfluorobutanesulfonyl fluoride
PFOSF	Perfluorooctanesulfonyl fluoride
PGMA	Poly(glycidylmethacrylate)
PHEMA	Poly(hydroxyethyl methacrylate)
PP	Plasma polymerization
p-Ps	Para-positronium
PPV	Poly(p-phenylene vinylene)
PPy	Polypyrrole
PSD	Photo-stimulated discharge
Ps	Positronium
ps	Picosecond (unit)
PV3D3	Poly(1,3,5-trivinyl-1,3,5-trimethylcyclotrisiloxane)
PVD	Physical vapor deposition
PVDF	Poly(1,1-difluoroethylene)
QMS	Quadrupole mass spectrometry
RS	Raman spectroscopy
SEM	Scanning electron microscopy
TBPO	Tert-butyl peroxide
TBPOB	Tert-butyl peroxybenzoate
TMGa	Trimethyl-gallium
TSC	Thermally stimulated current
TSD	Thermally stimulated discharge
TSPD	Thermally stimulated potential decay
UFF	Universal force field
µl	Microliter (unit)
µm	Micrometer (unit)
UV/VIS/NIR	Ultraviolet/visible/near-infrared spectroscopy
V	Volt (unit)
V3D3	1,3,5-trivinyl-1,3,5-trimethylcyclotrisiloxane
V3N3	1,3,5-trivinyl-1,3,5-trimethylcyclotrisilazane
V4D4	1,3,5,7-tetravinyl-1,3,5,7-tetramethylcyclotetrasiloxane
V4N4	1,3,5,7-tetravinyl-1,3,5,7-tetramethylcyclotetrasilazane

VASE	Variable angle spectroscopic ellipsometry
WCA	Water contact angle
XPS	X-ray photoelectron spectroscopy

List of Mathematical Symbols

A	Surface area
A_d	Associated area
$\mathrm{A_{fit}}$	Fitting parameter
β	Generation rate of charge carriers
$\mathrm{B_{fit}}$	Fitting parameter
β_h	heating rate
$\mathrm{c_B}$	BET constant
$\mathrm{C_{fit}}$	Fitting parameter
C_0	Geometry factor
C_a	Cahn number
c_D	Damping coefficient
C_g	Concentration in the gas
C_p	Heat capacity
C_s	Concentration at the surface
χ^*	Complex electric susceptibility
$\vec{D}$	Displacement field
$\hat{D}$	Amplitude
d_m	Stretch/compression distance
D_g	Gas diffusion coefficient
D_R	Rayleigh function
δ_L	Average thickness of boundary layer
δ_R	Electron layer thickness
E	Energy
E_a	Activation energy
$\vec{E}_{air}$	Electric field in air gap
$E_{a,t}$	Trap activation energy
E_d	Dissipated energy
$\vec{E}_i$	Internal electric field

ε_0	Vacuum permittivity
ε_r	Static relative permittivity
ε_r^*	Complex relative permittivity
ε_1	Real part of relative permittivity
ε_1	Imaginary part of relative permittivity
ε_{air}	Relative permittivity of air gap
ε_e	Relative permittivity of electret
ϵ_L	Mechanical strain
e_{re}	Release probability
η	Gas viscosity
η_v	Viscosoty
f	Associated function
f_0	Initial occupancy of energy traps
f_M	Force applied to system during deflection
F_r	Restoring force
f_V	Force exerted by voltage
G	Electrical conductivity
g	Carrier density ratio
ΔG_f	Gibbs free energy of a species
$\Delta G_{f,p}$	Gibbs free energy of products
$\Delta G_{f,r}$	Gibbs free energy of reactants
g_i	Generalized coordinate (i)
ΔG_r	Gibbs free energy of chemical reaction
γ	Cahn parameter
γ_{LG}	Surface tension at liquid-gas interface
γ_{SG}	Surface tension at solid-gas interface
γ_{SL}	Surface tension at solid-liquid interface
$\vec{H}$	Magnetic field strength
ΔH_f	Enthalpy of formation
ΔH_{vap}	Enthalpy of vaporization
h_g	Mass transfer coefficient
H_{vap}	Enthalpy of vaporization
i	Imaginary unit
I	Electric current
I^*	Complex electric current
$\vec{j}$	Current density
$\vec{j}_D$	Displacement current density
$\vec{j}_f$	Free current density

J_n	Mass flux
k	Rate constant (general)
$\mathrm{k_B}$	Boltzmann constant
k_d	Decomposition rate constant
k_{depo}	Deposition rate
k_f	Spring constant
k_p	Polymerization rate constant
k_s	Surface reaction rate constant
k_t	Termination rate constant
κ	Ratio parameter
L	Lagrangian
l	Length of a unit
λ_0	Spin averaged decay rate
L_p	Plate length
M	Mobility
m	Mass
$[\mathrm{M}_i]$	Monomer concetration of monomer i in the vapor phase
m_i	Amount of substance (in copolymer)
μ	Chemical potential
μ_e	Electron mobility
μ_h	Hole mobility
μ_M	Mobility
μ_o	Vacuum permeability
n	Charge carrier density
N	Number of segments
n_0	Initial charge carrier density
N_p	Number of units
n_r	Refractive index
N_t	Distribution of trap levels
ν	Gas viscosity
ω	Angular frequency
ω_f	Frequency factor
$\vec{P}$	Polarization
p	Pressure
p_{EG}	Partial pressure of ethylene glycol
p_m	Partial pressure of the monomer
P_s	Shape factor
p_{sat}	Saturated vapor pressure

$p_{sat,EG}$	Saturated vapor pressure of ethylene glycol
Φ	Electrostatic potential
ψ	Thermodynamic free energy
q	Electric charge
q_0	Initial electric charge
q_e	Electric charge at electret surface
R	Universal gas constant
R	Electrical resistance
R_c	Contour length
R_h	Hole radius
r_n	Reactivity ratio
ρ	Gas density
ρ_{el}	Specific electrical resistance
S	Entropy
σ	Surface charge
σ_L	Mechanical stress
T	Temperature
t	Time
T_0	Starting temperature
$\tan(\delta)$	Dissipation factor
τ	Time constant
τ_i	Positron lifetime
T_c	Critical temperature
t_d	Deposition time
T_g	Glass transition temperature
T_k	Total kinetic energy
T_m	Melting temperature
T_{mp}	Temperature at current peak
T_s	Substrate temperature
T_r	Room temperature
θ	Contact angle
u	Order parameter
$V*$	Complex voltage
v_0	Velocity
V_{ad}	Adsorbed volume
V_f	Free volume in the polymer
V_m	Volume of the molecular chains
V_{ml}	Monolayer volume

V_{mol}	Molar volume
V_p	Volume of the polymer
V_{pt}	Potential energy
V_s	Surface potential
x_0	Initial position
x_{air}	Air gap width
x_e	Electret film thickness
x_f	Film thickness
ξ	Pressure ratio
Z^*	Complex impedance
ζ	Damping ratio

List of Figures

List of Tables

1. Introduction

Polymer thin films have become an integral part of our everyday life. They consist of macromolecular organic chains and impress with their flexible properties, unique adjustable functionality via the choice of the monomer groups and low production costs [1]. For this reason, they open new pathways compared to crystalline metals or ceramics and are used nowadays in an increasingly large number of applications. These range, among others, from optical and sensor applications [2–6] to food packaging [7, 8] to photoresists in the semiconductor industry [9, 10]. In the semiconductor industry, too, the demand for high-quality polymer thin films is growing in the course of organic electronics, where devices such as organic field-effect transistors (OFET), organic light emitting diodes (OLED) or organic solar cells (OSC) are manufactured in large quantities from flexible, inexpensive polymers [11–13]. It is estimated that the market for OLEDs alone will grow above 300 billion US$ in 2025 [14]. Compared to their inorganic counterparts, which are mainly deposited by chemical vapor deposition (CVD) or physical vapor deposition (PVD) processes via the vapor phase, the production of polymer thin films in industry and research is currently in most cases based on wet chemical processes [15–17]. However, these wet-chemically produced films are now reaching their limits in the current development of advanced devices and organic electronics. The films often contain solvent residues and cannot be uniformly applied to complex substrate geometries. Also, it is not possible to apply ultra-thin films on the lower nanoscale (< 10nm) because surface-tension effects and dewetting lead to failure [18]. One approach to circumvent these problems are polymer thin film deposition processes from the vapor phase. For inorganic thin films vapor phase deposition processes have become an indispensable part of today's industrial production lines as well as research institutes. Especially CVD processes draw the attention of the industry as well as research facilities due to their high-quality films that can be homogeneously deposited on large-area substrates as well as complex geometries. The combination of CVD with organic chemistry is thus

an increasingly popular way to deposit conformal polymer thin films from the vapor phase [1, 19]. The aim is to provide high-quality, tunable films without the use of organic solvents. One process that meets these requirements is initiated chemical vapor deposition (iCVD). Ever since its development started in the mid-1990s in the Gleason group at the Massachusetts Institute of Technology (MIT) [20–22], it has impressively proven over the years that it can combine the advantages of CVD, namely conformal film growth and high film quality, with solvent-less polymer synthesis [1, 19, 23–28]. Today, it can be found in a wide range of applications and is gradually expanding into the industrial world. Among the extensive application fields that it covers are biomedical barrier films [29, 30], membrane applications [31, 32] and dielectric films [33, 34]. The latter are used as insulators in organic electronics applications due to the excellent nanoscale film control [33–37].

The first objective of this work is the establishment and expansion of the iCVD process at the Chair for Multicomponent Materials (Prof. Dr. Franz Faupel). For this purpose, an iCVD system is first set up, which enables batch processes. In order to achieve higher deposition rates, the system is then expanded to enable continuous flow operation. In order to better understand the underlying reaction processes and to obtain a more precise control of the reactor atmosphere, an additional in-situ quadrupole mass spectrometry (QMS) extension is added for the first time to the iCVD process in the progress of this work. Chapter 4 investigates how this extension can be used to study the underlying reaction kinetics of the iCVD process and how the process control can be extended by in-situ QMS.

The next objective is the deposition of fluoropolymer electret films from the vapor phase via the home-made iCVD setup. Electrets are important functional dielectrics which contain a quasi-permanent surface charge and thus have in analogy to a permanent magnet a quasi-permanent electric field. These materials are used, for example, in the world-famous and million-fold produced electret microphone [38–40], energy generators [41–47], dosimeters [48, 49], respiratory masks (e.g. FFP, N95 and KN95) [50, 51], memristors [52] and transistors [53–56]. The electrets are intended to be used in novel electrostatic magnetic field sensors developed in close cooperation with the Chair for Functional Nanomaterials (Prof. Dr. Rainer Adelung) as Project A2 within the Collaborative Research Centre (CRC) 1261. However, since fluoropolymers are best suited for long-term charge storage, the electrets are typically produced individually from foil or bulk material. The reason for this is that most fluoropolymers cannot be deposited in sufficient quality as thin films from the vapor phase. The work in this objective is based

on the long electret experience of the Chair for Multicomponent Materials, where thin film electrets were produced by thermal evaporation of commercial Teflon AF polymer over many years. The production of iCVD electrets is pursued, because it is not clear whether the iCVD fluoropolymers are even superior to Teflon AF. Furthermore, compared to thermal evaporation, which belongs to the physical vapor deposition (PVD) processes, the CVD-typical large-area deposition of iCVD can enable large-area production of electret films, homogeneous coating of complex geometries such as porous and flexible substrates as well as precise control of the film thickness. Chapter 5 therefore examines for the first time the applicability of polytetrafluoroethylene (PTFE) films deposited by iCVD as electret films.

A further objective that evolves from the results in Chapter 5 is to tailor electrets especially for sensor applications. Despite the very good charge storage properties of PTFE electrets, some potential problems appear which can limit the performance of electret-based sensors. This objective is divided into four chapters. It is important to develop first of all a deeper understanding of the electrets. Chapter 6 examines thus the influence of different end groups on the charge storage properties of polymer films. Due to the underlying free radical polymerization in the iCVD process it is investigated whether it is possible to individually tailor the electret properties by using different deposition conditions and monomer/initiator combinations. In order to estimate the most promising end group for deep-level trap states, quantum chemical calculations are performed. To identify relevant electret-related parameters for the novel electrostatic magnetic field sensor, the sensor is presented in more detail in Chapter 7. It is then investigated whether new organic multilayer electrets produced by iCVD can potentially improve the sensor performance and solve electret-related challenges of the sensor. Furthermore, approaches are demanded to increase not only the charge decay challenges but also the amount of total surface charge, which represents a further parameter in electret sensors or generators. For this purpose, in Chapter 8 the possibility to increase the effective surface area of the polymer thin films is investigated. It is examined whether nanosize pores can be created by phase separation during iCVD. Again, a better understanding of the underlying phase separation is required. In addition, a measuring method must be applied that can detect the potential pores on the nanometer range. In all chapters shown so far, insulators have been considered. To complete the picture, Chapter 9 examines whether it is also possible to deposit potentially semiconducting or conducting polymers via the iCVD process. This means, can conjugated polymers

be deposited via iCVD?

Another challenge that emerges during the application of the deposited films is the insufficient adhesion of the especially fluoropolymer films to the substrates. This is a general problem that is also known from PTFE-coated frying pans, for example. For this reason Chapter 10 demonstrates the precise deposition of novel nanoscale, bio-inspired gradient copolymer films via iCVD for the first time. The material changes its chemical composition from polymer type A to polymer type B. With the help of the enhanced process control provided by the in-situ QMS extension, it is examined up to which lower film thickness these films can be produced. This approach is then used to investigate whether the adhesion of the deposited polymer films can be improved in this way and which new possibilities the materials offer, as they exhibit completely new physical and chemical properties that cannot be achieved with materials currently in use.

2. Fundamentals

This chapter is intended to review basic terms and relationships of this thesis for the reader. For more extensive studies on specific topics, further literature recommendations are given in the respective sections.

2.1 Chemical Vapor Deposition (CVD)

Chemical vapor deposition (CVD) is a term for coating processes that can be used to deposit material thin films from the gas/vapor phase on substrates by a chemical reaction [57–59]. Originally coined by Blocher in the 1960s, all CVD processes involve a chemical reaction, which distinguishes them from physical vapor deposition (PVD) processes like evaporation and sputtering where the film is not deposited by a chemical reaction [60, 61]. CVD is an important process which is nowadays an established component in the large-scale industrial production of numerous products. Semiconductor industry [62–65], glass refinement [66], packaging [67, 68] and barrier layers [69–71] are just a few examples of the application areas. The CVD process is just as common in materials science and other research fields to deposit high-precision material thin films in the nanometer range that can later be used for functional applications. Some advantages of CVD are the highly conformal film growth, the excellent quality of the deposited films, the possibility to coat porous samples as well as the relatively easy and cost effective upscaling and integration into existing process lines [57, 58]. The individual CVD variants differ in the reactor design and the precursors used. A distinction is generally made between atmospheric pressure chemical vapor deposition (APCVD) at pressures around 1 atm and low pressure chemical vapor deposition (LPCVD) for deposition under vacuum conditions whereby the latter variant is more common nowadays. Besides the classical thermal CVD there are various variants where other ways are pursued to start the process. One

advantage is, for example, that lower temperatures are required for activation. This is the case in the well-known plasma-enhanced chemical vapor deposition (PECVD) variant, where a plasma is used to decompose the source gas [72, 73]. In the hot filament chemical vapor deposition (HFCVD) variant, also known as hot wire chemical vapor deposition (HWCVD) or catalytic chemical vapor deposition (CATCVD), substrate temperature and filament temperature can be controlled separately [74]. Laser chemical vapor deposition (LCVD) uses a laser to heat only a certain area on the substrate, which enables spot coating [75, 76]. To better understand these processes, it is important to first gain insight into the basic CVD process.

2.1.1 CVD Processes

The basic underlying process is often illustrated by the scheme shown in Figure 2.1. Typically, a viscous flow takes place in the reactor, in which the precursor

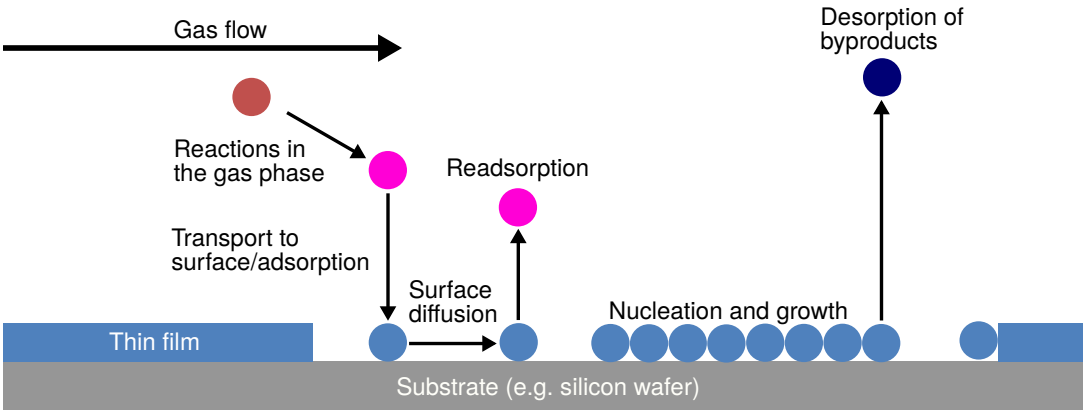

Figure 2.1: Schematic illustration of a conventional CVD process.

molecules move through the reactor at a certain velocity. Near the sample stage the velocity is reduced to zero, which leads to the formation of a so-called boundary layer. Its average thickness can be described by

$$\delta_L = \frac{10}{3} L_p \left(\frac{\eta}{v_0 \rho L_p} \right)^{\frac{1}{2}} \tag{2.1}$$

for a flow parallel to a plate of length (L_p) [57]. [1] The content of the square root is the inverse Reynolds number, which contains the gas viscosity (η) and the gas density (ρ). In the stagnant boundary layer diffusion takes place. The mass flux (J_1) can be described by

$$J_1 = \frac{D_g(C_g - C_s)}{\delta_L}. \tag{2.2}$$

The symbols D_g, C_g and C_s represent the diffusion coefficient, concentration in the gas and concentration at the surface, respectively. The expression

$$h_g = \frac{D_g}{\delta_L}. \tag{2.3}$$

is termed the mass transfer coefficient. Since δ_L is only weakly dependent on temperature, the temperature dependence of h_g is determined by D_g [57]. For gases this can be described by the Chapman-Enskog theory with the relation [79, 80]

$$D_g \propto T^{\frac{3}{2}}. \tag{2.4}$$

Once adsorption has occurred, surface diffusion and surface reaction, which lead to nucleation and film growth, take place. The flux can be described by the equation

$$J_2 = k_s C_s. \tag{2.5}$$

The symbol k_s is the rate constant for the surface reaction. First order kinetic is usually assumed for this reaction [57]. The rate constant follows Arrhenius behavior, hence

$$k_s \propto \exp\left(\frac{-E_a}{\mathrm{R}T}\right). \tag{2.6}$$

The symbols E_a and R represent the activation energy and the universal gas constant, respectively. During the surface diffusion the molecules can also be readsorbed. The byproducts of the reaction desorb and, once they have left the boundary layer, are transported out of the reactor by the gas flow and enter the exhaust filters of the pumping system. Some reactions can take place in the gas phase. For example, the precursor may be decomposed in the gas phase. However, the surface reaction, which forms the film, should take place as a heterogeneous reaction on the substrate. Predominantly homogeneous reactions in the gas phase, caused for example by wrong deposition parameters, can lead to powder formation

[1] This depends on the reactor design. A simple case is shown here. For more complex designs, it changes accordingly. Further details can be found in textbooks on fluid mechanics, e.g. by Durst [77] or Jayanti [78].

instead of film growth. Considering the state of equilibrium ($J_1 = J_2$), leads to the expression

$$C_s = C_g \left(\frac{k_s}{h_g} + 1 \right)^{-1} . \tag{2.7}$$

It is evident from equation 2.7 that the system for the case $k_s << h_g$ is controlled and limited by the surface reaction. A reasonable number of reactants is always available. In the case of $k_s >> h_g$ the surface concentration approaches zero. The regime is thus controlled and limited by the mass transport. Figure 2.2 shows schematically the typically observed deposition rate in these two regimes with increasing temperature. The growth is limited by the respective slower process.

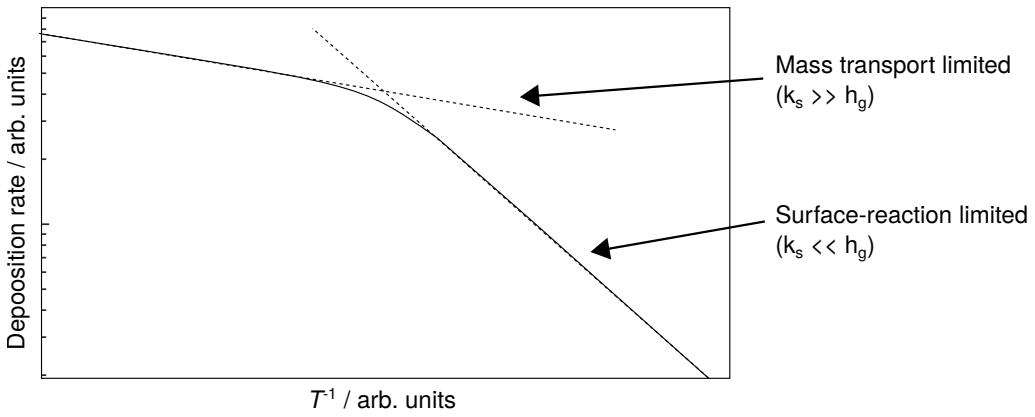

Figure 2.2: Illustration of typical surface-reaction limited and mass transport limited regimes of the deposition rate depending on the temperature in a CVD process.

According to equation 2.6, the temperature dependence of k_s is given by an exponential relationship, while h_g, as indicated in equation 2.3 and equation 2.4, follows a $T^{\frac{3}{2}}$-dependence. The growth of the film is finally determined by the growth mode. Generally, a distinction is made between island growth (Volmer-Weber growth)[81], layer-by-layer growth (Frank-van der Merwe growth)[82] and mixed growth (Stranski-Krastanov growth)[83], which are shown schematically in Figure 2.3. The surface diffusion and small sticking coefficient enables the mentioned powerful advantage of CVD to deposit highly conformal films as well as trenches and open porous structures. In PVD, where the particles reach the substrate by controlled transport via evaporation or sputtering without a chemical reaction, a line of sight growth is typically observed. Consequently,

fine structures such as trenches or open pores are not coated due to shadowing effects. Depending on the CVD precursors and processes, different material thin films can be produced. Some selected examples, which are also of high industrial importance, are presented in the following subsection.

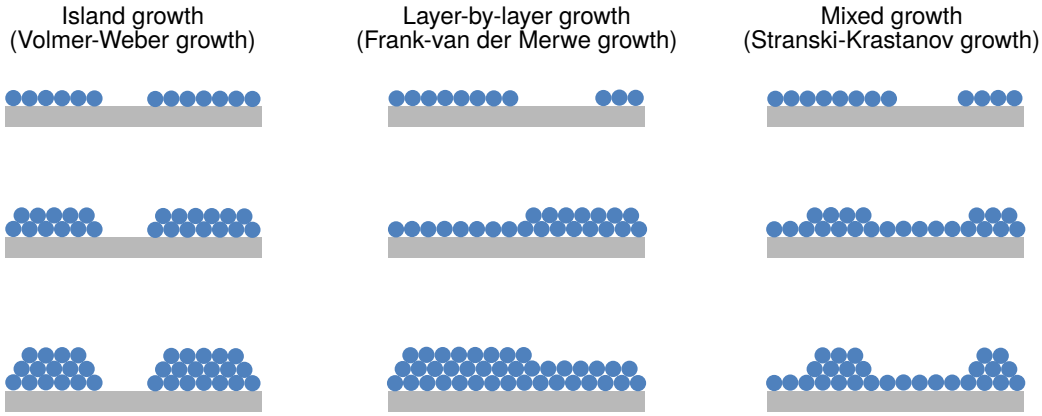

Figure 2.3: Different growth modes of a thin film (blue) deposited on a substrate (grey). Shown are island growth (Volmer-Weber growth), layer-by-layer growth (Frank-van der Merwe growth) and mixed growth (Stranski-Krastanov growth).

2.1.2 Reaction Processes

The Gibbs free energy of a species is given by [84]

$$\Delta G_f(T) = \Delta H_f^0 + \int_{T_r}^{T} C_p dT - TS^0 - \int_{T_r}^{T} \frac{C_p}{T} dT. \tag{2.8}$$

The symbols ΔH_f^0, T_r, S^0 and C_p represent the standard formation enthalpy, the room temperature, the standard entropy and the heat capacity, respectively. The Gibbs free energy of the chemical reaction can thus be expressed by [84]

$$\Delta G_r = \Sigma \Delta G_{f,p} - \Sigma \Delta G_{f,r}. \tag{2.9}$$

$\Delta G_{f,p}$ and $\Delta G_{f,r}$ represent the Gibbs free energy of the products and reactants, respectively. For the case $\Delta G_r < 0$ the reaction is favored, whereas for the case $\Delta G_r > 0$ the reaction does not occur. As shown in the following examples the CVD films can be formed by different types of reaction. These can include

pyrolysis, compound formation, oxidation and reduction [57, 85]. Metalorganic chemical vapor deposition (MOCVD) uses metalorganic precursors, which enables the deposition of III-V compound semiconductors. For the deposition of gallium nitride (GaN) based films, for example, trimethyl-gallium (TMGa) and ammonia (NH_3) can be used [57]:[2]

$$(CH_3)_3Ga_{(g)} + NH_{3\,(g)} \longrightarrow GaN_{(s)} + 3\ CH_{4\,(g)}$$

These III-V semiconductors are highly interesting for high performance III-V solar cells, LEDs and transistors. In PECVD, the introduced gases are activated by a plasma which leads to a deposition on the substrate. Well known examples are silicon nitrides (Si_3N_4) from silane (SiH_4) and NH_3 [57]:

$$SiH_{4\,(g)} + NH_{3\,(g)} \longrightarrow Si_3N_{4\,(s)} + 12\ H_{2\,(g)}\ ,$$

silicon dioxide (SiO_2) from SiH_4 and oxygen (O_2):

$$SiH_{4\,(g)} + O_{2\,(g)} \longrightarrow SiO_{2\,(s)} + 2\ H_{2\,(g)}$$

and amorphous silicon (a-Si) from SiH_4:

$$SiH_{4\,(g)} \longrightarrow Si_{(s)} + 2\ H_{2\,(g)}\ .$$

SiO_2 is used as dielectric thin films and a-Si as a thin film alternative to crystalline silicon solar cells. The combination of CVD with organic chemistry, which is also the topic of this work, has shown in recent years that even high quality polymer films can be deposited from the vapor phase. For this purpose, the basics of polymers will first be briefly reviewed in the next section to familiarize the reader with some important terms used throughout this thesis.

2.2 Polymers

Polymers have become an integral part of everyday life. Innumerable products ranging from lunch boxes to car parts are made of polymers. The advantages

[2] These chemical formulas, which are frequently given in the literature, summarize the general process. Typically, far more complex processes can take place, which lead to the film formation. For further details the reader is referred to the literature of Smith [85] and Ohring [57].

over metals or ceramics are often the lower costs, the lower weight and the simple production of molded parts, e.g. by extrusion processes. According to the International Union of Pure and Applied Chemistry (IUPAC), a polymer can be described as "A substance composed of macromolecules" [86]. The individual macromolecules of which the polymer is composed consist of many repeating units. Polymers usually have a carbon backbone, which is the reason why they are counted as organic materials. Figure 2.4a shows as an example a macromolecular chain of poly(ethylene) (PE) with the corresponding repeating unit in 2D representation, which is repeated n times. Different conformations of the repeating units can occur in the chains [87]. A roughly distinction is made between cis, gauche and trans. As illustrated in Figure 2.4b, the angle of coverage is decisive, i.e. the angle of rotation that determines the conformation. By steric hindrance certain conformations are energetically favored. The section of the PE macromolecule sequence in Figure 2.4a for instance shows the all-trans conformation. Short chains are often referred to as oligomers. The macromolecules can be cross-linked

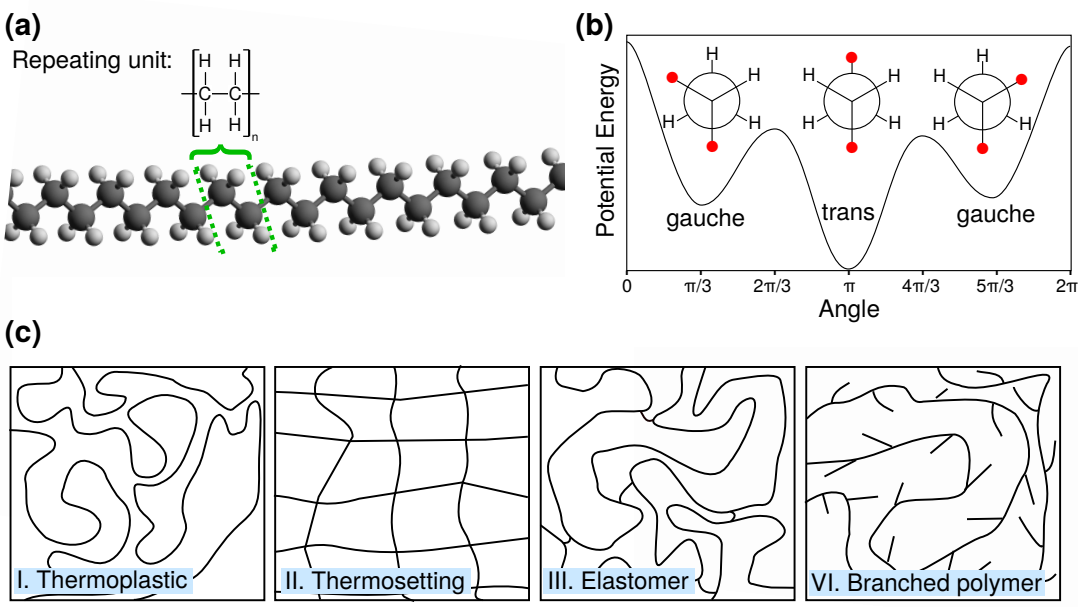

Figure 2.4: Introductive illustrations of polymers. (a) 3D illustration of PE macromolecular chain and the respective repeating unit. (b) Different conformations of the repeating units. (c) Illustration of different degrees of cross-linking between the macromolecular chains as well as branching and the respective terms used for the polymer.

with each other or be present as non cross-linked chains. Depending on the degree of cross-linking, a distinction is made between thermoplastics, thermosettings and elastomers, as shown in Figure 2.4c. Thermoplastics have no cross-linking and are present as long chains. Thermosettings and elastomers are cross-linked. Thermosettings have a high degree of cross-linking, which results in a dense organic network. Elastomers, on the other hand, have a much lower degree of cross-linking and are rather wide-meshed. Furthermore, the individual chains may have branches, therefore they are also referred to as branched polymers. Preferably in non-branched polymers without bulky side-groups, the chains often tend to arrange themselves into higher ordered regions. These polymers are referred to as semi-crystalline polymers and the degree of crystallization indicates how strong the crystalline portion in the polymer is in comparison to the amorphous part. If the degree of crystallization is zero, the polymer is referred to as amorphous. The amorphous, disordered arrangement in the polymer creates unoccupied space between the chains, which is called free volume. The volume of the polymer (V_p) is thus comprised of the volume of the molecular chains (V_m) and the free volume (V_f)

$$V_p = V_m + V_f. \tag{2.10}$$

In the amorphous regions there is a glass transition temperature (T_g) at which the polymer changes from a hard, brittle mechanical behavior to a rubber-like state. The origin is the onset of long range chain mobility when the glass transition temperature is reached. A definition can be given via the viscosity η_v:

$$T_g := T(\eta_v = 10^{12}\,\mathrm{Pa\,s}) \tag{2.11}$$

Once the polymer has reached this temperature the mechanical properties change and it can be molded into any shape. In semi-crystalline polymers apart from T_g there is also a melting range (T_m) in which the crystalline regions are detached. The ratio of T_g to T_m is typically

$$\frac{T_g}{T_m} = \kappa, \text{ with } 0.5 < \kappa < 0.8. \tag{2.12}$$

2.2.1 Polymer Functionality

The functional groups of the repeating units are decisive for the properties of the polymer. Some examples of important polymers are shown in Figure 2.5. Hydrocarbon based polymers with C-H bonds along the carbon backbone are very common. The simplest and best known example is PE [88]. In case the

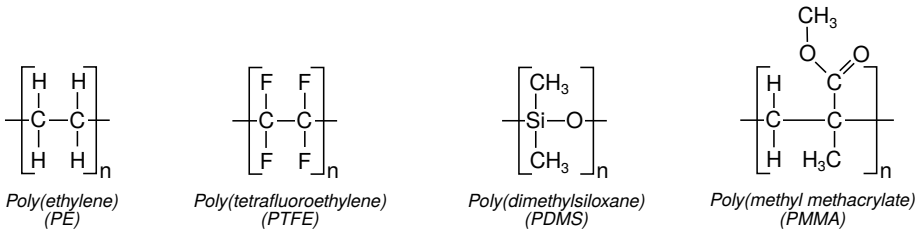

Figure 2.5: Examples of polymers with different functionalities.

polymer is a fluorocarbon, i.e. a polymer based on electronegative C-F bonds, it is termed fluoropolymer. Certainly the most important representative is poly(tetrafluoroethylene) (PTFE), which also has a carbon backbone like PE, but instead of C-H it exclusively has C-F bonds [88, 89]. This gives PTFE and other fluoropolymers a typically hydrophobic character and strong resistance to solvents, bases and acids. In case C-Si bonds occur in the polymer, the polymer is classified as an organosilicon [88]. The functional group Si-O-Si is specifically referred to as siloxane [88, 90]. A well-known example is poly(dimethylsiloxane) (PDMS), which is used, for example, in medical applications. Structural properties are also determined by the functional groups in the polymer. For example, polymers with bulky side-groups in the repeating units, such as poly(methyl methacrylate) (PMMA), tend to be completely amorphous. While the compact macromolecules of PTFE mentioned above have a high degree of crystallinity. This influences T_g and T_m and thus the mechanical character, as outlined above in Section 2.2. The above-mentioned degree of cross-linking also significantly changes the properties of the polymers. It determines whether the polymer exhibits thermoplastic, thermosetting or elastomeric behavior. The properties of the polymer can also be adjusted by adding other materials such as fibers, carbon nanotubes or nanoparticles. Among other things, modified mechanical behavior [91, 92] or electrical conductivity [93, 94] can be obtained in this way. The hybridization of the carbon atoms in the polymer backbone influences the electronic properties. For semiconducting or conducting polymers, for example, conjugated systems are of interest, in which single and double bonds alternate along the polymer backbone. Further details on conjugated polymers are given in Section 2.4.

2.2.2 Copolymers

If the macromolecule consists of two or more different repeating units, it is referred to as copolymer, terpolymer and so forth. Copolymers are most often

encountered. Depending on the arrangement of the repeating units, different types of copolymers can be distinguished, as illustrated in Figure 2.6. In random copolymers, the repeating units are randomly distributed. Alternating copolymers periodically switch between the two different repeating units. In block copolymers, block segments consisting of repeating units of one type alternate along the chain. Gradient copolymers start with repeating units of one type at one end of the chain and gradually change to the other type. Graft copolymers include homopolymer chains to which chains of repeating units of the other type are attached. A mixture of two different homopolymer chains that are not covalently bonded together is called a polymer blend and is not termed a copolymer. Copolymers can be used to build up different functional groups and thus change the properties in a targeted way. Well-known examples are styrene-butadiene, which is used millionfold in car tires, or the terpolymer acrylonitrile butadiene styrene, which is used among others in the automobile and electrical industry or for well-known plastic bricks (LEGO).

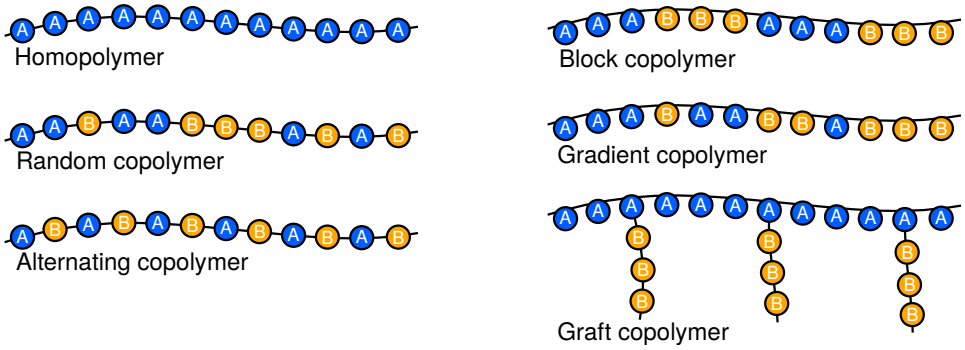

Figure 2.6: Schematic illustration of different copolymer types. A and B represent different repeating units.

2.2.3 Polymerization

Polymers are produced by polymerization. This can be divided into chain growth-reactions and step-growth reactions [95].

Chain-growth Reaction

In the chain-growth reaction, as demonstrated here in the example of free radical polymerization, the start takes place by the decomposition of initiator molecules

into radicals [96].

$$\mathrm{I} \longrightarrow 2\ \mathrm{R}\bullet$$

The rate for this can be described by [96]

$$R_d = 2fk_d[\mathrm{I}]. \tag{2.13}$$

The symbols f, k_d and [I] represent the initiator efficiency, the decomposition rate constant and the initiator concentration, respectively. The primary radicals reach the monomer molecules, which provide the first repeating units.

$$\mathrm{R}\bullet + \mathrm{M} \longrightarrow \mathrm{R\text{-}M_1}\bullet$$

The active chains then connect to further monomer molecules and turn them into repeating units of the active chain. This is the chain growth or propagation step.

$$\mathrm{R\text{-}M}_n\bullet + \mathrm{M} \longrightarrow \mathrm{R\text{-}M}_{n+1}\bullet$$

The termination of the chain growth can occur by the encounter of two active chains

$$\mathrm{R\text{-}M}_n\bullet + \mathrm{R\text{-}M}_m\bullet \longrightarrow \mathrm{R\text{-}M}_{n+m}\text{–R}$$

or for example by the encounter of an active chain and an initiator radical

$$\mathrm{R\text{-}M}_n\bullet + \mathrm{R}\bullet \longrightarrow \mathrm{R\text{-}M}_n\text{–R}$$

or even by the encounter of two initiator radicals.

$$\mathrm{R}\bullet + \mathrm{R}\bullet \longrightarrow \mathrm{I}$$

The rate of initiated polymerization is usually described by [96]

$$R_p = k_p[\mathrm{M}]\left(\frac{fk_d[\mathrm{I}]}{k_t}\right)^{\frac{1}{2}}. \tag{2.14}$$

The symbols k_p, [M] and k_t represent the polymerization rate constant, the monomer concentration and the termination rate constant, respectively.

Step-growth Reaction

In the chain-growth reaction the monomers were only able to react with the active chain. The step-growth reaction differs from this reaction because the monomers can react with each other [97]. Monomers which have two identical functional groups (X) react with monomers which have two functional groups of a different type (Y).

It is also possible to use monomers that exhibit both a functional group X as well as a functional group Y.

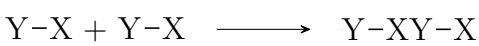

In this way, dimers are formed first, then trimers up to n-mers. H_2O is a typical by-product of these reactions. Important representatives here are polyester:

and polyamides:

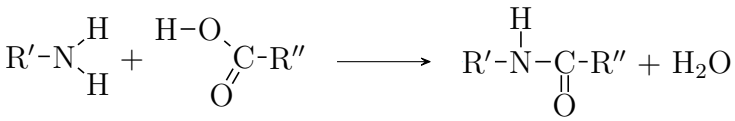

2.2.4 Polymer Thin Films

In order to fabricate a product from the polymer, thermoplastics are often formed into their final shape by the extrusion process [98]. In the case of thermosettings, cross-linking often takes place in the given mold already, since they cannot be further processed by, e.g. extrusion processes after the cross-linking. For many applications, however, polymer thin films are required that are supposed to have thicknesses in the lower micrometer or nanometer range. These include for instance photoresists for lithography in the semiconductor industry [9], protective coatings [99] and films for organic electronics [100]. Typically, a thermoplastic is dissolved in an organic solvent. This solution is then applied to the substrate to be coated using coating techniques such as spin coating, dip coating or drop casting [15]. After evaporation of the organic solvent, a thin film of the polymer remains

on the surface. Other processes such as the Langmuir-Blodgett techniques [101] or self-assambled monolayers (SAM) [102] allow organic molecular layers to be applied from a liquid phase to substrates. However, in the case of spin coating, dip coating and drop casting, there must always be a suitable solvent to dissolve the polymer. Many polymers such as PTFE are therefore not accessible with these techniques. Also, residual solvents in the film can change the properties or even cause film failure. Furthermore, it is difficult to deposit layers on the lower nanometer range uniformly on the substrates. Also with Langmuir-Blodgett or SAM techniques, which allow organic layers in the nanometer range, it is only possible to coat special small organic molecules that lack the macromolecular character of polymers. Even if wet chemical polymerization can take place directly on the substrate, there is a lack of precise layer thickness control in the nanometer range due to surface tension effects and dewetting [28], as well as a lack of conformal coating of structures on the substrate. In addition, impurities may also be present here, which can considerably reduce the film quality, especially for applications in organic electronics. In order to overcome these limitations, there is a growing interest in the ability to deposit high quality polymer thin films directly from the vapor phase. PVD of polymer thin films has been reported in numerous articles. The polymer films can be produced by rf sputtering [103, 104], thermal evaporation [105] or laser ablation [106, 107] for example. However, they are not based on well-controlled chemical reactions and high energies are often involved. They therefore do not preserve the macromolecular character of the polymers. The result is often a polymer thin film that deviate significantly from the original properties. CVD is based on chemical reactions that form the thin film. For this reason they are particularly attractive for the deposition of polymer thin films. A couple of processes have been established for this purpose, which will be introduced to the reader on the following pages.

2.3 Chemical Vapor Deposition of Polymers

As already outlined in Section 2.1 the combination of CVD with organic chemistry has shown in recent years that high quality polymer thin films can be deposited without the use of any solvents [1]. Meanwhile, a large number of different variants of organic CVD have emerged. Some of these processes are briefly introduced below and the advantages and disadvantages of each process are outlined.

2.3.1 Parylene Deposition

The deposition of poly(para-xylylene) (Parylene N) and its derivatives is used to deposit high quality, pinhole-free polymer thin films with different functionalities on large-area substrates [108, 109]. The basic process is shown in Figure 2.7a for the derivative Parylene C, which is commonly used. In the deposition process, a dimer is first vaporized and then brought to a temperature range around 650°C, resulting in two di-radicals [110]. These di-radicals react with each other and form the parylene polymer on cooled substrates in the reactor. Meanwhile, a large number of parylene derivatives exist for various applications. These range from barrier layers for biomedical devices to electronic applications [111]. The process is also used on an industrial scale. A limitation is that these derivatives often have to be specially prepared and the toolbox of monomers available in wet chemistry cannot be used. Complex synthesis steps are required to obtain starting materials with the desired functionality. Established, large-scale industrial polymers such as PTFE, PE or PS cannot be deposited by the process.

2.3.2 Plasma Polymerization (PP)

Plasma polymerization originates from the PECVD area. It is an established process using a plasma to deposit the polymer films with the help of a precursor gas [112]. This leads to a variety of processes that occur in the plasma. Yasuda has proposed a simplified mechanism for these processes [113], which is shown in Figure 2.7b. Due to the many processes and side reactions, the films deposited by plasma polymerization exhibit a high degree of cross-linking. The films show a very good adhesion to the substrate and high resistance to external stress and elevated temperatures. Due to the good adhesion and resistance of the films, they are often used as protective coatings [114]. Thermoplastics with long linear chains cannot usually be deposited using plasma polymerization. During the deposition of PTFE by hexafluoropropylene oxide (HFPO), for example, an organic network is formed rather than linear CF_2 chains, which is why it is often referred to as PTFE-like films. In addition, thicker layers above 1 µm can cause stress in the film, which can lead to the failure of the film. An alternative at the expense of the deposition rate is pulsed plasma polymerization, where the stress in the film can be reduced [115, 116].

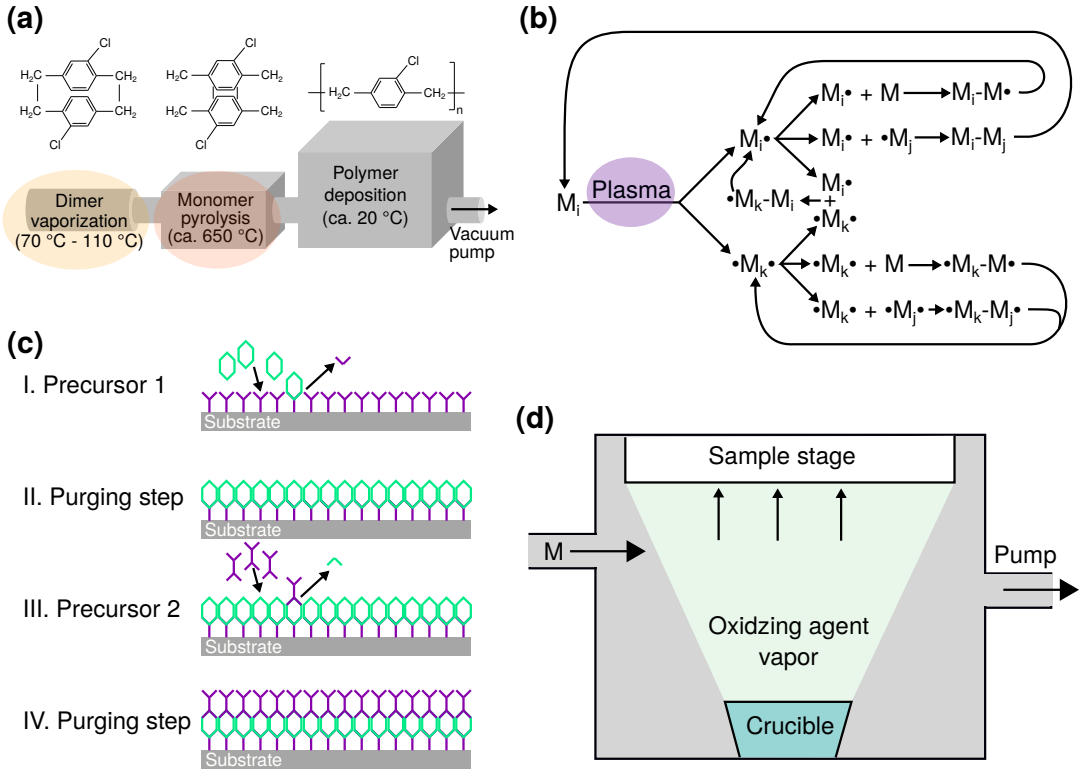

Figure 2.7: Schematic representation of different polymer CVD processes. (a) Parylene deposition is shown using the example of Parylene C. (b) Many processes take place during plasma polymerization. The figure shows a simplified process scheme according to Yasuda [113]. (c) The molecular layer deposition (MLD) cycle involves (I.) the introduction of a precursor which is then coupled to the functional groups on the substrate by a coupling reaction. (II.) A purging step is followed by (III.) the introduction of a further precursor, which again undergoes a coupling reaction with the functional groups on the surface. This is followed by (IV.) another purging step to remove the by-products. (d) In oxidative chemical vapor deposition (oCVD), an oxidizing agent is used to achieve step growth polymerization of an introduced monomer.

2.3.3 Molecular Layer Deposition (MLD)

Like the atomic layer deposition (ALD) process, the molecular layer deposition (MLD) process is based on a self-limiting surface reaction. In this way, the films can be applied layer by layer, enabling precise control at the molecular level [117]. This accuracy and pinhole free fabrication on the molecular level is not possible with other processes like spin coating and therefore it has found its place in many different applications such as packaging, solid-state batteries and catalysis [118]. The layers produced by MLD are often short oligomeric chains which are bound to the substrate. For the deposition of thicker films other techniques are therefore preferable. The underlying MLD process cycle, as illustrated in Figure 2.7c, involves (I.) the introduction of a bifunctional precursor that reacts with the functional groups on the surface [119, 120]. (II.) A subsequent purging step removes byproducts or excess molecules. (III.) A second bifunctional precursor is then introduced, which reacts with the functional groups on the new surface [119, 120]. (IV.) After this step another purging step is performed. This is referred to as an MLD cycle. The reactions often take place by amide coupling, urea coupling or other linking chemistry [120]. An example is the growth of polyamides [119]:

1.) $|\text{-}NH_2 + ClCO(CH_2)4COCl_{(g)} \longrightarrow |\text{-}NHCO(CH_2)4COCl + HCl_{(g)}$

2.) $|\text{-}NHCO(CH_2)4COCl + H_2N(CH_2)6NH_{2(g)} \longrightarrow$
$|\text{-}NHCO(CH_2)4CO\text{-}NH(CH_2)6NH_2 + HCl_{(g)}$

Other layers that can be synthesized in this way are for example polyurethane [121] and polythiourea [122].

2.3.4 Oxidative Chemical Vapor Deposition (oCVD)

Oxidative chemical vapor deposition (oCVD) enables the deposition of conjugated polymer systems from the vapor phase. The process is based on a step growth polymerization [123]. A monomer vapor and the vapor of an oxidizing agent (e.g. $Fe(III)Cl_3$), which is present in a crucible, are introduced into the reactor and a spontaneous reaction takes place on the substrate surface as shown schematically in Figure 2.7d. The oxidizing agent reacts with a monomer molecule, which then loses an electron and becomes a cation radical. The cation can now react with another monomer molecule to form a dimer, followed by a deprotonation [123, 124]. This is continued by further reactions with the oxidizing agent in a step growth

mechanism and a conjugated system is formed. In this way films like poly(3,4-ethylenedioxythiophene) (PEDOT) [123, 125] or polyaniline (PANI) [126, 127] can be deposited on the substrates and tuned by the deposition parameters. When depositing PEDOT with Fe(III)Cl_3, for example, the oxidizing agent also acts as a dopant by incorporating chlorine into the film [124]. These polymers are used as conductive layers in organic electronics devices. Further information on conductive polymers can be studied in Section 2.4.2 of this chapter.

2.3.5 Initiated Chemical Vapor Deposition (iCVD)

Besides the processes introduced above, initiated chemical vapor deposition (iCVD) is another solvent-free process for the deposition of highly conformal polymer thin films from the vapor phase. As it is a central part of this work, it is discussed in more detail here. In comparison with the processes presented in Section 2.3.1-2.3.4, it shows its strength in the film thickness range from about 10 nm to several µm as illustrated in Figure 2.8. It is thus a versatile tool for many different applications, as presented in the following.

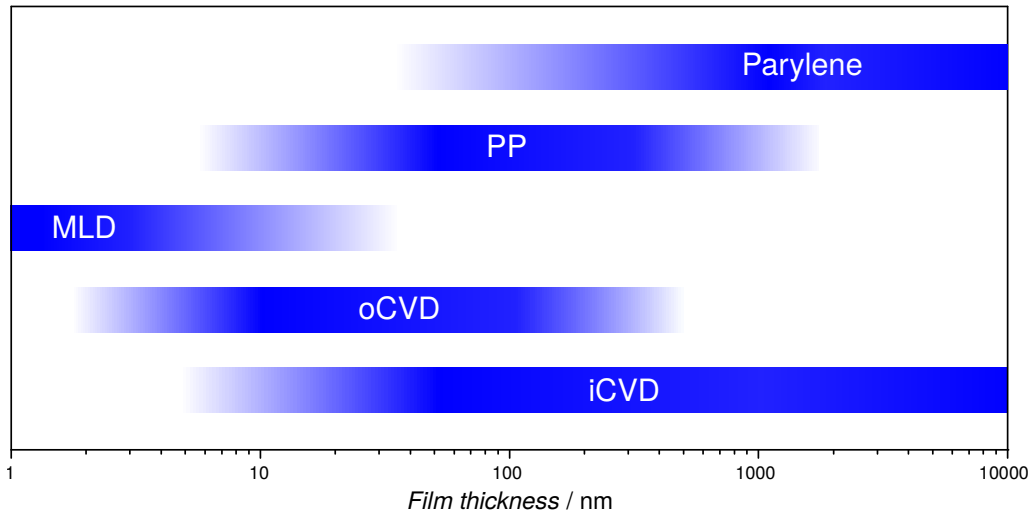

Figure 2.8: Classification of the different coating processes in relation to their typical coating thickness ranges. The values originate from [1, 27, 33, 128].

I. Introduction to iCVD

The origin of iCVD can be found in the Gleason group at the Massachusetts Institute of Technology (MIT) [19, 23–27]. The process has rapidly drawn the attention, because the CVD-typical growth enables chain-growth polymerization of high quality polymer films and conformal deposition on plain as well as porous substrates and other complex structures with nanoscale film thickness control [129]. Furthermore, mild deposition conditions enable the preservation of functional monomer groups and the coating of temperature sensitive substrates such as copy paper or flexible organic substrates. Meanwhile many different polymer films can be deposited by iCVD. Often acrylates or methacrylates are encountered as monomers. Important methacrylates are in this connection hydroxyethyl methacrylate (HEMA) for the deposition of hydrogels [30, 130] and glycidyl methacrylate (GMA) for the deposition of epoxy-like components [131, 132]. In the case of acrylates, for instance, n-butyl acrylate (nBA) to n-hexyl acrylate (nHA) [133, 134] as well as diethylaminoethyl acrylate (DEAEA)[135] can be found. Siloxane type polymers can be obtained by using the monomers 1,3,5-trivinyl-1,3,5-trimethylcyclotrisiloxane (V3D3), 1,3,5,7-tetravinyl-1,3,5,7-tetramethylcyclotetrasiloxane (V4D4), hexamethylcyclotrisiloxane (D3) or octamethylcyclotetrasiloxane (D4) [35, 136, 137] and silazane ones by applying 1,3,5-trivinyl-1,3,5-trimethylcyclotrisilazane (V3N3) or 1,3,5,7-tetravinyl-1,3,5,7-tetramethylcyclotetrasilazane (V4N4) [138]. Fluoropolymers can be deposited by hexafluoropropylene oxide (HFPO) [21, 139, 140] or by fluoroalkyls like 1H,1H,2H,2H-perfluorodecyl acrylate (PFDA) [141, 142]. [3] For this reason, iCVD can be found in many different applications ranging from organic electronics [33, 34] to anti-fouling layers [143, 144] to biomedical applications [29, 30]. The fundamental process is similar for all depositions.

II. The iCVD Process

The underlying mechanism in iCVD is a chain-growth reaction. The free radical polymerization variant can be found in almost all processes. Nevertheless, ionic polymerization is also demonstrated in some recent iCVD studies [145]. The first reports by Gleason et al. are about poly(tetrafluoroethylene) (PTFE) thin film deposition by thermal decomposition of self-initiating hexafluoropropylene oxide (HFPO) in a hot-filament CVD (HFCVD) reactor around 1996 [20]. This yields PTFE film forming difluorocarbene (CF_2) and a trifluoroacetyl fluoride

[3] This is by far not the complete list of polymers that can be deposited by iCVD. More comprehensive lists can be found in the literature [1, 28].

by-product [146].

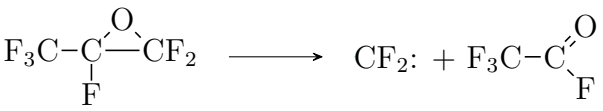

The same group reports in a later article the use of perfluorooctanesulfonyl fluoride (PFOSF) initiator to significantly increases the deposition rate of the PTFE process [21]. The initiator provides furthermore CF_3 end-groups to the CF_2 chains in order to prevent formation of polar end-groups [140]. After additional studies on organosilicon polymer thin films by thermal decomposition of D3 [147] they report that V3D3 can be grown at much lower filament temperatures when combined with the PFOSF initiator [148]. This effect is not observed for the combination of D3 and PFOSF. The polymerization is exclusively via the vinyl bonds of V3D3 and the cyclotrisiloxane ringstructure is preserved. The introduction of tert-butyl peroxide (TBPO) initiator is subsequently reported [22], which is up to now the most frequently used initiator [1]. At the same time the term iCVD starts to establish for all processes using such an initiator and many other monomer combinations are reported in the following years. The basic process begins with the introduction of monomer and initiator vapor into a HFCVD reactor as illustrated in Figure 2.9a,b. Polymerization starts as soon

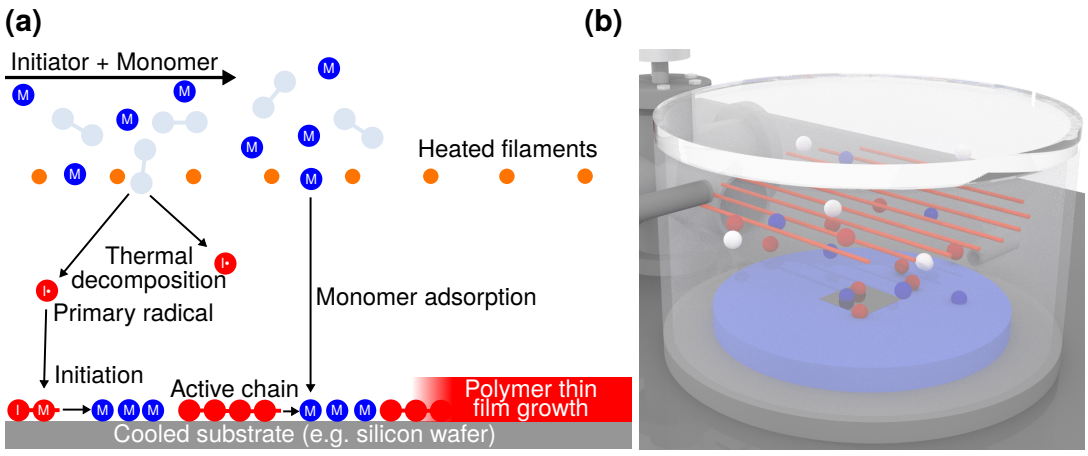

Figure 2.9: The iCVD process. (a) Schematic illustration of the iCVD process. M = monomer (blue), I· = Primary radical (red). (b) 3D illustration of the process in the typical HFCVD reactor geometry.

as the filaments are heated. The reaction kinetics are often described according to Lau and Gleason, who have conducted an extensive kinetic study [133, 134].

Considering the well-known initiator TBPO as an example, its decomposition provides two radicals:

$$\mathrm{I}_{(g)} \xrightarrow{\mathrm{k_{d1}}} 2\ \mathrm{R}^{\bullet}{}_{(g)}.$$

The temperature of the filament array is chosen in such a way that only the bonds of the initiator molecules break. In the case of TBPO, it is a weak peroxide bond. The functional groups of the monomer molecules are preserved in this way and the monomer is adsorbed at the cooled sample stage:

$$\mathrm{M}_{(g)} \xrightarrow{\mathrm{k_{ad,M}}} \mathrm{M}_{(ad)}.$$

Also the primary initiator radicals adsorb at the cooled sample stage but the dwell time of the primary initiator radicals is only very short:

$$\mathrm{R}^{\bullet}{}_{(g)} \xrightarrow{\mathrm{k_{ad,R}}} \mathrm{R}^{\bullet}{}_{(ad)}.$$

If the primary radical meets an adsorbed monomer molecule, the free radical polymerization will start at the cooled sample stage. Due to the short dwell time, the initiation of the primary radical and an adsorbed monomer molecule is best described by the Eley–Rideal mechanism [1, 149]. The reaction at the surface follows the kinetics for a free radical polymerization:

$$\mathrm{R}^{\bullet}{}_{(ad)} + \mathrm{M}_{(ad)} \xrightarrow{\mathrm{k_i}} \mathrm{M}_{1}{}^{\bullet}{}_{(ad)}$$

$$\mathrm{M}_{n}{}^{\bullet}{}_{(ad)} + \mathrm{M}_{(ad)} \xrightarrow{\mathrm{k_p}} \mathrm{M}_{n+1}{}^{\bullet}{}_{(ad)}$$

$$\mathrm{M}_{n}{}^{\bullet}{}_{(ad)} + \mathrm{M}_{m}{}^{\bullet}{}_{(ad)} \xrightarrow{\mathrm{k_t}} \mathrm{M}_{n+m\,(ad)} \text{ and } \mathrm{M}_{n\,(ad)} + \mathrm{M}_{m\,(ad)}$$

$$\mathrm{M}_{n}{}^{\bullet}{}_{(ad)} + \mathrm{R}^{\bullet}{}_{(ad)} \xrightarrow{\mathrm{k_{t2}}} \mathrm{M}_{n\,(ad)}$$

$$\mathrm{R}^{\bullet}{}_{(ad)} + \mathrm{R}^{\bullet}{}_{(ad)} \xrightarrow{\mathrm{k_{t3}}} \mathrm{R}_{2\,(ad)}$$

Depending on the deposition parameters, such as process pressure or filament temperature, these reactions can be influenced and thus the properties of the resulting polymer film.

III. iCVD Process Parameters

The rate of each reaction process can be controlled by the deposition parameters. The filament temperature, the process pressure as well as the partial pressure of the monomer and the substrate temperature are important parameters that determine a successful film deposition.

III.a. Substrate Temperature and Monomer Partial Pressure

One of the most important parameters is the substrate temperature (T_s) and the partial pressure of the monomers (p_m). The value for p_m and the corresponding saturated vapor pressure of the monomer (p_{sat}) at T_s result in the ratio

$$\xi = \frac{p_m}{p_{sat}}. \tag{2.15}$$

It is part of the adsorbtion isotherm in the Brunauer-Emmett-Teller (BET) theory

$$V_{ad} = \frac{V_{ml}\, \mathrm{c_B}\, \frac{p_m}{p_{sat}}}{\left(1 - \frac{p_m}{p_{sat}}\right)\left(1 - \left(1 - \mathrm{c_B}\right)\left(\frac{p_m}{p_{sat}}\right)\right)} \tag{2.16}$$

that accurately describes the adsorbtion in iCVD [133, 134, 150]. V_{ad}, V_{ml} and $\mathrm{c_B}$ represent the adsorbed volume, the monolayer volume and the BET constant, respectively. Best results can be obtained at $\xi \approx 0.3 - 0.5$, which corresponds approximately to monolayer adsorption. Liquid-like, supersaturated conditions can be expected for $\xi > 1$ which can lead to macroscopic droplet formation on the substrate and hence failure of the film. The vapor pressure can be estimated by the Clausius–Clapeyron relation according to

$$\ln\left(\frac{p_{sat,2}}{p_{sat,1}}\right) = \frac{\Delta H_{vap}}{\mathrm{R}}\left(\frac{1}{T_1} - \frac{1}{T_2}\right). \tag{2.17}$$

The symbols ΔH_{vap} and R represent the enthalpy of vaporization and the universal gas constant, respectively.

III.b. Filament Temperature and Deposition Rate

The filament temperature (T_f) influences the initiator decomposition rate (k_d) and is thus an important parameter in iCVD to control the generation of free radicals and deposition rate. In general, iCVD processes are operated at much lower temperatures, around 250 °C to 450 °C, than inorganic HFCVD processes,

where temperatures often exceed 800 °C. However, different growth regimes have also to be considered as described in Section 2.1. If the reaction is fast, the process is limited by the mass flow. In iCVD this is the adsorption process of the monomer. Since acrylates and methacrylates, which are often encountered as monomers in iCVD, usually have a fast propagation rate [28], the process is often limited by the adsorption process of the monomer. This is shown, inter alia, by the fact that the deposition rate increases with increasing overall flow rate [151].

III.c. Overall iCVD Process Pressure

The overall process pressure (p) is also an essential parameter. It is usually set between 25 Pa and 100 Pa. As mentioned in Section 2.1, high process pressures can cause the film-forming surface reaction to occur as a homogeneous reaction in the gas phase. This results in powder formation in the reactor. This is particularly pronounced with self-initiated monomers such as HFPO.

IV. Copolymers via iCVD

Copolymer synthesis is furthermore possible using different comonomers. The process introduced in subsection 2.3.5 II. involves now also the reactivity ratios ($r_1 = \mathrm{k_{11}/k_{12}}$ and $r_2 = \mathrm{k_{21}/k_{22}}$) of the comonomers where $\mathrm{k_{j,i}}$ is the respective rate constant. They describe which comonomer is preferentially added to the growing active chain. For iCVD the kinetics follow in this case the well-known Fineman-Ross equation[152]

$$\frac{[\mathrm{M_1}]}{[\mathrm{M_2}]}\left(1-\frac{m_2}{m_1}\right) = r_1\frac{[\mathrm{M_1}]^2 m_2}{[\mathrm{M_2}]^2 m_1} - r_2 \tag{2.18}$$

where $[\mathrm{M}_i]$ and m_i represent the comonomer concentrations in the vapor phase (the comonomer feed) and the amount of substance in the copolymer, respectively. Another possibility is to use the Kelen-Tüdős construction [153]. These approaches are based on the Mayo Lewis copolymerization equation [154]

$$\frac{\mathrm{m_1}}{\mathrm{m_2}} = \frac{[\mathrm{M_1}]}{[\mathrm{M_2}]}\frac{r_1[\mathrm{M_1}]+[\mathrm{M_2}]}{r_2[\mathrm{M_2}]+[\mathrm{M_1}]}. \tag{2.19}$$

The iCVD process enables a unique way to synthesize copolymers especially for combinations which lack a common solvent in traditional solution synthesis. In this way the degree of cross-linking in PHEMA can be changed by adding a cross-linker [30], or a fluoromonomer can be combined with an organosilicon [147].

This is only a short overview of the most important iCVD fundamentals related to this work. The reader is referred to the books and reviews of Gleason et al. for further insight into the topic [1, 19, 23–28].

2.4 Electronic Structure of Polymers

The electronic structure of polymers is of interest for many electrical and dielectric applications. Insulating polymers are used on a large industrial scale, for example as cable insulation [155] and electrets [156]. It is therefore important to examine their microscopic electronic structure in detail, as this has an effect on, e.g. electronic transport, breakthrough resistance and trap levels. Also polymer semiconductors and conductors are of great interest in the course of organic electronics and therefore their electronic structures to understand them better. In this section only a small insight can be given. Further information can be found in the excellent articles of Teyssedre and Laurent [157] or Hoffmann et al. [158].

2.4.1 Polymer Insulators

For a single atom, the individual orbitals (s-orbital, p-orbital, etc.) are considered. As soon as several atoms form molecules their wavefunctions overlap and the terms bonding and antibonding molecular orbital (MO) are used. This situation is shown schematically in Figure 2.10a. Looking at the hydrogen atom and the hydrogen molecule (H_2), the bonding MO is of lower energy and the antibonding MO is of higher energy than the atomic 1s orbital in hydrogen. Depending on how the atomic orbitals combine, constructive interference (bonding MO) or destructive interference (antibonding MO) occurs. The two electrons of the hydrogen molecule are thus typically present in the binding molecular orbital. As described above, the polymer backbone usually consist of carbon. It has six electrons per atom. Polymers are typically insulators because these carbon atoms are sp^3 hybridized as shown in Figure 2.10b. The sp^3 hybridization of carbon is well known from carbon in the form of diamond. The typical calculated density of states of diamond is shown in Figure 2.10c. In the case of polymers, however, there is the problem that no periodic boundary conditions can be set because the systems are amorphous or at most semi-crystalline. The larger and thus more complex the molecule becomes, the more orbital levels result. In the case of the long macromolecular chain, the representation soon becomes difficult to read, which is why often only highest occupied molecular orbital (HOMO) and lowest unoccupied molecular orbital (LUMO) are considered. They are often compared

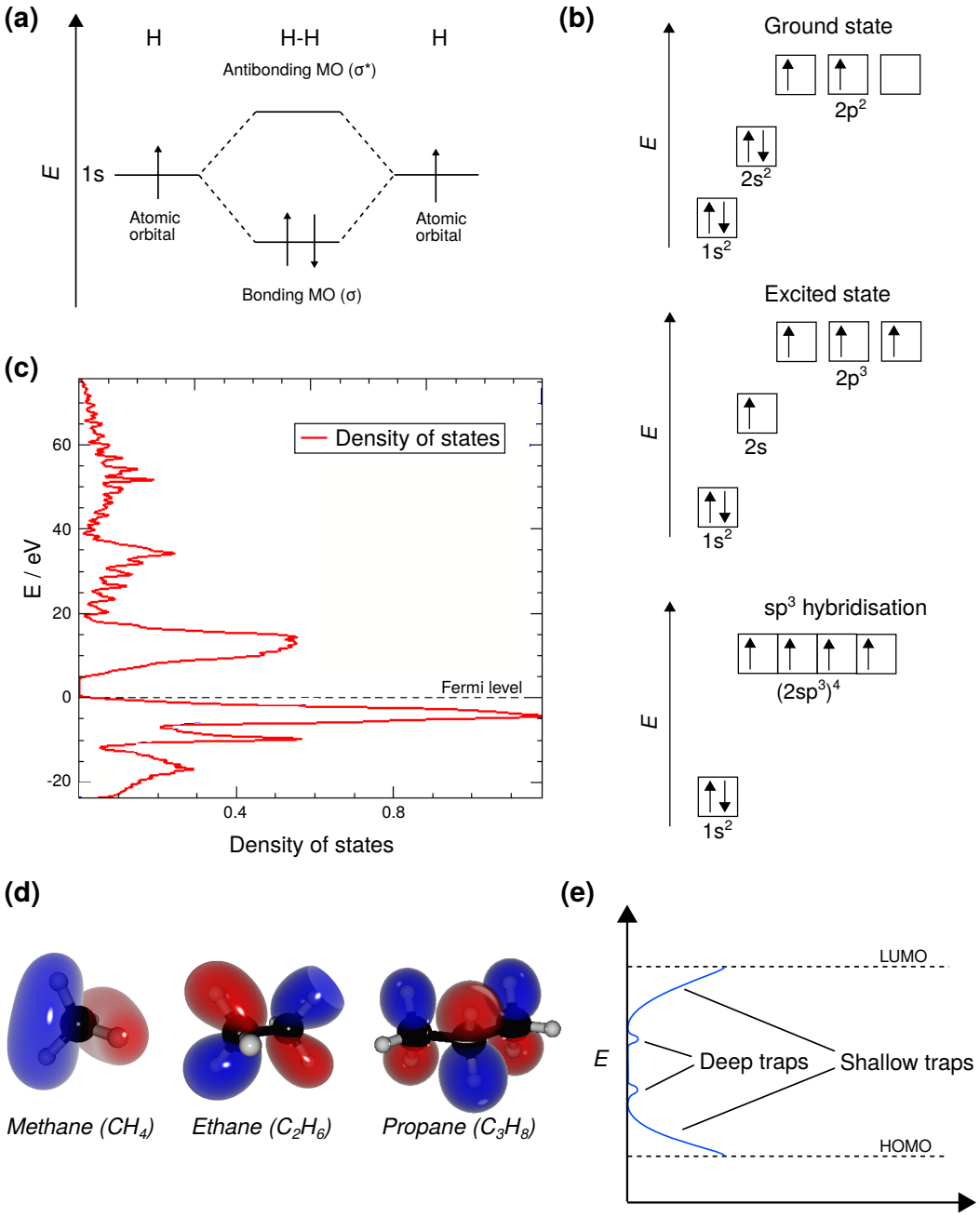

Figure 2.10: Electronic structure for polymer insulators. (a) Bonding and antibonding molecular orbitals illustrated by the hydrogen (H_2) molecule. (b) Illustration of the sp^3 hybridization typically found in the carbon backbone in polymers. (c) Typical density of states for sp^3 hybridized carbon (diamond) insulator obtained by Yet Another extended Hückel Molecular Orbital Package (YAeHMOP) (see 3.5 for details). (d) 3D orbital models of hydrocarbon chains of different lengths. (e) Schematic illustration of the density of states typically encountered in a polymer insulator.

with the well-known valence and conduction bands [159]. The development of the calculated HOMO for methane, ethane and propane is shown in Figure 2.10d. If this is continued, the information for a long poly(ethylene) chain is obtained. The region between HOMO and LUMO finally yields the band gap (E_g) of the insulator, in which no states exist. However, this only applies to ideal systems. In reality, additional trap states exist within the band gap. A distinction is made between shallow traps and deep traps. Shallow traps are created, for example, by different conformations of the macromolecule, which is most likely not in a perfect all-trans conformation [157]. As shown in Figure 2.10e, these shallow traps are located near the LUMO or HOMO band. They are also referred to as localized states in the band gap. Room temperature is often sufficient to release trapped carriers from these states so that they can hop to the next state. In this way they support the transport of charge to a certain extent [157]. The deep traps sit energetically much deeper in the band gap. They are caused by defects, interfaces and by-products [157] as well as certain chemical groups [160]. Carriers in the deep traps cannot be liberated so easily. For semiconducting and conducting polymers, as presented in the next subsection, these deep traps are therefore highly undesirable, which is why high quality, pinhole-free polymers without nanovoids are required here [161–164]. For other applications such as electrets, which are described in more detail in Section 2.5, the deep traps are on the other hand of great interest.

2.4.2 Semiconducting and Conducting Polymers

The development of semiconducting and conducting polymers was significantly influenced by the work of Heeger, MacDiarmid and Shirakawa in the 1970s [165, 166], for which they were awarded with the Nobel Prize in Chemistry in 2000 [167]. One of the first and best known polymers in which an extremely high electrical conductivity was discovered after appropriate doping is polyacetylene (PA). The conductivity here can reach up to 10^5 S/cm [168], which is roughly comparable to copper. The special feature that leads to this behavior in the polymer is the superposition of single and double bonds along the polymer chain. The carbon in this case is sp^2 hybridized similar to graphite. In this state the s-orbital and two p-orbitals form the hybrid orbitals as illustrated in Figure 2.11a. The remaining p-orbital (p_z) is in its original state. σ-bonds as well as π-bonds (overlapping of the p_z orbitals) can be formed to an adjacent carbon atom resulting in a double bond. This situation is schematically illustrated in Figure 2.11b. Because single and double bonds alternate along the carbon chain

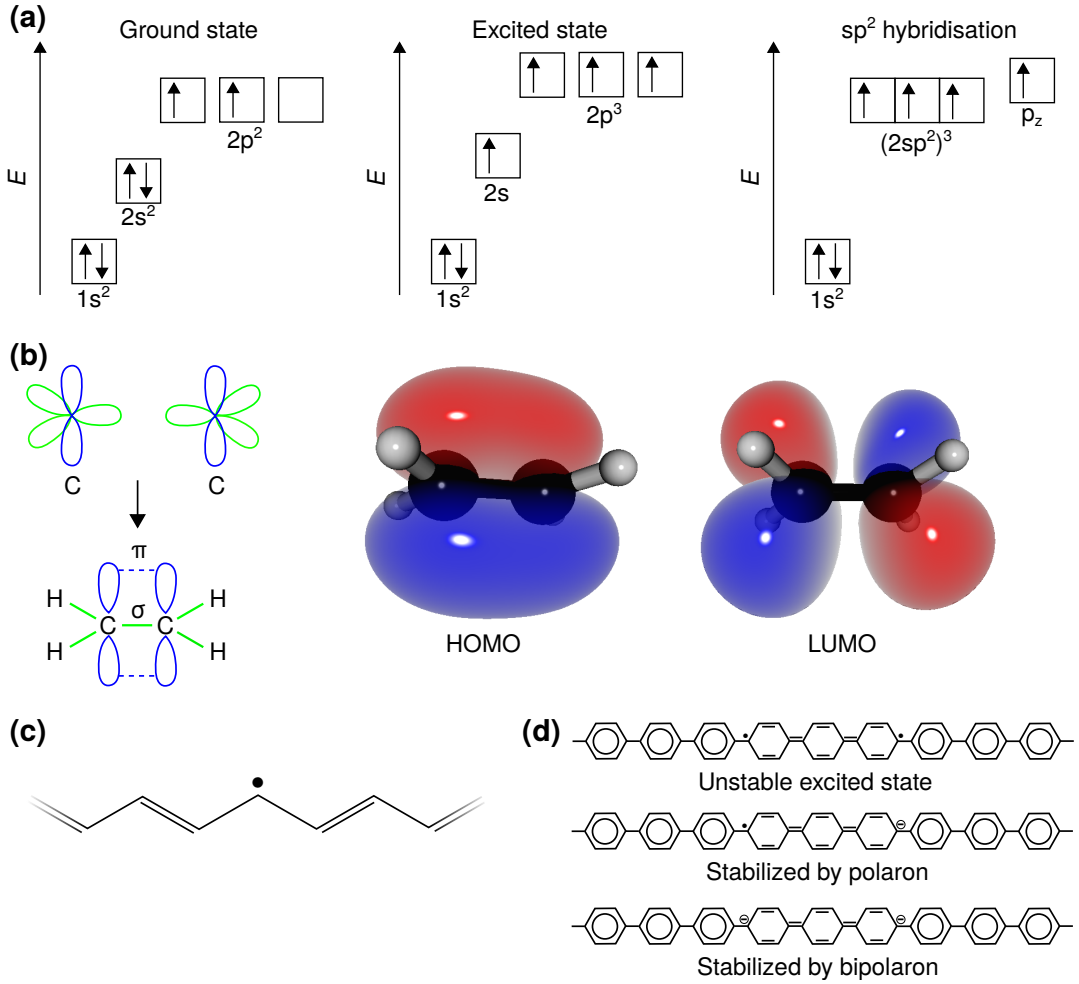

Figure 2.11: Semiconducting and conducting polymers. (a) Illustration of the sp^2 hybridization leading to a conjugated system along the polymer chain. (b) 3D model of the orbitals for sp^2 hybridized carbon. (c) The neutral soliton is a defect in the alternating bond pattern. It corresponds to a free radical defect. (d) The formation of a polaron or bipolaron after doping stabilizes the excited state necessary for electrical conductivity.

of the polymer, there are several possibilities of overlapping. However, the energy of a given boundary state exceeds that of the system. This means that there is a kind of state in which all structures are superimposed. This is referred to as a conjugated system. This leads to a delocalized π-electron system, in which π-bonds can no longer be localized. However, due to the Peierls instability this does not automatically lead to extremely high, metal-like electrical conductivity along the one-dimensional PA chain [158, 169]. Along the one-dimensional chain a so-called dimerization takes place. This dimerization costs elastic energy, which has to be counteracted. A state is reached in which the electronic energy is lowered to counteract the elastic energy. The lowering of the electronic energy results in the formation of a band gap and the PA chain thus behaves like an insulator or semiconductor. Further details can be found in the literature [158, 169]. In, e.g. trans-PA, bond defects in the alternating structure can occur. These are referred to as neutral solitons [170, 171] as illustrated in Figure 2.11c and correspond to a free radical defect. They are responsible for additional states within the band gap. The electrical conductivity can be further increased by doping, i.e. by adding or removing an electron. This differs from the doping of inorganic semiconductors, where acceptor or donor elements are introduced into the material. For PA it means, e.g. the oxidation, which involves the removal of an electron. In this way, positive (or negative) solitons are generated, which spread over several repeating units. This corresponds to adding an electron to the mid-gap state [168, 172]. At high doping concentrations these regions finally overlap and the emerging mid-gap band blends with the valence and conduction bands. The result is the metal-like conductivity along the polymer chain.
In polymers in which no soliton defects occur and no degenerated ground state is present, the conductivity after doping can take place via polarons [173]. This means that the excited state of the, e.g. benzenoid ground state is a state of higher energy which must be stabilized by the doping as illustrated in Figure 2.11d. This is done by replacing an unpaired electron by a charge, which stabilizes the excited state [168, 172]. If the second unpaired electron is also replaced by a charge, this is referred to as a bipolaron [172]. In contrast to solitons, where the movement is not hindered by any energy barrier, the movement of polarons occurs via thermally activated hopping. Another contribution is made by the shallow traps or localized states mentioned in Subsection 2.4.1. Often the ambient temperature is sufficient to release the trapped charge carriers, which then move from trap state to trap state. On the other hand, this also influences the mobility of the charge carriers. Besides PA, examples of well-known conducting or semiconducting polymers are poly(p-phenylene vinylene) (PPV), PEDOT, poly(3-hexylthiophene-2,5-diyl)

(P3HT), polypyrrole (PPy) and PANI [174–176]. As mentioned above, deep traps caused by nanovoids or impurities are undesirable in organic conductors and semiconductors. However, there are also electronic materials where deep traps are highly desirable. This is, e.g. the case for electrets, which are described in more detail in the next section. Here organic materials have to be used which provide many deep traps.

2.5 Polymer Electrets

Electrets are dielectric materials with a quasi-permanent real charge or quasi-permanent dipole polarization [156]. In analogy to a permanent magnet, they thus exhibit a quasi-permanent electric field. This feature also led to the name electret, which was first introduced by Heaviside in 1885 [177]. As the term 'quasi-permanent' implies, the electret state is a metastable one and the system seeks charge neutrality. However, by using appropriate electret materials, it has been possible to decelerate the charge decay to such an extent that it can be neglected compared to the device lifetime or application timespan in which the electret is used. For this reason, electrets are nowadays used in large-scale industrial applications and are the subject of current research. The best known example is certainly the electret microphone, which is produced over two billion times each year [40]. It was significantly influenced by Sessler and West around 1962 [38, 39]. Due to the built-in potential of the electret, no external bias voltage is required to operate the condenser microphone, allowing it to be used in small mobile applications such as mobile phones and hearing aids [39, 40, 156]. Other applications include electret generators for energy harvesting [41–47], electrostatic air filters (e.g. in FFP, N95 and KN95 masks) [50, 178], dosimeter [48, 49], organic transistor memory [53–56] and memristors [52]. Real charged polymer foams ("Piezoelectrets") can furthermore exhibit similar properties like piezoelectric materials and are used accordingly [179, 180].

2.5.1 Charging and Electret Materials

The real charge of non-polar electrets can be generated by electron or ion irradiation [51, 181, 182], contact electrification [183, 184] or other techniques. Ion irradiation in a corona discharge is the most commonly used charging technique in industry and research to fabricate electrets [156]. A point-to-plane arrangement as shown in Figure 2.12a is usually applied for this purpose. A high potential of several thousand Volt is applied to the tip electrode, resulting in a corona

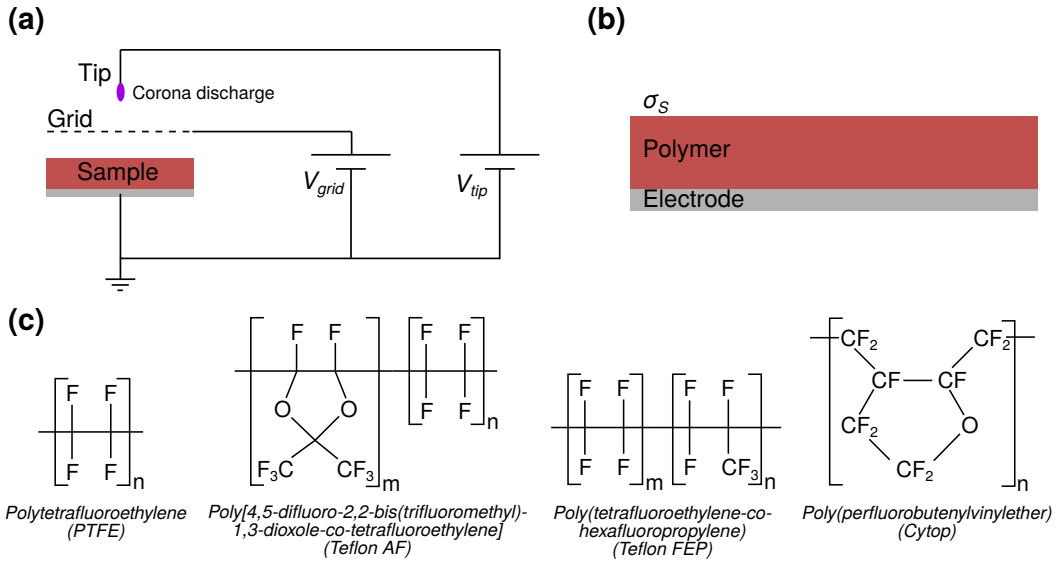

Figure 2.12: Basic illustrations for electrets. (a) Schematic illustration of a typical corona discharge setup used for the charging of the electrets. (b) Schematic illustration of a charged electret. (c) Structural formulas of known fluoropolymers, which are excellent for use as electrets.

discharge due to ionization of the air. The generated ions are accelerated to the ground plate and the polymer is irradiated with ions. The additional grid makes it possible to adjust the resulting surface potential more precisely and to obtain a more even distribution of the surface potential. Depending on the polarity of the tip, different ions are generated. Investigations with a mass spectrometer show that CO_3^- is preferably produced at negative potential in air [185]. It is generally assumed that these ions transfer their excess negative charge into the material and return neutralized to the surrounding atmosphere [156, 186]. After ion irradiation, the dielectric thus exhibits an effective surface charge (σ_S), as shown in Figure 2.12b. In the case of positively charged ions, electrons are accepted from the material. Often this injected real charge is also referred to as homocharge [187]. Fluoropolymers such as PTFE [156, 188–190], Teflon AF [191], Teflon FEP [192] and Cytop [193] have proven to be the best choice for this electret type. Their structural formulas are shown schematically in Figure 2.12c. Reasons for this are the extremely low electrical conductivity, high breakdown strength and hydrophobic character. Depending on the application, they are usually used in the form of thin foils with one-sided metalization. Inorganic dielectric materials

such as SiO_2 often suffer from humidity, which is why hydrophobic fluoropolymers are preferred. However, fluoropolymers cannot be used in some areas because PTFE, for example, cannot be deposited in sufficient quality by vapor deposition techniques. For this reason, SiO_2 thin films are often used when miniaturization of the electret device is desired [194]. If the charge has an opposite sign to the adjacent electrode, it is called a heterocharge. This is the result of orienting molecular dipoles, displacement of existing charge carriers in the material or ionizable impurities. Polar fluoropolymers, such as polyvinylidene fluoride (PVDF), have heterocharges due to their polarizable groups. However, they will not be discussed further in this thesis, since their main focus is on piezoelectric applications. The reader is therefore referred to the reviews of Ramadan et al. [195] and Mishra et al. [196] for further information on piezoelectric polymers.

2.5.2 Charge Carrier Trapping

It can now be assumed that an excess charge is brought into the system after the corona treatment. The injected real charge is presumed to be stored in the trap sites as described in Section 2.4. A good electret thus has many deep traps. The charge stability is often tested by thermal heating in thermally stimulated discharge (TSD) experiments, which were decisively advanced by van Turnhout [197, 198] or in isothermal long-term experiments [199]. Also photo-stimulated discharge (PSD) can be used in order to investigate traps in the material [200]. Further details on the experimental methods used for the electret characterization in this work are provided in Chapter 3. The fluoropolymers mentioned above (Section 2.5.1) obviously show many deep traps and therefore an excellent performance. The exact microscopic origin of these traps is still disputed and there are many different descriptions [157]. As discussed in Section 2.4, among other defects, nanovoids and interfaces can provide deep-level traps in the material. According to Sessler, these trap sites in the material can generally be described by three levels [160]: Primary traps are the traps that are formed at the functional groups of the polymer. Secondary traps are described as states when electrons between adjacent molecular chains are captured by charge affinity. The tertiary trap levels can be found at crystalline-amorphous interfaces if the polymer is a semi-crystalline one. Recently reported density functional theory (DFT) studies show that the polymer end-groups are furthermore crucial trap sites in Cytop fluoropolymers [201]. Other theoretical studies confirm that nanosize voids provide traps in the polymer [202]. The assumption that chemical defects, structures and impurities in the polymer lead to traps was also investigated in

this way [203–205]. Surface modification, for example RF plasma, can thus be used to produce new trap states and to influence the charge stability, as already shown experimentally [156, 190, 206, 207].

2.5.3 Charge Carrier Decay

As described, the state in the electret is only a metastable one. The occurring charge decay in the electret can be divided into internal and external decay processes [156].

Internal Decay

The internal decay is attributed to the Ohmic conductivity of the material as well as drift and diffusion of the charge carriers [156, 208]. Many different models, mostly based on kinetic equations, were proposed [199, 208–211]. But these models often do not describe the observed extraordinary long-term charge stability and the experimentally observed change from an initially fast charge decay to a slower long-term decay. Moreover, the experimentally determined values of the electrical conductivity (G) of typical electret materials and the observed extremely long charge lifetime often contradict each other. This can be shown with a simple example. With Ohm's law a simple relation can be found for the time constant (τ) and G, as outlined in more detail in Appendix A:

$$\tau = \frac{\varepsilon_0 \varepsilon_r}{G}. \tag{2.20}$$

The symbols ε_0 and ε_r represent the vacuum permittivity and the relative permittivity, respectively. Considering the conductivity of typical electret fluoropolymers, this would result in a calculated lifetime of only a few days. However, experimental studies show a significantly longer observed stability of the charge, which is still present even after several years [208]. A more accurate description was therefore published around 1999 by Małecki [212, 213]. In this theory, the strong electric field in the electret (E_i), which acts over a long period of time, is held responsible for the decrease in electrical conductivity. Under the assumption that the mobility ($\mu_M = \mu_e + \mu_h$) does not depend on the electric field in the electret, the decrease in electrical conductivity is caused by a decrease in carrier density (n) according to $G = nq\mu_M$. Here q represents the electric charge. The theory based on rate equations therefore considers activation and annihilation processes. Activation processes include the generation rate of carriers $\left(\beta = \left(\frac{dn}{dt}\right)_a\right)$. The annihilation processes take place at the electrode and by free carriers in the electret, as well

as by recombination processes. They outweigh the activation processes and the change of the carrier density as well as the change of the electrical conductivity can thus be described according to Małecki by a system of differential equations [213]:

$$\frac{dg(t)}{dt} = \frac{\beta}{n_0}(1 - g^2(t)) - \frac{\mu_M}{\varepsilon_0 \varepsilon_r x_e} g(t)\sigma'(t) \tag{2.21}$$

$$\frac{d\sigma'(t)}{dt} = -\frac{n_0 q \mu_M}{\varepsilon_0 \varepsilon_r} g(t)\sigma'(t), \tag{2.22}$$

with $g(t) = \frac{n(t)}{n_0}$ denoting the ratio of the time-dependent carrier density ($n(t)$) and initial carrier density (n_0). The symbol x_e represents the thickness of the electret. As shown in Figure 2.13, numerical solutions of the equations show that the initial exponential decrease, caused by Ohmic behavior, now changes into a linear one, which deviates from the Ohmic behavior. This is in good agreement with the experimentally observed behavior of the electrets, which initially shows a relatively fast exponential decay, that changes into a slower long-term decay. The external charge decay is typically neglected in all theories on the internal decay processes.

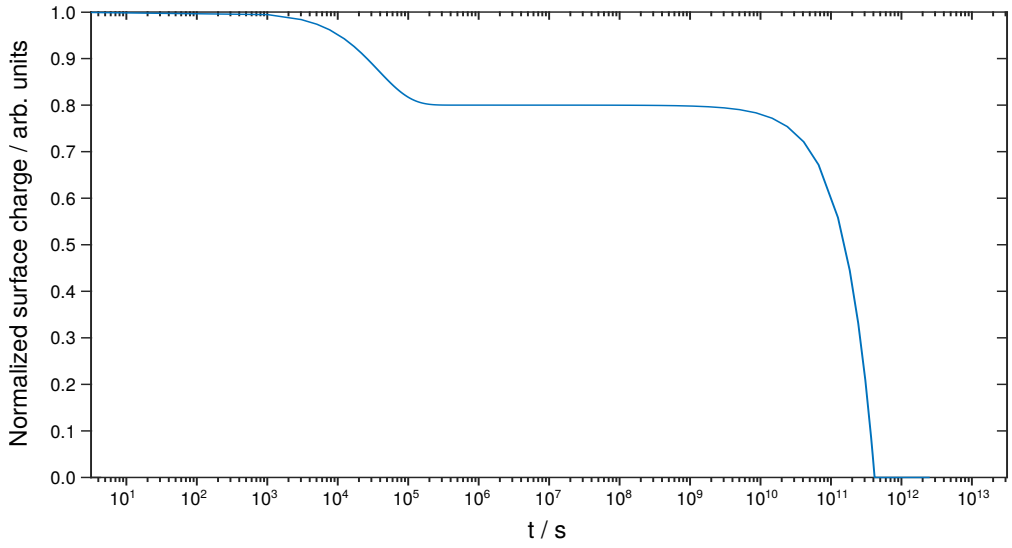

Figure 2.13: Theoretical long-term decay of the charges according to Małecki. The initial exponential decay, which is later replaced by a linear decay, describes very well the typical experimentally observed charge decay.

External Decay

The external decay processes depend strongly on the storage of the electret. If the electret is stored in the open atmosphere in which a constant exchange of air takes place, ions and polar molecules (H_2O) from this atmosphere are attracted by its surface charge. They compensate the charge quite rapidly and lead to a significantly accelerated decay. Electrets are therefore stored in small volumes in closed boxes or are immediately installed in the electret device and encapsulated there. Humidity is another factor which can lead to charge decay. The adsorption of water on the surface leads to conductive paths which can cause the charge to flow off. This situation can be described by percolation theory [214, 215]. Studies for corona-charged polypropylene (PP) electrets show good agreement of theory and observed charge decay in atmospheres with high humidity [214]. This can be significantly reduced by the use of fluoropolymers, as they usually show hydrophobic behavior (see Section 2.2.1), but it cannot be completely eliminated.

3. Experimental Details

This chapter provides insight into the details of the conducted experiments. The first section describes the initiated chemical vapor deposition (iCVD) system built within the framework of this thesis. The second section provides the parameters for the polymer thin film deposition performed in the iCVD system. All details on the thin film characterization are listed in the third section. It is further divided into the subsections chemical analysis and functional analysis.

3.1 Initiated Chemical Vapor Deposition Setup

A schematic overview of the entire iCVD system constructed within the framework of this work is given in Figure 3.1a. Apart from the electronic components and the pre-pump of the mass spectrometer, the entire system was built into a fume hood to prevent the release of gases and vapors into the ambient air of the room.

3.1.1 The Reactor

The centerpiece of the system is the hot filament CVD reactor. It was custom made by Stefan Rehders (Chair for Multicomponent Materials, Kiel University) and is not commercially available. Figure 3.1b shows a cross-section of the original reactor. It shows the cooled sample stage on which the substrates are placed. The stage can be cooled to temperatures between 5 °C and 45 °C by backside water cooling using a thermostat (CC-K6, Huber). The filament array, which is typically placed 20 mm above the sample stage, can be heated by a power supply (Polaris 65-10, Knürr-Heinzinger) to start the reaction (see Chapter 2 for details). Furthermore, the sample stage is adjustable in height, which allows the distance to the filament array to be varied between 10 mm and 35 mm. The filament array consists of a nickel-chromium alloy (Ni80/Cr20, Goodfellow). The diameter of

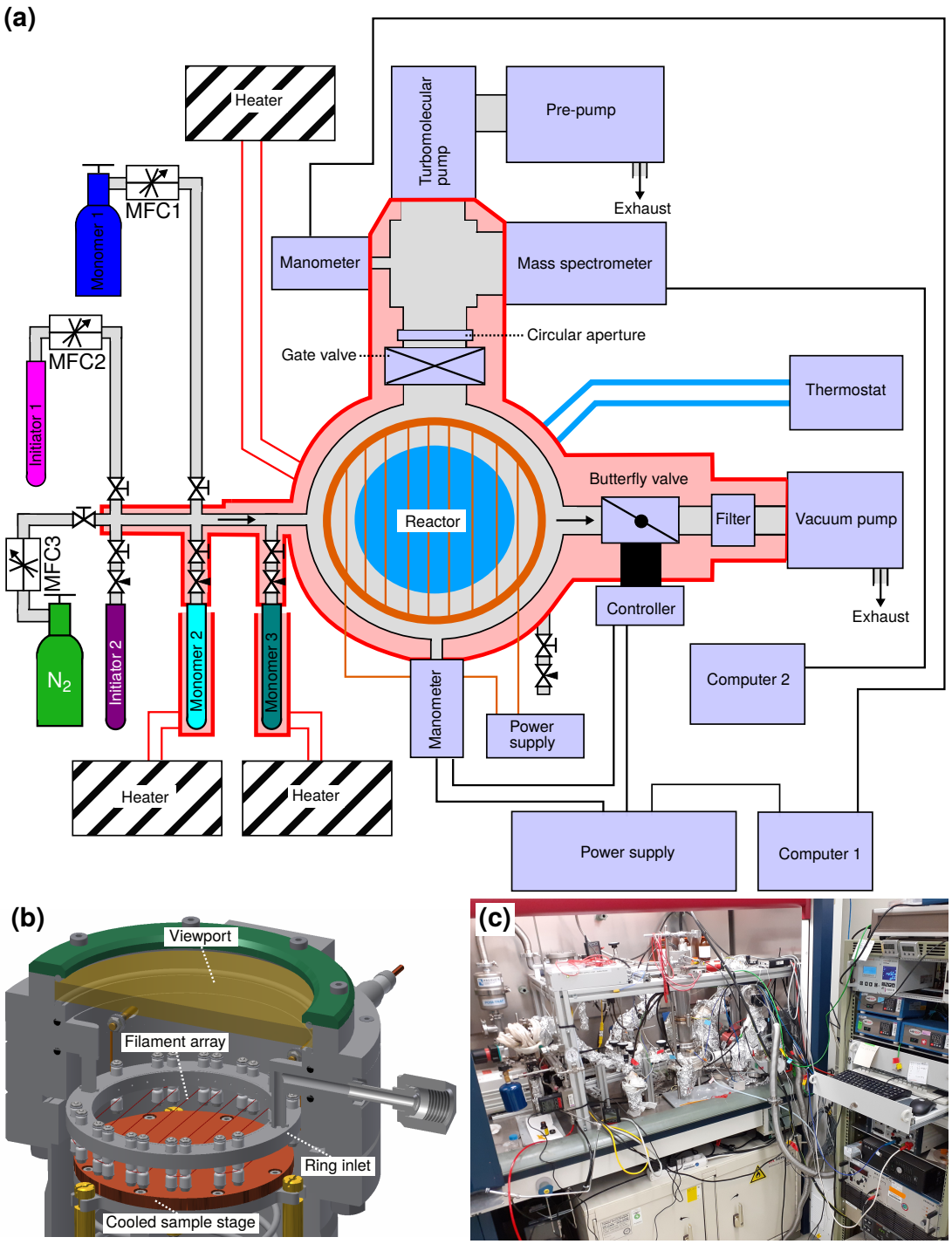

Figure 3.1: iCVD system constructed within the framework of this work. (a) Schematic overview of the entire iCVD system. (b) 3D cross section through the reactor. (c) Photograph of the iCVD system.

the filament is 0.5 mm. The viewport can be used to observe the process and the different gases and vapors can be introduced into the reactor via the ring-shaped gas inlet.

3.1.2 Gas/Vapor Supply

The gas/vapor supply consists of a main line that ends in the ring inlet of the reactor, as shown in Figure 3.1a. Different gases or vapors can be fed into the reactor through six inlets. The "Monomer 1" line is equipped with a mass flow controller (MFC) (MC series, Alicat Scientific) and is used to introduce monomers that are gaseous at room temperature as well as nitrogen (N_2). Two blocking valves (SS-6BG-MM, Swagelok) upstream and downstream of the MFC are used to completely disconnect the line. For monomers with lower vapor pressures which are present in the liquid state at room temperature, the "Monomer 2" and "Monomer 3" lines are provided. Each of these lines has a low flow metering valve (SS-SS4-VH, Swagelok) with a downstream blocking valve and an upstream blocking valve. The monomers are connected to the line in home-made glass jars and can be heated by temperature controllers (KM-RX1001, LabHEAT). Thus the vapor pressure of the liquids can be kept constant or, if necessary, the vapor pressure can be increased by higher temperatures. The initiators usually have such a high vapor pressure that they do not need to be heated. The setup has two initiator lines. Line "Initiator 1" features a MFC (MC series, Alicat Scientific) surrounded by blocking valves and line "Initiator 2" has a needle valve (Varian) surrounded by blocking valves. Like the monomers, the initiators are also attached to the line in home-made glass jars. The sixth line is configured for an inert gas that can be used to rinse the reactor or as a carrier gas. The gas supply is here also controlled by a MFC (MC series, Alicat Scientific), which is surrounded by two blocking valves.

3.1.3 Vacuum and Exhaust Management

The deposition is performed under vacuum conditions. The process pressure is usually selected between 30 Pa and 100 Pa. A scroll pump (nXDS10i, Edwards) is connected to one port of the reactor for this purpose. In the following time, this pump was replaced by a rotary vane pump (Duo 10, Pfeiffer Vacuum). Between the pump and the reactor there is a particle filter (Posi-Trap, Mass-Vac) and a home-made cold trap to protect the pump from contamination. In front of the particle filter and the cold trap is a butterfly valve (615, VAT), which receives

feedback from a capacitance manometer (Baratron, MKS instruments) located at the reactor. When gases/vapors are introduced during the process, the process pressure in the reactor can be kept constant and continuous flow processes can be carried out. For batch processes the butterfly valve can be closed completely after the introduction of gases/vapors. Further details on the valve section, such as response time, are provided in Appendix B. The areas marked in red in Figure 3.1a were permanently heated to 120 °C to avoid condensation of monomer vapor during deposition or condensation of water when the system was vented. For this purpose, the marked areas are wrapped with heating lines, which are kept at a constant temperature by two heating controllers (KM-RX1001, LabHEAT).

3.1.4 Mass Spectrometer

In the further developed iCVD setup, a mass spectrometer was added to observe the processes during polymerization. For this purpose a small additional analysis chamber was connected to the reactor, as shown in Figure 3.1a. It is separated from the reactor by a home-made circular aperture and a gate valve (VAT). The turbomolecular pump (HiPace 80, Pfeiffer Vacuum) with a pre-vacuum multi-stage roots pump (ACP15, Pfeiffer Vacuum) ensures that the base pressure in the analysis chamber is lower (2×10^{-4} Pa) than in the reactor. The pressure is monitored by an inverted magnetron full range gauge (PKR 251, Pfeiffer Vacuum). The mass spectrometer used is an open ion source mass spectrometer with quadrupole mass analyzer (PrismaPlus QMG 220, Pfeiffer Vacuum). Experimental details on the quadrupole mass spectrometry (QMS) studies can be found in Section 3.3.4.

3.2 Deposition Procedure by iCVD

In the initial state the system is under vacuum and heated. Before the deposition, the flows of the monomers and the initiator were first adjusted. The flow rates of the monomers/initiators, which are fed into the reactor by a MFC, were set directly at the MFC. An additional calibration step is necessary for all monomers/initiators which, due to their low vapor pressure or corrosive properties, must be fed into the reactor via a metering or needle valve. The desired flow rate is set on the MFC with the inert gas and the butterfly valve is closed. The pressure increase or leakage rate in the reactor was recorded over 60 s and corresponds to the actual flow rate of the MFC, which has been calibrated by the manufacturer for the inert gas. The flow with the inert gas was then stopped and the flow of the monomer or

initiator to be adjusted through the metering valve or needle valve was adjusted so that the leakage rate in the reactor exactly matched the calibrated flow rate. The flow of the adjusted monomer is then stopped via the blocking valve. In order to deposit polymer thin films in continuous flow mode, the reactor was first vented by closing the butterfly valve and opening the venting valve and the samples to be coated were placed on the sample stage. The sample stage was cleaned with an acetone tissue before and after each coating. After closing the venting valve and the reactor lid, the reactor was evacuated by stepwise opening the butterfly valve. Depending on the weight of the samples, this process was performed more slowly. Once the reactor was pumped down, it was rinsed with nitrogen from the inert gas line to remove any residual molecules from the air or possible outgassing molecules from the samples to be coated. Afterwards there was a waiting period of one hour so that equilibrium conditions were established. Then the lines of the calibrated monomer and initiator flows were opened and substrate cooling was switched on. The butterfly valve was now set to the desired process pressure and a short waiting period was required to create stable conditions. In order to start the polymerization the filament array was heated by the power supply. Details on the deposition process can be found in Chapter 2. Table 3.1 lists all parameters for the deposition of the respective polymers. After the desired coating time had passed, the power supply was switched off and the deposition stopped. The butterfly valve was then opened completely and all flows were stopped. After the pressure in the reactor had returned to the initial pressure setpoint, the reactor was ventilated again as described above and the coated samples were removed. Once the sample stage was cleaned with acetone, another set of samples was placed in the reactor for coating or the reactor was returned to the initial state without samples. In order to perform batch processes the butterfly valve was completely closed and the gas/vapors were introduced into the reactor up to the desired process pressure. To avoid an unwanted pressure increase during batch deposition due to the formation of reaction by-products, the butterfly valve was adjusted to the respective process pressure. Thus it remained closed and opened only slightly to adjust the pressure increase.

3.2.1 Deposition Parameters for the Polymer Thin Films

As initiators either tert-butyl peroxide (TBPO, Fluorochem, 97 %) or perfluorobutanesulfonyl fluoride (PFBSF, Fluorochem, 95 %) was used. They are liquid at room temperature, but due to their high vapor pressure it was possible to fed their vapor into the reactor through a needle valve or as in the case of TBPO

via a mass flow controller (MCF2) without additional heating. The gaseous hexafluoropropylene oxide (HFPO, Fluorochem, 97 %) was also fed into the reactor via a mass flow controller (MFC1). It served as a monomer for PTFE deposition. Since it is self-initiated, no initiator is required here, but the PFBSF initiator was typically used to provide CF_3 end-groups and to increase the deposition rate. 1,3,5-trivinyl-1,3,5-trimethylcyclotrisiloxane (V3D3, abcr, 95 %) and 1,3,5,7-tetravinyl-1,3,5,7-tetramethylcyclotetrasiloxane (V4D4, abcr, 97 %) were used as monomers or comonomers for organosilicon polymers. However, they had to be heated to 60 °C and 70 °C, respectively, in order to increase the vapor pressure. They were then fed into the reactor via one of the lines equipped with a low flow metering valve. Ethylene glycol dimethylacrylate (EGDMA, Sigma-Aldrich, 97 %) was used as monomer as well as comonomer/cross-linker and also had to be heated to 65 °C before it was fed into the reactor via a low flow metering valve. The same applies to 1H,1H,2H,2H-perfluorooctyl acrylate (C6PFA, Fluorochem, 95 %), which was also used as monomer or comonomer. Ethylene glycol (EG, Sigma-Aldrich, 97 %) has been used as a porogen in some depositions (Chapter 8). It had to be heated to 85 ° before it was fed into the reactor through a low flow metering valve. The monomers 1-nonyne (1N, abcr, 98 %), 1,8-nonadiyne (18N, abcr, 97 %) and 1-ethynyl-3-fluorobenzene (1E3F, abcr, 98 %) were used to prepare conjugated systems (Chapter 9) and were heated to 30 °C, 40 °C and 30 °C, respectively. They were then brought into the reactor via one of the ports with a low flow metering valve. A more detailed list with all necessary information on the respective chemicals is provided in Appendix C. Table 3.1 summarizes the respective deposition conditions used for the polymer thin film deposition in the iCVD system. For the studies in Chapter 6, a third initiator tert-butyl peroxybenzoate (TBPOB) was used. The combinations EGDMA+TBPO and EGDMA+TBPOB were deposited in a different iCVD system together with Wiebke Reichstein (Chair for Multicomponent Materials) in order to ensure that there is no fluorine in the films. Details regarding the iCVD system used for this purpose can be found in the literature [216].

Table 3.1: iCVD deposition parameters for the fabrication of the polymer thin films described in this thesis. The arrows found next to some flow rates represent "Flow is reduced from given value to zero (↓)" and "Flow is increased from zero to given value (↑)". Mi, I, fi, I, p, T and P represent the respective monomer, the initiator, the flow rate of the respective monomer or initiator, the process pressure, the substrate temperature and the applied power, respectively.

Polymer	M1	f_1/sccm	M2	f_2/sccm	I	f_I/sccm	p / Pa	T_S / °C	P / W
PTFE	HFPO	0.5	-	-	-	-	50	20	43-75
PTFE	HFPO	0.3-0.5	-	-	PFBSF	0.1	50	20	43-75
PV3D3	V3D3	0.2	-	-	TBPO	0.1	40	30	17-38
PV3D3	V3D3	0.2	-	-	PFBSF	0.1	40	30	17-38
PV3D3	V3D3	0.1	EG	0.1-1	PFBSF	0.1	40	30	38
P(V3D3-co-C6PFA)	V3D3	0.1-0.2	C6PFA	0.1	TBPO	0.1	40	30	17-38
P(V3D3-co-C6PFA)	V3D3	0.1-0.2	C6PFA	0.1	PFBSF	0.1	40	30	17-38
P(V3D3-grad-C6PFA)	V3D3	0.2↓	C6PFA	0.2↑	PFBSF	0.1	40	30	17-38
P(V3D3-co-TFE)	V3D3	0.1	HFPO	0.1-0.3	PFBSF	0.1	40	30	17-38
P(V3D3-grad-TFE)	V3D3	0.2↓	HFPO	0.5↑, 0.2↑	PFBSF	0.1	40	30	38
PC6PFA	C6PFA	0.2	-	-	PFBSF	0.1	40	30	17-38
P(C6PFA-co-EGDMA)*	C6PFA	0.5	EGDMA	0.05	TBPO	1	53.329	25	28
PEGDMA	EGDMA	0.2	-	-	PFBSF	0.1	40	30	38
PV4D4*	V4D4	0.3	-	-	TBPO	1	40	37.5	36
PV4D4*	V4D4	0.3	EG	9	TBPO	1	106.658	37.5	36
P1N	1N	0.1	-	-	PFBSF	0.1	50	20	30
P18N	18N	0.2	N_2	0.1	PFBSF	0.1	40	20	32
P1E3F	1E3F	0.2	N_2	0.1	PFBSF	0.1	40	20	34

* The deposition of these polymer films was performed in the group of Prof. Karen K. Gleason in the Department of Chemical Engineering (Massachusetts Institute of Technology, USA). More details regarding the reactors used there can be found in [217] and [218].

Substrates and Electrodes

In order to determine the deposition rate, silicon wafers (Si-Mat) were used as substrates. They were also used for the chemical characterization of the films. For some depositions, cover glasses (Menzel Gläser) were additionally coated in order to investigate the optical properties at a later stage. For electronic applications the films were deposited on electrodes. For this purpose, electrodes were deposited on borosilicate glass wafers (Borofloat 33, Schott) before the CVD coating. Aluminium electrodes were coated on the wafers with an evaporator (NTE-3500, Nano-Master Inc.) and a metal shadow mask, which is shown schematically in Figure 3.2. The base pressure was 4×10^{-5} Pa and increased to

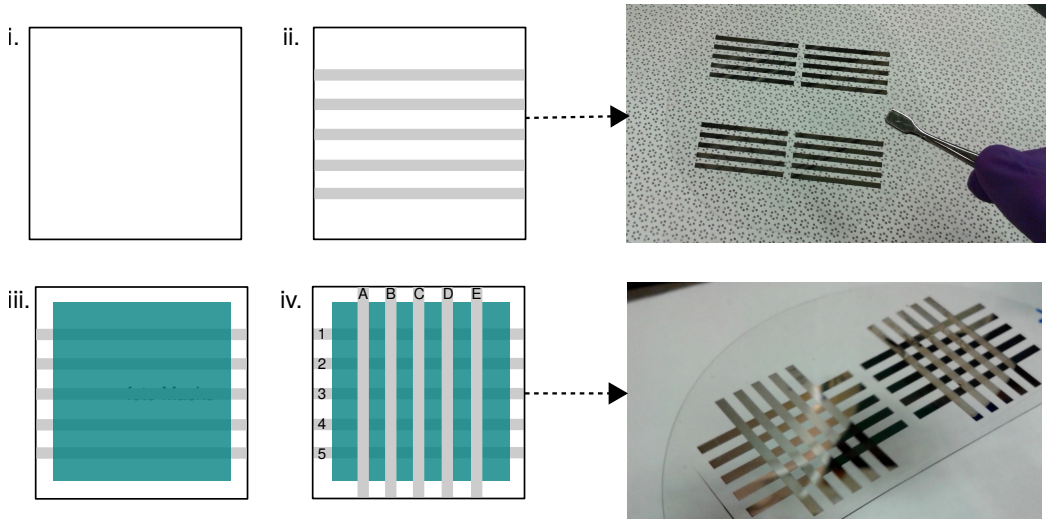

Figure 3.2: Schematic representation of the process steps for producing metal-insulator-metal (MIM) structures and photographs of selected steps. i.) Blank substrate. ii.) Deposition of bottom electrodes. iii.) iCVD thin film deposition. iv.) Deposition of top electrodes.

1.333×10^{-3} Pa during deposition. A film thickness of 200 nm was deposited at a deposition rate of 11.4 nm/min. Gold electrodes were applied with a sputter coater (Balzers SCD 050, BAL-TEC) and a metal shadow mask. After deposition of the polymer films, the electrode structures were coated offset by 90 degrees, resulting in Metal-Insulator-Metal (MIM) thin film devices, as shown in Figure 3.2, which can be individually addressed. In the case where the electrode should only be located on one side of the polymer film, films were deposited directly

onto n-doped conductive silicon wafers (Si-Mat) with specific electrical resistance $\rho_{el} < 0.005\,\Omega$cm, aluminum substrates or gold coated borosilicate glass. For the interface studies in Chapter 7, silicon wafers with 1 µm or 2 µm oxide layers (Si-Mat) were used.

3.2.2 Corona Discharge

For the production of electrets the polymer films were used which only have an electrode on one side. These films were charged using a home-made corona discharge setup. During the corona charging process the samples are irradiated with ions, which generates a quasi-permanent surface charge. Details of the processes involved have already been introduced in Chapter 2 and can be reviewed there. The setup used is a classic point-to-plane assembly. The samples were either charged with or without the use of an additional grid. The electrets fabricated with additional grid were charged with a potential of -4 kV at the tip and -200 V at the grid. For this purpose a high voltage power supply (HCN 14-6 500, FuG Elektronik) was connected to the tip and a medium voltage power supply (MCN35-350, FuG Elektronik) was connected to the grid. For some bulk samples or for experimental purposes charging was also performed without the grid. The potential at the tip was set to 6.5 kV for these samples. The corona treatment was performed for 60 s in ambient air for all samples.

3.3 Chemical Analysis of Deposited Thin Films

For the chemical analysis of the deposited thin films Fourier-transform infrared spectroscopy (FTIR), X-ray photoelectron spectroscopy (XPS) and Raman spectroscopy were used. For real-time investigations during depositions in-situ mass spectrometry was used. The techniques and details of the experiments are described in the following subsections.

3.3.1 Fourier-transform Infrared Spectroscopy (FTIR)

Fourier-transform infrared spectroscopy (FTIR) was used to investigate the functional groups in the polymer films. It is a variant of infrared spectroscopy [219, 220]. In the FTIR instrument a light beam of many different frequencies is directed onto the sample and the detector measures how much of this light is absorbed by the polymer film. Then the "composition" of the beam is changed and another data point is recorded. This process is repeated within a very short

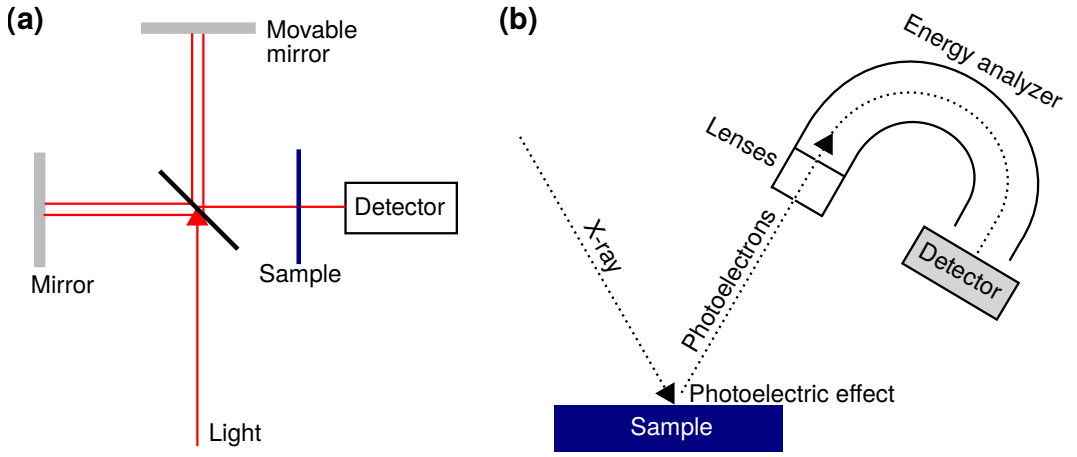

Figure 3.3: FTIR setup and XPS setup. (a) Michelson interferometer typically used in an FTIR instrument. (b) Schematic XPS setup.

time. For this purpose the FTIR device contains a Michelson interferometer [221]. Figure 3.3a shows a simplified setup. By wave interference, different wavelengths are allowed to pass or blocked depending on the position of the moving mirror. This leads to different spectra of the light beam. The computer uses this data to calculate what the absorption at each respective wavelength is. The absorption is due to the excitation of certain functional groups at the respective wavelength and thus provides information about the presence of this group in the sample [222, 223]. In this thesis all films were measured with the FTIR spectrometer (Vertex 80v, Bruker) in transmission mode. For this purpose films deposited on silicon wafers were used. The scan range was chosen from $500\,\mathrm{cm}^{-1}$ to $4000\,\mathrm{cm}^{-1}$ with a scan width of $4\,\mathrm{cm}^{-1}$ for all samples shown in this work. The measurements were performed in vacuum and prior rinsing with nitrogen to avoid unwanted contributions from the ambient atmosphere, such as water molecules. The recorded spectra were baseline corrected directly with the FTIR software (OPUS, Bruker) or with other plotting software (Origin 2017, OriginLab). A polynomial baseline correction was used for this purpose. After assignment of the bands from the literature [224], it was determined whether the polymerization was successful. For example, the bands around the vinyl group present in the monomer were first checked. The disappearance of these bands in the FTIR spectrum of the polymer thus indicated successful polymerization. Furthermore, it could be examined whether the functional groups and structures of the monomers were preserved after the deposition or whether copolymer

films show functionalities of both comonomers and thus indicate a successful copolymerisation.

3.3.2 X-ray Photoelectron Spectroscopy (XPS)

The chemical composition at the surface of the deposited polymer thin films was investigated by means of X-ray photoelectron spectroscopy (XPS). The technique is based on the photoelectric effect. As shown in Figure 3.3b, X-rays of known energy are used to remove photoelectrons from the thin film. The electrons near the surface leave the thin film in the vacuum chamber where they enter the analyzer and detector. Here the number of electrons per unit time (intensity) is measured as a function of the energy of these electrons. The technique is surface sensitive and the depth of information is only a few nm. For further information on XPS, the reader is referred to more detailed review articles in the literature [225–228]. In this work polymer films on silicon wafers were used as samples, as in the FTIR investigations. The XPS system (Omicron Full Lab, Omicron Nano-Technology) was operated with an Al Kα X-ray source at 240 W power. For the evaluation a special software (CasaXPS, Casa Software) was used. All XPS spectra shown in this thesis were evaluated by Dr. Oleksandr Polonskyi (Chair for Multicomponent Materials, Kiel University). A quantitative analysis and detailed peak deconvolution was performed for this purpose. The spectra of the deposited PTFE and the gradient layers with PTFE shown in Chapter 10 were charge referenced using the CF_2 peak located at 292.0 eV binding energy charge.

3.3.3 Raman Spectroscopy

Raman spectroscopy is based on the Raman effect [229–231]. It is used in Chapter 5 to investigate the micrometer range PTFE films deposited by iCVD as well as bulk PTFE. In Raman spectroscopy, the material is irradiated with a laser (monochromatic light). The incoming photons are most often elastically scattered, this is also referred to as Rayleigh scattering. A small amount is scattered inelastically and changes its energy. The reason is that the states of the atoms, molecules or functional groups are changed. The scattered light thus provides details about the excitation possibilities. This enables to draw conclusions about the vibrational modes and material properties. The event that the light transfers energy to the material is referred to as Stokes scattering. If energy is transferred from the material to the light, it is termed Anti-Stokes scattering. This is shown

schematically in Figure 3.4a. For the measurements performed in this work a confocal Raman spectroscopy microscope (Alpha300 RA, WITec) was used. A range from 200 cm^{-1} to 2000 cm^{-1} was investigated with a spectral resolution of 5 cm^{-1}. A Nd:YAG laser with a wavelength of 532 nm was used to investigate this range.

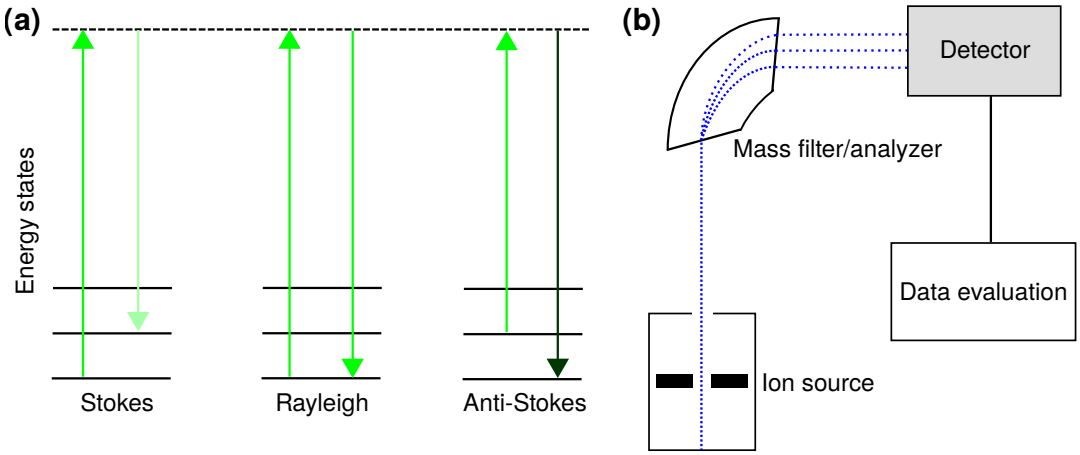

Figure 3.4: Raman spectroscopy and in-situ mass spectrometry. (a) Scattering events in Raman spectroscopy. (b) Schematic illustration of the components of a mass spectrometer.

3.3.4 In-situ Mass Spectrometry

In-situ mass spectrometry was used for better process control during the polymerization or copolymerization and to obtain insight into the reaction kinetics. Mass spectrometry enables the determination of the chemical composition of a gas phase [232–234]. As shown schematically in Figure 3.4b, mass spectrometers usually have an ion source, a mass filter/analyzer and a detector connected to a data evaluation system. The ion source ionizes the gas particles, which are then separated by the mass filter according to their mass/charge ratio. After the particles have left the filter/analyzer, the respective ion current is measured in the detector, which is then further processed by the evaluation unit and graphically displayed on a screen. There are different types of mass filter/analyzer. The time-of-flight (TOF) variant measures the flight time, which is used to determine the ratio [235, 236]. A quadrupole mass analyzer, which is built into the mass spectrometer used in this study, consists of four parallel rods on which an electric

field is generated. This means that only ions with a certain mass/charge ratio and thus the correct trajectory are allowed to travel to the detector. In this way, remarkable accuracy can be achieved even in different conditions [237, 238]. There are also differences in the detectors. In a Faraday detector the ions transfer their charge directly to the detector. In Secondary Electron Multiplier (SEM), the ions generate secondary electrons when they hit a layer of material deposited on a so-called dynode. These can now release further secondary electrons at other coated dynodes and an amplification of the incoming current takes place. The experiments were performed with the iCVD setup extension mentioned in Subsection 3.1.4. In order to perform the in-situ investigations, the gate valve of the iCVD system is opened during the deposition process. This causes the analysis chamber to be filled with molecules from the reactor and the pressure in the chamber to increase to 8×10^{-4} Pa to 1×10^{-3} Pa. The mass spectra were each recorded in Faraday scan mode from 1 amu – 100 amu at 200 ms/amu. Further details on the evaluation of the recorded mass spectra are discussed in Chapter 4 as well as Chapter 10.

3.4 Functional Characterization of Deposited Thin Films

In order to investigate the functional properties of the deposited polymer thin films different techniques were applied, as described in this section.

3.4.1 Variable Angle Spectroscopic Ellipsometry (VASE)

Variable angle spectroscopic ellipsometry (VASE) was used to determine the film thickness, refractive index and relative permittivity of the deposited polymer films. An ellipsometry device with variable angles (M-2000UI, J.A. Woollam Co.) was used for this purpose. Ellipsometers consist, as shown in Figure 3.5a, of a light source that sends light through a polarizer and finally hits the sample to be examined. The light reflected from the sample hits an analyzer and passes on to the detector. The change in the polarization state of the light is determined, from which the other properties can be derived [239, 240]. The samples were measured at four different angles (55°, 60°, 65°, 75°). The wavelength range was set from 250 nm to 1700 nm. Polymer films deposited on silicon wafers were used for this purpose. The films were modeled using the ellipsometry software (CompleteEASE, J.A. Woollam Co.). Three layers were used in this case, as

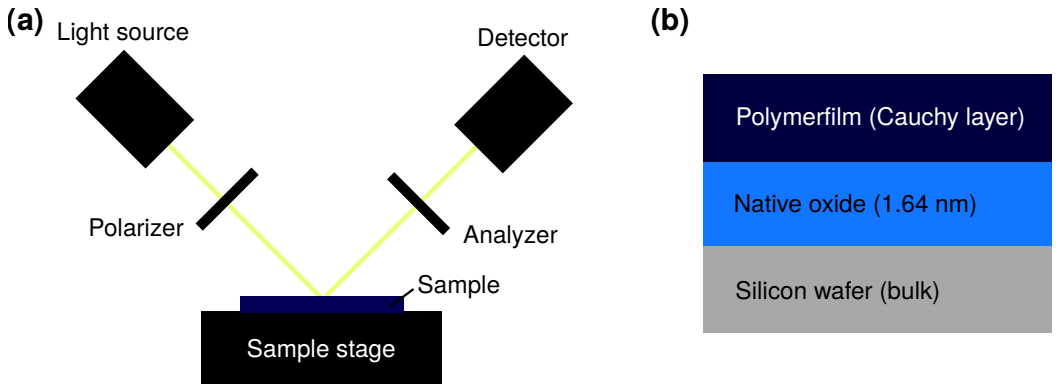

Figure 3.5: The ellipsometer. (a) Schematic illustration of an ellipsometer setup. (b) Layers used to model the polymer thin films deposited on silicon wafers via iCVD.

shown in Figure 3.5b. A silicon substrate layer from the CompleteEASE software library was used to represent the silicon wafer. A layer for the native oxide on the surface of the wafer was placed on this layer, which was also from the library of the software. The thickness of the native oxide layer was determined in a previous experiment using the same ellipsometry device to be 1.64 nm. A Cauchy layer was used over the native oxide layer to model the polymer film. This corresponds to the equation

$$n_r(\lambda) = \mathrm{A_{fit}} + \frac{\mathrm{B_{fit}}}{\lambda^2} + \frac{\mathrm{C_{fit}}}{\lambda^4} \tag{3.1}$$

which is valid for transparent films. The symbols n_r and λ represent the refractive index and the wavelength, respectively. $\mathrm{A_{fit}}$, $\mathrm{B_{fit}}$ and $\mathrm{C_{fit}}$ are the fitting parameters. With this model the film thickness (x_f) and the optical constants were determined. By measuring x_f a deposition rate according to

$$k_{depo} = \frac{x_f}{t_d} \tag{3.2}$$

was obtained. The symbol t_d represents the deposition time. The relative permittivity was estimated for nonpolar polymers according to

$$n = \varepsilon_r^{\frac{1}{2}}. \tag{3.3}$$

All gradient copolymer films shown in Chapter 10 were modeled using the graded layer option of the Cauchy layer.

3.4.2 Ultraviolet/Visible/Near-infrared Spectroscopy

The ellipsometer used in Subsection 3.4.1 was also applied to perform Ultraviolet / visible / near-infrared spectroscopy (UV/VIS/NIR) measurements. For this purpose the sample holder was changed and the instrument was put into transmission mode. A background spectrum was recorded followed by a spectrum with the sample. For each sample a range from 250 nm to 1700 nm was measured. In this way the transmittance of the films was determined.

3.4.3 Profilometry Measurements

A profilometry device (DektaktXT, Bruker) was used to determine the film thickness of samples with a film thickness around 1000 nm and higher. A line scan is performed for this purpose. The tip of the cantilever is in contact with the sample surface and moves slowly over this surface on a predetermined distance. The profilometry device registers height differences and records them in a height profile. A stylus force of 0.2 mg was selected. The line scan distance varied between 200 µm and 500 µm depending on the sample under investigation. To measure the layer thickness, a scratch was made in the polymer film before the measurement in order to obtain a step. The transition from the substrate to the polymer film gives the film thickness. All samples were examined at five different locations to obtain a mean value and standard deviation. According to equation 3.2 it was thus possible to determine deposition rates even for thicker films, where the fitting of the ellipsometry data became too inaccurate or impossible. In contrast, the profilometry data in the nanometer range became extremely inaccurate and the ellipsometry device delivered significantly more accurate values.

3.4.4 Surface Potential/ Surface Charge Measurements

The surface potential of the electrets produced by corona discharge was measured with an electrostatic voltmeter (344, Trek) (or for higher potentials: 347, Trek) as shown in Figure 3.6a. The electrostatic voltmeter is not in direct contact with the surface as it utilizes a field-nulling technique. The measuring head consists of a vibrating probe and forms a variable plate capacitor with the charged surface of the electret. The field-nulling technique brings the probe head/counter electrode to the same potential as the electret surface and the value displayed on the instrument corresponds to the surface potential of the electret as schematically illustrated in Figure 3.6b. The distance between the measuring head was always kept at 2 mm ±1 mm during the measurement. In this way, the surface potential

of the electrets was determined directly after charging. Or it was measured within the scope of long-term measurements after certain time intervals.

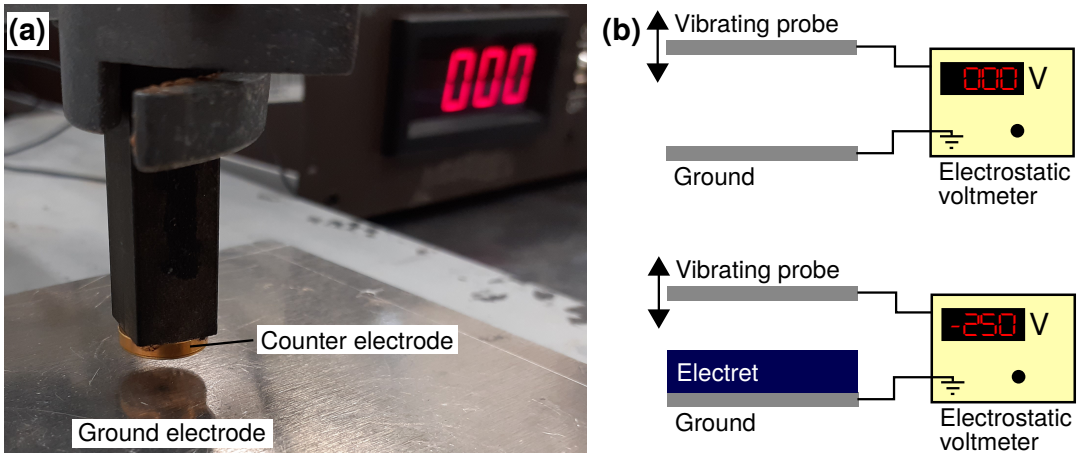

Figure 3.6: The electrostatic voltmeter. (a) Photograph of the probe without inserted electret. (b) Schematic illustration of the vibrating probe field-nulling technique.

Decay Measurement in Various Atmospheres

In order to determine the influence of the surrounding atmosphere on the charge decay, the ground electrode and the probe were placed in a glove box. The glovebox was then filled with air of different humidity or argon and the electret was brought between the ground electrode and the probe for the measurement. The surface potential was measured in this way over a fixed time period in the respective atmosphere. The air humidity in the glovebox was measured with a hygrometer (45.2006, TFA Dostmann).

3.4.5 Thermally Stimulated Discharge (TSD)

Since the surface charge is usually very stable, it takes several decades or even centuries[1] until the surface charge has completely disappeared. For this reason, thermally stimulated measurements are often performed in which the electret

[1]These time spans originated theoretical predictions, which are described in more detail in Chapter 2.

is heated at a fixed heating rate and the surface potential is recorded until it is completely discharged [197, 198]. There are sometimes different names for such measurements. Often, instead of the surface potential, the released current is measured, e.g. by an electrometer. This is then commonly referred to as thermally stimulated current (TSC) [241]. Both are well established techniques for the characterization of electrets. In this thesis the term thermally stimulated potential decay (TSPD) is used to clearly indicate that the surface potential has been measured. It allows to compare different electret materials. The setup used in Subsection 3.4.4 was used to perform these measurements. The ground electrode was placed on a self-made heating plate, which was heated by a power supply (Polaris 65-10, Knürr-Heinzinger) at a fixed heating rate. The heating rates were either 6 K/min or 3.75 K/min. In the plate that acted as the ground electrode, there was a built-in thermocouple which measured the temperature directly under the vibrating probe.

3.4.6 Impedance Spectroscopy

Impedance spectroscopy was used to determine the dielectric properties of the polymer films. For this purpose the MIM structures described in Subsection 3.2.1 were used. For the measurements an electrochemical interface (SI 1287, Solartron) and an impedance analyzer (SI 1260, Solartron) were used. In addition, the phase angle and the impedance (absolute value) in the range of 100 Hz to 1 MHz was measured with a programmable LCR meter (PM6306, Fluke).

3.4.7 Water Contact Angle (WCA) measurements

The water contact angle (WCA) measurements were used to detect hydrophobicity caused by surface functionalization with a fluoropolymer. The technique can also be used as a quick indicator to test whether the deposition process has been successful or not. The contact angle (θ) gives information about the wetting behavior of the surface. It can be found in the well-known Young's relation [242]

$$\gamma_{SG} = \gamma_{SL} + \gamma_{LG} \cos(\theta). \tag{3.4}$$

The symbols γ_{SG}, γ_{SL}, γ_{LG} and θ represent the surface tension at the solid-gas interface, the surface tension at the solid-liquid interface, the surface tension at the liquid-gas interface and the contact angle, respectively. If the contact angle is greater than 90°, the surface is referred to as hydrophobic, in the other case as hydrophilic [243]. Contact angles above 150° are often termed superhydrophobic

[244]. The WCA were measured in this work with a commercial contact angle setup (OCA 3, DataPhysics). A water drop with a volume of 10 µl was applied to the sample and the shape of the drop was recorded with a camera and transferred to the computer. Using the software of the WCA setup, the contact angle was determined. Five measurements of the WCA were made at different locations on the sample surface to obtain a mean value and a standard deviation.

3.4.8 Positron Annihilation Lifetime Spectroscopy (PALS)

Positron annihilation lifetime spectroscopy (PALS) is a well established technique to investigate material defects on the nanoscale. A positron is the antiparticle of an electron. In PALS the sample is investigated with positrons, which then interact with the sample. Due to interactions with electrons in the sample material, positrons and electrons annihilate and gamma rays are emitted. These gamma rays can be registered by a detector. The time from the emission of the positron to the detection of the gamma rays is referred to as positron lifetime. In materials with free electrons, e.g. metals, the positrons annihilate relatively quickly in a perfect crystal. However, if there are defects/pores in the material, the positrons can remain there for a longer time before they annihilate. In insulating polymers there are usually no free electrons available. Here, states are formed which are termed positronium. This is a bound state of one positron and one electron of the material. Depending on the orientation of the spins, a distinction is made between para-positronium (p-Ps) and ortho-positronium (o-Ps). Both states are metastable. In p-Ps the spins are antiparallel and the characteristic lifetime is 125 ps independent of the material. No spin flip is necessary for the decay. In an o-Ps the spins are parallel and the characteristic lifetime is 142 ns. Typically, the o-Ps lifetime is considered, which is quenched depending on the molecular environment in the polymer as shown in Figure 3.7. The reason is the so-called pick-off annihilation, in which the o-Ps is annihilated with an adjacent electron, which leads to a reduction of the o-Ps lifetime compared to the characteristic vacuum lifetime of 142 ns. In the polymer bulk it varies between 1-4 ns [245–247]. If larger pores are present in the polymer, this is reflected in o-Ps lifetimes of 10 ns and more. The relation between the lifetime (τ_i) and the hole radius (R_h) can be described by the Tao-Eldrup model according to [248]

$$\frac{1}{\tau_i} = \lambda_0 \left(1 - \frac{R_h}{R_h + \delta_R} + \frac{1}{2\pi} \sin\left(\frac{2\pi R_h}{R_h + \delta_R}\right)\right). \tag{3.5}$$

Here the interaction of the Ps with the pore wall is described by an infinite spheric-symmetrical potential well and an electron layer of thickness δ_R representing the pore wall as well as a wave function in the ground state for the Ps. The description is given by the overlapping of the electron layer with the wavefunction. The symbols λ_0 represents the spin averaged decay rate located at the edge of the potential well. The Tao-Eldrup model is applied for lifetimes up to 10 ns. Since in this thesis polymer thin films are investigated, a moderated low energy positron beam with implantation depths in the range of 100 nm are required. The low energy (approximately 1 keV) is used to get an appropriate depth resolution. The moderation is necessary for an accurate depth resolution and the timing is necessary for the start signal of the positron lifetime. For this reason the measurements were performed at the Electron Linac for Beams with high Brilliance and low Emittance (ELBE) at the Helmholtz-Zentrum Dresden-Rossendorf (HZDR). The measurements were performed for implantation depths from 1 keV to 12 keV to obtain depth profiles. For each energy the respective spectrum consisted of 5 million counts. The evaluation of the recorded data was performed by Dr. Maik Butterling, Dr. Christian Ohrt and Prof. Dr. Klaus Rätzke. Palsfit (DTU Denmark) [249] was used for this purpose. The best results were chosen according to low residuals and low χ-squared. Results with intensities lower than 1 % were neglected. The short p-Ps lifetime, the free positron lifetime and the longer o-Ps components were allocated with up to four exponential decay functions. In order to consider the energy where half of the positrons are already implanted in the substrate, this energy has been marked with a red line in all corresponding figures. To investigate the so-called Makhovian Implantation profiles for this purpose a home-made program was used. The values 1.7 g/cm^3 for non-porous samples and 1.4 g/cm^3 for porous samples were used for the densities.

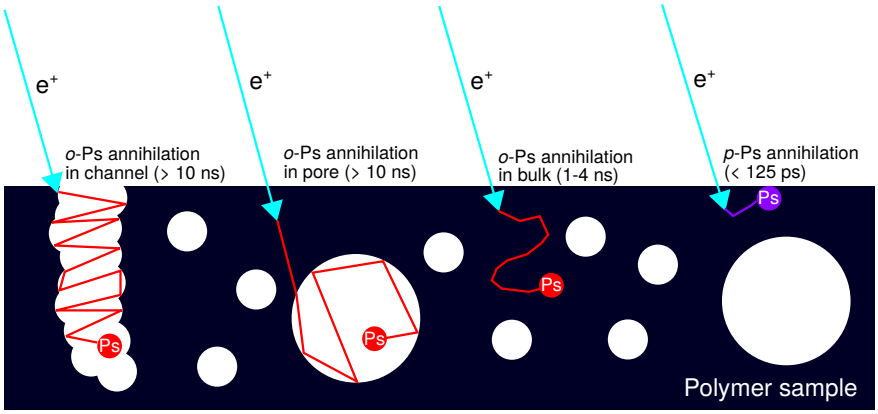

Figure 3.7: Possible annihilation processes when a positron (e^+) encounters a polymer sample containing pores and channels. A positronium (Ps) is typically formed in polymers or other insulators. It is a hydrogen-like state, which consists of one positron and one electron. For sake of clarity other processes like reemission of e^+ or annihilation of e^+ etc. are not included.

3.5 Computational Details

Some calculations and simulations shown in this thesis were performed with the support of a computer and different programs.

3.5.1 Calculations

All computer-based calculations were performed with the program Matlab (Matlab R2016a, MathWorks). For the calculation of electrostatic potentials the partial differential equation (PDE) Toolbox from Matlab was used, which applies the Poisson equation for such problems. The calculations shown in Chapter 8 based on the Cahn-Hilliard equation [250, 251] were performed using the semi-implicit approach of Eyre [252] implemented in a Matlab script.

3.5.2 Density of States Calculation

The density of states has been calculated by extended Hückel calculations. Yet Another extended Hückel Molecular Orbital Package (YAeHMOP) has been

applied for this purpose. It has been used as part of the molecule editor program Avogadro (Avogadro 1.2.0, Avogadro).

3.5.3 Geometry Optimization, Electronic Structure and Visualization of Orbitals

The molecular models that are used to illustrate the microscopic situations were first created with the molecule editor program Avogadro (Avogadro 1.2.0, Avogadro). The internal geometry optimization based on Merck molecular force field (MMFF94s) or universal force field (UFF) for larger molecules was initially used to obtain the molecule of interest. The obtained molecules were used to create an input script for further calculations in order to obtain information on the orbitals and electronic structure of the molecule. Using the Northwest Computational Chemistry Package (NWChem 6.8, Pacific Northwest National Laboratory) [253] the molecule was geometry optimized using density functional theory (DFT) and single point energies were calculated. The calculations were performed on a separately set up server (Supermicro). The hybrid functional Becke, 3-parameter, Lee-Yang-Parr (B3LYP) [254–256] was used for this purpose. Some calculations were perfromed using second order Møller–Plesset perturbation theory (MP2) [257]. DFT calculations were performed with the correlation-consistent polarized (valence-only) double-zeta (cc-pVDZ) [258] basis set or Pople basis set (e.g. 6-31G). For MP2 cc-pVDZ or cc-pVTZ basis sets have been applied. The exact basis sets and further details are given in the respective chapters in the results and discussion part of this thesis. The output was visualized and analyzed using the software Molden (Molden 6.1, CMBI) [259, 260].

4. Molecular insight into real-time reaction kinetics of free radical polymerization from the vapor phase by in-situ mass spectrometry

This chapter demonstrates a new extension of the initiated chemical vapor deposition (iCVD) process using in-situ quadrupole mass spectrometry (QMS). The approach enables a real-time determination of the reaction kinetics during the process as well as better process control, especially for copolymer depositions and depositions on the lower nanoscale.

The content of this chapter is published in:

> **S. Schröder**, A. M. Hinz, T. Strunskus, and F. Faupel. Molecular insight into real-time reaction kinetics of free radical polymerization from the vapor phase by in-situ mass spectrometry. *J. Phys. Chem. A*, 125:1661, 2021.

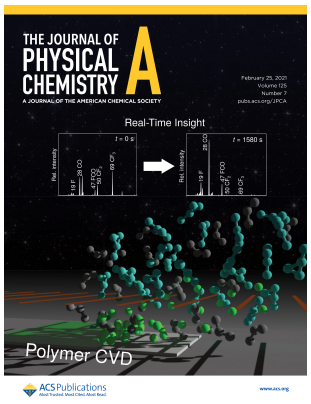

The approach was applied in the following publication:

S. Schröder, O. Polonskyi, T. Strunskus, and F. Faupel. Nanoscale gradient copolymer films via single-step deposition from the vapor phase. *Mater. Today*, 37:35, 2020.

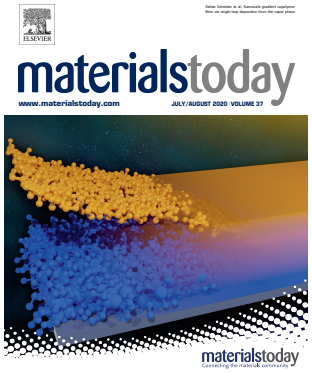

4.1 Introduction

The iCVD process has been established over the last years and is currently in the status of attracting the interest of the industry [1, 23, 261]. As already introduced in Chapter 2, the reason for this is that due to the typical CVD growth iCVD offers the same advantages like plasma-enhanced chemical vapor deposition (PECVD) or metalorganic chemical vapor deposition (MOCVD) processes, which are used on a large industrial scale, e.g. in the semiconductor industry. With the increasing application possibilities, new challenges are emerging for the process. For example, ultra-thin layers in the lower nanometer range or new types of copolymers that require improved process control. There is a need for new approaches that increase this process control and provide more precise insight into the process. The approach shown here enhances the iCVD process via in-situ mass spectrometry to enable improved control as well as the possibility to determine the reaction kinetics in real-time. By providing access to the molecular level of the reactor atmosphere, it provides much more detailed information and control on the process than relying on macroscopic system parameters like the reactor pressure. By using quadrupole mass spectrometers (QMS), which has already been described in more detail in Chapter 3, precise data can be obtained. As QMS are relatively affordable and can be readily integrated into iCVD/HFCVD-reactors they are ideally suited for this purpose. Even though their mass range is typically limited to a few hundred atomic mass units (amu) and thus too narrow to detect the complex and heavy molecules used in iCVD processes directly, these molecules can still be successfully identified by a QMS. As most molecules will undergo fragmentation in the ion source of the spectrometer one can associate a certain relative abundance of these lighter fragments, a so-called fingerprint, with the presence of the heavier parent molecules. This fingerprint can be assigned by matching with reference spectra and enables identification of the molecules even with QMS with a mass limitation of 100 amu. Furthermore, kinetic studies can be performed in this way by real-time monitoring of the reactions. It enables the determination of reaction pathways as well as rate constants. The presented approach is thus a versatile tool and allows better process control especially for the deposition of copolymers and for polymer film deposition on the lower nanoscale.

4.2 Real-time Observation of iCVD Reactions

The properties of the thin films produced by iCVD can be adjusted via the deposition parameters. Likewise, when new monomers are used, the optimized deposition parameters must be found in order to achieve effective deposition rates or a high molecular weight. To avoid tedious testing and parameter variations it is therefore of interest to collect information about the reaction kinetics in-situ during the deposition process. This enables to set the desired deposition conditions in a fast way.

4.2.1 Identification of Reaction Pathways

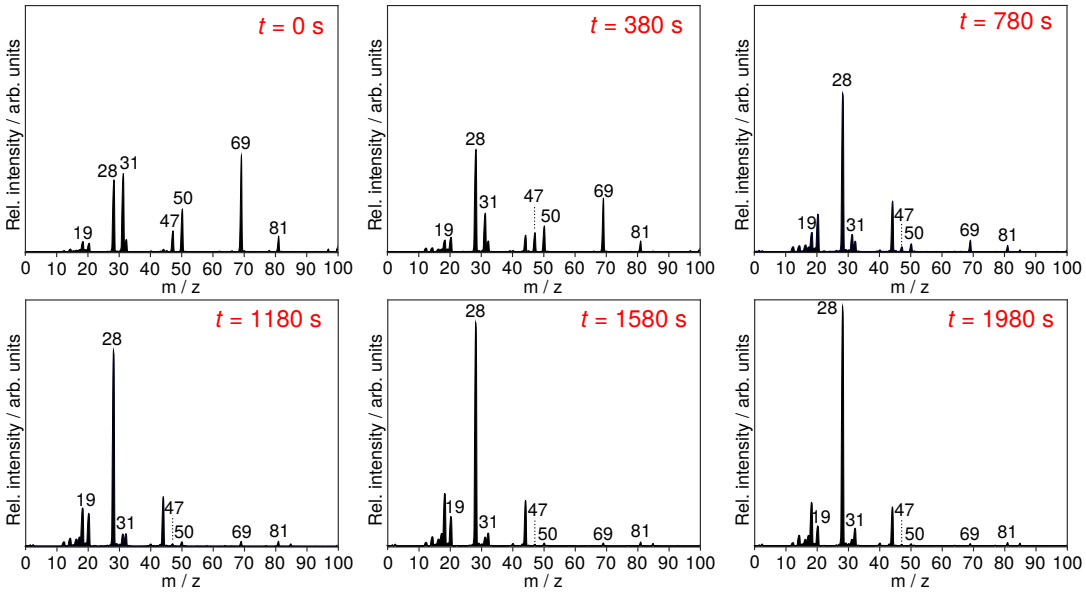

Figure 4.1: In-situ QMS observation of the temporal evolution of HFPO in a HFCVD/iCVD reactor while the filament array is heated. A change with time in the mass spectrum is clearly visible.

To demonstrate the ability to identify the reaction pathways in the iCVD/HFCVD process hexafluoropropylene oxide (HFPO) is investigated as an example. HFPO can be used to deposit PTFE thin films and is thus of great interest for many applications. It is self-initiated and thermally decomposes into difluorocarbene and a trifluoroacetyl fluoride byproduct [146, 262]:

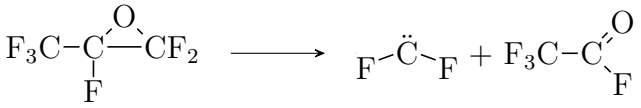

Difluorocarbene is present in a singlet state [263]. Figure 1 shows this process as observed by in-situ QMS in the iCVD/HFCVD reactor. The mass spectrum of the reactor atmosphere in a batch process changes over time from that of pure HFPO after starting the filament heating at $t = 0$s indicating the decomposition of the HFPO by the heated filaments. In order to identify the peaks in the obtained mass spectra the overall possible reaction pathways for the HFPO fragmentation have to be consulted. A lot of the reaction pathway studies for HFPO originate from pyrolysis experiments [116, 264, 265] or density functional theory (DFT) calculations [146, 262]. These possible reaction pathways for the HFPO fragmentation are summarized in Figure 4.2. First, the HFPO atmosphere appears in the mass spectrum while the filaments are not heated, as shown in Figure 1 at $t = 0$s. The above mentioned pathway via difluorocarbene (CF_2) and trifluoroacetyl fluoride (C_2F_4O) produces the peak at 50 m/z for the difluorocarbene. The fragmentation of trifluoroacetyl fluoride causes peaks at 69, which

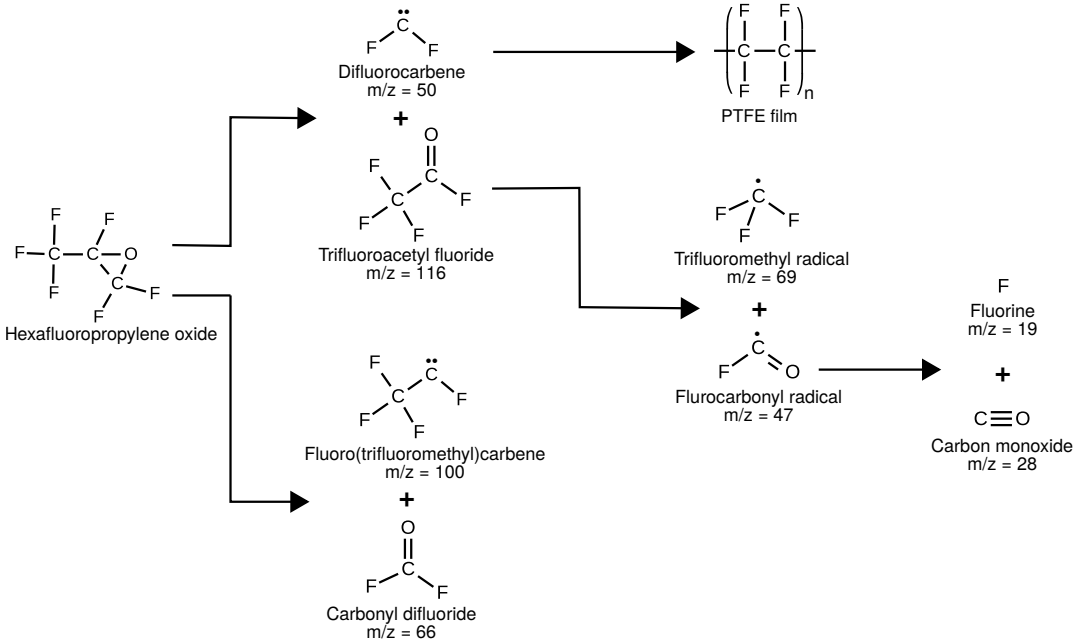

Figure 4.2: Proposed reaction pathways for the fragmentation of HFPO according to results reported in the literature[116, 264, 265].

can be assigned to the trifluoromethyl radicals, and the peak at 47 m/z for the fluorocarbonyl radicals. The fluorocarbonyl radicals are further fragmented into fluorine (F) and carbon monoxide (CO). The peaks for fluorine can be found around 19 m/z and the carbon monoxide peak is located at 28 m/z. The peak for the trifluoromethyl radicals can be found at 69 m/z and is initially the dominant peak in the mass spectrum. The additional smaller peaks around 12 m/z, 16 m/z and 29 m/z can also be associated with carbon monoxide. Once the filament heating in the iCVD/HFCVD reactor is started the intensity of the peak at 50 m/z decreases. This implies that difluorocarbene is removed from the gas phase, most likely by integration into the growing PTFE film. After about one third of the deposition, carbon monoxide becomes the new dominant peak. Figure 4.3 shows the time evolution of selected peaks during the deposition process. The temporal evolution of trifluoromethyl radicals, carbon monoxide, difluorocarbene and fluorocarbonyl radicals are illustrated in Figure 4.3a.

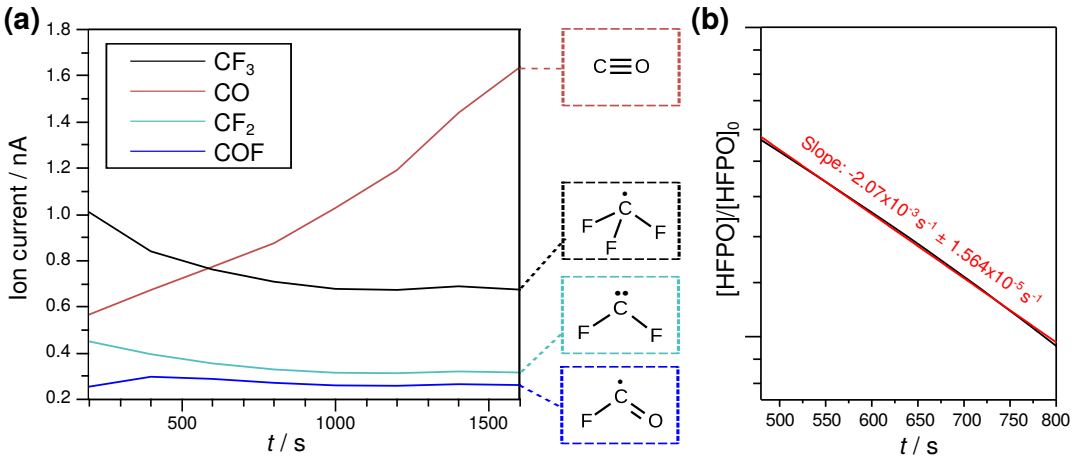

Figure 4.3: Extracted kinetic data for the deposition with HFPO. (a) The intensities of some important peaks during the deposition are shown as a time curve. (b) The semi-logarithmic plot of the overall HFPO concentration as a time curve provides the rate constant for this first order reaction.

The iCVD/HFCVD process with HFPO is thus in good accordance with the reaction pathways found in the literature[116, 262–265]. The secondary pathway for the initial decomposition of the HFPO molecule into fluoro(trifluoromethyle)carbene (C_2F_4) and carbonyl difluoride (COF_2) can be neglected:

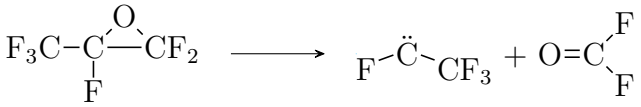

The peak intensity at 66 m/z for carbonyl difluoride is extremely low. The ion current is around 5 fA for the deposition process shown here with 31.74 W of filament power applied. This corresponds to a filament temperature around 500 K. This is in accordance with the observations for HFPO pyrolysis at low temperatures [265]. It is reported that the reaction pathway via fluoro(trifluoromethyle)carbene and carbonyl difluoride becomes more significant at higher temperatures above 900 K [262]. For the iCVD/HFCVD process the reaction pathway via difluorocarbene and trifluoroacetyl fluoride is thus the dominant one for the moderate filament temperature range.

4.2.2 Reaction Rate

The semi-logarithmic illustration of the derived overall HFPO concentration, as shown in Figure 4.3b shows straight line behavior. The linear regime is characteristic for first-order kinetics, according to

$$\frac{[\mathrm{HFPO}]}{[\mathrm{HFPO}]_0} = \exp(-kt). \tag{4.1}$$

[HFPO] and $[\mathrm{HFPO}]_0$ represent the current and the initial HFPO concentration, respectively. The CF_2 peak has been measured for this purpose. The symbol k is the rate constant, which can be determined from the slope in the semi-logarithmic plot. For the HFPO deposition conditions in the iCVD/HFCVD process used in this study it is subsequently -2.07 x $10^{-3}\,\mathrm{s}^{-1}$ $\pm$ 1.564 x $10^{-5}\,\mathrm{s}^{-1}$ for 500 K. This result is in good accordance with the values reported for the pyrolysis of HFPO [262, 266]. The half-life is consequently given by

$$t_{1/2} = \frac{\ln(2)}{k}, \tag{4.2}$$

and equals 335 s. The activation energy (E_a) can finally be calculated by a simple Arrhenius relation according to

$$E_a = -\ln\left(\frac{k}{A}\right)\mathrm{R}T. \tag{4.3}$$

The symbols R and A represent the universal gas constant and the pre-exponential factor, respectively. From measurements of k at different filament temperatures

Table 4.1: Integrated rate laws. The symbol [C] and $[C]_0$ represent the concentration and initial concentration, respectively.

Reaction order	Integrated rate law	Half-life
Zero order	$[C] = [C]_0 - kT$	$t_{1/2} = \frac{[C]_0}{2k}$
First order	$[C] = [C]_0 \exp(-kT)$	$t_{1/2} = \frac{\ln(2)}{k}$
Second order	$\frac{1}{[C]} = \frac{1}{[C]_0} + kT$	$t_{1/2} = \frac{1}{k[C]_0}$

an activation energy of 155 kJ/mol was obtained for the process presented in this work. Reactions of different order for other reaction processes can be identified by their respective rate law. Table 4.1 shows this for different cases. In order to predict at which bond e.g. molecule will decompose, at which point the functional groups of the monomer will decompose or to optimize the geometries, typical ab-initio calculations can be performed additionally. Figure 4.4 shows the resulting orbital levels for HFPO calculated by second order Møller–Plesset perturbation theory (MP2) using different basis sets. Certainly the cc-pVTZ basis set provides the most reliable values. The deviation of 6-31+G* can be explained by the included diffuse functions used here, which are typically used for ions. STO-3G represents a minimal basis set, which usually only provides a rough estimation. However, this requires only a very short calculation time. The deviations that occur in the STO-3G calculation should therefore be treated with caution. Further data can now be obtained from these results as described in detail for HFPO in the literature e.g. by Ng et al. or Lau et al. [146, 262].

4.3 In-situ Analysis of Depositions with Vapor Mixtures

Typically iCVD is performed with an initiator. This means, the vapor phase consists of initiator and monomer molecules. In order to determine the reaction pathways and reaction constants in such a vapor mixture, a similar procedure can be followed as described in the previous section. An additional process that must be considered here is the identification of each individual component in the vapor

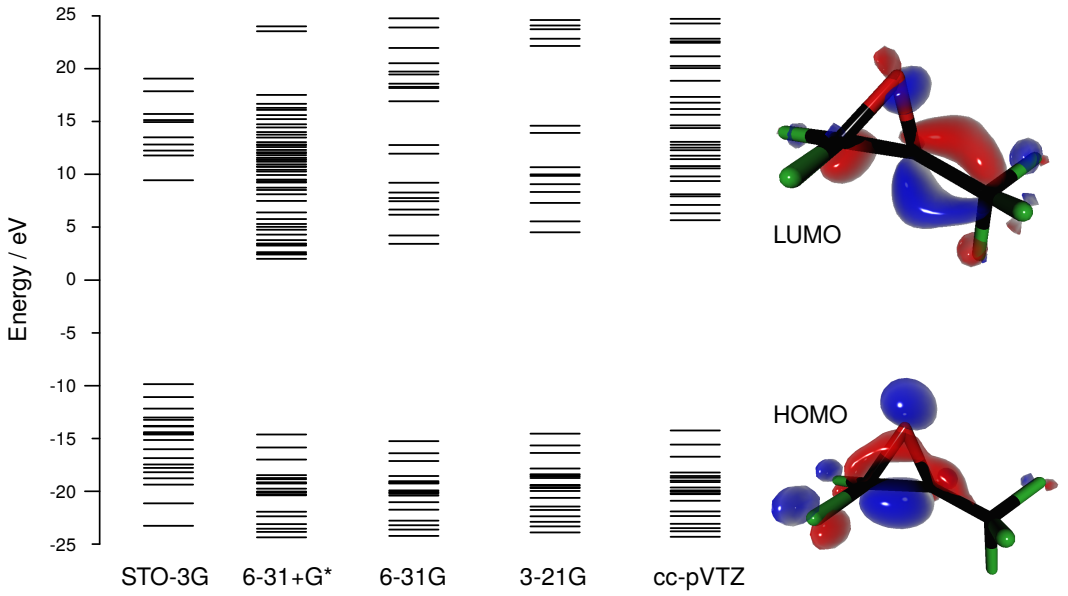

Figure 4.4: Orbital levels for HFPO obtained using MP2 and different basis sets.

mixture. Reference spectra of the individual components can be recorded for this purpose, which can then be used as a fingerprint for the individual component in the vapor mixture. An example for the deposition of copolymers where typically two co-monomers and one initiator are used is shown in Figure 4.5. The example in Figure 4.5 shows a vapor phase, which consists of the co-monomers 1,3,5-trivinyl-1,3,5-trimethylcyclotrisiloxane (V3D3) and 1H,1H,2H,2H-perfluorooctyl acrylate (C6PFA) as well as the initiator tert-butyl peroxide (TBPO). At first glance the mass spectrum of the vapor mixture appears to be too complex too be analyzed, but this is solved by application of the reference spectra of each individual component. They can be extracted from the mixed vapor phase diagram in a simple post processing step or even be identified in-situ with an appropriate script. Reference spectra can be found in Appendix D1 of this thesis. This fingerprinting also enables a precise determination of the individual contributions of each co-monomer in the vapor phase ($[M_i]$). More information on the program used for the fingerprinting is provided in Appendix D2. In addition to the rate constants, the reactivity ratios (r_1 and r_2) are of interest for copolymerizations. They can be calculated based on the Mayo-Lewis equation [154]

$$\frac{m_1}{m_2} = \frac{[M_1]}{[M_2]} \frac{r_1[M_1] + [M_2]}{r_2[M_2] + [M_1]}. \tag{4.4}$$

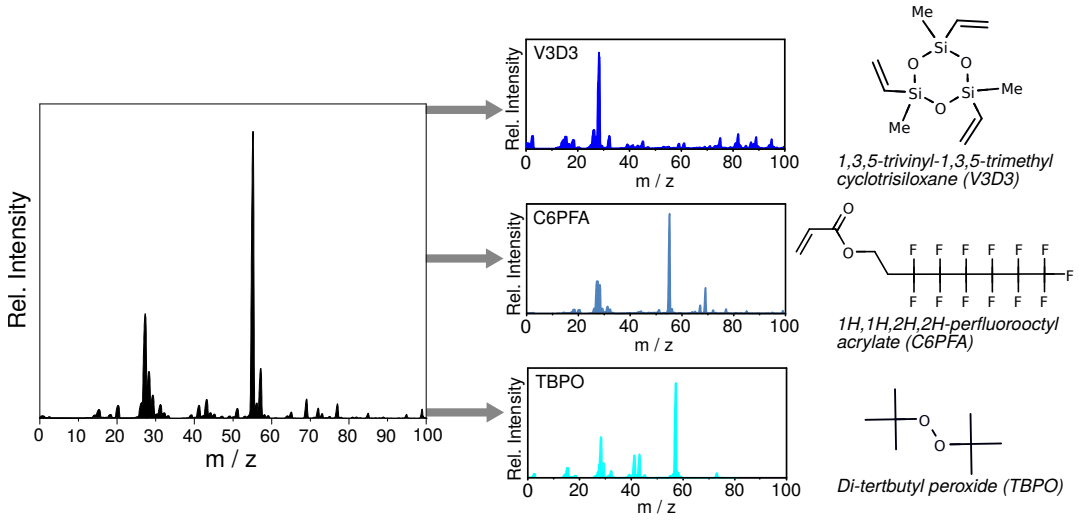

Figure 4.5: Example of a vapor phase used for copolymerization. The vapor phase consists of the comonomers 1,3,5-Trivinyl-1,3,5-Trimethylcyclotrisiloxane (V3D3) and 1H,1H,2H,2H-perfluorooctyl acrylate (C6PFA) as well as the initiator tert-butyl peroxide (TBPO). The individual contribution of each component can be identified by the respective reference spectra.

The symbol m_i is the amount of substance in the copolymer, which can be derived, e.g. by X-ray photoelectron spectroscopy (XPS). The Fineman-Ross representation [152],

$$\frac{[M_1]}{[M_2]}\left(1-\frac{m_2}{m_1}\right)=r_1\frac{[M_1]^2 m_2}{[M_2]^2 m_1}-r_2 \tag{4.5}$$

as well as the Kelen-Tüdős plot [153] have been reported to be well-suited for iCVD copolymerization, as mentioned in Chapter 2. With the obtained precise knowledge on the chemical composition of the vapor phase an accurate determination of the reactivity ratios is feasible.

4.4 Enhanced Process Control

Especially if low flow rates are set, inaccuracies may occur during the deposition. This is particularly severe for continuous flow processes where, in contrast to batch processes, the reactor atmosphere is constantly replaced. The problem

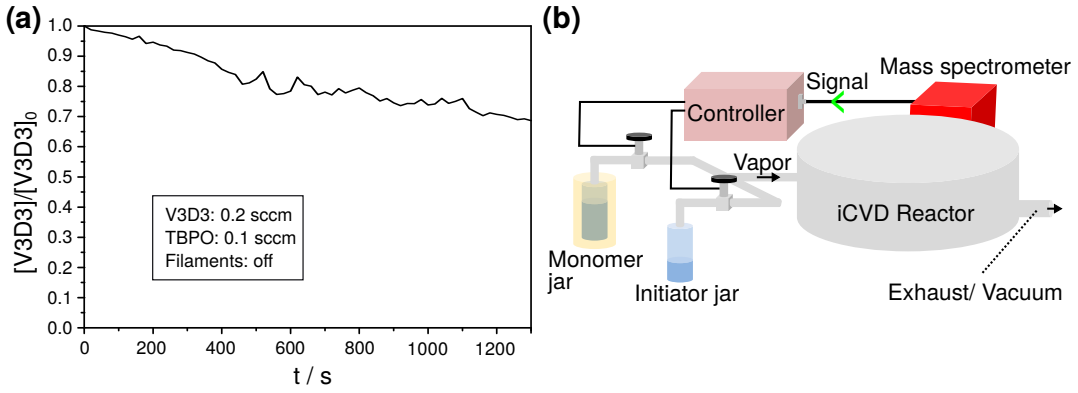

Figure 4.6: Enhanced iCVD process control. (a) Decrease of the monomer flow rate over time in a continuous flow process without deposition (filament heating switched off). (b) Proposed enhancement of the iCVD system to compensate decreasing flow rates during the deposition.

is shown as an example in Figure 4.6. A vapor mixture of TBPO and V3D3 is considered. V3D3 and TBPO are delivered to the reactor without filament heating. The flow rate of V3D3 decreases by about 25 % after 20 minutes. The decrease can be caused by, e.g. a change of the filling level in the monomer jar. This changes the V3D3 monomer partial pressure (p_m) and consequently the amount of monomer adsorbed onto the substrate. The Brunauer-Emmet-Teller (BET) theory, which was found to describe monomer adsorption behavior in iCVD processes accurately [133, 134], relates the adsorbed monomer volume to the monomer partial pressure as

$$V_{ad} = \frac{V_{ml}\, c_B \frac{p_m}{p_{sat}}}{\left(1 - \frac{p_m}{p_{sat}}\right)\left(1 - \left(1 - c_B\right)\left(\frac{p_m}{p_{sat}}\right)\right)} \tag{4.6}$$

The symbols V_{ml}, p_{sat} and c_b are the volume of a monolayer, the saturated vapor pressure of the monomer and the BET constant. This decrease in the flow rate can be detected by the QMS and a simple feedback system can be used to correct this flow rate. Once the flow rate falls below a certain value the computer sends a signal to an electrically controlled valve, as schematically illustrated in Figure 4.6b. The flow rate is now increased until the initial value of the flow rate is restored. Of course it would be cost-intensive to equip each reactor with a QMS as a permanent diagnostic tool. However, a QMS allows to determine the level of control needed for the process. Then decisions can be made for a more economical

solution for controlling the respective process. Recording and archiving of the deposition via in-situ QMS can also be of interest for industrial applications of iCVD, e.g. to trace the process conditions if a certain batch does not show the desired results.

4.5 Summary

In summary, in-situ QMS turned out to be a versatile tool for improving iCVD/HFCVD processes. It enables to obtain insight into real-time reaction kinetics as well as identification of reaction pathways. The fingerprint ability is a powerful tool to accurately determine the vapor phase composition during the deposition and to spontaneously adjust it if necessary. This is particularly interesting for copolymerization by iCVD or deposition on the lower nanometer scale. In this way better process control as well as the ability to perform extensive kinetic studies can be obtained. Thus, the parameters can be found where the conversion of the starting materials is the highest. This reduces the number of unreacted chemicals that are pumped out of the reactor.

5. iCVD Poly(tetrafluoroethylene) Thin Film Electrets

In this chapter poly(tetrafluoroethylene) (PTFE) thin films deposited in the initiated chemical vapor deposition (iCVD) setup built within the framework of this thesis are applied for the first time as electrets. PTFE is known for its excellent charge storage properties. Due to its chemical similarity to commercial PTFE, iCVD PTFE also exhibits similar storage properties which cannot be achieved with other processes such as sputtering or plasma polymerization. The extremely good charge stability of the synthesized films, the CVD-typical large-area growth characteristics as well as the precise film thickness control now enable access to ultra-stable PTFE electrets in MEMS technology for next generation electret applications.

Parts of this chapter are published in:

> **S. Schröder**, T. Strunskus, S. Rehders, K. K. Gleason, and F. Faupel. Tunable polytetrafluoroethylene electret films with extraordinary charge stability synthesized by initiated chemical vapor deposition for organic electronics applications. *Sci. Rep.*, 9:2237, 2019.

O. C. Aktas, **S. Schröder**, S. Veziroglu, M. Z. Ghori, A. Haidar, O. Polonskyi, T. Strunskus, K. K. Gleason and F. Faupel. Superhydrophobic 3D Porous PTFE/TiO2 Hybrid Structures. *Adv. Mater. Interfaces*, 6:1801967, 2019.

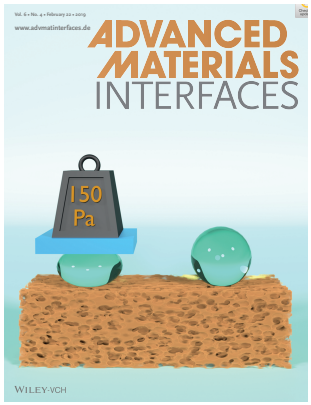

M. Mintken, M. Schweichel, **S. Schröder**, S. Kaps, J. Carstensen, Y. K. Mishra, T. Strunskus, F. Faupel, and R. Adelung. Nanogenerator and piezotronic inspired concepts for energy efficient magnetic field sensors. *Nano Energy*, 56:420-425, 2019.

5.1 Introduction

Electrets have become an essential part of everyday life, at least for users of mobile phones, hearing aids or other portable electronic devices in which electret microphones are installed [38, 39]. Furthermore, electrets are used in generators [41–47], electrostatic air filters [50, 178], dosimeter [48, 49] organic transistor memory [53–56] and memristors [52]. As already introduced in Chapter 2, PTFE is exceptionally well suited as an electret material [188, 189, 192]. However, the results refer to thick PTFE foils and PTFE bulk material. Accordingly, efforts are being made to produce this material in thin-film form to keep up with the trend of device miniaturization, flexible organic electronics and integration in state-of-the-art microelectronic processing lines. Many thin film deposition techniques have therefore already been investigated to produce PTFE thin films. However, the charge stored on these potential thin-film electrets was not very high and stable. Radio frequency (RF) sputtered PTFE films, for example, often show a deviation of the chemical character to highly cross-linked "PTFE-like" films, which often have higher dissipation factors [267–270]. PTFE thin films deposited by plasma polymerization also exhibit a high degree of cross-linking and polar group formation, which is reflected in the higher dissipation factor and worse electret performance [271, 272]. Other approaches like pulsed laser deposition (PLD) are not compatible with large-area synthesis [273] for, e.g. industrial applications. The iCVD process has proven to be capable of depositing high quality PTFE films, which are chemically almost identical to commercial PTFE products [21, 37, 139, 274–279]. Here the question will be answered whether the iCVD PTFE is also suitable as a thin-film electret material due to these promising prerequisites.

5.2 Performance of iCVD PTFE as Electret Thin Films

First of all, a chemical analysis of the PTFE thin films deposited in the iCVD system set up in the scope of this thesis is performed. Hexafluoropropylene oxide (HFPO) and perfluorobutanesulfonyl fluoride (PFBSF) were used for the deposition according to the parameters listed in Chapter 3. X-ray photoelectron spectroscopy (XPS), Raman spectroscopy (RS) and Fourier-transform infrared spectroscopy (FTIR) show that the iCVD PTFE films in this study are almost identical to commercial PTFE as shown in Figure 5.1. The XPS scan in Figure

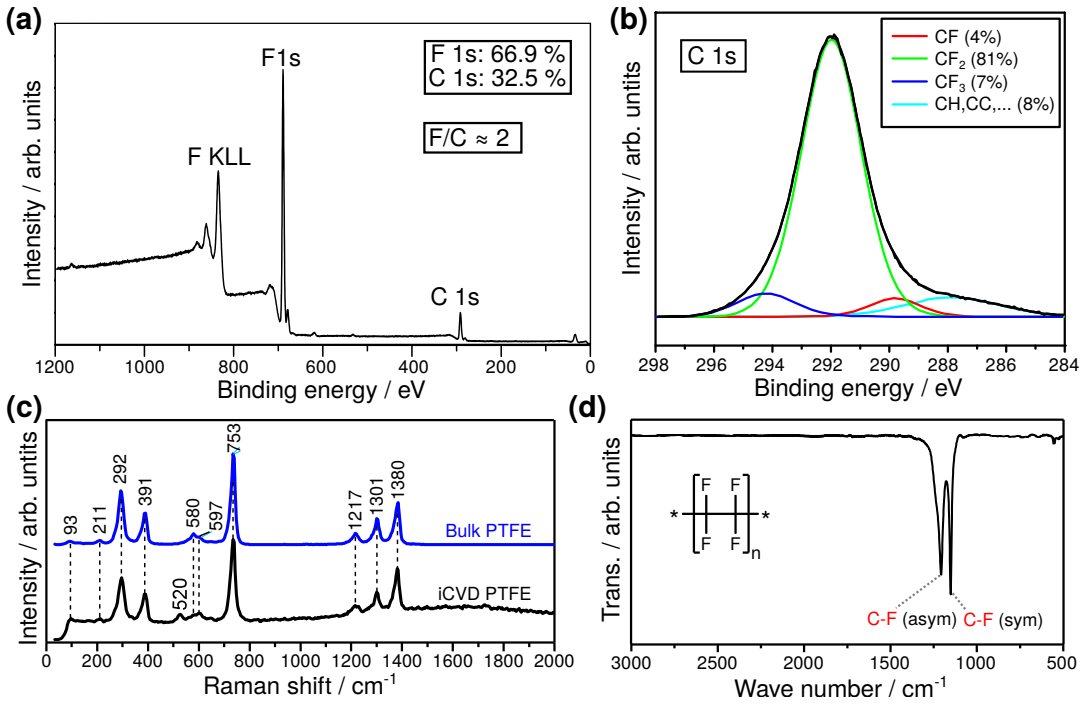

Figure 5.1: Chemical characterization of the PTFE thin films deposited with the iCVD system built in the scope of this thesis. (a) XPS of iCVD PTFE, (b) XPS high resolution C 1s scan of iCVD PTFE, (c) Raman spectroscopy of commercial PTFE and iCVD PTFE and (d) FTIR of iCVD PTFE.

5.1a shows clear peaks for both F 1s and C 1s. The chemical composition F/C at the surface is about F/C ≈ 2. This indicates a linear CF_2 character, which is typical for PTFE. The XPS high resolution C 1s peak in Figure 5.1b demonstrates furthermore the CF_2 character of iCVD PTFE. The CF_3 peak can be explained by the end-groups of the polymer chains as well as condensation of some PFBSF initiator molecules on the surface. The presence of CH and CC can be explained by slight surface contamination because the samples were exposed to the atmosphere before the XPS measurement. The Raman spectra in Figure 5.1c underline the similarity of iCVD and commercial PTFE. The bands can be assigned to PTFE typical groups and are listed in detail in Table 5.1. The exclusive band at 520 cm^{-1} in iCVD PTFE can be attributed to the silicon substrate because the PTFE films are deposited on silicon wafers. The FTIR spectrum in Figure 5.1d shows a transmission measurement. The spectrum shows bands at 1151 cm^{-1} and 1208 cm^{-1} for symmetric C−F stretch and asymmetric C−F stretch in CF_2,

Table 5.1: Suggested band assignment for the Raman spectra of bulk PTFE and iCVD PTFE.

Raman shift / cm^{-1}	assignment	Reference
211	CF_2 rocking (E_1)	[280–282]
292	CF_2 twist (E_1)	[282]
391	CF_2 twisting or scissoring (A_1)	[280, 282]
520	c-Si substrate peak	[283, 284]
580	CF_2 wagging, rocking (E_2)	[282]
753	CF_2 symmetric stretch (A_1) (and C−C symmetric stretch)	[280, 285]
1217	C−C stretching (and CF_2 asymmetric stretch (E_2)	[280, 282, 285]
1301	C−C stretch (E_1) (and CF_2 symmetric or asymmetric stretch)	[282, 285]
1380	CF_2 asymmetric stretch (A_1)	[282, 285]

respectively. All applied chemical characterization techniques show that PTFE films synthesized by the constructed iCVD system are almost indistinguishable from commercial PTFE. This is also confirmed by many other authors [23, 37]. These are indeed good prerequisites for the electret application. The iCVD PTFE has a linear CF_2 character like commercial PTFE and is not marked by strong cross-linking or polar groups like in the other physical vapor deposition (PVD) coating processes of PTFE mentioned in the introduction.

A view on the electronic structure can be approximated by the increasing length of fluorocarbons. Corresponding second order Møller–Plesset perturbation theory (MP2) calculations are shown in Figure **??**. As basis set the correlation-consistent basis set cc-pVTZ was used. Even if the calculation shown is only an approximation for a long PTFE chain, it is immediately clear that there is a large distance between HOMO and LUMO band. This is consistent with the experimental observations for the excellent insulating properties. The gap between the bands can thus contain sufficient deep level traps that can be occupied by the charge carriers. The dielectric properties of iCVD PTFE are determined by the impedance. For this purpose thin film capacitors made of iCVD PTFE are measured. The vertical line in Figure 5.3a shows capacitive behavior. The complex impedance (Z^*) is used to determine the dielectric properties. Based on

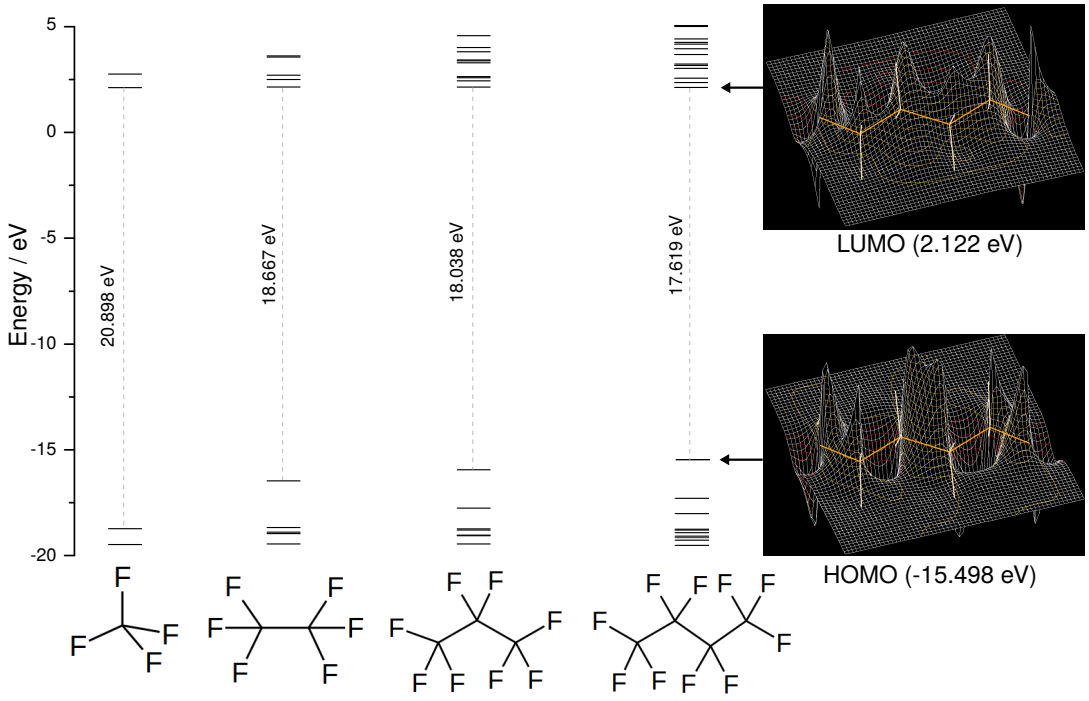

Figure 5.2: Approximation of the electronic structure of a PTFE chain by the calculation of growing fluorocarbons. For the calculation second order Møller–Plesset perturbation theory (MP2) with the correlation-consistent basis set cc-pVTZ was applied. The gap between HOMO and LUMO band approaches that of a PTFE chain.

the Maxwell equation

$$\vec{\nabla} \times \vec{H} = \vec{j}_f + \frac{\partial \vec{D}}{\partial \vec{t}}, \tag{5.1}$$

a relation between the measured impedance and the relative permittivity can be obtained. This is

$$\varepsilon_r^* = (i\omega C_0 Z^*)^{-1} \tag{5.2}$$

and yields the value $\Re(\varepsilon_r^*) = 2.1$ for the static relative permittivity of the film. The symbols $\vec{H}$, $\vec{j}_f$ $\vec{D}$, ω and C_0 represent the magnetic field strength, the free current density, the displacement field, the angular frequency and the geometry factor, respectively. The complete derivation of this relation can be found in Appendix E of this thesis. The dissipation factor, given by

$$\tan(\delta) = \frac{\varepsilon_2}{\varepsilon_1}, \tag{5.3}$$

also shows no differences between iCVD PTFE and commercial PTFE in the setup used to measure the impedance. According to $\varepsilon_r^* = \varepsilon_1 + i\varepsilon_2$ the symbol ε_1 represents the real part and the symbol ε_2 the imaginary part. The dissipation factor is therefore lower than for other deposition processes, because the formation of polar end-groups (e.g. C=O) can be excluded by using the PFBSF initiator and the mild deposition conditions as also confirmed by the chemical characterization in the beginning of this section. After charging the iCVD PTFE films in a corona setup, thermally stimulated potential decay (TSPD) measurements are performed. The result in Figure 5.3b is compared with conventional spin-coated Teflon AF electret films and bulk poly(methyl methacrylate) (PMMA) electrets. The measurement first of all demonstrates that fluoropolymers such as PTFE and Teflon AF are generally superior to non-fluoropolymers, as seen in the comparison with PMMA. The iCVD PTFE film electrets further show a higher stability than electrets made of commercial Teflon AF films. The reasons for this may be the glass transition at $T_g = 160\,^{\circ}\mathrm{C}$ and residual solvent in the Teflon AF polymer film. In addition, film inhomogeneities can occur during the manufacturing process, as several layers had to be spin-coated to achieve a sufficient layer thickness. The initial increase in the iCVD PTFE curve can be explained by thermal expansion [286]. Due to a phase transition in the crystalline regions in PTFE at about $30\,^{\circ}\mathrm{C}$ from a hexagonal (15/7 helix) to a pseudo-hexagonal structure [287], the increase is very pronounced. In the amorphous samples (Teflon AF and PMMA) no increase was observed. The corresponding value for the released current calculated according to the equation [288]

$$\frac{\mathrm{d}n}{\mathrm{d}t} = \frac{\varepsilon_0 \varepsilon_r}{x_e} \beta_h \frac{\mathrm{d}V_s}{\mathrm{d}T}. \tag{5.4}$$

is shown in Figure 5.3c. x_e, β_h and T represent the electret film thickness, the heating rate and the temperature, respectively. According to Simmons, the use of

$$\frac{\mathrm{d}n}{\mathrm{d}t} = \int_{E_0}^{E} f_0(E) N_t(E) P_s(E,T)\,\mathrm{d}E \tag{5.5}$$

enables the current to be described in terms of the initial occupancy of energy traps (f_0), the energy distribution of trap levels (N_t) and a shape-factor (P_s) [286, 289, 290]. The product of f_0 and N_t is consequently the initial number density [291, 292]. P(E,T) can be described as

$$P(E,T) = e_{re}(E,T) \exp\left(-\frac{1}{\beta}\int_{T_0}^{T} e_{re}(E,T)\,\mathrm{d}T\right). \tag{5.6}$$

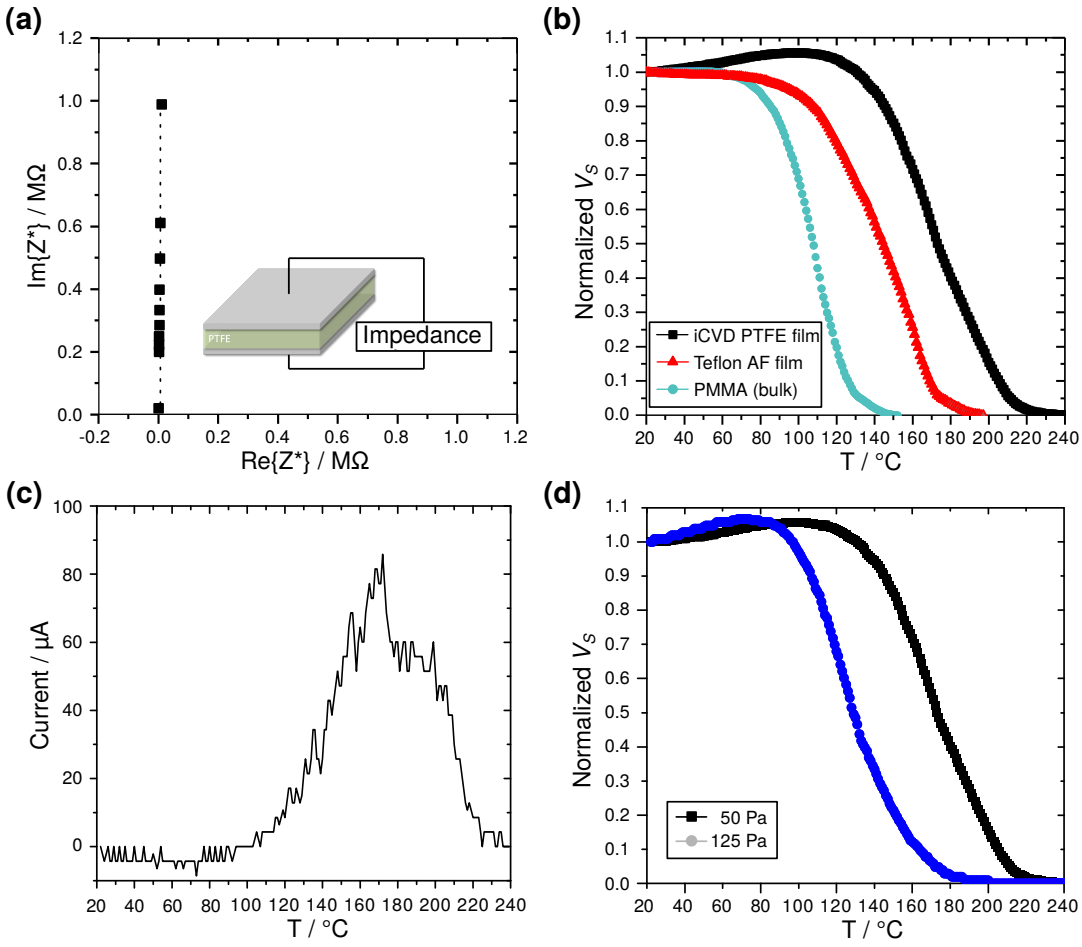

Figure 5.3: iCVD PTFE thin film electrets. (a) The impedance measurement shows capacitive behavior. (b) Thermally stimulated surface potential decay curves. The surface potential of iCVD PTFE thin film electrets shows a higher thermal stability compared to PMMA bulk samples and commercial Teflon AF thin films. (c) Calculated release current curve according to equation 5.4. (d) iCVD PTFE electret performance can be tuned by the deposition parameters. Shown here is the thermal stability of the surface charge for iCVD PTFE films deposited at different process pressures (50 Pa and 125 Pa).

e_{re} is the release probability and expressed by:

$$e_{re}(E,T) = \omega_f \exp\left(-\frac{E}{\mathrm{k_B}T}\right). \tag{5.7}$$

The symbol ω_f and $\mathrm{k_B}$ represents the frequency factor and the Boltzmann constant, respectively. Taking the associated area (A_d) into consideration, equation 5.6 can be approximated by a δ-function [289]:

$$P(E,T) = A_d \delta(E - E_{max}). \tag{5.8}$$

Equation 5.5 consequently becomes:

$$\frac{\mathrm{d}n}{\mathrm{d}t} \approx A_d f_0(E) N(E_{max}) \tag{5.9}$$

With dP/dE the possible solution

$$E = T\left(a_1 \log\left(\frac{\omega}{\beta}\right) + a_2\right) - a_3 \tag{5.10}$$

now appears. The measurements at two different heating rates (here: $\beta_{h,1} = 3.75\,\mathrm{K\ min^{-1}}$ and $\beta_{h,2} = 6\,\mathrm{K\ min^{-1}}$) allow the estimation of ω_f. The values $a_1 = 1.92 \times 10^{-4}$, $a_2 = 3.2 \times 10^{-4}$ and $a_3 = 1.5 \times 10^{-2}$ are selected for the parameters [289]. The value of $3.6 \times 10^{-13}\,\mathrm{Hz}$ determined in this way is in excellent agreement with values reported for commercial PTFE ($7 \times 10^{-13}\,\mathrm{Hz}$ [286]). The value for the activation energy of the traps is estimated to be $E_{a,t} = 1.136\,\mathrm{eV}$. An interesting observation is that this behavior can be influenced by the deposition parameters. For example, iCVD PTFE films deposited at higher process pressures (125 Pa) show a lower thermal stability of the charges as shown in Figure 5.3d. This opens new doors for the selective tuning of the trap landscape for applications and studies where the long-term stability of the charge is not necessarily important. However, for most applications it is desired that the charge remains for a long time. To determine the theoretical long-term stability of the fabricated iCVD PTFE electrets, the rate equations of Małecki are considered [212, 213], which have been introduced in Chapter 2. The model does not provide the actual real lifetime, because it depends on many other variables (also storage etc.), but it is used to compare the samples with each other. Application of the set of differential equations

$$\frac{dg(t)}{dt} = \frac{\beta_h}{n_0}(1 - g^2(t)) - \frac{\mu_M}{\varepsilon_0 \varepsilon_r x_e} g(t)\sigma(t) \tag{5.11}$$

$$\frac{d\sigma'(t)}{dt} = -\frac{n_0 q \mu_M}{\varepsilon_0 \varepsilon_r} g(t)\sigma(t), \tag{5.12}$$

yields the curve shown in Figure 5.4a. With $g(t) = \frac{n(t)}{n_0}$ denoting the ratio of the time-dependent carrier density ($n(t)$) and initial carrier density (n_0). The values for the initial carrier density (n_0), ε_r and x_e were determined from the measurements shown above. The values for the generation rate of charge carriers (β_h) and the mobility (μ_M) are taken from the literature [212, 213]. ε_0, σ and q represent the vacuum permittivity, the surface charge and the elementary charge, respectively. A 20 µm film, which has been charged to -400 V, is simulated. The results show that the surface charge or surface potential decreases exponentially in the first hours immediately after charging, as seen in the inset of Figure 5.4a. This typical initial exponential decay is also observed in the measurement of a real electret immediately after charging, as shown in Figure 5.4b. After that, however, the decay shown in Figure 5.4a changes into a linear long-term behavior, as described by Małecki [212, 213]. The surface charge only decreases to half of its initial value after more than 20000 years. Of course this theoretical value is strictly related to the material. External decay processes like described in Chapter 2 shorten this time. They depend considerably on the storage of the electret, a multifaceted variable that is difficult to capture in a model for the long-term prediction of the charge stability. An additional comment on this topic is provided in Appendix F. The statement that can be made, however, is that the charge decay of the iCVD PTFE thin film electrets can very well be neglected compared to device lifetimes in which the films are applied. The log-scale in Figure 5.4c reveals this in more detail. Assuming the iCVD PTFE electret is to be mounted in an electret sensor/generator device. After the initial stabilization of the charge in the first days after charging, the iCVD PTFE electret is placed in the device on the third day. The charge can now be assumed to be constant until the end of the device lifetime, which is approximately 10 years as shown in Figure 5.4c.

5.3 Summary

In this chapter it was investigated whether iCVD PTFE thin films are suitable as electret material. Due to the excellent chemical similarity of the iCVD PTFE films to commercial PTFE, this statement can now be confirmed. The films can be sufficiently highly charged and show a very low charge decay over time which can be neglected compared to device lifetimes. The CVD-typical character

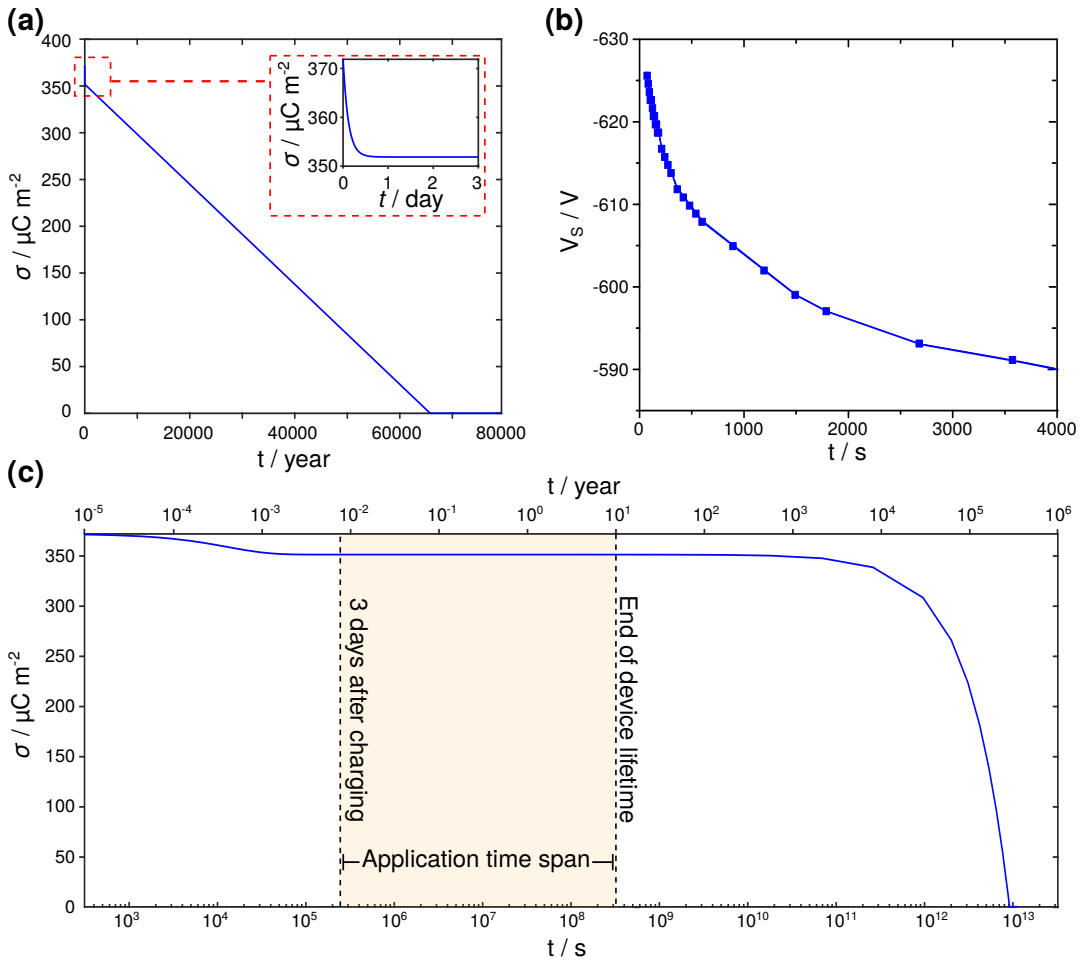

Figure 5.4: Theoretical calculation of the surface potential decay at room temperature. (a) After initial short-term exponential decay (as seen in the inset), a linear long-term decay as predicted by Małecki [212, 213] can be observed. (b) Typical measurement of fluoropolymer surface potential decay over one hour starting from the time of charging ($t = 0$). (c) The plot on the log scale reveals the different regimes of decay. Theoretically, the charge only begins to decrease significantly after a thousand years. Assuming that the iCVD PTFE electret is placed in an electret generator/transducer device on the third day after corona charging (after initial stabilization of the surface charge) and is in operation for 10 years, the surface charge can be assumed to be constant and the internal charge decay can be neglected.

of the process and the ability to tune the properties of the films make the approach attractive for large-area industrial deposition as well as for further device miniaturization and new approaches in organic electronics. A special advantage of iCVD is the ability to specifically tailor the charge storage properties of the polymer thin films by the deposition conditions. This will be discussed in more detail in the next chapter.

6. The Effect of Different End-groups on the Charge Trapping in Poly(ethylene glycol dimethylacrylate)

Based on the previous chapter, the approach in this chapter uses the unique ability of the initiated chemical vapor deposition (iCVD) process to tailor polymer thin film properties. As an example poly(ethylene glycol dimethylacrylate) (PEGDMA) is considered, which is each polymerized with a different initiator. This results in different end-groups in the polymer, which influence the charge storage after corona treatment by providing different trap states. This enables trap state fine tuning as well as a better understanding of the processes of charge storage in electrets. In this chapter tert-butyl end-groups, phenyl end-groups and perfluorobutyl end-groups are investigated for this purpose. PEGDMA is furthermore a fluorine-free polymer and could be used as a more environmentally friendly alternative to fluoropolymer electrets.

The complete content of this chapter is submitted for publication:

> **S. Schröder**, W. Reichstein, T. Strunskus, and F. Faupel. Influence of different end groups on the electret effect in poly(ethylene glycol dimethacrylate) thin films deposited from the vapor phase. *submitted*, 2020.

6.1 Introduction

A major advantage of iCVD is the possibility to tailor the thin films specifically by the deposition parameters and the monomer/initiator combinations. Also for electrets this seems to be a promising way to influence the charge storage properties. In this way, it can be specifically investigated which functional groups are particularly well suited for charge storage. This helps to understand the general mechanism of charge storage in electrets. The storage of the charge carriers is typically described in terms of trap states located inside the band gap of the polymer. A good electret has many deep-level traps that store the charge over a long period of time. This is in complete contrast to organic semiconductors and organic conductors, where these trap states are completely undesirable because they impede the charge transport [161, 202, 293]. For this purpose it is important to get insight into the electronic structure of a polymer insulator. The electronic structure of the repeating units of the polymer provides the highest occupied molecular orbital (HOMO) and the lowest unoccupied molecular orbital (LUMO), as also introduced in more detail in Chapter 2. The gap between these two bands is the band gap of the polymer, in which no states exist. However, this accounts only for an ideal polymer. It is known that in the real world additional trap states can occur in this band gap. A distinction is made here between the abovementioned shallow traps and deep-level traps. Shallow traps can be caused by different conformations within the polymer chain, for example [157]. Often the room temperature is sufficient to release the charge carriers from these traps. They are found near the HOMO and LUMO edges. Deep-level traps are located deep in the band gap of the polymer and higher energy is required to release trapped charge carriers from these states. These traps can be caused by impurities, certain functional groups or interfaces in the polymer, for example [157]. Nanosize voids have furthermore been reported to provide states for deep level traps [202]. Kim et al. demonstrated in a recent study by density functional theory (DFT) and experimental results, that the end groups play furthermore a crucial role for the charge trapping in commercial Cytop fluoropolymers [201]. In this chapter different initiators are used to polymerize poly(ethylene glycol dimethacrylate) (PEGDMA) thin films using the iCVD process. The respective initiator used in the iCVD process provides the end groups in the polymer thin film, as shown in Figure 6.1a. Here, PEGDMA is used as a model system in order to examine whether different end groups can be obtained via the iCVD process and whether the use of these end groups has an influence on the charge trapping behavior. The idea is to create additional trap states in the band gap

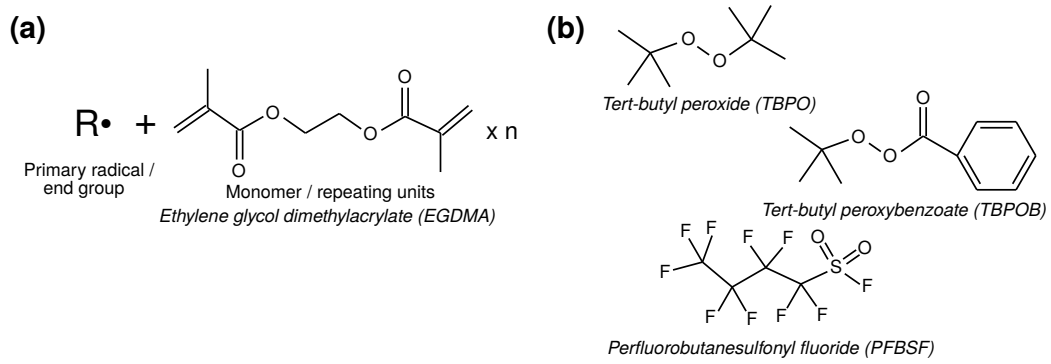

Figure 6.1: Different initiator and monomer combinations. (a) Illustration of the initiation process. The primary radical of the initiator attacks the vinyl group of the monomer and provides thus the end group. (b) Structural formulas of the initiators used in this study.

of the polymer between the HOMO and LUMO bands. The electronic structure of the end groups can in this connection be estimated by quantum chemical calculations. In the future, this could lead to a targeted trap state engineering in order to individually adjust the trap landscape of the polymer thin films. This helps to better understand the origin of deep-level traps in the polymer and the underlying mechanisms during the charge trapping. It may also provide in the future a possible new pathway for the fabrication of more environmentally friendly, fluorine-free electrets. In the synthesis of fluoropolymers, substances are used that are persistent, bioaccumulative and toxic. Especially the C8 and C6-based substances are already partly banned, because they are proven to cause long-term damage in organisms, since they can not be decomposed by them [294].

6.2 Charge Trapping in Different PEGDMA End-groups

All three monomer + initiator combinations yield thin films. The deposition rates are 16.97 nm/min, 77.14 nm/min and 88.2 nm/min for EGDMA+TBPO, EGDMA+TBPOB and EGDMA+PFBSF, respectively. Due to the relatively high deposition rates, the layer thickness of more than 1 µm required for the electret application can be achieved relatively fast. It is also possible to further increase the rates by the deposition parameters. The FTIR spectra of the deposited

thin films are shown in Figure 6.2. Absence of major bands above 3000 cm^{-1}

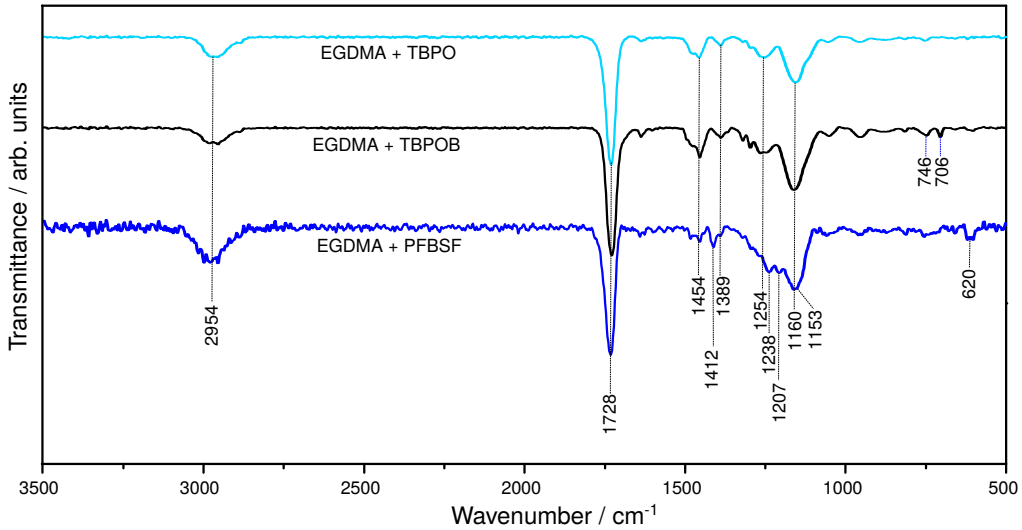

Figure 6.2: FTIR spectra of the three different thin films obtained from the monomer + initiator combinations EGDMA+TBPO (cyan), EGDMA+TBPOB (black) and EGDMA+PFBSF (blue).

for the C−H stretch at vinyl groups as well as bands in the region 1500 cm^{-1} - 1600 cm^{-1} for the vinyl groups confirm absence of these groups in the thin films and thus successful polymerization of PEGDMA in all three cases [295]. Preserved monomer functionality is shown by the band at 1728 cm^{-1} for the C=O stretch in the ester group of EGDMA monomer, due to the mild deposition conditions during the iCVD process [296]. Each of the three combinations yields slightly different bands, due to different end groups. The FTIR spectrum of EGDMA+TBPOB shows additional small bands at 746 cm^{-1} and 706 cm^{-1}. These bands can be assigned to the phenyl end groups in the polymer film. The EGDMA+PFBSF film shows additional bands which correspond to the additional fluorine functionality. The band at 1207 cm^{-1} as well as the band at 1153 cm^{-1}, which is partially overlapping with the C−O stretch at 1160 cm^{-1}, are assigned to the asymmetric and the symmetric C−F stretch, respectively [285]. The assignment of further bands in the FTIR spectrum can be found in the Table 6.1. DFT calculations are used to compare the computed HOMO and LUMO levels of the end groups and the polymer. The results are shown in Figure 6.3. The end groups provided by the primary radicals of the TBPO initiator are represented by tetramethylmethane (I) and tert-butanol (II). The energy levels are located outside of the HOMO-LUMO

Table 6.1: Suggested band assignment for the FTIR spectra of PEGDMA grown with different initiators.

Band / cm^{-1}	Assignment	Reference
$\approx$ 2954	C−H symmetric and asymmetric stretching in CH_3, C−H symmetric and asymmetric stretching in CH_2	[297]
1728	C=O stretch in ester	[296]
1454	asymmetric CH_3 deformation vibration in $C(CH_3)_3$ end-group	[297]
1412	C−F stretch in CF_3	[285]
1389	symmetric CH_3	[297]
1254	$C(CH_3)_3$ rocking vibration	[297]
1238	C−F stretch in CF_3	[285]
1207	C−F asymmetric stretch	[285]
1160	C−O stretch in ester	[298]
1153	C−F symmetric stretch	[285]
746	phenyl group	[299]
706	phenyl group	[299]
620	CF_3 asymmetric deformation vibration	[285]
611	CF_3 symmetric deformation vibration	[285]

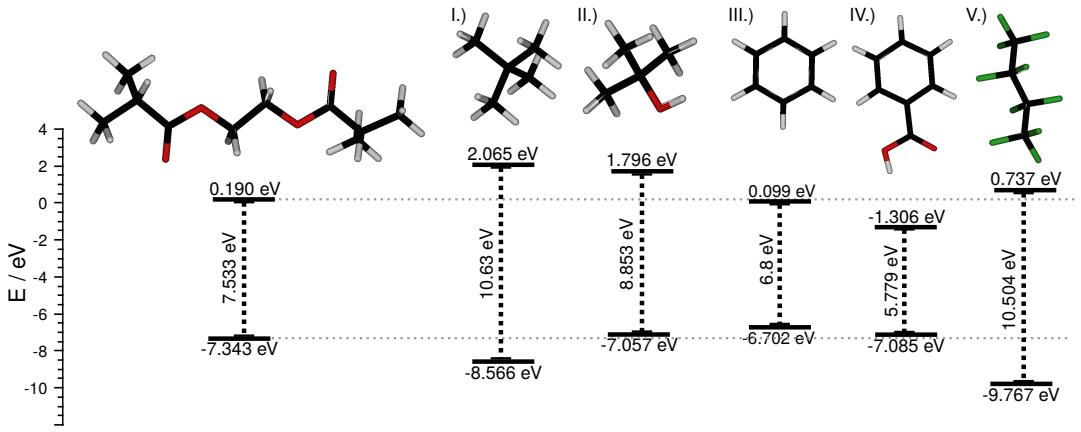

Figure 6.3: Theoretically estimated HOMO and LUMO energies using B3LYP/6-31G* density functional theory. The repeating unit is used to estimate the energy levels of the polymer.

gap of the EGDMA molecule, representing the repeating unit of the polymer. It can be assumed that for this reason probably no new trap states are created. Only the HOMO level of tert-butanol (II) is about 0.286 eV above the HOMO level of EGDMA. This would, however, produce at best unstable traps, which could even be emptied at room temperature and might even promote the electrical conductivity through the thin film by thermal activated hopping. The same applies to the end groups of the PFBSF initiator. They are represented by the perfluorobutane (V). The HOMO and LUMO level are also located outside the band gap of EGDMA. Benzene (III) and a benzoate molecule (IV) are used to represent the additional end groups which originate from the primary radicals of the TBPOB initiator. According to the calculation the energy levels of the orbital of both molecules are located inside the band gap of EGDMA. In form of end groups and thus part of the polymer they might provide additional distortion in the band gap of the repeating units. This could then be associated with the formation of additional trap states. The thermal stability of the corona charged samples of all three combinations is investigated using thermally stimulated potential decay (TSPD) measurements. The PEGDMA electrets, displayed in Figure 6.4, show a dependence of the end group on the charge storage. The measured surface potential (V_s) shown in the figure is related to the surface charge (σ) via

$$\sigma = V_s \frac{\varepsilon_0 \varepsilon_r}{x_e} \tag{6.1}$$

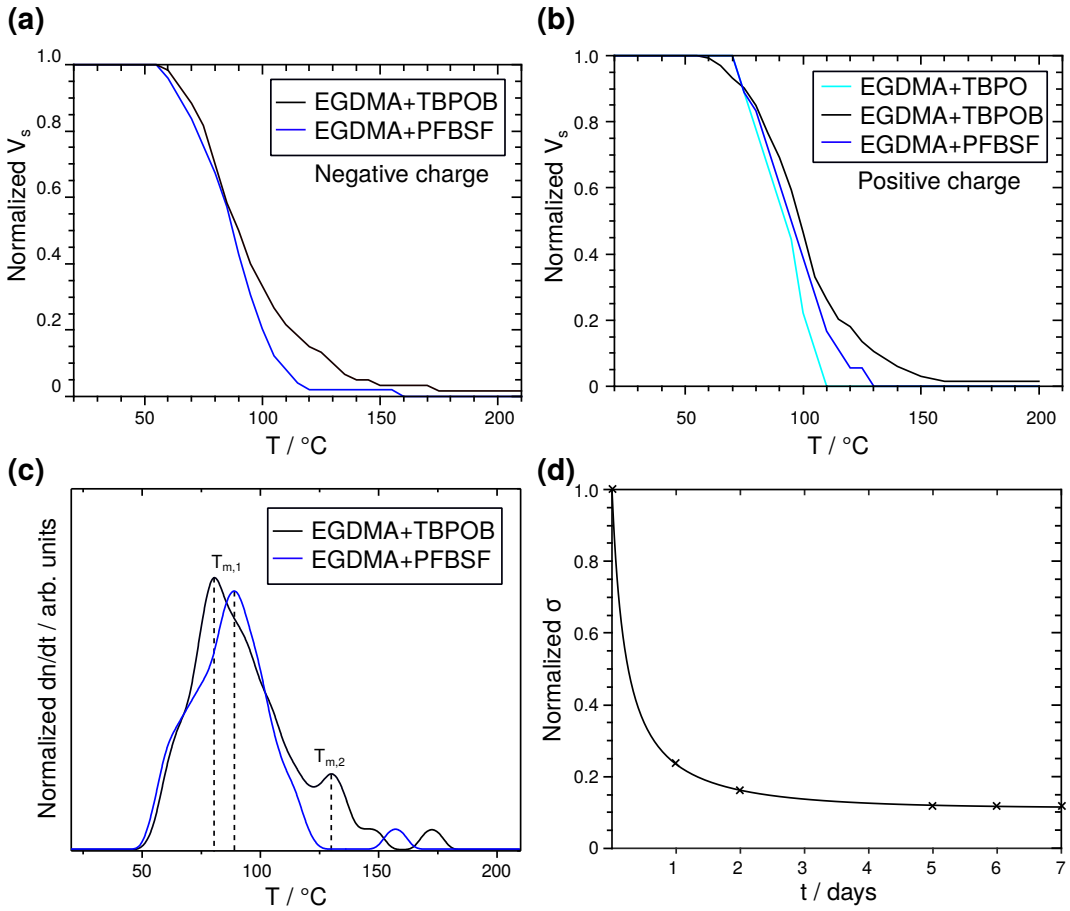

Figure 6.4: TSPD measurements of the fabricated thin film electrets. (a) TSPD of the negatively charged electrets. The charge of the films grown from the combination of EGDMA+TBPO decayed already after 72 h at room temperature. (b) TSPD of the positively charged electrets. (c) Theoretically calculated released current of negatively charged EGDMA+TBPOB and EGDMA+PFBSF. (d) initial decay at room temperature (x) fitted with the Małecki model.

The symbols x_e, ε_0 and ε_r represent the film thickness, the relative permittivity and the vacuum permittivity, respectively. The films in Figure 6.4a are negatively charged. The tert-butyl end groups provided by the combination of EGDMA+TBPO do not appear to create significant deep traps and the occupied trap states are emptied at relatively low temperatures. It was not possible to measure these samples by TSPD as the surface charge already completely decayed during the initial storage time of 72 h. Samples deposited with TBPOB initiator as well as samples deposited with PFBSF initiator show better charge storage properties for the negatively charged case and allow TSPD measurements. At low temperatures the combination of EGDMA+PFBSF as well as the combination of EGDMA+TBPOB initially follow the same curve. At 60 °C the surface charge starts to decay. However, at higher temperatures, it becomes apparent that some charge carriers in the combination EGDMA+TBPOB must be located in deeper traps, since higher temperatures are necessary to completely release all charge carriers. This seems to be due to the phenyl groups present in the polymer film deposited with TBPOB. This indicates that initially traps of relatively low energy are emptied, most probably located in the repeating units of the polymer. The phenyl end groups seems then to provide trap states that can be occupied in the band gap of the repeating units of the polymer, which require more energy to be emptied. For PFBSF this seems not to be the case. The energy levels of the perfluorobutyl end groups seems thus not to fall into the band gap of the repeating units, as also calculated in Figure 6.3. The same accounts for the positively charged case shown in Figure 6.4b. Here it is possible to measure a curve for the combination of EGDMA+TBPO. Also for the positively charged case all three TSD curves follow initially the same behavior at low temperatures indicating detrapping from trap states provided by the PEGDMA repeating units. At higher temperatures again more energy is required to empty all traps for the combination of EGDMA+TBPOB. Thus the different end groups seem to have an influence on the respective charge trapping of PEGDMA. They can in the case of the TBPOB variant probably provide additional deep traps, while the other groups do not provide additional traps. The TSD data is transferred to the released current I(T) by the relation

$$I(T) = \frac{\varepsilon_0 \varepsilon_r}{x_e} \beta_h \frac{\mathrm{d}V_s}{\mathrm{d}T}. \tag{6.2}$$

The symbols β and T represent the heating rate and the temperature, respectively. The obtained curve is shown in Figure 6.4c for negative charged EGDMA+TBPOB and EGDMA+PFBSF. It is noticeable that there are two

peaks for EGDMA+TBPOB. The activation energy for the trap can be estimated by the initial rise method [300]

$$\frac{dI(T)}{1/T} = -\frac{E_{a,t}}{\mathrm{k_B}}, \tag{6.3}$$

or by the equation [301, 302]

$$E_{a,t} = \mathrm{k_B} T_{mp} \ln\left(\frac{T_{mp}^4}{\beta}\right) \tag{6.4}$$

providing the mean trap energy ($E_{a,t}$). T_{mp} and $\mathrm{k_B}$ are the temperature at the current peak and the Boltzmann constant, respectively. In this work equation 6.4 is used for the estimation in the TSD curve obtained by simple heating from T_{Start} to T_{Stop}. The first peak, which appears for EGDMA+TBPOB as well as for EGDMA+PFBSF has thus a depth between $E_{a,t,1} = 0.66 \pm 6.10 \times 10^{-4}\,\mathrm{eV}$. It can probably be assigned to traps provided by the repeating units of the polymer. Another peak occurs only in the combination EGDMA+TBPOB at about 130 °C. This is most likely related to the phenyl end groups provided by the TBPOB. According to the calculation the depth of this trap state is $E_{a,t,2} = 0.77 \pm 6.23 \times 10^{-4}\,\mathrm{eV}$. All obtained values are listed in Table 6.2. As already shown in Chapter 5, the long-term stability can be estimated using the rate equation model of Małecki [212, 213].

$$\frac{dg(t)}{dt} = \frac{\beta_h}{n_0}(1 - g^2(t)) - \frac{\mu_M}{\varepsilon_0 \varepsilon_r x_e} g(t)\sigma(t) \tag{6.5}$$

$$\frac{d\sigma'(t)}{dt} = -\frac{n_0 q \mu_M}{\varepsilon_0 \varepsilon_r} g(t)\sigma(t). \tag{6.6}$$

The symbols β_h, n_0, μ_M, σ and q represent the generation rate of carriers, initial carrier density, mobility, surface charge and charge, respectively. The parameter $g(t)$ represents the carrier density ratio $g(t) = n(t)/n_0$. Fitting of the experimentally observed decay to the model, as shown in Figure 6.4d yields the theoretical estimated long-term stability as well as characteristic values for the investigated monomer + initiator combinations. Regarding the values calculated here it has to be considered, that the model only includes the internal charge decay. External charge decay processes are ignored.

Table 6.2: Summary of obtained values for the different monomer + initiator combinations investigated in this study. (k_{depo} = deposition rate, n = refractive index, $E_{a,ti}$ = estimated trap depth).

Combination	k_{depo} / nm/min	n	$E_{a,t1}$ /eV	$E_{a,t2}$ / eV
EGDMA	16.97	1.51	0.66	-
+TBPO		$\pm 5.88 \times 10^{-4}$	$\pm 1.43 \times 10^{-3}$	
EGDMA	77.14	1.52	0.66	0.77
+TBPOB		$\pm 4.95 \times 10^{-4}$	$\pm 6.10 \times 10^{-4}$	$\pm 6.23 \times 10^{-4}$
EGDMA	88.20	1.48	0.68	-
+PFBSF		$\pm 1.35 \times 10^{-3}$	$\pm 1.97 \times 10^{-3}$	

6.3 Summary

The PEGDMA electret films investigated in this study are certainly no alternative to the ultrastable fluoropolymer electret thin films currently in use. However, a dependence of the deposited PEGDMA thin films and the respective end groups has been identified. In this way the charge storage properties can be tuned by the choice of the initiator. Especially the phenyl-termination seems to enhance the charge trapping of the PEGDMA films by providing additional deep traps for the charge carriers. In the future additional combinations could be investigated in this way to find further functional groups and their contribution to the charge trapping. This can be used to customize the trap landscape in the electronic structure of the polymers to systematically investigate the dependence of different functional groups on the charge trapping in electrets. In the future this can enhance the general understanding of the microscopic origin of the trap states in electrets and the respective location of the trap sites. It might furthermore lead to the fabrication of new environmentally friendly non-fluoropolymer electrets. Quantum chemical calculations can be used to find more specific combinations that can generate energy states in the band gap of the polymer to yield more efficient electret materials. By finding new combinations via previous estimation of the electronic structures, many new candidates can certainly be found here. This can also be interesting for new applications of the electrets. Some of these new approaches and possibilities will be discussed in the following chapter.

7. Organic Multilayer Electrets for Sensor Applications

This chapter presents new multilayer electrets. They are enabled due to the precise film thickness control and conformal growth in the initiated chemical vapor deposition (iCVD) process. The electret properties can be specifically tailored for more enhanced applications. This is demonstrated by a novel magnetic field sensor, which was developed in close collaboration with the Chair for Functional Nanomaterials (Prof. Dr. Rainer Adelung). The multilayer approach enables in this connection the electrets to be operated in principle without encapsulation and prevents unwanted shifting of the resonance frequency and burst noise in the sensor signal.

Parts of this chapter are published in:

> M. Mintken, M. Schweichel, **S. Schröder**, S. Kaps, J. Carstensen, Y. K. Mishra, T. Strunskus, F. Faupel, and R. Adelung. Nanogenerator and piezotronic inspired concepts for energy efficient magnetic field sensors. *Nano Energy*, 56:420-425, 2019.
>
> **S. Schröder**, T. Strunskus, S. Rehders, K. K. Gleason, and F. Faupel. Tunable polytetrafluoroethylene electret films with extraordinary charge stability synthesized by initiated chemical vapor deposition for organic electronics applications. *Sci. Rep.*, 9:2237, 2019.

7.1 Introduction

The findings for the iCVD PTFE presented in the Chapter 5 already show that the stability of the iCVD electrets is sufficiently high and can be neglected compared to the device lifetimes. A further parameter is the amount of charge that has been injected. A higher surface charge can increase the output, especially with regard to electret sensors or electret generators. The task is to convert external signals into an electrical signal (sensor/transducer) or to generate energy by an external signal (generator). Examples are microphones that convert sound waves into an electrical signal or generators that use vibrations to power small electrical devices [41–47]. In order to understand where the requirements for the electret material are, a transducer/generator of this type should first be considered. For this purpose a new type of magnetic field sensor is shown. These sensors were developed in close collaboration with the Chair for Functional Nanomaterials (Prof. Dr. Rainer Adelung). The magnetic component as well as all measurements of the sensor were carried out by the cooperation partners. In this section only the contribution of the electrets is discussed. For further details about the magnetic materials and characterization of the sensors, the reader is referred to the joint publication [303]. The development of these sensors has the aim to measure the weak biomagnetic signals of the human body. Starting from magnetoelectric sensors, in which magnetostrictive and piezoelectric thin films are traditionally deposited on a silicon cantilever [304, 305], the new approach eliminates all passive components such as the silicon substrate. This allows losses or noise originating from these components to be prevented. Here it will be shown which requirements are demanded for the iCVD electret thin films. It turns out that new organic multilayer films can be tailored for such applications.

7.2 Electrets for Magnetic Field Sensors

As described above in the introduction, a new type of magnetic field sensor based on the principle of the electret transducer/generator is considered first. The system can be assumed as a parallel plate capacitor where, as shown in Figure 7.1a, one electrode is variable and the other is covered with an electret. Figure 7.1b shows the structure used in the experiments. It is a setup where a magnetostrictive/magnetoactive cantilever can oscillates over the electret.

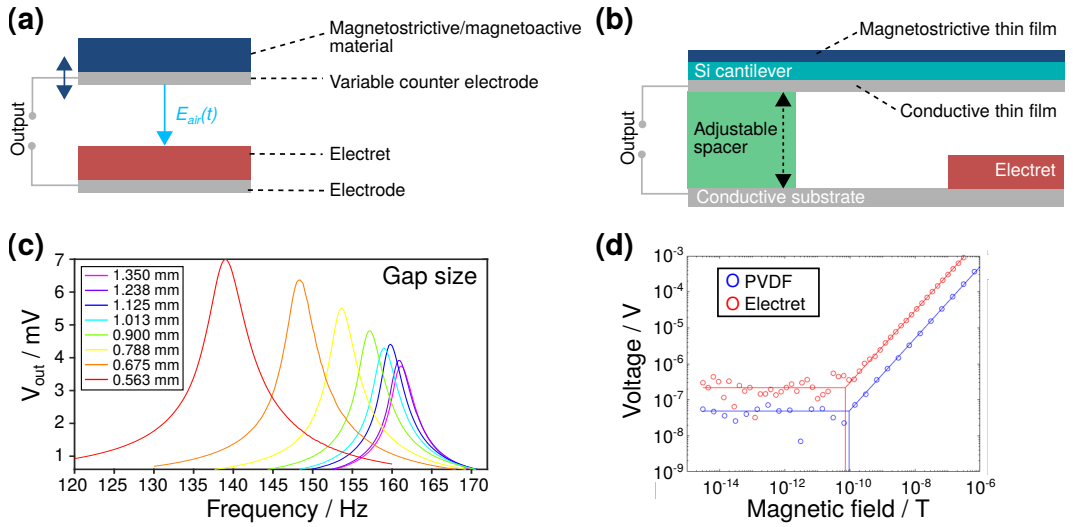

Figure 7.1: Magnetic field sensors based on electrets. (a) Schematic illustration of the sensor components. (b) Cantilever-type sensor setup used for the measurement. (c) Measurement of output voltage (V_{out}) as a function of frequency. This measurement has been performed by Dr. Sören Kaps (Chair for Functional Nanomaterials, Kiel University). (d) Comparison of the noise behavior of readout via piezoelectric poly(1,1-difluoroethylene) (PVDF) and readout via poly(tetrafluoroethylene) (PTFE) electret synthesized in this work. The measurement has been performed by Dr. Sören Kaps (Chair for Functional Nanomaterials, Kiel University)

Once the sensor is exposed to a magnetic AC field, the magnetostrictve material begins to periodically deform resulting in the displacement of the counter-electrode. The electric field in the air gap ($\vec{E}_{air}$) generated by the electret becomes time-dependent and, according to Maxwell, a displacement current ($\vec{j}_D$) follows

$$\vec{j}_D = \mu_0 \varepsilon_0 \frac{\partial \vec{E}_{air}}{\partial t}. \tag{7.1}$$

The symbols μ_0 and ε_0 represent the vacuum permeability and vacuum permittivity, respectively [1]. In other words, the charge on the counter electrode changes depending on its position. This change of the charge over time results in a current ($I = dq/dt$) and a signal, for example in the form of a voltage, which can be

[1] Here the air in the air gap is treated as a vacuum. Otherwise, the electric displacement field ($\vec{D}$) with the vector field for the polarization ($\vec{P}$) must be considered.

measured via a resistor at the sensor output. It can be observed in Figure 7.1c that the resonance frequency and amplitude can be adjusted by changing the air gap between electret and counter-electrode. The cantilever can be made softer in this way. The reason for this is the electret which generates an additional attractive Coulomb potential. Figure 7.1d shows the comparison of the presented electret sensor with a classic ME sensor, where a piezoelectric poly(1,1-difluoroethylene) (PVDF) thin film is applied to the bending beam. The limit of detection (LOD) were 73 $\mathrm{pT/Hz^{\frac{1}{2}}}$ at 321 Hz for the electret sensor and 96 $\mathrm{pT/Hz^{\frac{1}{2}}}$ at 322.5 Hz for the ME sensor readout. In comparison, the same signal-to-noise ratio is achieved with both sensors. The signal of the electret sensor is larger by a factor of about 6. All measurements shown in Figure 7.1c and Figure 7.1d have been performed by Dr. Sören Kaps (Chair for Functional Nanomaterials). To identify the relevant parameters for the electret, simple equations of motion can be determined using the Lagrange formalism. According to $L = T_k - V_p$ the total kinetic energy (T_k) and the total potential energy (V_p) of the system are considered for the Lagrangian. The approach for transducer is based on Hawley and Romanow [306]. For the novel magnetic field sensor, equations for T_k and V_p must therefore first be found. For a more detailed derivation the reader is referred to Appendix G. The potential energy is a combination of the field energy and the energy stored in the mechanical components

$$V_p = \frac{1}{2}k_F(x_0 + x)^2 + \frac{(x_{air} - x_0 - x)(q_0 + q)^2}{2\varepsilon_{air}A} + \frac{x_e(q_e + q_0 + q)^2}{2\varepsilon_e A}. \tag{7.2}$$

Here k_F, x_0, x_{air}, x_e, q_0, q_e, ε_{air}, ε_e and A are the spring constant, the initial position of the counterelectrode, the air gap width, the electret film thickness, the initial charge on the counter electrode, the charge at the electret surface, and the area of the electrodes, respectively. ε_{air} is the product of ε_0 and the relative permittivity in the air gap. ε_e is the product of ε_0 and the relative permittivity of the electret. The kinetic part is represented by

$$T_k = \frac{1}{2}m\dot{x}^2, \tag{7.3}$$

where m denotes the mass. In this way, an equation can be found for the Lagrangian using equation 7.3 and equation 7.2. It is

$$L = \frac{1}{2}m\dot{x}^2 - \frac{1}{2}k_F(x_0 + x)^2 - \frac{(x_{air} - x_0 - x)(q_0 + q)^2}{2\varepsilon_{air}A} - \frac{x_e(q_e + q_0 + q)^2}{2\varepsilon_e A}. \tag{7.4}$$

The Rayleigh function is used to include the dissipation in the system. It is given by

$$D_R = \frac{1}{2}R\dot{q}^2 + \frac{1}{2}c_D\dot{x}^2. \tag{7.5}$$

and includes the electrical resistance (R) of a resistor connected to the output of the sensor, which can be, e.g. the internal resistance of the measurement device, as well as the mechanical damping coefficient c_D. Continuing with the Lagrange equation given by

$$\frac{d}{dt}\left(\frac{\partial L}{\partial \dot{g}_i}\right) - \frac{\partial L}{\partial g_i} + \frac{\partial D_R}{\partial \dot{g}_i} = f, \tag{7.6}$$

x and q are chosen as generalized coordinates. The associated forcing functions are the force applied to the system during deflection (f_M) and the force simultaneously exerted by the voltage (f_V). The resulting equations of motion are

$$\ddot{x} + 2\zeta\omega_0\dot{x} + \omega_0^2(x_0 + x) - \frac{(q_0 + q)^2}{2m\varepsilon_{air}A} = \frac{f_M}{m} \tag{7.7}$$

$$R\dot{q} + \frac{(q + q_0)(x_{air} - x_0 - x)}{\varepsilon_{air}A} + \frac{x_e(q_e + 1 + q)}{\varepsilon_e A} = f_V. \tag{7.8}$$

The symbol ζ represents the damping ratio. As already noted, a more detailed derivation can be found in Appendix G. From an electret point of view it is obvious that a high surface potential is an important parameter. Electret-related challenges that affect the sensor performance can also be identified. Figure 7.2 shows three different scenarios that can occur during sensor operation. It is of great importance to prevent the release of charge carriers from the electret. If charge carriers are released due to temperature fluctuations, this is reflected as burst noise in the sensor signal. This can be compared to the thermally stimulated potential decay (TSPD) measurements in Section 5.2, where the charge carriers are released by a temperature increase. Even at low temperatures this can happen because of the shallow traps present in the electronic structure, as illustrated in Figure 7.2a. Furthermore, as illustrated in Figure 7.2b, compensating ions or polar molecules can be attracted from the ambient atmosphere by the surface potential of the electret. As seen in the equations of motion, this reduces the signal output of the sensor. Figure 7.2c shows that also temperatures above 30 °C should be avoided. Otherwise expansion effects due to phase transitions in the crystalline regions of the poly(tetrafluoroethylene) (PTFE), as observed in Chapter 5, can occur. The reason is that this changes the distance between the electret surface and the counter electrode, causing a shift in the resonant frequency similar like

the effect shown in Figure 7.1c. Only that the shift in the resonance frequency is involuntary this time and it leads to a measurement at a slightly shifted resonance frequency at which the full potential of the sensor is not exploited.

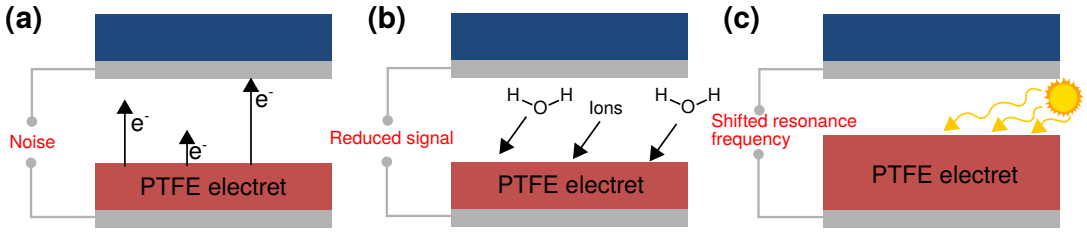

Figure 7.2: Electret-related challenges for the electrostatic magnetic field sensor. (a) Detrapping of charge carriers from shallow traps can cause burst noise in the sensor signal during the measurement. (b) Ions and polar molecules (e.g. H_2O) in the atmosphere are attracted by the surface potential of the electret and compensate the surface charge. As identified in the equations of motion, the output signal decreases with decreasing surface potential. (c) Temperatures above 30 °C cause a thermal expansion of the PTFE. The result is a change of the air gap width and thus an unwanted shift in the resonance frequency during the measurement.

7.3 Organic Multilayer Electrets

The now possible integration of electret thin films by iCVD demonstrated in Chapter 5 as well as electret tunability presented in Chapter 6 open up further possibilities for these special applications. The precise control on the nano- and micrometer scale makes it possible to address new approaches to further enhance the performance of the electret films. The iCVD process offers a unique possibility to deposit several different polymer films on top of each other in a controlled way. The aim of this section is to investigate whether the electret properties can be specifically influenced by a multilayer approach. In this way, the organic films could be tailor-made for the respective application.

7.3.1 Protection Against External Decay and Release from Shallow Traps

In a first step, the application of an additional protection layer for the avoidance of external decay processes will be investigated. In the case of the films with protection layer, an additional iCVD PTFE layer is applied after charging the electrets via corona discharge. Due to the mild deposition conditions, the electrets are not exposed to extremely high temperatures and do not lose their entire charge. Samples with and without protection layer are prepared and initially stored for several weeks in a small sealed volume so that the quasi-permanent state can be established. After this time they are exposed to the open atmosphere and the surface potential is measured at room temperature for several days. It is to be expected that the surface charge will decay due to external processes. These include the attraction of compensating counterions from the surrounding atmosphere as well as humidity condensing on the electret surface, as introduced in more detail in Chapter 2. In the experiment shown in Figure 7.3a, the samples with the protection layer (orange curve) show no decay of the charge within four days in the open atmosphere. This means that the external charge decay was

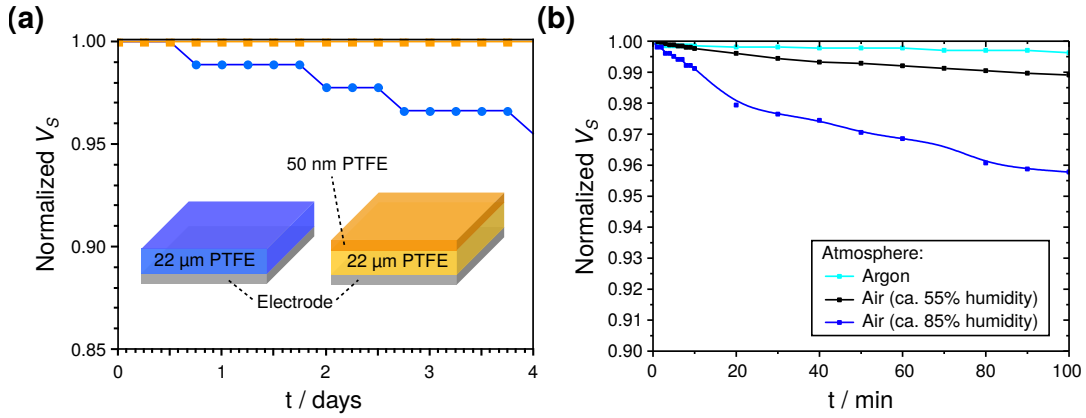

Figure 7.3: Additional protection layer deposited via iCVD on top of an electret. (a) Comparison of the surface potential of PTFE electrets with (orange) and without (blue) PTFE protection layer deposited by iCVD. (b) Observed initial charge decay of unprotected PTFE electrets in different atmospheres.

probably slowed down compared to the sample without protection layer (blue curve). The attraction of counterions from the air cannot be prevented. They are still attracted by the surface charge. They may not neutralize the charge of the

samples with the protection layer, but they may continue to accumulate on the surface of the protection layer and thus affect the effective value of the surface potential. However, no decrease in potential was measured within four days for the samples with the protection layer. It is therefore likely that contact with air humidity also has a significant influence on the external charge decay. The humidity can form conductive paths on the surface, as described by Yovcheva and Kuzmin [214, 215]. Even though poly(tetrafluoroethylene) (PTFE) is hydrophobic and prevents the formation of conduction paths, it cannot be avoided that the H_2O molecules come into contact with the charged PTFE surface. In the case that an additional protection layer is deposited, the molecules only have contact with the surface of the protection layer and not with the charged surface. This seems to increase the stability against humidity. Indeed, even in the case of hydrophobic PTFE electret films, the atmosphere shows a clear influence on the external charge decay, as the next experiment shows. A PTFE film is charged and immediately transferred into a glovebox without having an additional protection layer. In this glovebox a certain atmosphere is present. The charge decay is now monitored over the next 100 minutes for this sample. Then the process is repeated with a new charged PTFE sample, which is now exposed to a different atmosphere. The results are shown in Figure 7.3b. A faster decay can clearly be observed with increasing humidity. The samples in the argon atmosphere probably show only the initial exponential decay, which will later change into a linear one, as described in Chapter 2 and Chapter 5. However, the use of a protection layer seems to offer additional shielding and it slows down the decay. This seems to be a possible approach to be able to operate electrets without encapsulation in novel sensor types, such as the ones described above in Section 7.2 in the beginning of this chapter. It furthermore hinders the unintentional release of charge carriers from shallow traps. It can thus eliminate the burst noise in the sensor signal, which occurs when detrapped charge carriers from the electret reach the counter electrode.

7.3.2 Manipulation of the Internal Decay

For the internal long-term decay, as already applied in Chapter 5, the rate model of Małecki has proven to be an effective approach [212, 213]. The initial electrical conductivity of the electret material seems to have a considerable influence on the resulting long-term stability of the charge. Two polymers, which are deposited by iCVD, are investigated. One is PTFE, which has already been examined in Chapter 5. The other polymer is poly(1,3,5-trivinyl-1,3,5-

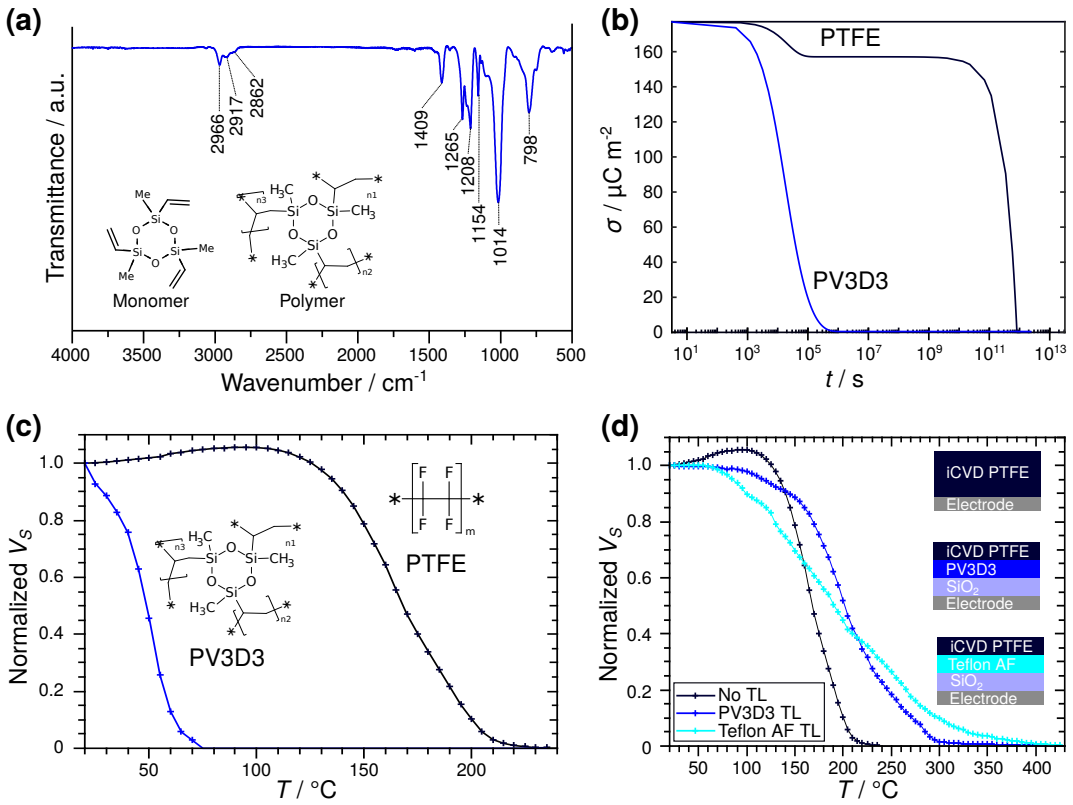

Figure 7.4: Electret multilayer components. (a) FTIR spectrum of a deposited PV3D3 thin film. (b) Stability prediction of PTFE and PV3D3 based on the model of Małecki. (c) Comparison of the TSPD measurements for PTFE and PV3D3. (d) Fabricated multilayer electret show enhaced stability.

trimethylcyclotrisiloxane) (PV3D3), which can be deposited with the monomer 1,3,5-trivinyl-1,3,5-trimethylcyclotrisiloxane (V3D3). The exact parameters of the film deposition are listed in Chapter 3. It is often used in the iCVD process for the deposition of low k dielectric films [33, 36, 307]. Figure 7.4a shows a Fourier-transform infrared spectroscopy (FTIR) spectrum of the deposited PV3D3 film. The insets show the molecule (V3D3) and the resulting polymer (PV3D3). The proposed assignment of the bands in the FTIR spectrum can be found in Table 7.1. Due to the absence of bands for the vinyl (C=C) stretch at $1645\,\mathrm{cm}^{-1}$ - $1640\,\mathrm{cm}^{-1}$ [295] as well as symmetric and asymmetric C−H stretch in the vinyl group at $3000\,\mathrm{cm}^{-1}$ - $3150\,\mathrm{cm}^{-1}$ [295], a successful polymerization can be assumed. The preservation of the siloxane ring due to the mild deposition

Table 7.1: Band assignment for the FTIR spectrum of the deposited PV3D3 film.

Band / cm^{-1}	Assignment	Reference
798	CH_3 rocking in Si−CH_3 and Si−C stretch (and Si−H deformation and C−F deformation)	[285, 308]
1014	Si−O−Si stretch (cyclic trimer)	[308, 309]
1154	C−F symmetric stretch	[285]
1208	C−F asymmetric stretch	[285]
1265	symmetric deformation of CH_3 in Si−CH_3	[297, 308]
1409	asymmetric deformation of CH_3 in Si−CH_3	[297, 308]
2862	CH_2 symmetric stretch and CH_3 symmetric stretch	[297, 309]
2917	CH_2 asymmetric stretch	[297, 309]
2966	CH_3 asymmetric stretch	[297, 309]

conditions can be seen from the band at $1014\,cm^{-1}$ for the Si−O−Si stretch [308, 309]. A typical value for the electrical conductivity of PV3D3 was taken from the literature [136, 310]. The long-term prediction in Figure 7.4b shows that the charge in PV3D3 decays after only a few days. This is in good agreement with the experimentally observed charge decay of PV3D3 at room temperature, which leads to a complete discharge within ten days. [2] Furthermore, it can be observed that the charge is not as thermally stable as in PTFE, which is shown in the TSPD measurement in Figure 7.4c. PV3D3 does not seem to provide many deep-level traps as it is the case in PTFE. The deep-level traps as well as the electrical conductivity of the films have a significant influence on the internal decay process and thus the long-term stability of the charge. How can this be further influenced? In organic electronics, for example, the use of a blocking layer in solar cells is well-known [311, 312]. Also for organic electrets, additional interfaces in the material could enhance the stability or even provide additional deep-level traps. It has been found that inorganic Si_3N_4/SiO_2 interfaces actually provide additional deep-level traps for charge carriers [313, 314]. It might be

[2] This is a slightly shorter time than it was predicted by the model. The reason is that, as mentioned in Chapter 5, the model only considers internal decay and assumes that the sample is encapsulated immediately. In order to measure the sample, it had to be taken out of the sample box several times, which means that it is highly probable that the mentioned external processes also contributed partially to the observed decay.

possible that this could also be used for polymer electrets. The iCVD process allows different polymer thin films to be deposited with nanoscale control without the need to break the vacuum, providing a unique capability to produce new organic multilayer electrets. Figure 7.4d shows the measurement of fabricated multilayer electrets. The insets show their exact arrangement. The multilayer electrets are fabricated using the sequence PTFE/PV3D3/SiO_2 (blue curve). Additional multilayer electrets with PTFE/Teflon AF/SiO_2 sequence (cyan curve) are also fabricated. The substrates are conductive silicon wafers coated with an SiO_2 layer (2 µm). PV3D3 (1 µm) or Teflon AF (1 µm) serve as transport layer (TL) and PTFE (1 µm) as active layer. These multilayers are compared with the single PTFE layer investigated in Chapter 5. The thickness of the single PTFE layer is 22 µm (black curve). Indeed, as shown in Figure 7.4d, the multilayers show improved stability at higher temperatures. Since the stability of the pure iCVD PTFE films was already found to be very good and sufficiently stable for applications in Chapter 5, there are other effects that make this approach even more attractive. Especially the multilayer systems with the PV3D3 TL show about the same stabilized surface potential as the single iCVD PTFE layers. The stabilized initial surface potential of the multilayer system is $V_S = -518\,\mathrm{V}$ and the potential of the pure PTFE is $V_S = -519\,\mathrm{V}$. The big advantage is that the PTFE/PV3D3/SiO2 multilayer is much thinner (4 µm) to reach this surface potential than the single PTFE layer (22 µm). It seems that the multilayer films can store more charge than the single PTFE film. The interfaces most likely provide additional deep-level traps for the charge carriers. By increasing the film thickness even further, higher surface potentials could be achieved. This is very interesting to increase the output of the demonstrated magnetic field sensor or other electret energy generators. Also, on an industrial level, it has the advantage that more samples can be produced in less time. As here, conductive silicon wafers with an additional oxide layer can be purchased, which can then be coated with PV3D3 and PTFE via iCVD without breaking the vacuum. Another finding that can be obtained from the measurement is that the charge carriers are indeed not only localized on the surface but actually reach the interface, where they are held for a long time. This happens either during the charging process or due to the increased temperature. This hypothesis is supported by the comparison between the samples with the PV3D3 TL (blue curve) and the Teflon AF TL (cyan curve), where the other layers of the multilayer system are identical. The choice of the TL has here an effect on the final charge decay. A further advantage for the sensor, also shown in Figure 7.4d, is that the lower proportion of PTFE reduces the initial expansion effect of the PTFE. As mentioned in Chapter 5, the

PTFE shows a phase transition slightly above 30 °C due to its semi-crystallinity [287]. This leads to an expansion of the film, which reduces the distance between the charged PTFE surface and the probe in the measurement setup and slightly increases the surface potential of the film during the measurment. This effect is observed in Figure 7.4d for the single 22 µm PTFE layer by the initial increase in the normalized surface potential above 1. But this also means that in the case of the introduced electret magnetic field sensor the distance of the air gap can vary. This can lead to a shift in the resonance frequency of the sensor, as shown in the measurement in Figure 7.1c, when measuring over 30 °C, e.g. on a hot summer day or in direct contact with a patient. The frequency that was previously assumed to be the resonance frequency of the sensor and at which the sensor is consequently excited is now no longer the real resonance frequency. It has been shifted slightly due to the expansion effect and the full potential of the sensor can no longer be used because it is not excited at the correct frequency. The measurement would now be performed at a wrong resonance frequency and the full potential of the sensor cannot be used. The result is a deterioration of the LOD. Due to the fact that the PTFE proportion of the multilayer system is much smaller, the expansion effect is barely noticeable as seen in the measurement in Figure 7.4d. In addition, the PTFE film is no longer on a hard metal electrode or silicon wafer, but on another polymer, which can further reduce the expansion effect due to its softer mechanical character. The problem of the unintentional resonance shift due to thermal expansion of the electret can thus be avoided with the multilayer approach.

7.4 Summary

This chapter first presented a novel magnetic field sensor based on the electret transducer/generator principle, which was developed in close collaboration with the Chair for Functional Nanomaterials (Prof. Dr. Rainer Adelung)). First of all, equations of motion for the sensor were formulated and the special requirements for the electret material were determined on the basis of these equations. These requirements were finally addressed by the introduction of new organic multilayer electret systems. In this way, external decay influences such as humidity can be reduced by an additional iCVD protection layer. This enables the sensor to be operated without encapsulation. Furthermore, the unintentional release of charge carriers from shallow traps can be reduced by this protection layer. With respect to the described sensor, this can reduce the burst noise in the sensor signal,

which occurs when detrapped charge carriers from the electret reach the counter electrode. Regarding the internal charge decay, the temperature stability of the charge can be increased by creating additional interfaces in the electret. It also shows that, compared to a single layer of PTFE, only 1/5 of the electret thickness is required to store the same charge. It is likely that additional deep-level traps are provided by the interface to store the additional charge. For the sensor shown, the resulting higher surface potential results in a stronger signal. A further benefit of the multilayer approach is the reduction of the PTFE content, which minimizes the thermal expansion of the electret. With respect to the sensor, this prevents an unintended shift in the resonance frequency during measurements at elevated temperatures. In the future the stored charge can be further increased by increasing the effective surface area. The deposited iCVD films are highly conformal and have a very low roughness. One approach would be to deposit the electret on a highly porous substrate. Another approach would be to synthesize it on a previously deposited porous layer as part of a multilayer system. Again, the vacuum does not have to be broken and everything can take place in one reactor. A microporous thin film with pore sizes smaller than 2 nm would be suited for such a porous component. It has many small pores and thus an extremely large surface area. In addition, the nanoscale voids provide additional deep traps in the polymer [161, 202, 293]. This makes it possible to further tailor the electronic structure of the polymers. The next chapter covers exactly this deposition of microporous polymer thin films via iCVD for the potential use as porous layers in electret multilayer systems as well as in many other applications.

8. Controlled Large-area Synthesis of Microporous Polymer Network Films with sub 2 nm Pore Size Enabled by Initiated Chemical Vapor Deposition

In order to be able to add a surface-enlarging component to the multilayers shown in the previous chapter, as well as for new low k films and many other applications in general, the deposition of microporous thin films with pore sizes below 2 nm is demonstrated in this chapter. The large-area synthesis of such microporous polymers is extremely difficult with wet chemical approaches. By adding an additional chemical, a so-called porogen, to the vapor phase in the initiated chemical vapor deposition (iCVD) reactor, a phase separation can be generated during the deposition. The resulting porosity after removal of the porogen by a further heating step is examined by means of positron annihilation lifetime spectrosopy (PALS).

8.1 Introduction

Materials with pore sizes below 2 nm, also referred to as mircoporous materials, have drawn the attention for numerous applications such as membranes for desalination and water purification [315], hydrogen storage [316], nuclear waste treatment [317, 318], catalysis [319], antireflective coatings [320] or low k dielectrics [321]. Furthermore, they can be used as porous base layers to increase the surface in multilayer systems, such as the organic multilayer electrets shown in the previous chapter. Compared to zeolites and metal-organic frameworks (MOFs), microporous polymers are a relatively new candidate among microporous materials. They are of great interest because they enable a unique tunability and combination of functional properties via the selected monomer [322]. A key challenge in the fabrication of such materials is still their large-area synthesis as conformal thin films and the precise control of the pore size [315, 319, 322]. Microporous polymers, for instance, typically consist of a highly cross-linked network which cannot be melted or solved in organic solvents and are thus extremely difficult to synthesize [322]. A technique well known from wet chemistry to achieve open porosity in polymer is the use of an additional chemical in the monomer feed, a so-called porogen [323, 324]. It is typically selected based on a different Hildebrand parameter compared to the monomer according to

$$\delta_H = \left(\frac{\Delta H_{vap} - \mathrm{R}T}{V_{mol}} \right)^{1/2} . \tag{8.1}$$

The symbols H_{vap}, R, T and V_{mol} represent the enthalpy of vaporization, universal gas constant, temperature and molar volume, respectively. Porogen and monomer separate into different phases and only the monomer rich regions polymerize. After polymerization, the porogen is removed in a subsequent heating step and an open porous polymer network remains without the need for an additional template or mold. A first approach to use this technique from the vapor phase has already been reported for macroporous poly(glycidylmethacrylate) (PGMA) by iCVD under supersaturated growth conditions [325, 326]. By adding a porogen to the gas phase it forces a phase separation as soon as the vapor adsorbs on the cooled substrates. During polymerization, only the monomer-rich regions polymerize and in a subsequent heating step the porogen can be removed, which leaves an open porous polymer network as schematically illustrated in Figure 8.1a. As mentioned above, microporous polymer networks with pore sizes below 2 nm are extremely challenging to synthesize. Regarding polymerization from the vapor phase as in iCVD, it is essential to have (I.) a highly cross-linked

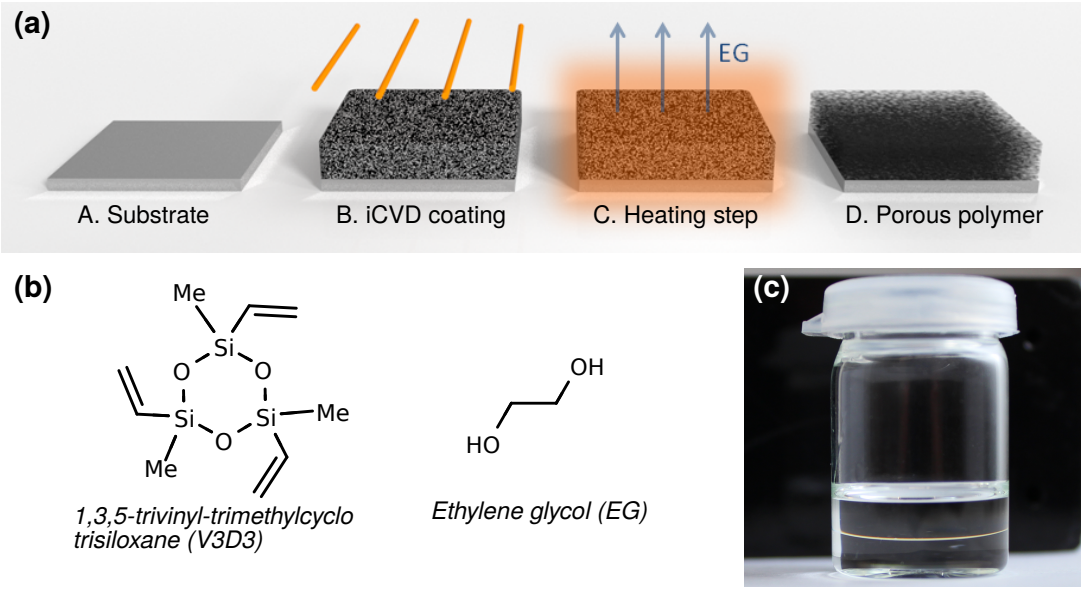

Figure 8.1: Phase separation during iCVD. (a) Schematic illustration of the deposition procedure. A. The substrate is placed in the iCVD reactor. B. During the process an additional porogen is fed into the reactor and a phase separation takes place at the cooled sample stage. C. A subsequent heating step removes the porogen from the polymer. D. At the end an open-porous polymer network remains. (b) Structural formula of the monomer (1,3,5-trivinyl-1,3,5-trimethylcyclotrisiloxane, V3D3) and of the porogen (ethylene glycol, EG) used for the phase separation. (c) A clear phase separation can be observed when V3D3 and EG are added together.

polymer network that retains the porous form (i.e. thermosets), (II.) precise film control as well as (III.) a reliable way to actually probe the pores on the lower nanoscale. Referring to the first point (I.) the monomer 1,3,5-trivinyl-1,3,5-trimethylcyclotrisiloxane (V3D3, Figure 8.1b) is used which already appeared in the previous chapter for the synthesis of the PV3D3 transport layers. It is part of the cyclosiloxane family and is highly cross-linked due to the three vinyl groups. By using ethylene glycol (EG, Figure 8.1b), which was selected due to the different Hildebrand parameter, an open microporous network is to be formed. V3D3 and EG show a clear phase separation when the two substances are put together as shown in Figure 8.1c. After polymerization, V3D3 forms a cross-linked network that is not affected by long range chain mobility (i.e. glass transition) and thus maintains the microporous form. In order to address the second point

(II.), the precise film control, the demixing process that takes place during the adsorption on the substrate has to be further understood. For this purpose, a simple description is given by the Cahn-Hilliard phase field model [250, 251] and integrated into the general kinetic theory of Lau and Gleason [133, 134] which is shown in more detail in Chapter 2. Originally used for the phase separation in metal alloys, the Cahn-Hilliard phase field model is meanwhile used in many other areas ranging from inpainting of binary images [327] to topology optimization [328]. The model can be used here to understand the underlying processes during the phase separation. Finally, with regard to the third point (III.), a probe on the nanoscale is required to detect the pores and channels on the nanoscale. For this purpose positron annihilation lifetime spectroscopy (PALS) is used here, which is described in more detail in Chapter 3. For a possible open porosity in the films, a long ortho-positronium (o-Ps) lifetime above 10 ns is to be expected. This would confirm that there is an additional open porosity in the films, as bulk polymer is expected to result in an o-Ps lifetime between 1 ns and 4 ns [245–247]. Since thin films around 600 nm to 1000 nm have been produced here, low-energy positrons with implantation depths around 100 nm are necessary. For this purpose the measurements were performed at the Electron Linac for Beams with high Brilliance and low Emittance (ELBE) in Dresden Rossendorf [329–331].

8.2 Phase Separation During Adsorption

In the vapor phase, initiator, monomer and porogen mix as the reactor and all feed and exhaust lines in the iCVD process are heated to avoid condensation. This also means that the vapor mixture is kept above the critical temperature (T_c) until it adsorbs on the cooled substrate surface. The adsorbed volume (V_{ad}) can be estimated by the Brunauer–Emmett–Teller (BET) theory, as already outlined in detail in Chapter 2, according to

$$V_{ad} = \frac{V_{ml}\, c_{\mathrm{B}}\, \frac{p_m}{p_{sat}}}{\left(1 - \frac{p_m}{p_{sat}}\right)\left(1 - \left(1 - c_{\mathrm{B}}\right)\left(\frac{p_m}{p_{sat}}\right)\right)}. \tag{8.2}$$

The symbols V_{ml}, $\mathrm{c_B}$, p_m and p_{sat} represent the volume of a monolayer, the BET constant, the partial pressure of the respective component and the saturated vapor pressure of the component, respectively. At the time of adsorbtion a phase separation takes place because the substrate has a temperature below T_c due to the cooling. The initiator usually exhibits a very high vapor pressure and therefore only a short dwell time on the substrate surface. The initiation process

in iCVD is therefore often described by the Eley-Rideal mechanism [332]. For this reason, it is assumed in the following that the initiator does not participate in the phase separation. The adsorbed layer is assumed to be a binary system of monomer (V3D3) and porogen (EG). The diffusion driven part is described by the Cahn-Hilliard phase field model [250, 251]. The Cahn-Hilliard equation,

$$\frac{\delta u}{\delta t} = \Delta(M \nabla \mu), \tag{8.3}$$

contains the chemical potential (μ), a mobility (M) and the order parameter (u). The chemical potential depends on the term with the derivative of the free energy (ψ) and the parameter γ, which is connected to the Cahn number by $\gamma = C_a^2$, and is given by

$$\mu = \frac{d\psi}{du} - \gamma \nabla u. \tag{8.4}$$

Cahn and Hilliard suggest

$$\psi = \frac{\mathrm{k_B} T}{2}((1+u)\log(1+u) + (1-u)\log(1-u)) - \frac{\mathrm{k_B} T_c}{2} u^2 \tag{8.5}$$

for the free energy by a mean field model [250, 251]. The symbol $\mathrm{k_B}$ represents the Boltzmann constant. To find the typical double-well type of free energy with two minima at $u_1 = 1$ and $u_2 = -1$, the well-known approximation

$$\psi = \frac{(u^2 - 1)^2}{4} \tag{8.6}$$

is used here. This results in a nonlinear term for the derivative

$$\frac{d\psi}{du} = u^3 - u. \tag{8.7}$$

The equation can be solved numerically. For the time discretization different methods are tested. Straightforward explicit methods, i.e. the Euler forward scheme, result in a low stability of the simulation. The method of Eyre [252] is a semi-implicit method in which the free energy is separated into contractive and expansive parts. It showed the best stability of all tested methods as seen in Figure 8.2. The results in the figure show the view from above on the substrate surface. This two-dimensional view of the phase separation shows a change in the monomer (V3D3, red color) and porogen (EG, blue color) regions over time. The step at $t = 1$ shows the moment when the molecules from the vapor mixture adsorb onto the substrate. The temperature of the mixture falls below T_c and

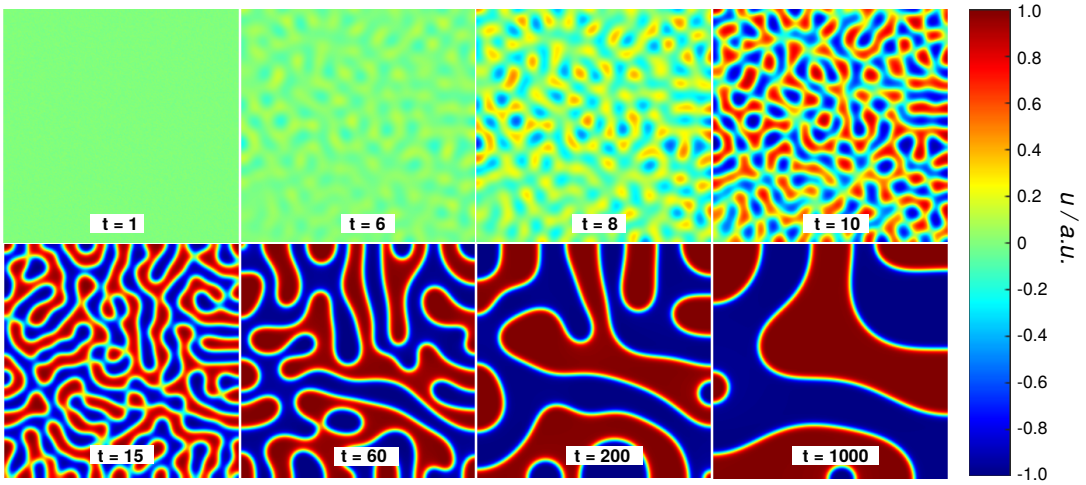

Figure 8.2: Simulation result for the phase separation on the sample surface. View from above on the substrate surface where the phase separation takes place. The simulation was performed with the Cahn-Hilliard phase field model. It shows the moment when the mixture of V3D3 and EG reaches the substrate surface causing the temperature of the mixture to decrease below the critical temperature (T_c).

the demixing begins. At first glance it is apparent that the longer the system has time to separate, the larger the individual regions become. This depends on the rate constants of the polymerization, which can be determined by in-situ quadrupole mass spectrometry presented in Chapter 4. It seems that the system has less time to demix for fast reactions. During polymerization, the monomer regions (red color) become immobile as they combine to form the repeating units of the polymer. The vapor pressure at the surface changes and new molecules adsorb from the mixed gas phase. Here a second question arises, namely how high the respective adsorbed volume (V_{ad}) should be. Submonolayer adsorption will not lead to phase separation because no regions can form before the monomers polymerize. It is therefore advisable to grow near or in supersaturated conditions ($p_{EG}/p_{sat,EG} \approx 1$). Also supported by the observations of Tao and Anthamatten, the porosity of the polymer film becomes coarser with increasing porogen content [325, 326]. However, it must be taken into account that GMA and the cross-linker EGDA were used in the study of Tao and Anthamatten. The cross-linker flow rate was comparatively low and was further diluted with increasing Porogen flow rate. As only V3D3 is used in this study, which cross-links itself through

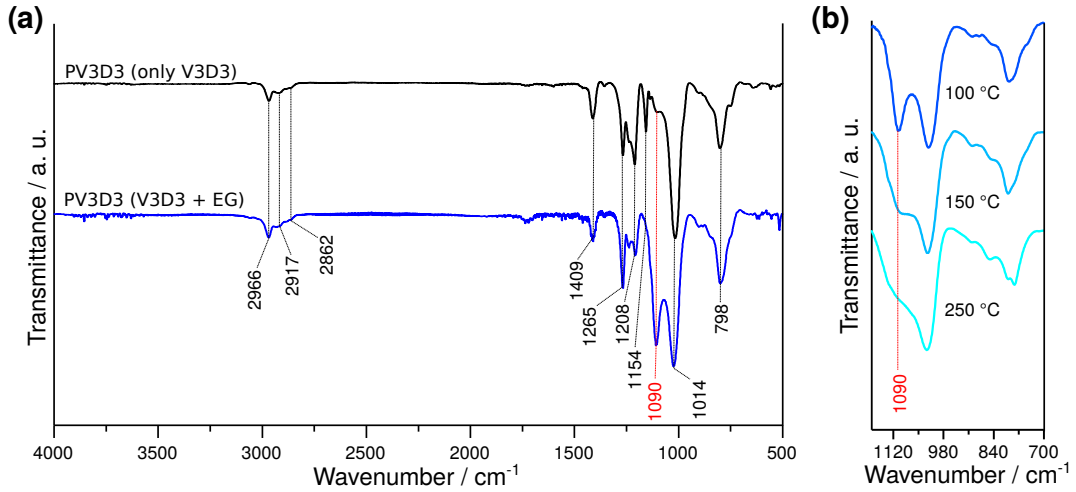

Figure 8.3: FTIR investigation. (a) The comparison of thin films deposited only with V3D3 and thin films deposited with V3D3+EG reveals an additional band at 1090 cm^{-1}. (b) The intensity of the band at 1090 cm^{-1} varies after the heating step depending on the temperature.

the three vinyl groups, the proportion of cross-linking molecules is significantly higher. Therefore V3D3 is run below one and EG is varied near one. Indeed, deposition in these conditions yields a PV3D3 film with EG content. This can be seen in the Fourier-transform infrared spectroscopy (FTIR) spectrum in Figure 8.3a. The reference sample where no EG was used shows the typical bands for PV3D3. The presence of the band at 1014 cm^{-1} shows that the cyclosiloxane ring is preserved in iCVD due to the mild deposition conditions. Absence of bands around 1600 cm^{-1} for the vinyl group (C=C) and above 3000 cm^{-1} for the C−H stretch at the vinyl group (C=C−H) shows that the film is succesfully polymerized. The polymer backbone is indicated by the CH_2 symmetric and asymmetric stretch at 2862 cm^{-1} and 2917 cm^{-1}, respectively. The nearby or partially overlapping bands are assigned to the CH_3 of the methyl groups at the cyclosiloxane ring. The proposed assignment for all bands is shown in Table 8.1. When EG is added under supersaturated conditions ($p_{EG}/p_{sat,EG} > 1$) during the deposition, additional characteristic bands for EG appear in the FTIR spectrum of the film as seen in the blue curve in Figure 8.3a. The band marked in red at about 1090 cm^{-1} is characteristic for the C−C−O stretch of EG and underlines the assumption that EG is now successfully embedded in the PV3D3 film. The formation of a copolymer can be excluded because of the demonstrated phase

Table 8.1: Proposed assignment of the bands that appear in the FTIR spectra of the deposited PV3D3 films.

Band / cm^{-1}	Assignment	Reference
798	CH_3 rocking in Si−CH_3 and Si−C stretch (and Si−H deformation and C−F deformation)	[285, 308]
1014	Si−O−Si stretch (cyclic trimer)	[308, 309]
1090	CCO stretch (in primary alcohol, EG)	[298]
1154	C−F symmetric stretch	[285]
1208	C−F asymmetric stretch	[285]
1265	symmetric deformation of CH_3 in Si−CH_3	[297, 308]
1409	asymmetric deformation of CH_3 in Si−CH_3	[297, 308]
2862	CH_2 symmetric stretch and CH_3 symmetric stretch	[297, 309]
2917	CH_2 asymmetric stretch	[297, 309]
2966	CH_3 asymmetric stretch	[297, 309]

separation and the absence of vinyl groups in the EG molecule. Whether there are inclusions or a connected network is tested by heating. The samples are heated at different temperatures (100 °C, 150 °C or 200 °C) for 60 min in order to remove the porogen. For inclusions or a transition state, the signal for EG will probably still be present after heating. On the other hand, if an interconnected EG network has formed, the signal for EG will disappear as it is driven out of the film during the heating step. The EG bands start to disappear after heating, as seen in Figure 8.3b. It is shown that the C-C-O band is still clearly visible in samples heated at 100 °C despite the heating process. At 150 °C, the intensity of the band decreases slightly after heating. At 200 °C, it can be seen that the band now begins to disappear completely. This indicates that the EG, which has a boiling point of 197 °C, is now removed and an open porous network has formed.

8.3 Verification of Microporosity

In order to confirm the formation of the pores and channels after the heating out positron annihilation lifetime spectroscopy (PALS) is used. As discussed in Chapter 3, *o*-Ps formation and lifetime can be used to detect unoccupied space in polymers. Usually, free volume results in lifetimes in the range of 1-4 ns

[245–248]. Larger space, i.e. channels or pores, should result in lifetimes above 10 ns. Since the samples are thin films, the energy of the incoming positrons must be moderated to obtain depth profiles. A typical set of positron beam data is shown in Figure 8.4. In Figure 8.4a, the positron lifetime, in particular $\tau_3 = o$-Ps lifetime, is plotted as a measure of the average hole size versus the positron implantation energy, which is a measure of implantation and thus information depth within the sample. The o-Ps lifetime of approximately 3 ns is representative for bulk polymers[245–247]. All lifetimes are independent of the implantation

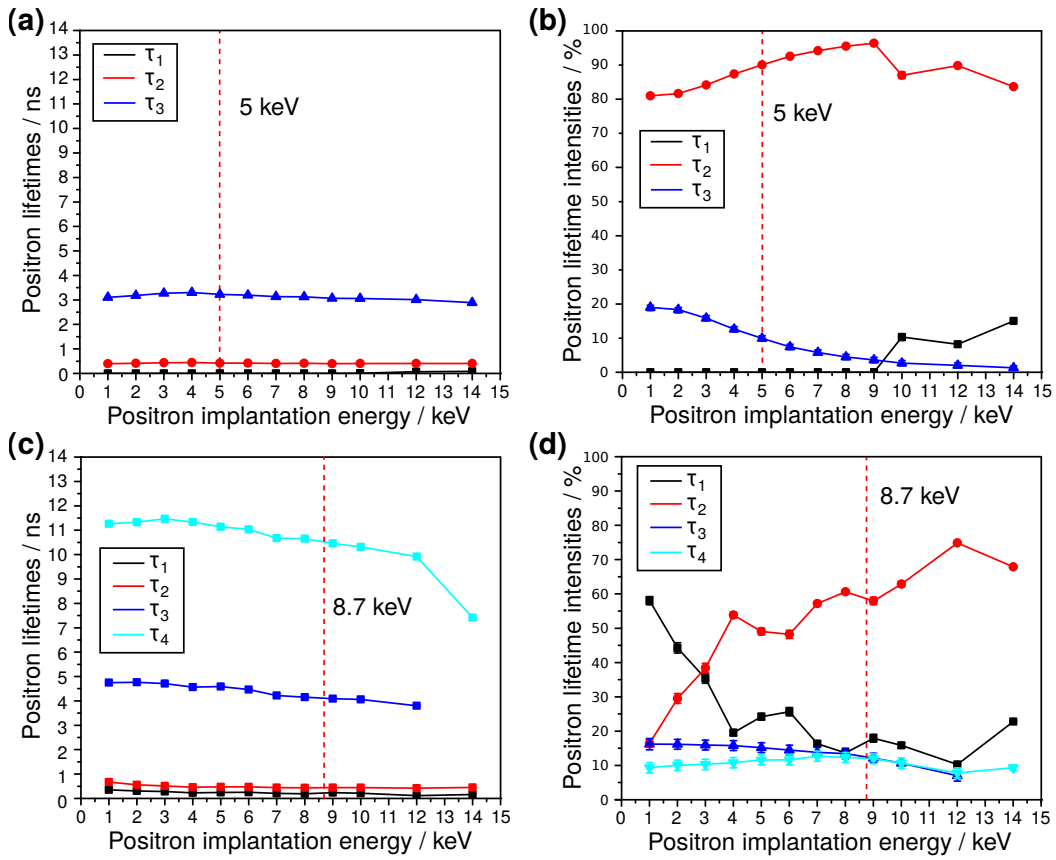

Figure 8.4: PALS measurements. (a) Positron lifetimes of a non-porous PV3D3 sample. (b) Corresponding positron lifetime intensities of the non-porous PV3D3 sample. (c) The PV3D3 sample, where EG was added during deposition and a subsequent heating step was performed, shows an additional long lifetime (cyan curve) when measuring the positron lifetimes. (d) Corresponding positron lifetime intensities for the sample shown in (c).

energy, which indicates that the polymer structure is unchanged throughout the thickness of the film. Figure 8.4b shows the corresponding intensities, i.e. the relative contribution of the three decay channels of the implanted positrons versus the implantation energy. The vertical line is the energy at which 50 % of the positrons are implanted into the substrate and thus do not contribute to *o*-Ps annihilation. This is consistent with the decrease in *o*-Ps intensity (I_3) at this energy to half of the initial value. Figures 8.4c and 8.4d show the data set as in Figures 8.4a and 8.4b but this time for a sample where porogen content and heating is supposed to create open porosity (supersaturated sample, compare FTIR plot in Figure 8.3). This is clearly reflected in the additional lifetime τ_4 of approximately 11 ns (Figure 8.4c), which is almost constant throughout the sample. The lifetime is, as explained in more detail in Chapter 3, a measure of the average hole size and can be expressed by [248]

$$\frac{1}{\tau_3} = \lambda_0 \left(1 - \frac{R_h}{R_h + \delta_R} + \frac{1}{2\pi} \sin\left(\frac{2\pi R_h}{R_h + \delta_R}\right)\right). \tag{8.8}$$

The symbols λ_0, R_h and δ_R represent the spin averaged decay rate, the average free volume hole radius and the thickness of the electron layer, respectively. An *o*-Ps lifetime of approximately 11 ns corresponds to an average diameter of about 1.3 nm for the channels. The detected size of the nano channels in the molecular structure is finally visualized using geometry optimization in Figure 8.5 based on the results obtained in this study.

8.4 Summary

This chapter demonstrated the deposition of microporous PV3D3 polymer networks from the vapor phase. For this purpose an additional porogen was added to the vapor phase during deposition. The resulting phase separation was investigated in a simplified way with the Cahn-Hilliard model and successful porogen inclusions were confirmed by FTIR. After removal of the porogen by an additional heating step, the formation of open microporosity in the thin films deposited under supersaturated conditions was verified by PALS. By selecting a different initiator, similar like in Chapter 6, the functional groups can be changed, which can be used to modify the properties (e.g. membrane selectivity). Also the choice of other monomers or addition of comonomers can influence the properties of the microporous layer significantly. Due to the CVD-typical growth characteristics of the iCVD process large-area substrates as well as complex structures can be

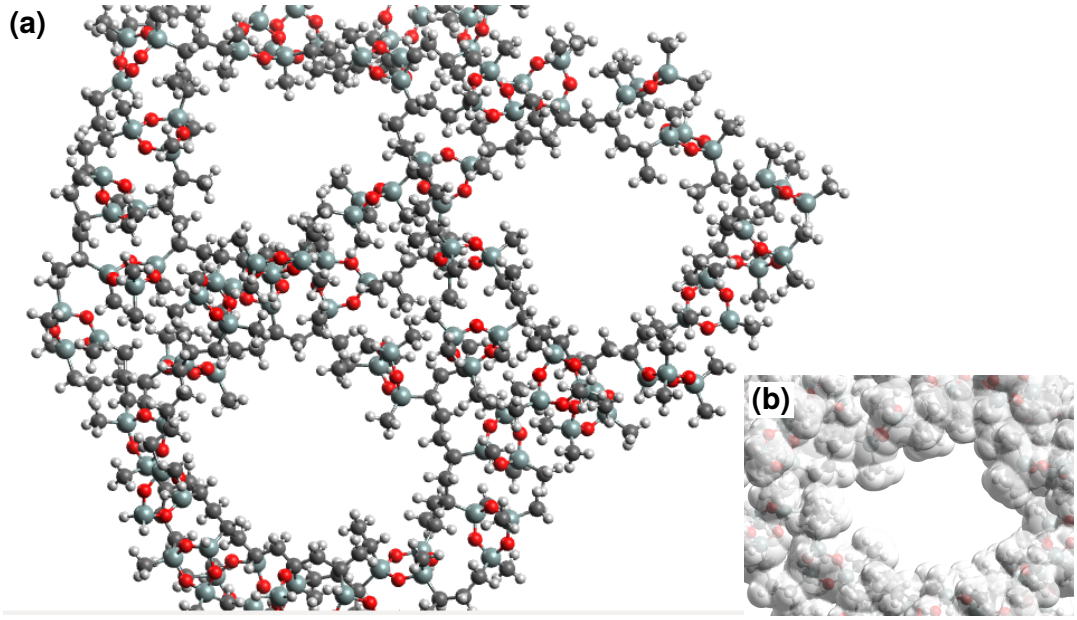

Figure 8.5: Classification of the measured data. (a) Molecular visualization of the resulting pore size obtained by geometry optimization based on the results obtained in this chapter. (b) Calculated van der Waals surface of one pore.

coated with the thin films. It is also possible to produce freestanding films/foils, which can be used as a membrane for example. Besides the use as flexible organic low k material these microporous films can also be used in the future as part of the organic multilayer electrets presented in the previous chapter. This increases the surface area and thus the effective surface charge.

9. Conjugated Organic Thin Films by Initiated Chemical Vapor Deposition

This chapter is intended to investigate the feasibility to deposit new conjugated polyacetylene-like thin films from the vapor phase via initiated chemical vapor deposition (iCVD). These organic thin films could be used for possible semiconductor applications in the future. In this case, in contrast to electrets, it is important to have as few deep traps as possible in the polymer. For this reason, a solvent-less and pinhole-free deposition is required. These films might later be used as a basis for a reduction of the Peierls distortion by stabilizing functional groups, thus enabling targeted bandgap engineering and device fabrication without breaking the vacuum.

9.1 Introduction

In this thesis only insulators have been considered so far. In order to look at the other side, a brief look at semiconducting and conducting polymers should be given. Organic semiconductors and conductors are of great interest for applications in organic light-emitting diodes (LED) [333, 334], organic field-effect transistors (OFET) [335–338], organic memory [339, 340] and organic solar cells (OSC) [341–343], among others. The first and best known polymer representative is polyacetylen (PA). However, in the meantime many other polymers have become well established as conductive/semiconductive polymers. This includes polythiophenes like poly(3,4-ethylene dioxythiophene) (PEDOT) (or poly(3,4-ethylene dioxythiophene) polystyrene sulfonate (PEDOT:PSS)), polyaniline (PANI) and polypyrrole (PPy). The vapor phase deposition of high quality conjugated/conductive polymer thin films, such as PEDOT or PANI, is typically achieved by oxidative chemical vapor deposition (oCVD) [123–126], which is described in more detail in Chapter 2. The iCVD process typically provides insulating polymers due to free radical polymerization via vinyl groups. This results in the formation of a sp^3 hybridized carbon backbone. The deposited polymers, such as poly(1,3,5-trivinyl-1,3,5-trimethylcyclotrisiloxane) (PV3D3), have been successfully used as dielectric films in a variety of organic electronics applications [33, 36, 344]. Combined with the deposition of semiconductor layers by iCVD, it would be possible to produce entire organic electronic devices in one reactor without breaking the vacuum. Breaking the vacuum would, for example, result in the accumulation of impurities at the interfaces of the individual layers, and the layers would come into contact with the air humidity that can penetrate into nanoscale voids. As described in the previous chapter, nanoscale voids in particular are highly undesirable for organic semiconductors, since the penetration of water into these nanopores generates additional traps that significantly impair the performance [161–164]. The production of organic electronic devices in an iCVD process without breaking the vacuum enables the active semiconductor layer to be immediately sealed with the next layer without coming into contact with the atmosphere and humidity/water. The iCVD technique is known to provide solvent-free, pinhole-free coatings of high quality, whose performance will not be degraded by nanovoid formation or residual solvent molecules. The CVD-typical growth further enables the deposition of the organic films on large-area substrates. One approach for the deposition of conjugated polymers, i.e. a sp^2 hybridized carbon backbone, by underlying free radical polymerization from the vapor phase is the use of acetylene-like monomers with carbon triple bonds

instead of the typically used vinyl groups [345]. This seems to be quite promising and a conjugated system that behaves like a one-dimensional metal should be created immediately. However, this approach is usually impeded by the Peierls instability, which is presented in more detail in Chapter 2. This leads to a band gap formation, which degrades the system from potential metallic conductivity to a much lower electrical conductivity. This has already been known from PA, which only exhibits metal-like electrical conductivity after appropriate doping. In this short communication-type chapter the topic is approached from another direction. The additional functional groups along the conjugated chain could influence the electronic properties of the chain. In addition, different functional groups probably also influence the elastic properties that affect the band gap. This could enable specific band gap engineering for conjugated polymer films and has the additional advantage that whole organic electronic devices could be produced in one reactor without breaking the vacuum.

9.2 The Polymerization of new Acetylene-type Monomers

For the deposition, the monomers 1-nonyne, 1,8-nonadiyne and 1-ethynyl-3-fluorobenzene, which have not previously been deposited by iCVD, are investigated as examples. The chemical structures of these monomers are shown in Figure 9.1a. It has to be examined whether these can be polymerized and thereby form a conjugated system. With the parameters used, which are listed in Chapter 3, thin films were successfully deposited with all three monomers in the iCVD process. The deposition rate for poly(1-nonyne) (P1N) with the 1-noonyne monomer is 10 nm/min. For poly(1,8-nonadiyne) (P18N) with 1,8-nonadiyne it is 15 nm/min and for poly(1-ethynyl-3-fluorobenzene) (P1E3F) with 1-ethynyl-3-fluorobenzene it is 12 nm/min. The resulting thin films on silicon wafers are examined by Fourier-transform infrared spectroscopy (FTIR) and the results are shown in Figure 9.1b. Furthermore, data for the 1-nonyne monomer are added from the literature as reference spectrum [346]. Typically, strong bands between $3300\,\mathrm{cm^{-1}}$ - $3340\,\mathrm{cm^{-1}}$ are observed for the C−H stretch in mono-substituted alkyne groups (—C≡C−H) [347] and bands between $2150\,\mathrm{cm^{-1}}$ - $2100\,\mathrm{cm^{-1}}$ are observed for the alkyne stretch (—C≡C—) [347]. These bands are also clearly visible in the 1-nonyne reference (black line), for example. In all three polymer films these bands have completely disappeared, which confirms the successful polymerization. Furthermore, all three polymers have additional bands in the region $1587\,\mathrm{cm^{-1}}$ -

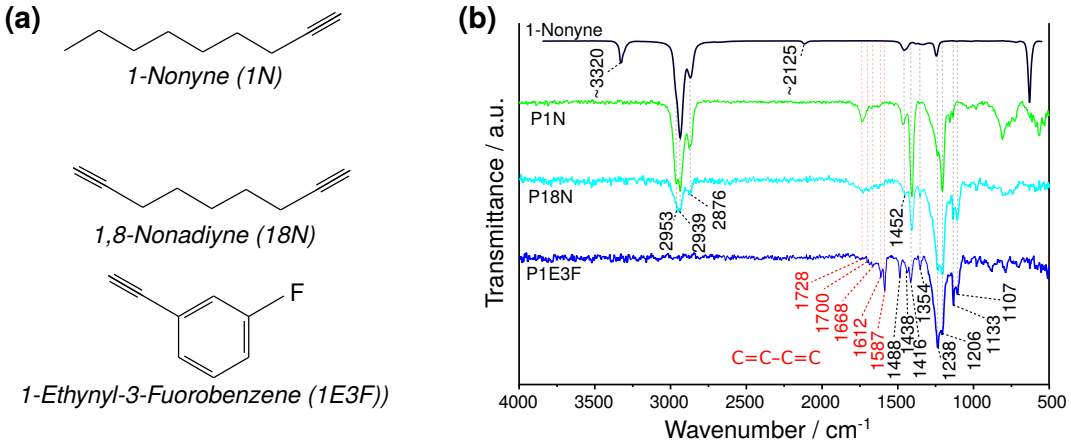

Figure 9.1: Acetylene-type monomers with different functional groups. (a) Molecular structure of 1-nonyne, 1,8-nonadiyne and 1-ethynyl-3-fluorobenzene. (b) FTIR spectra of poly(1-nonyne) (P1N, green curve), poly(1,8-nonadiyne) (P18N, cyan curve) and poly(1-ethynyl-3-fluorobenzene) (P1E3F, blue curve) polymer thin films after the iCVD process compared to the spectrum of the 1-nonyne monomer (black curve). The spectrum for the 1-nonyne monomer (black curve) was adapted from the literature [346].

1728 cm^{-1}. These are marked in red in Figure 9.1. They are characteristic for conjugated systems with alternating single and double bonds [295]. This shows that it is indeed possible to produce conjugated systems with the iCVD process that have different side-groups. As outlined in the introduction, the additional functional groups could have an influence on the resulting band gap. Similar to PA, it can also be assumed that the mechanism of electrical conductivity takes place via solitons, since there is most probably also a degenerated ground state.

9.3 Summary

Absence of bands for alkyne stretch and C-H stretch in mono-substituted alkyne groups by FTIR shows successful polymerization of acetylene-based monomers from the vapor phase. The appearance of new characteristic bands associated with alternating single and double bonds after polymerization indicates that a conjugated system has formed. The films could be the basis for new semiconducting polymer films.

10. Nanoscale Gradient Copolymer Films via Single-step Deposition From the Vapor Phase

This chapter reports on the deposition of noval nanoscale gradient copolymer films via initiated chemical vapor deposition (iCVD). In these films the chemical composition changes gradually from polymer type A to polymer type B. By enhancing the iCVD process with the in-situ mass spectrometry approach reported in Chapter 4, it was possible to produce these materials at film thicknesses below 30 nm. The combination of two material states in one material opens up completely new chemical and physical properties that cannot be achieved with materials currently in use.

The content of this chapter is published in:

> **S. Schröder**, O. Polonskyi, T. Strunskus, and F. Faupel. Nanoscale gradient copolymer films via single-step deposition from the vapor phase. *Mater. Today*, 37:35, 2020.

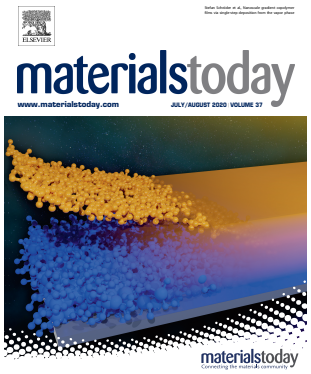

Details for the in-situ mass spectrometry approach are submitted for publication:

> **S. Schröder**, A. M. Hinz, T. Strunskus, and F. Faupel. Molecular insight into real-time reaction kinetics of free radical polymerization from the vapor phase by in-situ mass spectrometry. *J. Phys. Chem. A*, 125:1661, 2021.

10.1 Introduction

The interested reader of this thesis will certainly encounter the question why especially the shown fluoropolymer films do not delaminate when deposited, e.g. on silicon wafers. Their mechanical properties are so different. This must inevitably lead to weak adhesion. Indeed, the poly(tetrafluoroethylene) (PTFE) films deposited on silicon wafers show delamination on all length scales as shown in Figure 10.1a,b. This is intensified by the phase transitions in the crystalline regions of PTFE, which were already observed in Chapter 5 and Chapter 7. In order to solve this problem a look into the natural world is attempted. It becomes apparent that nature is filled with sophisticated organic materials with inherent functional or structural gradients. This means that the chemical composition and properties change gradually along the material dimensions as illustrated in Figure 10.1c. Examples owed to such gradients are the extraordinary stability and resistance of the windowpane oyster as well as squid beaks [348–352]. In addition, the complex eye lenses of many living organisms such as squids or humans have complex gradients in the refractive index [353, 354]. Gradients are also found in mussel byssus and tendon, where they enable exceptionally good adhesion of soft material to hard structures [355, 356]. For example, mussels can adhere firmly to rocks, piers or other hard objects in the water without being washed away by the waves as seen in the photo in Figure 10.1d. Polymers are therefore promising candidates for the transfer of these organic gradients to the laboratory [357, 358]. The synthesis of organic gradient materials also paves the way for many other fields of application, including functional implant coatings [359, 360], flexible gradient index optics [361] and tissue engineering [358]. However, the synthesis of gradient copolymers is extremely challenging. It has been possible to synthesize gradient copolymers with wet chemistry approaches using ionic or controlled radical polymerization [362, 363]. However, these approaches are not suitable for conformal coating on large-area substrates or complex geometries, which is essential for many applications. Furthermore, copolymer synthesis in wet chemistry is often limited to monomer pairs that share a common solvent. This prevents access to many important combinations, since often exactly two types with completely different characteristics are required. Here the deposition of gradient copolymer materials via iCVD is shown, which can overcome these limitations. The chemical composition of the deposited films changes gradually from polymer type A to polymer type B. By extending the iCVD process with in-situ massspectrometry, which was presented in Chapter 4, these materials were deposited with layer thicknesses below 30 nm. This combination of two material

states in one material opens up completely new chemical and physical properties that cannot be achieved with current materials.

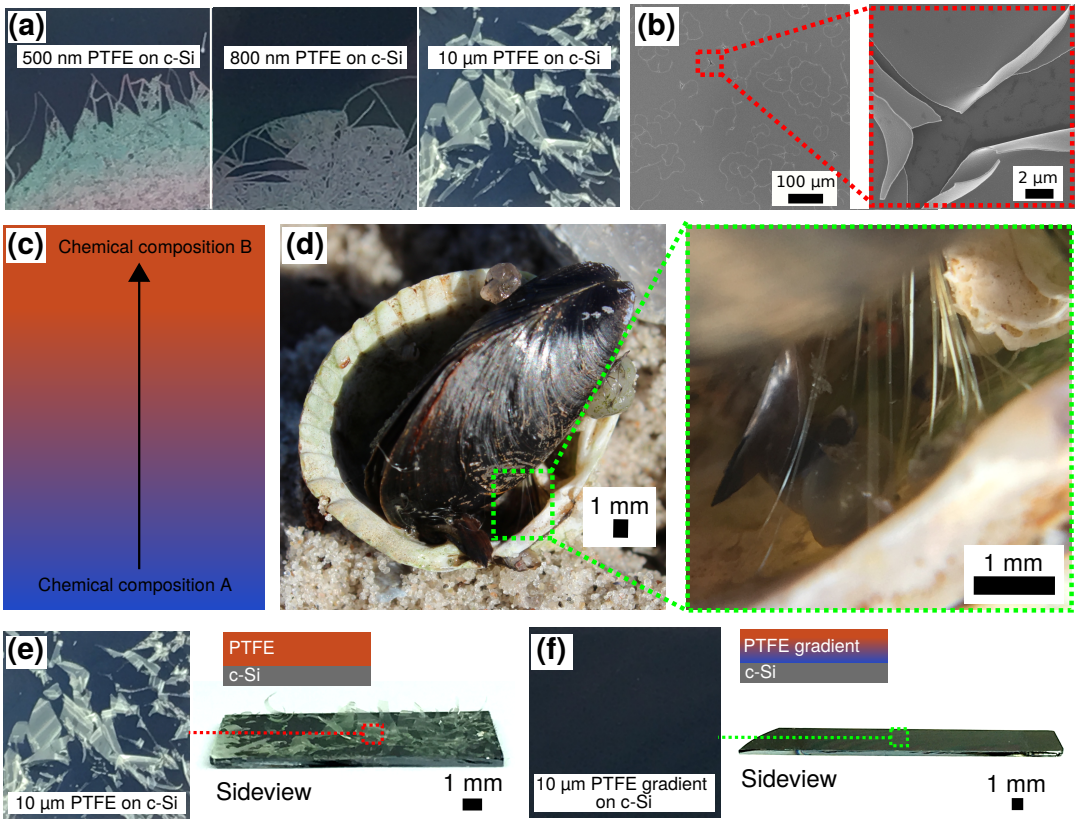

Figure 10.1: Delamination of PTFE. (a) View from above on PTFE films of different layer thickness deposited on silicon wafers by iCVD. The delamination occurs spontaneously directly after deposition. (b) Even ultra thin PTFE films show cracking due to poor adhesion, as can be seen on this scanning electron microscopy (SEM) image. (c) In case of a gradient in the material, the chemical composition changes along the material and consequently also the properties. (d) Photo of a mussel attached to the shell of a cockle. The enlargement shows the mussel byssus which is responsible for the excellent adhesion of the mussel. (e) The 10 µm pure PTFE film delaminates while the 10 µm PTFE gradient film in (f) is firmly attached to the silicon wafer.

10.2 Bioinspired Organic Gradient Films

In order to get back to the original example in the introduction, an attempt is made to improve the adhesion of the PTFE films with the aid of a gradient. Polymer A at the interface to the wafer must ensure good adhesion and polymer B at the surface must be fully functional PTFE. The two monomers 1,3,5-trivinyl-1,3,5-trimethylcyclotrisiloxane (V3D3) and hexafluoropropylene oxide (HFPO) already presented in the other chapters of this thesis are used for this purpose. V3D3 with its organosilicon character should adhere well at the interface to the silicon wafer. This is on the one hand due to the strongly cross-linked thermosetting character because of the three vinyl groups in the V3D3 monomer and on the other hand due to a possible covalent bonding to the native oxide of the silicon substrate because of the similarity to typical organosilane adhesion promoters. HFPO is intended to provide CF_2 repeating units as usual to obtain the desired linear PTFE character. The composition of the vapor phase is changed gradually from V3D3 to HFPO during deposition. Precise control can be achieved with the in-situ mass spectrometry presented in Chapter 4 by fingerprinting the spectra. The resulting films actually show significantly improved adhesion, as shown in Figure 10.1e,f. Here a 10 µm thick pure PTFE film is shown (Figure 10.1e) and a 10 µm gradient PTFE film (Figure 10.1f). This eliminates the need for additional adhesion promoters, substrate pretreatment by etching processes or other chemical treatments to adhere PTFE to the desired substrate (e.g. cookware). A lot of chemical waste could be avoided at industrial level by this new process. Both films show the same PTFE functionality on the surface. To experimentally verify this, the synthesis of the gradient films is stopped after different stages and the surface is investigated using X-ray photoelectron spectroscopy (XPS). The results are shown in Figure 10.2a-c. As shown in Figure 10.2a, by increasing the fluoromonomer concentration and simultaneously decreasing the organosilicon monomer concentration, the enrichment of CF_2 is clearly visible in the C1s high resolution scan. Accompanied by the observation of the simultaneous reduction of the Si 2p peak, which can be seen in Figure 10.2b, the material appears to change its chemical character from an organosilicon (PV3D3) to a fluoropolymer (PTFE). Figure 10.2c shows the total change in chemical composition determined by XPS at the surface. The initial high fluorine concentration is explained by the perfluorobutanesulfonyl fluoride (PFBSF) initiator. The cyclic siloxane trimer of the V3D3 results in a ratio of about 1:1 between silicon and oxygen. The oxygen content is slightly increased and varies.

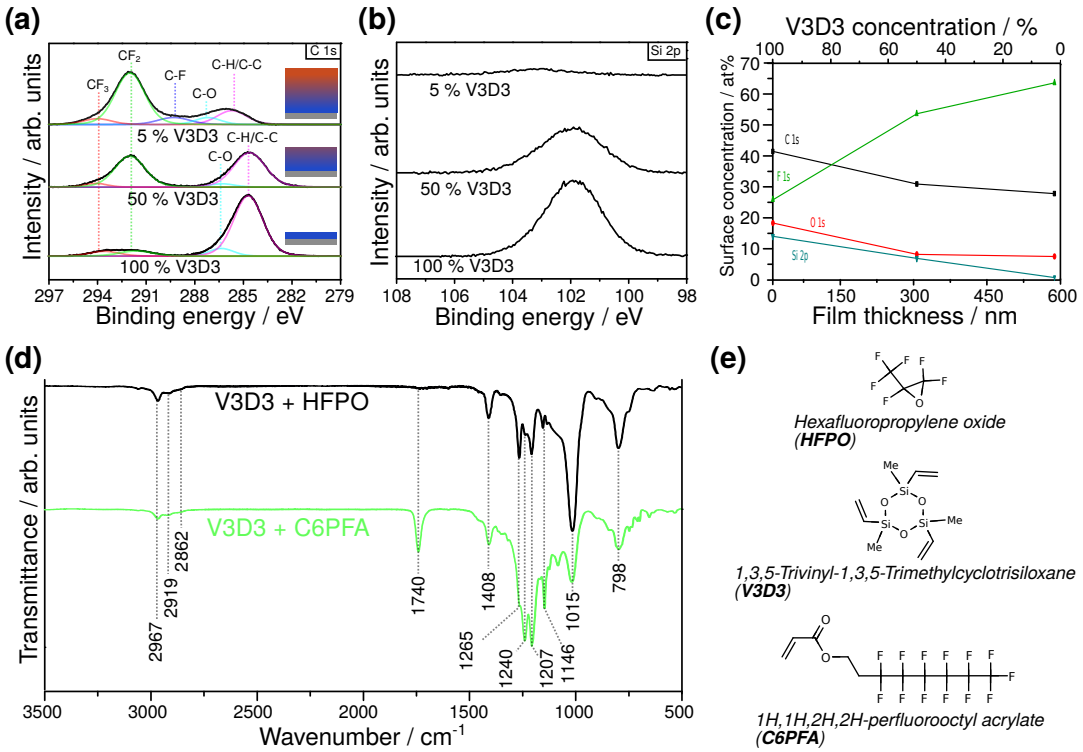

Figure 10.2: Chemical characterization of the gradient coplymer films. (a) The C 1s high resolution XPS scan shows that the CF_2 character increases with increasing film thickness. The insets show the current position of the respective measurement. (b) The Si 2p high resolution XPS scan shows a gradual decrease of the peak with decreasing V3D3 monomer concentration and increasing HFPO fluoromonomer concentration. (c) Variation of the surface concentration with increasing film thickness determined from the XPS measurements. (d) The FTIR spectra show preserved functionality of all groups within the gradient polymer film deposited by V3D3 and HFPO (black curve). To show the versatility of the approach, gradient films were also deposited using V3D3 and C6PFA (green curve). The FTIR also shows full functionality of both comonomers. The proposed assignment of the individual bands can be found in Table 10.1. (e) Chemical structures of the monomers used in the depositions.

This can be attributed to the surface contamination of the samples, since the samples were exposed to the ambient atmosphere prior to the XPS characterization. The carbon content is slightly reduced due to the lower occurrence of V3D3 and its methyl groups. At 95 % HFPO and 5 % V3D3, the fluorine/carbon ratio

approaches 2, indicating that the organosilicon network is gradually changing to linear CF_2 PTFE chains. The Fourier-transform infrared spectroscopy (FTIR) transmission spectrum in Figure 10.2d (black curve) shows that all functional groups are preserved. A detailed assignment of the bands can be found in Table 10.1. For the sake of clarity, Figure 10.2e once again shows the corresponding chemical structures of the respective monomers. The important preservation of the cyclic siloxane trimer structure, which typically lies between $1020\,cm^{-1}$ and $1010\,cm^{-1}$, is confirmed by the band at $1015\,cm^{-1}$ [308]. The fluoropolymer character is shown by the bands at $1146\,cm^{-1}$ and $1207\,cm^{-1}$, which represent the symmetric and the asymmetric C−F stretch. Polymer backbone formation is shown by the absence of bands for the vinyl groups between $1590\,cm^{-1}$ and $1615\,cm^{-1}$. This approach can be transferred to many other comonomer pairs. Due to the advantage of iCVD that no common solvent is required for copolymerization, a wide range of different functions can be covered. For this reason, the combination of V3D3 and 1H,1H,2H,2H-perfluorooctyl acrylate (C6PFA) gradients is furthermore demonstrated. The FTIR spectrum of the gradient grown in V3D3 and C6PFA in Figure 10.2d (green curve) shows also full functionality. An additional band at $1740\,cm^{-1}$ is given by the carbonyl group in C6PFA.

Table 10.1: Proposed assignment of the bands that appear in the FTIR spectra of the deposited gradient films.

Band / cm^{-1}	Assignment	Reference
798	CH_3 rocking in Si−CH_3 and Si−C stretch (and Si−H deformation and C−F deformation)	[285, 308]
1014	Si−O−Si stretch (cyclic trimer)	[308, 309]
1146	C−F symmetric stretch	[285]
1207	C−F asymmetric stretch	[285]
1240	C−F stretch in CF_3	[285]
1265	symmetric deformation of CH_3 in Si−CH_3	[297, 308]
1408	asymmetric deformation of CH_3 in Si−CH_3	[297, 308]
1740	C=O carbonyl stretch	[296]
2862	CH_2 symmetric stretch and CH_3 symmetric stretch	[297, 309]
2919	CH_2 asymmetric stretch	[297, 309]
2967	CH_3 asymmetric stretch	[297, 309]

C6PFA is a good alternative to C8-based coatings to prevent the release of bioaccumulative and persistent perfluorooctanoic acid and perfluorooctanesulfonic acid [217, 294, 364]. The chemical composition gradually changes from an organosilicon to a fluoropolymer and all functional groups are preserved. A property that also changes gradually is the cross-linking in the polymer film. V3D3 has three vinyl groups and forms a highly cross-linked network. If the amount of V3D3 is gradually reduced and HFPO (or C6PFA) is simultaneously increased, their repeating units are gradually incorporated into the network. This leads to a gradual decrease in the degree of cross-linking and a rather broad-meshed cross-linked structure is formed, since the fluoromonomers HFPO and C6PFA cannot form cross-links. At the end of the synthesis, when V3D3 is no longer present, the polymer finally exhibits linear chains. This change from a stiff thermoset to a softer thermoplastic thus changes the Young's modulus with increasing film thickness, similar to the mussel byssus. It can be determined from the respective homopolymers that it varies between 1.514 GPa for PV3D3 and 0.335 GPa for PTFE. The similar chemical character of the organosilicon to silicon also improves the adhesion to silicon wafers, as it is also known from the chemically similar silane adhesion promoters. Thus, as demonstrated at the beginning of this section, the soft PTFE surface adheres better to hard silicon wafers and does not delaminate after deposition as it is the case with the PTFE homopolymer, as shown in Figure 10.1e,f. Since everything is part of the gradient network, internal phase transitions in the PTFE-rich region and external stress caused by, e.g. impacts can be dissipated in the network. This can be treated in a similar way as a viscoelastic region. The dissipated energy is given here by

$$E_d = \oint \sigma_L \mathrm{d}\epsilon_L. \tag{10.1}$$

The symbols σ_L and ϵ_L represent the stress and the strain, respectively. The process is potentially reversible. The recovery of the process could be driven by the increase in entropy previously reduced by the external stress that aligns the local chain segments by extension or compression. The broad-meshed cross-linked area in the gradient could thus show a similar effect like entropy-elasticity in elastomers. In this case the entropy change (ΔS) for the one-dimensional case would be given by

$$\Delta S = -\frac{1}{2}\mathrm{k_B} N \ln((1+\lambda)^{1+\lambda}(1-\lambda)^{1-\lambda}). \tag{10.2}$$

$\lambda = d_m/R_c$ consists of stretch/compression distance (d_m) and contour length (R_c), with $R_c = N_p l$. N_p and l are the symbols for number of units and length of

the unit, respectively. The symbol k_B represents the Boltzmann constant. The restoring force would thus be given by

$$F_r = \frac{k_B T}{2l} \ln\left(\frac{1+\lambda}{1-\lambda}\right), \tag{10.3}$$

in which T represents the temperature. In this way, even in the case of PTFE, the phase transitions in the PTFE-rich regions can be compensated, since they are bound to the network. The result is the improved adhesion as initially demonstrated.

10.3 Gradient Copolymer Films on the Nanoscale

By using the in-situ massspectrometry introduced in Chapter 4, it is possible to monitor the composition of the vapor phase very accurately. Thus it is possible to deposit the gradient copolymer thin films shown here on the lower nanoscale. They can enable completely new physical and chemical properties. Figure 10.3a shows a cross-section through such a thin film. The optical properties of the nanogradients are investigated by variable angle spectroscopic ellipsometry (VASE). The results are shown in Figure 10.3b. A film deposited with V3D3 at the interface to the wafer and 1H,1H,2H,2H-perfluorooctyl acrylate (C6PFA) at the top side was examined here. It can be clearly observed that the refractive indices on the top (red dotted curve) and bottom side (blue curve) differ. They show the values of the respective homopolymers poly(1H,1H,2H,2H-perfluorooctyl acrylate) (PC6PFA) and PV3D3. A copolymer without a gradient shows refractive indices at the top and bottom, which are very close together (black curve and black dotted curve). The refractive index varies gradually as a function of film thickness. The respective reactivity ratios must be taken into account as they influence the gradient profile. Figure 10.3c shows as an example the linear gradual variation from V3D3 to HFPO (green curve) compared to the one from V3D3 to C6PFA (purple curve). By taking this into account, different profiles can be created. Some of them are shown schematically in Figure 10.3d. This is of great interest for gradient refractive index (GRIN) lenses that can now be produced as flexible films on soft substrates as shown in Figure 10.3e as well as for antireflective coatings or for other advanced optical subwavelength devices [361].

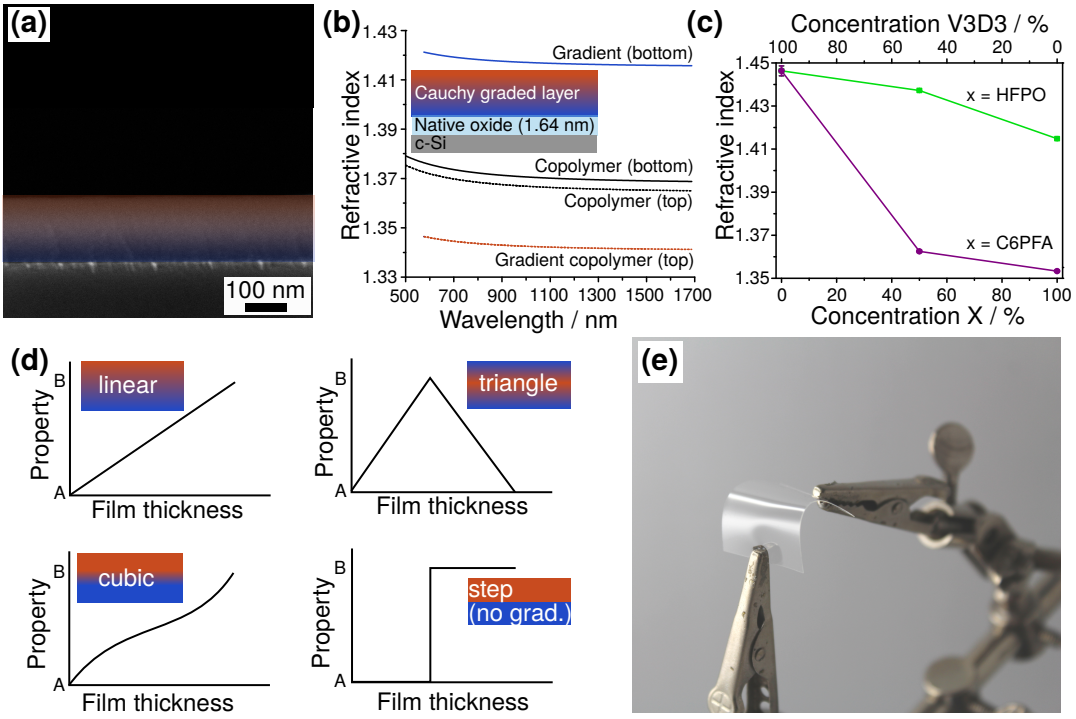

Figure 10.3: Nanoscale gradient copolymer films. (a) SEM cross-section of a gradient copolymer film on the nanoscale. (b) VASE reveals different refractive indices at the top and bottom of gradient copolymer films deposited with V3D3 and C6PFA compared to normal copolymer films deposited with V3D3 and C6PFA. (c) The refractive index profile depends on the reactivity ratios of the comonomers. Here the difference for V3D3 and HFPO compared to V3D3 and C6PFA is clearly visible. (d) Some possible gradient profiles that can be produced. (e) Photo of a gradient copolymer film used as GRIN lens on a flexible organic substrate.

Another application are anti-ice coatings on glass. These coatings should adhere well, must be hydrophobic and the film thickness should be below the visible wavelength of light. With the demonstrated in-situ massspectrometry approach it is possible to deposit PTFE gradient films with 21 nm thickness. As shown in Figure 10.4a, these films do not influence the transmission of the incident light and enable an effortless removal of water on the surface (see insets of figure). For such applications it is important that the films withstand several cycles of de-icing. For this reason several cycles are tested. For each cycle the water contact angle (WCA) is measured first. Then the sample is placed in a freezer together

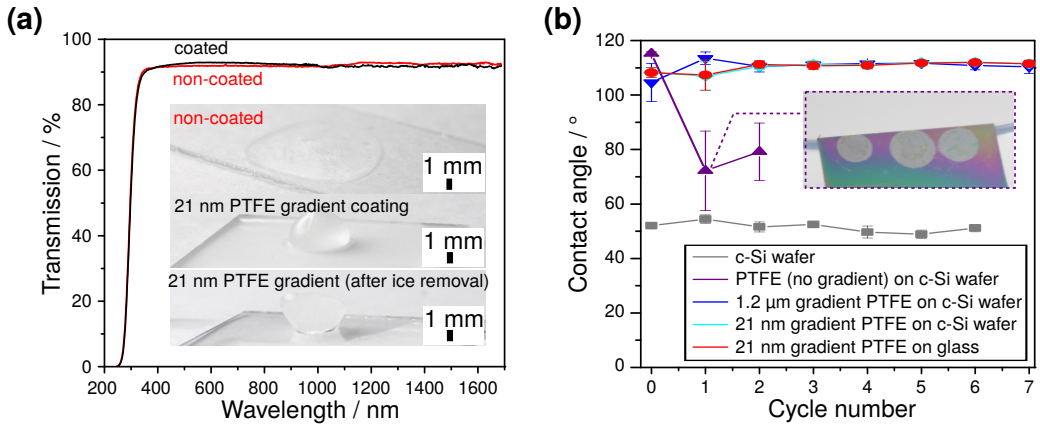

Figure 10.4: Anti-icing application of nanoscale gradient copolymer films. (a) Transmission measurement of uncoated and coated glass plate. The optical properties of the glass are not influenced by the nanoscale coating. However, as can be seen in the insets, the water-repellent effect is very good. The hydrophilic wetting changed to hydrophobic behavior and ice can thus be easily removed. (b) Compared to pure PTFE coatings (purple curve), the gradient PTFE coatings withstand several cycles of de-icing without delamination (blue, cyan and red curve). The inset shows how the PTFE already delaminates after the first cycle.

with the drop of water from the WCA measurement. After several hours the sample is removed from the freezer and the frozen drop is mechanically removed while everything is still frozen. Then the WCA of the sample is measured again and the value is written down. This cycle is repeated several times in order to test the stability. The results are shown in Figure 10.4b. The samples tested are 1.2 µm PTFE gradient on silicon wafer (blue curve), 21 nm PTFE gradient on silicon wafer (cyan curve), 21 nm PTFE gradient on glass (red curve) and PTFE without gradient on silicon wafer (purple curve). The measurement with the uncoated silicon wafer (grey curve) is shown to identify the systematic and statistical error of the measurement. It can be seen that pure PTFE coatings (purple curve) fail after the first cycle due to their poor adhesion. The inset in Figure 10.4a shows a photo of the pure PTFE coating after the first cycle. The positions at which the water drops were placed are clearly visible. The WCA does not fall back to the reference value for the silicon wafer, because there are still fragments of PTFE on the surface. These fragments cause very large differences in the WCA values, which can also be seen from the large error bars. It is therefore no longer possible to speak about a reproducible situation.

In contrast, the adhesion of the PTFE gradients remains stable for all tested substrates and layer thicknesses (blue, cyan and red curves). The functionality of the PTFE gradient films is ensured even after several cycles. Not only planar substrates can be coated with the gradients. Due to the CVD character of iCVD, even complex geometries and large-area substrates can be homogeneously coated. Complex structures such as medical implants can be coated in this way. Figure 10.5a-c shows SEM images of uncoated and coated fine metal meshes. The coating exactly reproduces the structure of the mesh surface. This also changes the WCA of the metal mesh as seen in Figure 10.5d-g. By turning the coated grid upside down, the same WCA can be measured on the bottom side. The contact angle on the bottom side is even slightly higher on the bottom side, which however falls within the measuring error, as seen in the error bars in Figure 10.5h.

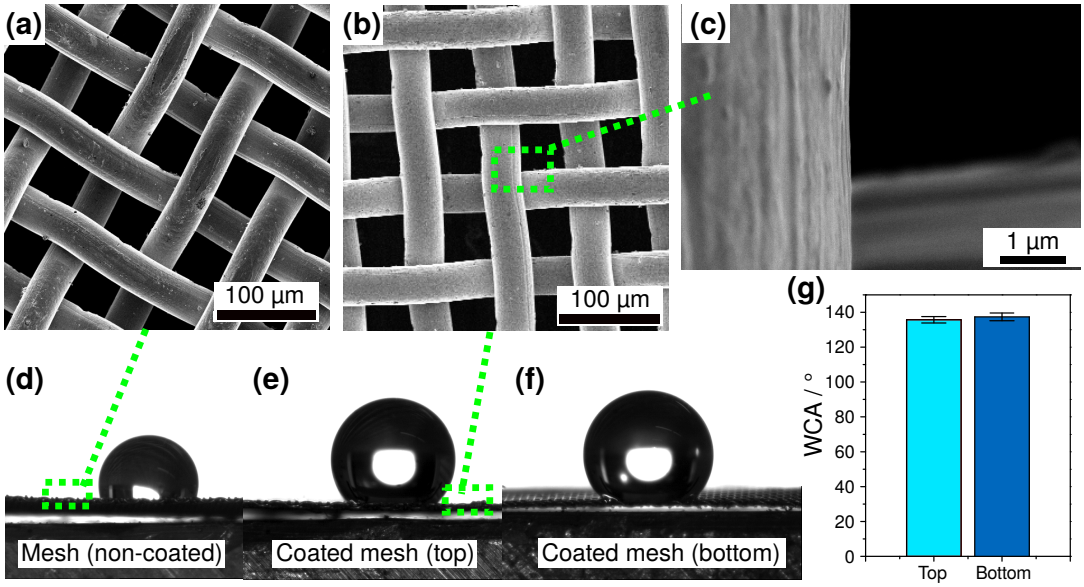

Figure 10.5: Nanoscale gradient copolymer films on complex geometries. (a) SEM image of an uncoated metal mesh. (b) SEM image of a coated metal mesh showing that the gradient copolymer coating homogeneously follows the structures of the mesh. (c) An enlarged view of a junction in the coated net. (d) WCA of the uncoated metallic mesh. The drop sinks into the mesh. (e) The coated metallic mesh shows hydrophobic behavior. (f) Also the bottom side of the coated metallic mesh shows hydrophobic behavior. (g) The measured WCAs on the top and bottom of the coated mesh are identical.

10.4 Summary

In this chapter the deposition of novel gradient copolymer films via iCVD was reported. The chemical composition of the film changes gradually from polymer type A to polymer type B along the thickness of the film. By using the in-situ mass spectrometry approach presented in Chapter 4, these films were deposited with thicknesses below 30 nm. The combination of two material states in one material opens up completely new chemical and physical properties that cannot be achieved with materials currently in use. The comonomer combinations of V3D3 and HFPO as well as V3D3 and C6PFA were demonstrated. However, this approach can be transferred to many other comonomer pairs. Due to the advantage of iCVD that no common solvent is required for copolymerization, a wide range of different functionalities can be covered. The CVD-typical growth and mild deposition conditions enable the coating of complex geometries, flexible substrates and large-area substrates with these new gradient films.

11. Summary and Conclusion

The detailed summaries of the individual chapters are already provided at the end of each chapter. This chapter is intended to put the most important findings into the general context of this thesis and to provide an outlook for future work on this topic. The first objective of this thesis was to establish the initiated chemical vapor deposition process (iCVD) at the Chair for Multicomponent Materials (Prof. Dr. Franz Faupel). Initially, a reactor was operated in batch mode for the deposition of the first poly(tetrafluoroethylene) (PTFE) films. In order to increase the deposition rate, this system was converted to a continuous flow system shortly thereafter. Meanwhile the iCVD process is used in many different projects at the Chair for Multicomponent Materials and also in collaboration with other chairs at Kiel University and external partners. A new approach developed during this thesis, which contributes to the general understanding of the iCVD process as well as improved process control, was the addition of in-situ mass spectrometry as presented in Chapter 4. It turned out that with this approach the reaction pathways and kinetic constants during deposition can be determined. In addition, process control can be improved by fingerprinting reference spectra using a self developed program. This allowed the deposition of extremely precise films on the lower nanoscale. Furthermore, the optimum process parameters for the different polymer deposition were identified. At these parameters monomer and initiator were converted most effectively in order to reduce the amount of unreacted starting materials. The presented in-situ mass spectrometry thus proved to be a very useful and versatile extension for the iCVD process.

Based on the ability to deposit insulating polymer films by iCVD, the next objective was the deposition of iCVD fluoropolymer films for the first-ever use as thin film electrets. As already known, PTFE shows typically the best performance for the application as electrets. Since the deposited iCVD PTFE films were

chemically identical to commercial PTFE films, they showed very good charge stability, which was even higher than spin-coated, commercial Teflon AF thin film electrets. This has not been achieved with other deposition techniques such as rf sputtering or plasma polymerization, as these approaches change the chemical structure of the PTFE significantly. This enabled the fabrication of fluoropolymer thin film electrets also via an upscalable CVD process with nanoscale control for, e.g. MEMS technology or advanced organic electronics devices. Furthermore, the deposition parameters were used to specifically manipulate the charge storage behavior.

In order to use the electrets specifically for novel, electrostatic magnetic field sensors, which were developed in close cooperation with the Chair for Functional Nanomaterials (Prof. Dr. Rainer Adelung), the next objective was to tailor the thin-film electrets for this application. For this purpose it was first necessary to obtain a more detailed understanding of the charge storage processes in electrets. Using poly(ethylene glycol dimethylacrylate) (PEGDMA) electrets as an example, the unique tunability of the thin film properties, which is enabled by iCVD, was demonstrated in Chapter 6. A variation of the end-groups on the PEGDMA example system showed a change in the electronic structure of the polymer in the form of different trap states. The most promising groups were estimated in advance using quantum chemical calculations. This allowed not only to specifically adjust the electret films, but also to extend the general understanding of charge storage in electrets. The introduction of the organic multilayer electrets shown in Chapter 7 has provided a toolkit that enables to adapt the electrets to the application. For this purpose the electrostatic magnetic field sensor sensor was presented first. Compared to magnetoelectric sensors, this new sensor type already shows a very promising limit of detection (LOD) of $73\,\mathrm{pT/Hz^{\frac{1}{2}}}$ at 321 Hz. Additionally, it was possible to adjust the resonance frequency and amplitude by adjusting the air gap between the counter electrode and the electret. Using simple equations of motion the electret-related parameters were identified. Initially, it was demonstrated that additional top layers reduce the influence of external decay processes of the charge. Also the release of charge carriers from shallow traps, which would lead to noise in the sensor, was reduced. Furthermore, it was shown that by using, e.g. fluoropolymer-organosilicon multilayer systems, the amount of PTFE was reduced while maintaining the same surface potential. It was identified that the thermal expansion of the PTFE portion was minimized in this way. This prevented an unintentional shift in the resonance frequency, which would hinder the sensor to work at its full performance. At the same time

it was demonstrated that the interfaces provide additional deep-level traps. They provide a better thermal charge stability than pure PTFE films as well as the same surface potential, although only about a quarter of the film thickness compared to pure PTFE was required. In order to increase the total chargeable area, the possibility of producing microporous polymers by forced phase separation during deposition and subsequent heating out of the second phase was investigated in Chapter 8 using poly(1,3,5-trivinyl-1,3,5-trimethylcyclotrisiloxane) (PV3D3) as an example. The underlying process of phase separation during deposition was investigated using the Cahn-Hilliard phase field model. A resulting pore size of 1.4 nm was measured by positron annihilation lifetime spectroscopy (PALS). Since only insulators with deep-level traps were investigated so far, the other side was examined in Chapter 9 to complete the scope. These are organic conductors and semiconductors, where such trap states are extremely undesirable. By using three different novel acetylene-like iCVD monomers it was demonstrated that it is possible to produce films that indicate a conjugated character as well as different side groups via iCVD. These provide the basis for new semiconducting polymer films.

Another challenge that emerged during the work on this topic was the insufficient adhesion between the deposited fluoropolymers and the substrates. For this purpose novel gradient copolymer films were presented in Chapter 10. They were inspired by the numerous gradient structures in the natural world and were initially made to overcome the adhesion problems. With this approach, excellent adhesion of the fluoropolymer films was achieved even for 10 µm films, which are usually required for the electret application. Coupled with the in-situ mass spectrometry approach demonstrated in Chapter 4, this gradient concept was furthermore successfully transferred to the nanoscale, to film thicknesses below 30 nm. This allowed enhancements in many application fields, which were demonstrated in Chapter 10. The films enabled completely new physical and chemical properties that cannot be achieved with materials currently in use.

12. Outlook

The in-situ QMS extension, reported in Chapter 4, which is currently installed at the reactor, will be separated from the reactor as a next step and rebuilt as an independent, easy to connect, mobile device. This will allow the other iCVD systems at the Chair for Multicomponent Materials to use this approach for studying reaction kinetics and to improve process control. Time-consuming parameter variations, for example for new monomers, can thus be shortened considerably. In this way it is possible to easily find the parameters for the most effective initiator/monomer conversion to minimize the loss of unreacted starting materials.

For the iCVD PTFE electret films, as shown in Chapter 5, a dependence of the charge storage properties on the process parameters has been identified. The process parameters that provide the highest deposition rate do not necessarily provide the best electret properties. It is recommended to systematically investigate further parameters and to identify the resulting molecular changes in iCVD PTFE as well as the correlations to the charge storage properties of the iCVD PTFE electret films. With the iCVD process, this can be specifically tailored via the deposition parameters. Examples are the crystallinity and the molecular weight. In the future, this can help to enhance the general understanding of factors such as crystallinity and molecular weight on charge storage properties in polymer thin films.

The approach demonstrated in Chapter 6 with the example of PEGDMA to systematically investigate the influence of functional groups on the charge stability of the polymer can be extended to many other polymers. The computational estimation of the electronic states of each functional group can be used to find potentially promising groups that provide deep-level traps in the band gap of the repeating units. Here also machine learning approaches would be attractive, which select the most promising combinations from a large database in order to find combinations for deep-level trap formation. This could drastically expand

the basic understanding of the charge storage in electrets in the future. The approaches to tailor the electret films for the applications in the novel sensors presented in Chapter 7 raise additional questions that require further investigation. Especially the long-term stability in an unshielded environment and the direct influence on the sensor noise have to be examined and demonstrated by further measurements. Another point that needs further study is the enhanced number of charges that can be stored in the presented multilayer electrets. Here it is important to identify whether the charge carriers are trapped at the interface during the heating process or whether they enter the traps directly during the charging process in the corona discharge. In addition new experiments and samples could clarify whether more trap states can be created in thin films with many interfaces. Also the phase-separated microporous films demonstrated in Chapter 8 as well as the deposition of iCVD electret films on porous substrates can be used to enlarge the chargeable surface and increase the surface potential. Actual sensor measurements are furthermore necessary to investigate how the higher surface potential and the other approaches described above affect the sensor signal. These questions were included in the proposal for the continuation of the Collaborative Research Centre (CRC) 1261 (Project A2) and will be further investigated therein in the future. The acetylene-like films presented in Chapter 9 could be used in the future to influence the Peierls transition and thus the resulting band gap. This would enable a possible band-gap engeneering for organic semiconductors that were deposited from the vapor phase. The advantages would be, on the one hand, the possibility to conformally deposit semiconductors from the vapor phase on large flexible substrates or complex geometries. On the other hand, iCVD typically polymerizes polymers with a large variety of functional groups, e.g. barrier layers, via the vinyl groups and the availability of semiconductors in the same process is a powerful tool for the production of organic devices, as the films are not exposed to the air during the device fabrication. However, it is furthermore to be clarified whether the conductivity in these thin films also occurs via solitons. In addition, measurements of the electrical conductivity before and after possible doping and the influence of different functional groups on the band gap created by the Peierls transition have to be investigated in the future.
The nanoscale gradient copolymers demonstrated in Chapter 10 can solve further existing adhesion problems in many different applications as well as enable the use of new gradient refractive index (GRIN) lenses in advanced subwavelength devices or provide new approaches in organic electronics. Since the gradient ideas found in the natural world, may it be of optical or structural kind, can now be transferred to the lower nanoscale, these materials may also be suitable for use in

molecular machines that could use these functions. All in all the demonstrated results show that the iCVD process provides many new pathways for various applications and even enables advanced multifunctional thin film materials for completely new applications.

Bibliography

[1] Karen K. Gleason, editor. *CVD Polymers - Fabrication of organic surfaces and devices*. Wiley-VCH Verlag GmbH & Co. KGaA, Weinheim, Germany, 1st edition, apr 2015.

[2] M. Ibn-Elhaj and M. Schadt. Optical polymer thin films with isotropic and anisotropic nano-corrugated surface topologies. *Nature*, 410(6830):796–799, apr 2001.

[3] M. A. Uddin, H. P. Chan, C. K. Chow, and Y. C. Chan. Effect of spin coating on the curing rate of epoxy adhesive for the fabrication of a polymer optical waveguide. *J. Electron. Mater.*, 33(3):224–228, mar 2004.

[4] Y. Sakai, Y. Sadaoka, and M. Matsuguchi. Humidity sensors based on polymer thin films. *Sensors Actuators B Chem.*, 35(1-3):85–90, sep 1996.

[5] H.-K. Lee, S.-I. Chang, and E. Yoon. A Flexible Polymer Tactile Sensor: Fabrication and Modular Expandability for Large Area Deployment. *J. Microelectromechanical Syst.*, 15(6):1681–1686, dec 2006.

[6] M. Calleja, M. Nordström, M. Álvarez, J. Tamayo, L. M. Lechuga, and A. Boisen. Highly sensitive polymer-based cantilever-sensors for DNA detection. *Ultramicroscopy*, 105(1-4):215–222, nov 2005.

[7] J.-M. Lagarón. Multifunctional and nanoreinforced polymers for food packaging. In *Multifunct. Nanoreinforced Polym. Food Packag.*, pages 1–28. Elsevier, 2011.

[8] M. Ozdemir, C. U. Yurteri, and H. Sadikoglu. Physical Polymer Surface Modification Methods and Applications in Food Packaging Polymers. *Crit. Rev. Food Sci. Nutr.*, 39(5):457–477, jul 1999.

[9] A. del Campo and C. Greiner. SU-8: a photoresist for high-aspect-ratio and 3D submicron lithography. *J. Micromechanics Microengineering*, 17 (6):R81–R95, jun 2007.

[10] T. Yada, T. Maejima, A. Masaru, and M. Umesaki. Thin-Film Formation by Spin Coating: Characteristics of a Positive Photoresist. *Jpn. J. Appl. Phys.*, 34(Part 1, No. 11):6279–6284, nov 1995.

[11] A. Facchetti, M.-H. Yoon, and T. J. Marks. Gate Dielectrics for Organic Field-Effect Transistors: New Opportunities for Organic Electronics. *Adv. Mater.*, 17(14):1705–1725, jul 2005.

[12] X. Zhao and X. Zhan. Electron transporting semiconducting polymers in organic electronics. *Chem. Soc. Rev.*, 40(7):3728, 2011.

[13] M. Fahlman, S. Fabiano, V. Gueskine, D. Simon, M. Berggren, and X. Crispin. Interfaces in organic electronics. *Nat. Rev. Mater.*, 4(10): 627–650, oct 2019.

[14] X. Guo and A. Facchetti. The journey of conducting polymers from discovery to application. *Nat. Mater.*, 19(9):922–928, sep 2020.

[15] K. Norrman, A. Ghanbari-Siahkali, and N. B. Larsen. 6 Studies of spin-coated polymer films. *Annu. Reports Sect. "C" (Physical Chem.*, 101:174, 2005.

[16] N. Sahu, B. Parija, and S. Panigrahi. Fundamental understanding and modeling of spin coating process: A review. *Indian J. Phys.*, 83(4):493–502, apr 2009.

[17] S. K. Wilson, R. Hunt, and B. R. Duff. The rate of spreading in spin coating. *J. Fluid Mech.*, 413:65–88, jun 2000.

[18] K. K. Gleason. Overview of Chemically Vapor Deposited (CVD) Polymers. In Karen K. Gleason, editor, *CVD Polym.*, pages 1–12. Wiley-VCH Verlag GmbH & Co. KGaA, Weinheim, Germany, apr 2015.

[19] A. Asatekin, M. C Barr, S. H. Baxamusa, K. K. S. Lau, W. E. Tenhaeff, J. Xu, and K. K. Gleason. Designing polymer surfaces via vapor deposition. *Mater. Today*, 13(5):26–33, may 2010.

[20] S. J. Limb, C. B. Labelle, K. K. Gleason, D. J. Edell, and E. F. Gleason. Growth of fluorocarbon polymer thin films with high CF 2 fractions and low dangling bond concentrations by thermal chemical vapor deposition. *Appl. Phys. Lett.*, 68(20):2810–2812, may 1996.

[21] H. G. Pryce Lewis, J. A. Caulfield, and K. K. Gleason. Perfluorooctane Sulfonyl Fluoride as an Initiator in Hot-Filament Chemical Vapor Deposition of Fluorocarbon Thin Films. *Langmuir*, 17:7652–7655, 2001.

[22] W.S. O'Shaughnessy, M. Gao, and K. K. Gleason. Initiated Chemical Vapor Deposition of Trivinyltrimethylcyclotrisiloxane for Biomaterial Coatings. *Langmuir*, 22(16):7021–7026, aug 2006.

[23] A. M. Coclite, R. M. Howden, D. C. Borrelli, C. D. Petruczok, R. Yang, J. L. Yagüe, A. Ugur, N. Chen, S. Lee, W. J. Jo, A. Liu, X. Wang, and K. K. Gleason. 25th Anniversary Article: CVD Polymers: A New Paradigm for Surface Modification and Device Fabrication. *Adv. Mater.*, 25(38): 5392–5423, oct 2013.

[24] N. Chen, D. H. Kim, P. Kovacik, H. Sojoudi, M. Wang, and K. K. Gleason. Polymer Thin Films and Surface Modification by Chemical Vapor Deposition: Recent Progress. *Annu. Rev. Chem. Biomol. Eng.*, 7:373–393, 2016.

[25] M. Wang, X. Wang, P. Moni, A. Liu, D. H. Kim, W. J. Jo, H. Sojoudi, and K. K. Gleason. CVD Polymers for Devices and Device Fabrication. *Adv. Mater.*, 29(11):1604606, mar 2017.

[26] K. K. Gleason. Chemically vapor deposited polymer nanolayers for rapid and controlled permeation of molecules and ions. *J. Vac. Sci. Technol. A*, 38(2):020801, mar 2020.

[27] K. K. Gleason. Nanoscale control by chemically vapour-deposited polymers. *Nat. Rev. Phys.*, jun 2020.

[28] K. K. Gleason. Organic Polymer Synthesis by Cat-CVD-Related Technology - Initiated CVD (iCVD). In *Catal. Chem. Vap. Depos. - Technol. Appl. Cat-CVD*, chapter 6, pages 179–248. Wiley-VCH, Weinheim, Germany, 1st edition, 2019.

[29] K. K. S. Lau and K. K. Gleason. Particle functionalization and encapsulation by initiated chemical vapor deposition (iCVD). *Surf. Coatings Technol.*, 201(22-23):9189–9194, sep 2007.

[30] P. Christian, S. Tumphart, H. M. A. Ehmann, H. Riegler, A. M. Coclite, and O. Werzer. Controlling Indomethacin Release through Vapor-Phase Deposited Hydrogel Films by Adjusting the Cross-linker Density. *Sci. Rep.*, 8(1):7134, dec 2018.

[31] J. Zhao and K. K. Gleason. Solvent-Less Vapor-Phase Fabrication of Membranes for Sustainable Separation Processes. *Engineering*, may 2020.

[32] A. T. Servi, E. Guillen-Burrieza, D. M. Warsinger, W. Livernois, K. Notarangelo, J. Kharraz, J. H. Lienhard V, H. A. Arafat, and K. K. Gleason. The effects of iCVD film thickness and conformality on the permeability and wetting of MD membranes. *J. Memb. Sci.*, 523:470–479, feb 2017.

[33] H. Moon, H. Seong, S. Woo Cheol, W.-T. Park, M. Kim, S. Lee, J. H. Bong, Y.-Y. Noh, B. J. Cho, S. Yoo, and S. G. Im. Synthesis of ultrathin polymer insulating layers by initiated chemical vapor deposition for low-power soft electronics. *Nat. Mater.*, 14:628–635, 2015.

[34] S. Lee, H. Seong, S. G. Im, H. Moon, and S. Yoo. Organic flash memory on various flexible substrates for foldable and disposable electronics. *Nat. Commun.*, 8(1):725, dec 2017.

[35] H. Seong, J. Choi, B. J. Kim, H. Park, and S. G. Im. Vapor-phase synthesis of sub-15 nm hybrid gate dielectrics for organic thin film transistors. *J. Mater. Chem. C*, 5(18):4463–4470, 2017.

[36] M. H. Woo, B. C. Jang, J. Choi, K. J. Lee, G. H. Shin, H. Seong, S. G. Im, and S.-Y. Choi. Low-power nonvolatile charge storage memory based on MoS2 and an ultrathin polymer tunneling dielectric. *Adv. Funct. Mater.*, 27:1703545, 2017.

[37] K. K. S. Lau, S. K Murthy, H. G. Pryce Lewis, J. A. Caulfield, and K. K. Gleason. Fluorocarbon dielectric via hot filament chemical vapor deposition. *J. Fluor. Chem.*, 122:93–96, 2003.

[38] G. M. Sessler and J E West. Self-biased condenser microphone with high capacitance. *J. Acoust. Soc. Am.*, 34:1787–1788, 1962.

[39] G. M. Sessler and J E West. Electret transducers: A review. *J. Acoust. Soc. Am*, 53:1589–1600, 1973.

[40] J E West. Electret microphones. *J. Acoust. Soc. Am*, 136:2130, 2014.

[41] S. Gong, J. Zhang, C. Wang, K. Ren, and Z. L. Wang. A monocharged electret nanogenerator-based self-powerded device for pressure and tactile sensor applications. *Adv. Funct. Mater.*, 29:1807618, 2019.

[42] Y Chiu and S.-H. Wu. Flexible electret energy harvesters with parylene electret on PDMS substrate. In *J. Phys. Conf. Ser.*, volume 476, page 12037. IOP Publishing Ltd, 2013.

[43] F. Hu, Q. Cai, F. Liao, M. Shao, and S.-T. Lee. Recent advancements in nanogenerators for energy harvesting. *Small*, 11:5611–5628, 2015.

[44] J. Hillenbrand, P. Pondrom, and G. M. Sessler. Electret transducer for vibration-based energy harvesting. *Appl. Phys. Lett.*, 106:183902, 2015.

[45] S. Gong, C. Wang, J. Zhang, C. Zhang, J .E. West, and K. Ren. Monocharged electret generator for wearable energy harvesting applications. *Adv. Sustain. Syst.*, page 1700178, 2018.

[46] P. Pondrom, G. M. Sessler, J. Bös, and T. Melz. Compact electret energy harvester with high power output. *Appl. Phys. Lett.*, 109:53906, 2016.

[47] J. Zhong, Q. Zhong, G. Chen, B. Hu, S. Zhao, X. Li, N. Wu, W. Li, H. Yu, and J. Zhou. Surface charge self-recovering electret film for wearable energy conversion in a harsh environment. *Energy Environ. Sci.*, 9:3085–3091, 2016.

[48] M.A. Parada and A. de Almeida. Teflon electret radiation dosimeter. *Nucl. Instruments Methods Phys. Res. Sect. B Beam Interact. with Mater. Atoms*, 191(1-4):820–824, may 2002.

[49] B. A. MacDonald, B. G. Fallone, and L. N. Ryner. Feasibility study of an electret dosimetry technique. *Phys. Med. Biol.*, 37(10):1825–1836, oct 1992.

[50] J. Van Turnhout, J. W. C. Adamse, and W. J. Hoeneveld. Electret filters for high-efficiency air cleaning. *J. Electrostat.*, 8(4):369–379, apr 1980.

[51] M. Nifuku, Y. Zhou, A. Kisiel, T. Kobayashi, and H. Katoh. Charging characteristics for electret filter materials. *J. Electrostat.*, 51-52:200–205, may 2001.

[52] Y.-N. Zhong, T Wang, X Gao, J.-L. Xu, and S.-D. Wang. Synapse-like organic thin film memristors. *Adv. Funct. Mater.*, 28:1800854, 2018.

[53] Y.-H. Chou, H.-C. Chang, C.-L. Liu, and W.-C. Chen. Polymeric charge storage electrets for non-volatile organic field effect transistor memory devices. *Polym. Chem.*, 6:341–352, 2015.

[54] G Gelinck. Trapped fast at the gate. *Nature*, 445:268–270, 2007.

[55] K.-J. Baeg, Y.-Y. Noh, J. Ghim, S.-J. Kang, H. Lee, and D.-Y. Kim. Organic non-volatile memory based on pentacene field-effect transistor using a polymeric gate electret. *Adv. Mater.*, 18:3179–3183, 2006.

[56] T. B. Singh, N. Marjanovic, G. J. Matt, N. S. Sariciftci, R. Schwödiauer, and S. Bauer. Nonvolatile organic field-effect transitor memory element with a polymeric gate electret. *Appl. Phys. Lett.*, 85:5409–5411, 2004.

[57] M. Ohring. Chemical Vapor Deposition. In *Mater. Sci. Thin Film.*, chapter 4, pages 147–194. Academic Press, San Diego, CA, USA, 1st editio edition, 1992.

[58] W. Kern and K. K. Schuegraf. Deposition Technologies and Applications: Introduction and Overview. In Krishna Seshan, editor, *Handb. Thin-Film Depos. Process. Tech.*, chapter 1, pages 11–43. Noyes Publications, William Andrew Publishing, Norwich, NY, USA, 2nd edition, 2002.

[59] Yi Zhang, L. Zhang, and C. Zhou. Review of Chemical Vapor Deposition of Graphene and Related Applications. *Acc. Chem. Res.*, 46(10):2329–2339, oct 2013.

[60] G. Wahl. Dr John M Blocher Jr: 90 Years Young. *Chem. Vap. Depos.*, 15 (1-3):9–9, mar 2009.

[61] D. M. Mattox. *Handbook of Physical Vapor Deposition (PVD) Processing.* Elsevier, 2nd edition, 2010.

[62] A. G. Thompson. MOCVD technology for semiconductors. *Mater. Lett.*, 30(4):255–263, mar 1997.

[63] H. Wang and G. Yu. Direct CVD Graphene Growth on Semiconductors and Dielectrics for Transfer-Free Device Fabrication. *Adv. Mater.*, 28(25): 4956–4975, jul 2016.

[64] S. Faÿ, J. Steinhauser, N. Oliveira, E. Vallat-Sauvain, and C. Ballif. Opto-electronic properties of rough LP-CVD ZnO:B for use as TCO in thin-film silicon solar cells. *Thin Solid Films*, 515(24):8558–8561, oct 2007.

[65] A. Heya, T. Minamikawa, T. Niki, S. Minami, A. Masuda, H. Umemoto, N. Matsuo, and H. Matsumura. Cat-CVD SiN passivation films for OLEDs and packaging. *Thin Solid Films*, 516(5):553–557, jan 2008.

[66] R. J. McCurdy. Successful implementation methods of atmospheric CVD on a glass manufacturing line. *Thin Solid Films*, 351(1-2):66–72, aug 1999.

[67] H. Matsumura, A. Masuda, and H. Umemoto. Present status and future feasibility for industrial implementation of Cat-CVD (Hot-Wire CVD) technology. *Thin Solid Films*, 501(1-2):58–60, apr 2006.

[68] X. Zhu and D. M. Aslam. CVD diamond thin film technology for MEMS packaging. *Diam. Relat. Mater.*, 15(2-3):254–258, feb 2006.

[69] H. Nakayama and M. Ito. Super H2O-barrier film using Cat-CVD (HWCVD)-grown SiCN for film-based electronics. *Thin Solid Films*, 519 (14):4483–4486, may 2011.

[70] K. S. Forcey, A. Perujo, F. Reiter, and P. L. Lolli-Ceroni. The formation of tritium permeation barriers by CVD. *J. Nucl. Mater.*, 200(3):417–420, may 1993.

[71] S. Majee, M. F. Cerqueira, D. Tondelier, J. C. Vanel, B. Geffroy, Y. Bonnassieux, P. Alpuim, and J. E. Bourée. Permeation barrier performance of Hot Wire-CVD grown silicon-nitride films treated by argon plasma. *Thin Solid Films*, 575:72–75, jan 2015.

[72] A. Stoffel, A. Kovács, W. Kronast, and B. Müller. LPCVD against PECVD for micromechanical applications. *J. Micromechanics Microengineering*, 6 (1):1–13, mar 1996.

[73] M. Meyyappan, L. Delzeit, A. Cassell, and D. Hash. Carbon nanotube growth by PECVD: a review. *Plasma Sources Sci. Technol.*, 12(2):205–216, may 2003.

[74] H. Matsumura, H. Umemoto, K. K. Gleason, and R. E. I. Schropp. Fundamentals for Studying the Physics of Cat-CVD and Differences from PECVD. In *Catal. Chem. Vap. Depos. - Technol. Appl.*, chapter 2, pages 11–39. Wiley-VCH, Weinheim, Germany, 1st edition, 2019.

[75] S.D. Allen. Laser chemical vapor deposition: A technique for selective area deposition. *J. Appl. Phys.*, 52(11):6501–6505, nov 1981.

[76] C. R. Moylan, T. H. Baum, and C. R. Jones. LCVD of copper: Deposition rates and deposit shapes. *Appl. Phys. A Solids Surfaces*, 40(1):1–5, may 1986.

[77] F. Durst. *Fluid Mechanics*. Springer Berlin Heidelberg, Berlin, Heidelberg, 1st edition, 2008.

[78] S. Jayanti. *Computational Fluid Dynamics for Engineers and Scientists*. Springer Netherlands, Dordrecht, 1st edition, 2018.

[79] S. Chapman and T. G. Cowling. *The Mathematical Theory of Non-uniform Gases*. Cambridge University Press, 3rd editio edition, 1991.

[80] Y. K. Chae. Chemical Vapor Deposition Reactor Design Using Small-Scale Diagnostic Experiments Combined with Computational Fluid Dynamics Simulations. *J. Electrochem. Soc.*, 146(5):1780, 1999.

[81] M. Volmer and A. Weber. Keimbildung in übersättigten Gebilden. *Zeitschrift für Phys. Chemie*, 119U(1), jan 1926.

[82] F. C. Frank and J. H. van der Merve. One-dimensional dislocations. I. Static theory. *Proc. R. Soc. London. Ser. A. Math. Phys. Sci.*, 198(1053): 205–216, aug 1949.

[83] I. N. Stranski and L. Krastanow. Zur Theorie der orientierten Ausscheidung von Ionenkristallen aufeinander. *Monatshefte für Chemie*, 71(1):351–364, dec 1937.

[84] Y. Xu and X.-T. Yan. Thermodynamics and Kinetics of CHemical Vapour Deposition. In *Chem. Vap. Depos. - An Integr. Engeneering Des. Adv. Mater.*, chapter 4, pages 129–164. Springer, London Dordrecht Heidelberg New York, 2010.

[85] D. L. Smith. CHemical Vapor Deposition. In *Thin-film Depos. Princ. Pract.*, chapter 7. McGraw-Hill, New York, USA, 1995.

[86] Miloslav Nič, Jiří Jirát, Bedřich Košata, Aubrey Jenkins, and Alan McNaught, editors. *IUPAC Compendium of Chemical Terminology*. IUPAC, Research Triagle Park, NC, jun 2009.

[87] J. M. G. Cowie. Polymer Stereochemistry. In *Polym. Chem. Phys. Mod. Mater.*, chapter 6, pages 123–139. Blackie Academic & Professional, London, UK, 2nd edition, 1991.

[88] J. M. G. Cowie. Introduction. In *Polym. Chem. Phys. Mod. Mater.*, chapter 1, pages 1–25. Blackie Academic & Professional, London, UK, 2nd edition, 1991.

[89] S. K. Biswas and K. Vijayan. Friction and wear of PTFE — a review. *Wear*, 158(1-2):193–211, oct 1992.

[90] F. Abbasi, H. Mirzadeh, and A.-A. Katbab. Modification of polysiloxane polymers for biomedical applications: a review. *Polym. Int.*, 50(12):1279–1287, dec 2001.

[91] D. N. Saheb and J. P. Jog. Natural fiber polymer composites: A review. *Adv. Polym. Technol.*, 18(4):351–363, 1999.

[92] R Andrews and M.C Weisenberger. Carbon nanotube polymer composites. *Curr. Opin. Solid State Mater. Sci.*, 8(1):31–37, jan 2004.

[93] C Hanisch, A Kulkarni, V. Zaporojtchenko, and F. Faupel. Polymer-metal nanocomposites with 2-dimensional Au nanoparticle arrays for sensoric applications. *J. Phys. Conf. Ser.*, 100(5):052043, mar 2008.

[94] J. Li and J.-K. Kim. Percolation threshold of conducting polymer composites containing 3D randomly distributed graphite nanoplatelets. *Compos. Sci. Technol.*, 67(10):2114–2120, aug 2007.

[95] G. Odian. Introduction. In *Princ. Polym.*, pages 1–38. John Wiley & Sons, Inc., Hoboken, NJ, USA, 1st edition, jan 2004.

[96] G. Odian. Radical Chain Polymerization. In *Princ. Polym.*, chapter 3, pages 198–349. John Wiley & Sons, Inc., Hoboken, NJ, USA, 1st edition, jan 2004.

[97] G. Odian. Step Polymerization. In *Princ. Polym.*, chapter 2, pages 39–197. John Wiley & Sons, Inc., Hoboken, NJ, USA, 1st edition, jan 2004.

[98] P. D. Coates, S. E. Barnes, M. G. Sibley, E. C. Brown, H. G. M. Edwards, and I. J. Scowen. In-process vibrational spectroscopy and ultrasound measurements in polymer melt extrusion. *Polymer (Guildf).*, 44(19):5937–5949, sep 2003.

[99] N. S. Sangaj and V. C. Malshe. Permeability of polymers in protective organic coatings. *Prog. Org. Coatings*, 50(1):28–39, jun 2004.

[100] S. R. Forrest and M. E. Thompson. Introduction: Organic Electronics and Optoelectronics. *Chem. Rev.*, 107(4):923–925, apr 2007.

[101] J. Zasadzinski, R. Viswanathan, L. Madsen, J. Garnaes, and D. Schwartz. Langmuir-Blodgett films. *Science (80-.).*, 263(5154):1726–1733, mar 1994.

[102] A. Ulman. Formation and Structure of Self-Assembled Monolayers. *Chem. Rev.*, 96(4):1533–1554, jan 1996.

[103] O. Kylián, A. Shelemin, P. Solař, P. Pleskunov, D. Nikitin, A. Kuzminova, R. Štefaníková, P. Kúš, M. Cieslar, J. Hanuš, A. Choukourov, and H. Biederman. Magnetron Sputtering of Polymeric Targets: From Thin Films to Heterogeneous Metal/Plasma Polymer Nanoparticles. *Materials (Basel).*, 12(15):2366, jul 2019.

[104] S. Iwamori, K. Kezuka, and A. Uemura. Characterization of Polymer Thin Films Sputtered onto a Copper Substrate with Two Kinds of Polyimide Targets. *Mol. Cryst. Liq. Cryst.*, 471(1):99–111, sep 2007.

[105] N. Yi, S. Bao, H. Zhou, Y. Xin, A. Huang, Y. Ma, R. Li, and P. Jin. Preparation of microstructure-controllable superhydrophobic polytetrafluoroethylene porous thin film by vacuum thermal-evaporation. *Front. Mater. Sci.*, 10(3):320–327, sep 2016.

[106] S. Ravi-Kumar, B. Lies, H. Lyu, and H. Qin. Laser Ablation of Polymers: A Review. *Procedia Manuf.*, 34:316–327, 2019.

[107] G. B. Blanchet, C. R. Fincher, C. L. Jackson, S. I. Shah, and K. H. Gardner. Laser Ablation and the Production of Polymer Films. *Science (80-.).*, 262 (5134):719–721, oct 1993.

[108] P. Baumann, M. Gersdorff, J. Kreis, M. Kunat, and M. Schwambera. Carrier gas-enhanced polymer vapor-phase deposition (PVPD): Industrializatied solutions by example of deposition of parylene films for large-area applications. In K K Gleason, editor, *CVD Polym. – Fabr. Org. surfaces devices*, chapter 20, pages 431–453. Wiley-VCH, Weinheim, Germany, 1st edition, 2015.

[109] J. Lahann. Vapor-based polymer coatings for potential biomedical applications. *Polym. Int.*, 55(12):1361–1370, dec 2006.

[110] H. Kong, C. Li, Z. Guo, W. Zhang, J. Yao, H. Zhu, R. Yan, L. Wang, J. Li, W. Wei, and L. Zhou. Sensitivity improved with Parylene-C passivized on Lamb wave sensor for aPTT measurement through monitoring whole blood reaction. *Sensors Actuators B Chem.*, 285:479–486, apr 2019.

[111] B. J. Kim and E. Meng. Micromachining of Parylene C for bioMEMS. *Polym. Adv. Technol.*, 27(5):564–576, may 2016.

[112] M. Shen and A. T. Bell. A Review of Recent Advances in Plasma Polymerization. In *ACS Symp. Ser. Vol. 108*, pages 1–33. ACS, sep 1979.

[113] H. Yasuda. Glow discharge polymerization. *J. Polym. Sci. Macromol. Rev.*, 16:199–293, 1981.

[114] H. Yasuda. Plasma polymerization for protective coatings and composite membranes. *J. Membr. Sci.*, 18:273–284, 1984.

[115] J Friedrich. Mechanisms of plasma polymerization - Reviewed from a chemical point of view. *Plasma Process. Polym.*, 8:783–802, 2011.

[116] A. Carletto and J. P. S. Badyal. Mechanistic reaction pathway for hexafluoropropylene oxide pulsed plasma deposition of PTFE-like films. *J. Phys. Commun.*, 1(5):055024, dec 2017.

[117] P. Sundberg and M. Karppinen. Organic and inorganic-organic thin film structures by molecular layer deposition: A review. *Beilstein J. Nanotechnol.*, 5:1104–1136, 2014.

[118] Y. Zhao, K. Zheng, and X. Sun. Adressing interfacial issues in liquid-based and solid-state batteries by atomic and molecular layer deposition. *Joule*, 2:2583–2604, 2018.

[119] X Meng. An overview of molecular layer deposition for organic and organic-inorganic hybrid materials: Mechanisms, growth characteristics, and promising applications. *J. Mater. Chem. A*, 5:18326–18378, 2017.

[120] H. Zhou and S. F. Bent. Fabrication of organic interfacial layers by molecular layer deposition: Present Status and future opportunities. In K. K. Gleason, editor, *CVD Polym. – Fabr. Org. surfaces devices*, chapter 7, pages 133–170. Wiley-VCH, Weinheim, Germany, 1st edition, 2015.

[121] J. S. Lee, Y.-J. Lee, E. L. Tae, Y. S. Park, and K. B. Yoon. Synthesis of zeolite as ordered multicrystal arrays. *Science (80-.).*, 301:818–821, 2003.

[122] P. W. Loscutoff, H.-B.-R. Lee, and S. F. Bent. Deposition of ultrathin polythiourea films by molecular layer deposition. *Chem. Mater.*, 22:5563–5569, 2010.

[123] M. H. Gharahcheshmeh and K. K. Gleason. Device Fabrication Based on Oxidative Chemical Vapor Deposition (oCVD) Synthesis of Conducting Polymers and Related Conjugated Organic Materials. *Adv. Mater. Interfaces*, 6:1801564, 2019.

[124] R. M. Howden. Conjugated CVD polymers: Conductors and semiconductors. In Karen K. Gleason, editor, *CVD Polym. – Fabr. Org. surfaces devices*, chapter 11, pages 233–252. Wiley-VCH, Weinheim, Germany, 1st edition, 2015.

[125] X. Wang, X. Zhang, L. Sun, D. Lee, S. Lee, M. Wang, J. Zhao, Y. Shao-Horn, M. Dincă, T. Palacios, and K. K. Gleason. High electrical conductivity and carrier mobility in oCVD PEDOT thin films by engineered crystallization and acid treatment. *Sci. Adv.*, 4:eaat5780, 2018.

[126] Y. Y. Smolin, M. Soroush, and K. K. S. Lau. Influence of oCVD Polyaniline Film Chemistry in Carbon-Based Supercapacitors. *Ind. Eng. Chem. Res.*, 56:6221–6228, 2017.

[127] Y. Y. Smolin, K. L. van Aken, M. Boota, M. Soroush, Y. Gogotsi, and K. K. S. Lau. Engineering Ultrathin Polyaniline in Micro/Mesoporous Carbon Supercapacitor Electrodes Using Oxidative Chemical Vapor Deposition. *Adv. Mater. Interfaces*, 4:1601201, 2017.

[128] Coatings Materials and Surface Coatings. chapter 17, pages 1–3. CRC press, Boca Raton, USA, 1st edition, 2006.

[129] S. H. Baxamusa, S. G. Im, and K. K. Gleason. Initiated and oxidative chemical vapor deposition: a scalable method for conformal and functional polymer films on real substrates. *Phys. Chem. Chem. Phys.*, 11:5227–5240, 2009.

[130] L. Ghasemi-Mobarakeh, O. Werzer, R. Keimel, D. Kolahreez, P. Hadley, and A. M. Coclite. Manipulating drug release from tridimensional porous substrates coated by initiated chemical vapor deposition. *J. Appl. Polym. Sci.*, 136(33):47858, sep 2019.

[131] R. Bakker, V. Verlaan, C. H. M. van der Werf, J. K. Rath, K. K. Gleason, and R. E. I. Schropp. Initiated chemical vapour deposition (iCVD) of thermally stable poly-glycidyl methacrylate. *Surf. Coatings Technol.*, 201 (22-23):9422–9425, sep 2007.

[132] S. Yoshida, T. Kobayashi, M. Kumano, and M. Esashi. Conformal coating of poly-glycidyl methacrylate as lithographic polymer via initiated chemical vapor deposition. *J. Micro/Nanolithography, MEMS, MOEMS*, 11(2): 023001–1, may 2012.

[133] K. K. S. Lau and K. K. Gleason. Initiated Chemical Vapor Deposition (iCVD) of Poly(alkyl acrylates): An Experimental Study. *Macromolecules*, 39:3695–3703, 2006.

[134] K. K. S. Lau and K. K. Gleason. Initiated Chemical Vapor Deposition (iCVD) of Poly(alkyl acrylates): A Kinetic Model. *Macromolecules*, 39: 3695–3703, 2006.

[135] T. P. Martin and K. K. Gleason. Combinatorial Initiated CVD for Polymeric Thin Films. *Chem. Vap. Depos.*, 12(11):685–691, nov 2006.

[136] W.S. O'Shaughnessy, D. J. Edell, and K. K. Gleason. Initiated chemical vapor deposition of biopassivation coatings. *Thin Solid Films*, 516(5): 684–686, jan 2008.

[137] H. G. Pryce Lewis, T. B. Casserly, and K. K. Gleason. Hot-Filament Chemical Vapor Deposition of Organosilicon Thin Films from Hexamethylcyclotrisiloxane and Octamethylcyclotetrasiloxane. *J. Electrochem. Soc.*, 148(12):F212, 2001.

[138] B. Reeja-Jayan, N. Chen, J. Lau, J. A. Kattirtzi, P. Moni, A. Liu, I. G. Miller, R. Kayser, A. P. Willard, B. Dunn, and K. K. Gleason. A Group of Cyclic Siloxane and Silazane Polymer Films as Nanoscale Electrolytes for Microbattery Architectures. *Macromolecules*, 48(15):5222–5229, aug 2015.

[139] B. A. Cruden, K. K. Gleason, and H. H. Sawin. Relationship of CF2 concentration to deposition rates in the pyrolytic chemical vapor deposition process. *J. Vac. Sci. Technol. B Microelectron. Nanom. Struct.*, 20(2):690, 2002.

[140] K. K. S. Lau, J. A. Caulfield, and K. K. Gleason. Structure and Morphology of Fluorocarbon Films Grown by Hot Filament Chemical Vapor Deposition. *Chem. Mater.*, 12(10):3032–3037, oct 2000.

[141] M. Gupta and K. K. Gleason. Initiated Chemical Vapor Deposition of Poly(1H,1H,2H,2H-perfluorodecyl Acrylate) Thin Films. *Langmuir*, 22(24): 10047–10052, nov 2006.

[142] A. M. Coclite, Y. Shi, and K. K. Gleason. Controlling the Degree of Crystallinity and Preferred Crystallographic Orientation in Poly-Perfluorodecylacrylate Thin Films by Initiated Chemical Vapor Deposition. *Adv. Funct. Mater.*, 22(10):2167–2176, may 2012.

[143] R. Yang, J. Xu, G. Ozaydin-Ince, S. Y. Wong, and K. K. Gleason. Surface-Tethered Zwitterionic Ultrathin Antifouling Coatings on Reverse Osmosis Membranes by Initiated Chemical Vapor Deposition. *Chem. Mater.*, 23(5): 1263–1272, mar 2011.

[144] R. Yang and K. K. Gleason. Ultrathin Antifouling Coatings with Stable Surface Zwitterionic Functionality by Initiated Chemical Vapor Deposition (iCVD). *Langmuir*, 28(33):12266–12274, aug 2012.

[145] Y. Gao, B. Cole, and W. E. Tenhaeff. Chemical Vapor Deposition of Polymer Thin Films Using Cationic Initiation. *Macromol. Mater. Eng.*, 303: 1700425, 2017.

[146] K. K. S. Lau, K. K. Gleason, and B. L. Trout. Thermochemistry of Gas Phase CF2 Reactions: A Density Functional Theory Study. *J. Chem. Phys.*, 113:4103–4108, 2000.

[147] S. K Murthy and K. K. Gleason. Fluorocarbon-Organosilicon Copolymer Synthesis by Hot Filament Chemical Vapor Deposition. *Macromolecules*, 35:1967–1972, 2002.

[148] S. K. Murthy, Bradley D. Olsen, and K. K. Gleason. Initiation of Cyclic Vinylmethylsiloxane Polymerization in a Hot-Filament Chemical Vapor Deposition Process. *Langmuir*, 18(16):6424–6428, aug 2002.

[149] G. Ozaydin-Ince and K. K. Gleason. Tunable Conformality of Polymer Coatings on High Aspect Ratio Features. *Chem. Vap. Depos.*, 16(1-3): 100–105, mar 2010.

[150] G. Aresta, J. Palmans, M. C. M. van de Sanden, and M. Creatore. Initiated-chemical vapor deposition of organosilicon layers: Monomer adsorption, bulk growth, and process window definition. *J. Vac. Sci. Technol. A Vacuum, Surfaces, Film.*, 30(4):041503, jul 2012.

[151] G. Ozaydin-Ince and K. K. Gleason. Transition between kinetic and mass transfer regimes in the initiated chemical vapor deposition from ethylene glycol diacrylate. *J. Vac. Sci. Technol. A Vacuum, Surfaces, Film.*, 27(5): 1135–1143, sep 2009.

[152] M. Fineman and S. D. Ross. Linear method for determining monomer reactivity ratios in copolymerization. *J. Polym. Sci.*, 5(2):259–262, apr 1950.

[153] T. Kelen and F. Tüdős. Analysis of the Linear Methods for Determining Copolymerization Reactivity Ratios. I. A New Improved Linear Graphic Method. *J. Macromol. Sci. Part A - Chem.*, 9(1):1–27, jan 1975.

[154] F. R. Mayo and F. M. Lewis. Copolymerization. I. A Basis for Comparing the Behavior of Monomers in Copolymerization; The Copolymerization of Styrene and Methyl Methacrylate. *J. Am. Chem. Soc.*, 66(9):1594–1601, sep 1944.

[155] T. L. Hanley, R. P. Burford, R. J. Fleming, and K. W. Barber. A general review of polymeric insulation for use in HVDC cables. *IEEE Electr. Insul. Mag.*, 19(1):13–24, jan 2003.

[156] G M Sessler, editor. *Electrets*. Springer, Berlin Heidelberg New York, 2nd edition, 1987.

[157] G. Teyssedre and C Laurent. Charge transport modeling in insulating polymers: From molecular to macroscopic scale. *IEEE Trans. Dielectr. Electr. Insul.*, 12:857–875, 2005.

[158] R. Hoffmann, C. Janiak, and C. Kollmar. A chemical approach to the orbitals of organic polymers. *Macromolecules*, 24:3725–3746, 1991.

[159] John A. Carr and S. Chaudhary. The identification, characterization and mitigation of defect states in organic photovoltaic devices: a review and outlook. *Energy Environ. Sci.*, 6(12):3414, 2013.

[160] G. M. Sessler. Physical Principles of Electrets. In G. M. Sessler, editor, *Electrets*, chapter 2, pages 13–80. Springer, Berlin Heidelberg New York, 2nd edition, 1987.

[161] D. J. Yaron and T. Kowaleski. Beware the nanovoids. *Nat. Mater.*, 18: 1146–1155, 2019.

[162] N. B. Kotadiya, A. Mondal, P. W. M. Blom, D. Amdrienko, and G.-J. A. H. Wetzelaer. A window to trap-free charge transport in organic semiconducting thin films. *Nat. Mater.*, 18:1182–1186, 2019.

[163] G. Zuo, M. Linares, T. Upreti, and M. Kemerink. General rule for the energy of water-induced traps in organic semiconductors. *Nat. Mater.*, 18: 588–593, 2019.

[164] M. Nikolka, K. Broch, J. Armitage, D. Hanfifi, P. J. Nowack, D. Venkateshvaran, A. Sadhanala, J. Saska, M. Mascal, S.-H. Jung, J.-K. Lee, I. McCulloch, A. Salleo, and H. Sirringhaus. High-mobility, trap-free charge transport in conjugated polymer diodes. *Nat. Commun.*, 10:2122, 2019.

[165] H. Shirakawa, E. J. Louis, A. G. MacDiarmid, C. K. Chiang, and A. J. Heeger. Synthesis of electrically conducting organic polymers: halogen derivatives of polyacetylene, (CH)x. *J. Chem. Soc. Chem. Commun.*, (16): 578, 1977.

[166] C. K. Chiang, C. R. Fincher, Y. W. Park, A. J. Heeger, H. Shirakawa, E. J. Louis, S. C. Gau, and A. G. MacDiarmid. Electrical Conductivity in Doped Polyacetylene. *Phys. Rev. Lett.*, 39(17):1098–1101, oct 1977.

[167] A. J. Heeger. Nobel Lecture: Semiconducting and metallic polymers: The fourth generation of polymeric materials. *Rev. Mod. Phys.*, 73(3):681–700, sep 2001.

[168] J. M. G. Cowie. Polymers for the Electronics Industry. In *Polym. Chem. Phys. Mod. Mater.*, chapter 17, pages 400–431. Blackie Academic & Professional, London, UK, 2nd edition, 1991.

[169] S. Roth and M. Filzmoser. Conducting polymers thirteen years of Polyacetylene Doping. *Adv. Mater.*, 2(8):356–360, aug 1990.

[170] A. J. Heeger, S. Kivelson, J. R. Schrieffer, and W. P. Su. Solitons in conducting polymers. *Rev. Mod. Phys.*, 60(3):781–850, jul 1988.

[171] S. Roth and H. Bleier. Solitons in polyacetylene. *Adv. Phys.*, 36(4):385–462, jan 1987.

[172] J. L. Bredas and G. B. Street. Polarons, bipolarons, and solitons in conducting polymers. *Acc. Chem. Res.*, 18(10):309–315, oct 1985.

[173] A. J. Heeger. Charge Storage in Conducting Polymers: Solitons, Polarons, and Bipolarons. *Polym. J.*, 17(1):201–208, jan 1985.

[174] A. J. Heeger. Semiconducting polymers: the Third Generation. *Chem. Soc. Rev.*, 39(7):2354, 2010.

[175] T. Nezakati, A. Seifalian, A. Tan, and A. M. Seifalian. Conductive Polymers: Opportunities and Challenges in Biomedical Applications. *Chem. Rev.*, 118 (14):6766–6843, jul 2018.

[176] M. Jaiswal and R. Menon. Polymer electronic materials: a review of charge transport. *Polym. Int.*, 55(12):1371–1384, dec 2006.

[177] O. Heaviside. Electromagnetic induction and its propagation. Electrization and electrification. Natural Electrets. *Electr.*, pages 230–231, 1885.

[178] H. Shu, C. Xiangchao, L. Peng, and G. Hui. Study on Electret Technology of Air Filtration Material. *IOP Conf. Ser. Earth Environ. Sci.*, 100:012110, dec 2017.

[179] G. S. Neugschwandtner, R. Schwödiauer, S. Bauer-Gogonea, S. Bauer, M. Paajanen, and J. Lekkala. Piezo- and pyroelectricity of a polymer-foam space-charge electret. *J. Appl. Phys.*, 89(8):4503–4511, apr 2001.

[180] S. Bauer, S. Bauer-Gogonea, F. Camacho-Gonzales, M. Dansachmuller, I. Graz, M. Kaltenbrunner, J.G. Leonhartsberger, and R. Schwödiauer. Ferroelectrets: Polymer-foam space-charge electrets with ferroelectric-like behaviour. In *2005 12th Int. Symp. Electrets*, pages 23–27. IEEE, 2005.

[181] C. J. Dias, J. N. Marat-Mendes, and J. A. Giacometti. Effects of a corona discharge on the charge stability of Teflon FEP negative electrets. *J. Phys. D. Appl. Phys.*, 22(5):663–669, may 1989.

[182] R. Gerhard-Multhaupt, M. Haardt, W. Eisenmenger, and G. M. Sessler. Electric-field profiles in electron-beam-charged polymer electrets. *J. Phys. D. Appl. Phys.*, 16(11):2247–2256, nov 1983.

[183] L. S. McCarty and G. M. Whitesides. Electrostatic Charging Due to Separation of Ions at Interfaces: Contact Electrification of Ionic Electrets. *Angew. Chemie Int. Ed.*, 47(12):2188–2207, mar 2008.

[184] D. K. Donald. Contact Electrification of Insulators and Its Relevance to Electrets. *J. Electrochem. Soc.*, 115(3):270, 1968.

[185] M. M. Shahin. Nature of charge carriers in negative coronas. *Appl. Opt.*, 8: 106–110, 1969.

[186] K C Kao, editor. *Dielectric Phenomena in Solids*. Elsevier, 1st edition, 2004.

[187] A. Germant. Recent investigations on electrets. *Philos. Mag.*, 20:929–952, 1935.

[188] Z. Xia, A. Wedel, and R. Danz. Charge storage and its dynamics in porous polytetrafluoroethylene (PTFE) film electrets. *IEEE Trans. Dielectr. Electr. Insul.*, 10:102–108, 2003.

[189] R. L. Remke and H. von Seggern. Modeling of thermally stimulated currents in polytetrafluoroethylene. *J. Appl. Phys.*, 54:5262–5266, 1983.

[190] Q. Chen. PTFE electret negative charge stability after RF plasma treatment. *J. Phys. D Appl. Phys.*, 35:2939–2944, 2002.

[191] P. Gunther, H. Ding, and R. Gerhard-Multhaupt. Electret properties of spin-coated Teflon AF films. In *Proc. IEEE Conf. Electr. Insul. Dielectr. Phenom.* IEEE, 1993.

[192] D. Rychkov, A. Rychkov, N. Efimov, A. Malygin, and R. Gerhard. Higher stabilities of positive and negative charge on tetrafluoroethylene-hexafluoropropylene copolymer (FEP) electrets treated with titanium-tetrachloride vapor. *Appl. Phys. A*, 112:283–287, 2013.

[193] U. Bartsch, J. Gaspar, and O. Paul. Characterization of the charging and long-term perfromance of cytop electret layers for MEMS applications. *Mater. Res. Soc. Symp. Proc.*, 1134:1117–1134, 2009.

[194] Y. Yasuno. Heat-resistance evaluation of SiO2 electret for microphones. In *2008 13th Int. Symp. Electrets*, pages C136–C136. IEEE, sep 2008.

[195] K. S. Ramadan, D. Sameoto, and S. Evoy. A review of piezoelectric polymers as functional materials for electromechanical transducers. *Smart Mater. Struct.*, 23(3):033001, mar 2014.

[196] S. Mishra, L. Unnikrishnan, S. K. Nayak, and S. Mohanty. Advances in Piezoelectric Polymer Composites for Energy Harvesting Applications: A Systematic Review. *Macromol. Mater. Eng.*, 304(1):1800463, jan 2019.

[197] J. Van Turnhout. Thermally Stimulated Discharge of Polymer Electrets. *Polym. J.*, 2(2):173–191, mar 1971.

[198] J. van Turnhout. Thermally stimulated discharge of electrets. In Gerhard M. Sessler, editor, *Electrets*, chapter 3, pages 81–215. Springer Berlin Heidelberg New York, 2nd edition, 1987.

[199] W.-W. Shen, H.-B. Mu, G.-J. Zhang, J.-B. Deng, and D.-M. Tu. Identelectrets of electron and hole trap based on isothermal surface potential decay model. *J. Appl. Phys.*, 113:83706, 2013.

[200] L. Boudou, F. Zheng, and G. Teyssedre. Photo-stimulated discharge current measurements on biaxially oriented polypropylene thin films (BOPP). In *2018 12th Int. Conf. Prop. Appl. Dielectr. Mater.*, pages 722–725. IEEE, may 2018.

[201] S. Kim, K. Suzuki, A. Sugie, H. Yoshida, M. Yoshida, and Y. Suzuki. Effect of end group of amorphous perfluoro-polymer electrets on electron trapping. *Sci. Technol. Adv. Mater.*, 19(1):486–494, dec 2018.

[202] D. Cubero, N. Quirke, and D. F. Coker. Electronic states for excess electrons in polyethylene compared to long-chain alkanes. *Chem. Phys. Lett.*, 370 (1-2):21–25, mar 2003.

[203] M. Meunier, N. Quirke, and A. Aslanides. Molecular modeling of electron traps in polymer insulators: Chemical defects and impurities. *J. Chem. Phys.*, 115(6):2876–2881, aug 2001.

[204] A. Huzayyin, S. Boggs, and R. Ramprasad. Density functional analysis of chemical impurities in dielectric polyethylene. *IEEE Trans. Dielectr. Electr. Insul.*, 17(3):926–930, jun 2010.

[205] T. Takada, H. Kikuchi, H. Miyake, Y. Tanaka, M. Yoshida, and Y. Hayase. Determination of charge-trapping sites in saturated and aromatic polymers by quantum chemical calculation. *IEEE Trans. Dielectr. Electr. Insul.*, 22 (2):1240–1249, apr 2015.

[206] Q. Chen. Investigation of corona charge stability mechanisms in polytetrafluoroethylene (PTFE) teflon films after plasma treatment. *J. Electrostat.*, 59: 3–13, 2003.

[207] A. A. Rychkov and V G Boitsov. Charge relaxation in PTFE-Al structures having interfacial region modified by the glow discharge. In *10th Int. Symp. Electrets (ISE 10). Proc. (Cat. No. 99CH36256)*, pages 91–94. IEEE, 1999.

[208] G. M. Sessler. Electrets: recent developments. *J. Electrostat.*, 51-52:137–145, 2001.

[209] H J Wintle. Surface-charge decay in insulators with nonconstant mobility and with deep trapping. *J. Appl. Phys.*, 43:2927–2930, 1972.

[210] H J Wintle. Space charge limited currents in graded Films. *Thin Solid Films*, 21:83–90, 1974.

[211] H. von Seggern. A new model of isothermal charge transport for nenegative corona-charged Teflon. *J. Appl. Phys.*, 50:7039–7043, 1979.

[212] J. A. Małecki. Electrical conductivity and electret stability. Why electrets are so stable? In X Zhongfu and Z Hongyan, editors, *9th Int. Symp. Electrets (ISE 9) Proc.* IEEE, 1996.

[213] J. A. Małecki. Linear decay of charge in electrets. *Phys. Rev. B*, 59: 9954–9960, 1999.

[214] T. A. Yovcheva, G. A. Mekishev, and A. T. Marinov. A percolation theory analysis of surface potential decay related to corona charged polypropylene (PP) electrets. *J. Phys. Condens. Matter*, 16:455–464, 2004.

[215] Y I Kuzmin. Charge transport, adsorption and percolation transitions on electrified surface. In A A Konsta, A Vassilikou-Dova, and K Vartzeli-Nikaki, editors, *10th Int. Symp. Electrets (ISE 10). Proc. (Cat. No.99 CH36256)*. IEEE, 1999.

[216] W. Reichstein, L. Sommer, S. Veziroglu, S. Sayin, S. Schröder, Y. K. Mishra, I. E. Saygili, Y. Acil, J. Wiltfang, A. Gülses, O. C. Aktas, and F. Faupel. Functionalization of Polylactic Acid-Marine Algae Composite Patch by initiated Chemical Vapor Deposition for Enhanced Osteoblast Proliferation. *Submitt. Manuscr.*, 2020.

[217] A. Liu, E. Goktekin, and K. K. Gleason. Cross-linking and ultrathin grafted gradation of fluorinated polymers synthesized via initiatech chemical vapor deposition to prevent surface reconstruction. *Langmuir*, 30:14189–14194, 2014.

[218] A. T. Paxson, J. L. Yagüe, K. K. Gleason, and K. K. Varanasi. Stable Dropwise Condensation for Enhancing Heat Transfer via the Initiated Chemical Vapor Deposition (iCVD) of Grafted Polymer Films. *Adv. Mater.*, 26(3):418–423, jan 2014.

[219] R. S. McDonald. Review: infrared spectrometry. *Anal. Chem.*, 58(9): 1906–1925, aug 1986.

[220] J. J. Workman. Review of Process and Non-invasive Near-Infrared and Infrared Spectroscopy: 1993–1999. *Appl. Spectrosc. Rev.*, 34(1-2):1–89, jul 1999.

[221] A. A. Michelson. The relative motion of the Earth and of the luminiferous ether. *Am. J. Sci.*, s3-22(128):120–129, aug 1881.

[222] John R. Ferraro and K. Krishnan, editors. *Practical Fourier Transform Infrared Spectroscopy*. Elsevier, 1990.

[223] Z. Movasaghi, S. Rehman, and I. ur Rehman. Fourier Transform Infrared (FTIR) Spectroscopy of Biological Tissues. *Appl. Spectrosc. Rev.*, 43(2): 134–179, feb 2008.

[224] G. Socrates. *Infrared and Raman Characteristic Group Frequencies: Tables and Charts*. John Wiley & Sons Ltd, Chichester, England, 3rd edition, 2004.

[225] G. Greczynski and L. Hultman. X-ray photoelectron spectroscopy: Towards reliable binding energy referencing. *Prog. Mater. Sci.*, 107:100591, jan 2020.

[226] C. S. Fadley. X-ray photoelectron spectroscopy: Progress and perspectives. *J. Electron Spectros. Relat. Phenomena*, 178-179:2–32, may 2010.

[227] P. S. Bagus, E. S. Ilton, and C. J. Nelin. The interpretation of XPS spectra: Insights into materials properties. *Surf. Sci. Rep.*, 68(2):273–304, jun 2013.

[228] C. J. Powell. Improvements in the Reliability of X-ray Photoelectron Spectroscopy for Surface Analysis. *J. Chem. Educ.*, 81(12):1734, dec 2004.

[229] L.M. Malard, M.A. Pimenta, G. Dresselhaus, and M.S. Dresselhaus. Raman spectroscopy in graphene. *Phys. Rep.*, 473(5-6):51–87, apr 2009.

[230] K. Kneipp, H. Kneipp, I. Itzkan, R. R. Dasari, and M. S. Feld. Ultrasensitive Chemical Analysis by Raman Spectroscopy. *Chem. Rev.*, 99(10):2957–2976, oct 1999.

[231] J. Schwan, S. Ulrich, V. Batori, H. Ehrhardt, and S. R. P. Silva. Raman spectroscopy on amorphous carbon films. *J. Appl. Phys.*, 80(1):440–447, jul 1996.

[232] A. El-Aneed, A. Cohen, and J. Banoub. Mass Spectrometry, Review of the Basics: Electrospray, MALDI, and Commonly Used Mass Analyzers. *Appl. Spectrosc. Rev.*, 44(3):210–230, apr 2009.

[233] A. Somogyi. Mass spectrometry instrumentation and techniques. In *Med. Appl. Mass Spectrom.*, chapter 6, pages 93–140. Elsevier, 2008.

[234] W. G. Bley. Quantitative measurements with quadrupole mass spectrometers: important specifications for reliable measurements. *Vacuum*, 38(2): 103–109, jan 1988.

[235] U. Boesl. Time-of-flight mass spectrometry: Introduction to the basics. *Mass Spectrom. Rev.*, 36(1):86–109, jan 2017.

[236] K. F. Medzihradszky, J. M. Campbell, M. A. Baldwin, A. M. Falick, P. Juhasz, M. L. Vestal, and A. L. Burlingame. The Characteristics of Peptide Collision-Induced Dissociation Using a High-Performance MALDI-TOF/TOF Tandem Mass Spectrometer. *Anal. Chem.*, 72(3):552–558, feb 2000.

[237] R. E. Ellefson. Methods for in situ QMS calibration for partial pressure and composition analysis. *Vacuum*, 101:423–432, mar 2014.

[238] R. Mutschler, W. Luo, E. Moioli, and A. Züttel. Fast real time and quantitative gas analysis method for the investigation of the CO 2 reduction reaction mechanism. *Rev. Sci. Instrum.*, 89(11):114102, nov 2018.

[239] D.E. Aspnes. Spectroscopic ellipsometry — Past, present, and future. *Thin Solid Films*, 571:334–344, nov 2014.

[240] S. Kohli, C. D. Rithner, P. K. Dorhout, A. M. Dummer, and C. S. Menoni. Comparison of nanometer-thick films by x-ray reflectivity and spectroscopic ellipsometry. *Rev. Sci. Instrum.*, 76(2):023906, feb 2005.

[241] H. von Seggern. Identification of TSC peaks and surface-voltage stability in Teflon FEP. *J. Appl. Phys.*, 50(4):2817–2821, apr 1979.

[242] T. Young. III. An essay on the cohesion of fluids. *Philos. Trans. R. Soc. London*, 95:65–87, dec 1805.

[243] P. Dimitrakellis and E. Gogolides. Hydrophobic and superhydrophobic surfaces fabricated using atmospheric pressure cold plasma technology: A review. *Adv. Colloid Interface Sci.*, 254:1–21, apr 2018.

[244] L. Feng, S. Li, Y. Li, H. Li, L. Zhang, J. Zhai, Y. Song, B. Liu, L. Jiang, and D. Zhu. Super-Hydrophobic Surfaces: From Natural to Artificial. *Adv. Mater.*, 14(24):1857–1860, dec 2002.

[245] O. E. Mogensen. *Positron Annihilation in Chemistry*, volume 58 of *Springer Series in Chemical Physics*. Springer Berlin Heidelberg, Berlin, Heidelberg, 1995.

[246] H. H. Yin, Y. Zejie, T. Shibiao, and H. Huan. Investigation of SPPO Membranes by Positron Annihilation Lifetime Spectroscopy. *Plasma Sci. Technol.*, 8(5):573–576, sep 2006.

[247] E. E. Abdel-Hady, H. F. M. Mohamed, and M. R. M. El-Sharkawy. Temperature effect on free volume of polymethylpentene studied by positron annihilation technique. *Phys. status solidi*, 6(11):2420–2422, nov 2009.

[248] Y. C. Jean, P. E. Mallon, and D. M. Schrader. *Principles and Applications of Positron and Positronium Chemistry*. World Scientific, apr 2003.

[249] P. Kirkegaard, J. V. Olsen, M. M. Eldrup, and N. J. Pedersen. PALSfit: A computer program for analysingpositron lifetime spectra. Technical report, Danmarks Tekniske Universitet, Risø Nationallaboratoriet for Bæredygtig Energi. Denmark. Forskningscenter Risoe. Risoe-R, No. 1652(EN), Risø, DK, 2009.

[250] J. W. Cahn and J. E. Hilliard. Free energy of a nonuniform system. I. interfacial free energy. *J. Chem. Phys.*, 28:258–267, 1958.

[251] J W Cahn. On spinodal decomposition. *Acta Met.*, 9:795–801, 1961.

[252] D. J. Eyre. Unconditionally Gradient Stable Time Marching the Cahn-Hilliard Equation. In *MRS Proc.*, volume 529, page 39, feb 1998.

[253] M. Valiev, E. J. Bylaska, N. Govind, K. Kowalski, T. P. Straatsma, H. J. J. Van Dam, D. Wang, J. Nieplocha, E. Apra, T. L. Windus, and W. A. de Jong. NWChem: A comprehensive and scalable open-source solution for large scale molecular simulations. *Comput. Phys. Commun.*, 181(9): 1477–1489, sep 2010.

[254] A. D. Becke. Density-functional exchange-energy approximation with correct asymptotic behavior. *Phys. Rev. A*, 38(6):3098–3100, sep 1988.

[255] C. Lee, W. Yang, and R. G. Parr. Development of the Colle-Salvetti correlation-energy formula into a functional of the electron density. *Phys. Rev. B*, 37(2):785–789, jan 1988.

[256] A. D. Becke. Density-functional thermochemistry. III. The role of exact exchange. *J. Chem. Phys.*, 98(7):5648–5652, apr 1993.

[257] C. Møller and M. S. Plesset. Note on an Approximation Treatment for Many-Electron Systems. *Phys. Rev.*, 46(7):618–622, oct 1934.

[258] T. H. Dunning. Gaussian basis sets for use in correlated molecular calculations. I. The atoms boron through neon and hydrogen. *J. Chem. Phys.*, 90 (2):1007–1023, jan 1989.

[259] G. Schaftenaar and J. Noordik. Molden: a pre- and post-processing program for molecular and electronic structures. *J. Comput. Aided Mol. Des.*, 14: 123–134, 2000.

[260] G. Schaftenaar, E. Vlieg, and G. Vriend. Molden 2.0: quantum chemistry meets proteins. *J. Comput. Aided. Mol. Des.*, 31(9):789–800, sep 2017.

[261] H. G. Pryce Lewis, N. P. Bansal, A. J. White, and E. S. Handy. HWCVD of polymers: Commercialization and scale-up. *Thin Solid Films*, 517(12): 3551–3554, apr 2009.

[262] M. Ng, D. K.W. Mok, J. M. Dyke, and E. P.F. Lee. Decomposition reactions of hexafluoropropylene oxide (HFPO): Rate coefficients calculated at different temperatures using ab initio and DFT reaction paths. *J. Fluor. Chem.*, 159:29–37, mar 2014.

[263] D. L. S. Brahms and W. P. Dailey. Fluorinated Carbenes. *Chem. Rev.*, 96 (5):1585–1632, jan 1996.

[264] R. Craig Kennedy and J. B. Levy. The pyrolysis of hexafluoropropylene oxide. *J. Fluor. Chem.*, 7(1-3):101–114, jan 1976.

[265] W. Mahler and P. R. Resnick. The reversible difluorocarbene elimination from hexafluoropropylene epoxide. *J. Fluor. Chem.*, 3(3-4):451–452, jan 1974.

[266] P. J. Krusic, D. C. Roe, and B. E. Smart. Kinetics of Hexafluoropropylene Oxide Pyrolysis Studied by Gas-Phase NMR. Kinetic Measurements Made Easy. *Isr. J. Chem.*, 39(2):117–123, 1999.

[267] R. Kacprzyk and J. Ziaja. Properties of corona charged plasma vapour deposited PTFE film. *J. Electrostat.*, 40-41:319–323, 1997.

[268] D. T. Morrison and T. Robertson. R.F. sputtering of plastics. *Thin Solid Films*, 15:87–101, 1973.

[269] U. Schürmann, H. Takele, V. Zaporojtchenko, and F. Faupel. Optical and electrical properties of polymer metal nanocomposites prepared by magnetron co-sputtering. *Thin Solid Films*, 515(2):801–804, oct 2006.

[270] U. Schürmann, W. Hartung, H. Takele, V. Zaporojtchenko, and F. Faupel. Controlled syntheses of Ag–polytetrafluoroethylene nanocomposite thin films by co-sputtering from two magnetron sources. *Nanotechnology*, 16(8): 1078–1082, aug 2005.

[271] N. Amyot, J. E. Klemberg-Sapieha, M. R. Wertheimer, Y. Segui, and M. Moisan. Electrical and structural studies of plasma-polymerized fluorocarbon films. *IEEE Trans. Electr. Insul.*, 27(6):1101–1107, 1992.

[272] U. Hetzler and E. Kay. Conduction mechanism in plasma-polymerized tetrafluoroethylene films. *J. Appl. Phys.*, 49:5617–5623, 1978.

[273] R. Schwödiauer, S. Bauer-Gogonea, S. Bauer, J. Heitz, E. Arenholz, and D. Bäuerle. Charge stability of pulsed-laser deposited polytetrafluoroethylene film electrets. *Appl. Phys. Lett.*, 73:2941–2943, 1998.

[274] K. K. S. Lau and K. K. Gleason. Pulsed plasma enhanced and hot filament chemical vapor deposition of fluorocarbon films. *J. Fluor. Chem.*, 104(1): 119–126, jun 2000.

[275] E. Ölçeroğlu, C.-Y. Hsieh, M. M. Rahman, K. K. S. Lau, and M. McCarthy. Full-Field Dynamic Characterization of Superhydrophobic Condensation on Biotemplated Nanostructured Surfaces. *Langmuir*, 30(25):7556–7566, jul 2014.

[276] E. D. Laird, R. K. Bose, H. Qi, K. K. S. Lau, and C. Y. Li. Electric Field-Induced, Reversible Lotus-to-Rose Transition in Nanohybrid Shish Kebab Paper with Hierarchical Roughness. *ACS Appl. Mater. Interfaces*, 5 (22):12089–12098, nov 2013.

[277] J. Lin, S. K. Murthy, Bradley D. Olsen, Gleason K. K, and A. M. Klibanov. Making thin polymeric materials, including fabrics, microbicidal and also water-repellent. *Biotechnol. Lett.*, 25:1661–1665, 2003.

[278] H. J. Qi, K. B. K. Teo, K. K. S. Lau, M. C. Boyce, W. I. Milne, J. Robertson, and K. K. Gleason. Determination of mechanical properties of carbon nanotubes and vertically aligned carbon nanotube forests using nanoindentation. *J. Mech. Phys. Solids*, 51(11-12):2213–2237, nov 2003.

[279] K. K. S. Lau, J. Bico, K. B. K. Teo, M. Chhowalla, G. A. J. Amaratunga, W. I. Milne, G. H. McKinley, and K. K. Gleason. Superhydrophobic Carbon Nanotube Forests. *Nano Lett.*, 3(12):1701–1705, dec 2003.

[280] C. J. Peacock, P. J. Hendra, H. A. Willis, and M. E. A. Cudby. Raman spectrum and vibrational assignment for poly(tetrafluoroethylene). *J. Chem. Soc. A Inorganic, Phys. Theor.*, page 2943, 1970.

[281] J. Mihály, S. Sterkel, H. M. Ortner, L. Kocsis, L. Hajba, É. Furdyga, and J. Mink. FTIR and FT-Raman Spectroscopy Study on Polymer Based High Pressure Digestion Vessels. *Croat. Chem. Acta*, 79:497–501, 2006.

[282] J. F. Rabolt and B. Fanconi. Raman Scattering from Finite Polytetrafluoroethylene Chains and a Highly Oriented TFE-HFP Copolymer Monofilament. *Macromolecules*, 11(4):740–745, jul 1978.

[283] K. Uchinokura, T. Sekine, and E. Matsuura. Raman scattering by silicon. *Solid State Commun.*, 11(1):47–49, jul 1972.

[284] J. P. Russell. Raman Scattering In Silicon. *Appl. Phys. Lett.*, 6(11):223–224, jun 1965.

[285] G. Socrates. Organic Halogen Compounds. In *Infrared Raman Charact. Gr. Freq. Tables Charts*, chapter 15, pages 198–208. John Wiley & Sons Ltd, Chichester, England, 3rd edition, 2004.

[286] D. Rychkov, R. Gerhard, A. Kuznetsov, and A. Rychkov. Modeling isothermal charge decay of modified polytetrafluoroethylene electrets from their thermally stiumulated discharge. In *IEEE Conf. Electr. Insul. Dielectr. Phenom.* IEEE, 2016.

[287] E. N. Brown and D. M. Dattelbaum. The role of crystalline phase on fracture and microstructure evolution of polytetrafluoroethylene (PTFE). *Polymer (Guildf).*, 46:3056–3068, 2005.

[288] A. Thyssen, K. Almdal, and E. V. Thomsen. Electret stability related to the crystallinity in polypropylene. *IEEE Trans. Dielectr. Electr. Insul.*, 24: 3038–3046, 2017.

[289] J. G. Simmons, G. W. Taylor, and M. C. Tam. Thermally stimulated currents in semiconductors and insulators having arbitrary trap distributions. *Phys. Rev. B*, 7:3714–3719, 1973.

[290] A. A. Rychkov, G. H. Cross, and M. G. Conchart. Charge relaxation in structures containing non-polar polymer-metal interfaces. *J. Phys. D Appl. Phys.*, 25:986–991, 1992.

[291] J G Simmons and G. W. Taylor. High-field isothermal currents and thermally stimulated currents in insulators having discrete trapping levels. *Phys. Rev. B*, 5:1619–1629, 1972.

[292] J G Simmons and M. C. Tam. Theory of isothermal currents and the direct determination of trap parameters in semiconductors and insulators containing arbitrary trap distributions. *Phys. Rev. B*, 7:3706–3713, 1973.

[293] D. Cubero, G. Marcelli, and N. Quirke. Electronic states of excess electrons in polyethylene. In *Proc. IEEE Conf. Electr. Insul. Dielectr. Phenom.*, pages 430–433. IEEE, 2002.

[294] J.-Q. Huang, W.-D. Meng, and F.-L. Qing. Synthesis and repellent properties of vinylidene fluoride-containing polyacrylates. *J. Fluor. Chem.*, 128: 1469–1477, 2007.

[295] G. Socrates. Alkenes, Oximes, Imines, Amidines, Azo Compounds: C=C, C=N, N=N Groups. In *Infrared Raman Charact. Gr. Freq. Tables Charts*, chapter 3, pages 68–81. John Wiley & Sons Ltd, Chichester, England, 3rd edition, 2004.

[296] G. Socrates. The Carbonyl Group: C=O. In *Infrared Raman Charact. Gr. Freq. Tables Charts*, chapter 10, pages 115–156. John Wiley & Sons Ltd, Chichester, England, 3rd edition, 2004.

[297] G. Socrates. Alkane Group Residues: C-H Group. In *Infrared Raman Charact. Gr. Freq. Tables Charts*, chapter 2, pages 50–67. John Wiley & Sons Ltd, Chichester, England, 3rd edition, 2004.

[298] G. Socrates. Hydroxyl Group Compunds: O-H Group. In *Infrared Raman Charact. Gr. Freq. Tables Charts*, chapter 6, pages 94–100. John Wiley & Sons Ltd, Chichester, England, 3rd edition, 2004.

[299] G. Socrates. Aromatic compounds. In *Infrared Raman Charact. Gr. Freq. Tables Charts*, chapter 11, pages 157–167. John Wiley & Sons Ltd, Chichester, England, 3rd edition, 2004.

[300] G. F. J. Garlick and A. F. Gibson. The Electron Trap Mechanism of Luminescence in Sulphide and Silicate Phosphors. *Proc. Phys. Soc.*, 60(6): 574–590, jun 1948.

[301] J. A. Carr and S. Chaudhary. The identification, characterization and mitigation of defect states in organic photovoltaic devices: a review and outlook. *Energy Environ. Sci.*, 6(12):3414, 2013.

[302] Z. Fang, L. Shan, T.E . Schlesinger, and A. G. Milnes. Study of defects in LEC-grown undoped SI-GaAs by thermally stimulated current spectroscopy. *Mater. Sci. Eng. B*, 5(3):397–408, feb 1990.

[303] M. Mintken, M. Schweichel, S. Schröder, S. Kaps, J. Carstensen, Y. K. Mishra, T. Strunskus, F. Faupel, and R. Adelung. Nanogenerator and piezotronic inspired concepts for energy efficient magnetic field sensors. *Nano Energy*, 56:420–425, feb 2019.

[304] J. Reermann, P. Durdaut, S. Salzer, T. Demming, A. Piorra, E. Quandt, N. Frey, M. Höft, and G. Schmidt. Evaluation of magnetoelectric sensor systems for cardiological applications. *Measurement*, 116:230–238, feb 2018.

[305] H. Greve, E. Woltermann, R. Jahns, S. Marauska, B. Wagner, R. Knöchel, M. Wuttig, and E. Quandt. Low damping resonant magnetoelectric sensors. *Appl. Phys. Lett.*, 97(15):152503, oct 2010.

[306] M. S. Hawley and F. F. Romanow. Electret transducer equations by Lagrange's equation. *J. Acoust. Soc. Am.*, 64:694–696, 1978.

[307] N. J. Trujillo, Q. Wu, and K. K. Gleason. Ultralow dielectric constant tetravinyltetramethylcyclotetrasiloxane films deposited by initiated chemical vapor deposition (iCVD). *Adv. Funct. Mater.*, 20:607–616, 2010.

[308] G. Socrates. Organic Silicon Compounds. In *Infrared Raman Charact. Gr. Freq. Tables Charts*, chapter 18, pages 241–246. John Wiley & Sons Ltd, Chichester, England, 3rd edition, 2004.

[309] J. Coates. Interpretation of Infrared Spectra, A Practical Approach. In *Encycl. Anal. Chem.* John Wiley & Sons, Ltd, Chichester, UK, sep 2006.

[310] W.S. O'Shaughnessy, D. J. Edell, and K. K. Gleason. Initiated chemical vapor deposition of a siloxane coating for insulation of neural probes. *Thin Solid Films*, 517(12):3612–3614, apr 2009.

[311] R. Wu, J. Yang, J. Xiong, P. Liu, C. Zhou, H. Huang, Y. Gao, and B. Yang. Efficient electron-blocking layer-free planar heterojunction perovskite solar cells with a high open-circuit voltage. *Org. Electron.*, 26:265–272, nov 2015.

[312] M. Morsli, J.C. C Bernède, L. Cattin, F. Dahou, and A. Khelil. On the Exciton Blocking Layer at the Interface Organic/Cathode in Multiheterojunction Organic Solar Cells. *Energy Procedia*, 31:74–80, 2012.

[313] X. Zhang and G. M. Sessler. Charge dynamics in silicon nitride/silicon oxide double layers. *Appl. Phys. Lett.*, 78(18):2757–2759, apr 2001.

[314] V. Leonov and C. Van Hoof. Multilayer Inorganic Electrets with SiO2 and Si3N3. *Smart Mater. Res.*, 2012:1–9, 2012.

[315] J. R. Werber, C. O. Osuji, and M. Elimelech. Materials for next-generation desalination and water purification membranes. *Nat. Rev. Mater*, 1:1–15, 2016.

[316] N. B. McKeown and P. M. Budd. Polymers of intrinsic microporosity (PIMs): Organic materials for membrane separations and hydrogen storage. *Chem. Soc. Rev.*, 35:675–683, 2006.

[317] R. O. A. Rahman, H. A. Ibrahium, and Y.-T. Hung. Liquid radioactive wastes treatment: A review. *Water*, 3:551–565, 2011.

[318] A. Dyer and K. Y. Mikhail. The use of zeolites for the treatment of radioactive waste. *Miner. Mag.*, 49:203–210, 1985.

[319] P. Kaur, J. T. Hupp, and S. T. Nguyen. Porous organic polymers in catalysis: Oportunities and challenges. *ACS Catal.*, 1:819–835, 2011.

[320] S. Walheim, E. Schäffer, J. Mlynek, and U. Steiner. Nanophase-separated polymer films as high-performance antireflection coatings. *Science (80-.).*, 283:520–522, 1999.

[321] A. Grill, S. M. Gates, T. E. Ryan, S. V. Nguyen, and D. Priyadarshini. Progress in the development and understanding of advanced low k and ultralow k dielectrics for very large-scale integrated interconnects - State of the art. *Appl. Phys. Rev.*, 1:11306, 2012.

[322] N. Chaoui, M. Trunk, R. Dawson, J. Schmidt, and A. Thomas. Trends and challenges for microporous polymers. *Chem. Soc. Rev.*, 46:3302–3321, 2017.

[323] F. Svec and J. M. J. Frechet. New Designs of Macroporous Polymers and Supports: From Separation to Biocatalysis. *Science (80-.).*, 273(5272): 205–211, jul 1996.

[324] M. V. Badinger, M. E. McNeill, and N. B. Graham. Porogens in the preparation of microporous hydrogels based on poly(ethylene oxides). *Biomaterials*, 14:1059–1063, 1993.

[325] R. Tao and M. Anthamatten. Porous polymers by controlling phase separation during vapor deposition polymerization. *Macromol. Rapid. Commun.*, 34:1755–1760, 2013.

[326] R. Tao and M. Anthamatten. Quenching phase separation by vapor deposition polymerization. *Macromol. Mater. Eng.*, 301:99–109, 2016.

[327] A. L. Bertozzi, S. Esedoglu, and A. Gillette. Inpainting of binary images using the Cahn-Hilliard equation. *IEEE Trans. Image Process.*, 16:285–291, 2007.

[328] S. Zhou and M. Y. Wang. Multimaterial structural topology optimization with a generalized Cahn-Hilliard model of multiphase transition. *Struct. Multidisc. Optim.*, 33:89–111, 2007.

[329] R. Krause-Rehberg, S. Sachert, G. Brauer, A. Rogov, and K. Noack. EPOS—An intense positron beam project at the ELBE radiation source in Rossendorf. *Appl. Surf. Sci.*, 252(9):3106–3110, feb 2006.

[330] R. Krause-Rehberg, M. Jungmann, A. Krille, B. Werlich, A. Pohl, W. Anwand, G. Brauer, M. Butterling, H. Büttig, K. M. Kosev, J. Teichert, A. Wagner, and T. E. Cowan. Use of superconducting linacs for positron generation: the EPOS system at the Forschungszentrum Dresden-Rossendorf (FZD). In *J. Phys. Conf. Ser.*, volume 262, page 012003, jan 2011.

[331] A. Wagner, M. Butterling, M. O. Liedke, K. Potzger, and R. Krause-Rehberg. Positron annihilation lifetime and Doppler broadening spectroscopy at the ELBE facility. In *AIP Conf. Proc.*, page 040003, 2018.

[332] K. K. S. Lau. Growth Mechanism, Kinetics, and Molecular Weight. In K.K. Gleason, editor, *CVD Polym. – Fabr. Org. surfaces devices*, chapter 2, pages 15–44. Wiley-VCH, Weinheim, Germany, 1st edition, 2015.

[333] Z. A. Page, B. Narupai, C. W. Pester, R. Bou Zerdan, A. Sokolov, D. S. Laitar, S. Mukhopadhyay, S. Sprague, A. J. McGrath, J. W. Kramer, P. Trefonas, and C. J. Hawker. Novel Strategy for Photopatterning Emissive Polymer Brushes for Organic Light Emitting Diode Applications. *ACS Cent. Sci.*, 3(6):654–661, jun 2017.

[334] M. Mizukami, S. Cho, K. Watanabe, M. Abiko, Y. Suzuri, S. Tokito, and J. Kido. Flexible Organic Light-Emitting Diode Displays Driven by Inkjet-Printed High-Mobility Organic Thin-Film Transistors. *IEEE Electron Device Lett.*, 39(1):39–42, jan 2018.

[335] K. Fukuda, Y. Takeda, Y. Yoshimura, R. Shiwaku, L. T. Tran, T. Sekine, M. Mizukami, D. Kumaki, and S. Tokito. Fully-printed high-performance organic thin-film transistors and circuitry on one-micron-thick polymer films. *Nat. Commun.*, 5(1):4147, sep 2014.

[336] K. Fukuda, T. Minamiki, T. Minami, M. Watanabe, T. Fukuda, D. Kumaki, and S. Tokito. Printed Organic Transistors with Uniform Electrical Performance and Their Application to Amplifiers in Biosensors. *Adv. Electron. Mater.*, 1(7):1400052, jul 2015.

[337] Y. Kimura, T. Nagase, T. Kobayashi, A. Hamaguchi, Y. Ikeda, T. Shiro, K. Takimiya, and H. Naito. Soluble Organic Semiconductor Precursor with Specific Phase Separation for High-Performance Printed Organic Transistors. *Adv. Mater.*, 27(4):727–732, jan 2015.

[338] Z. A. Lamport, H. F. Haneef, S. Anand, M. Waldrip, and O. D. Jurchescu. Tutorial: Organic field-effect transistors: Materials, structure and operation. *J. Appl. Phys.*, 124(7):071101, aug 2018.

[339] L.-H. Xie, Q.-D. Ling, X.-Y. Hou, and W. Huang. An Effective Friedel-Crafts Postfunctionalization of Poly(N -vinylcarbazole) to Tune Carrier Transportation of Supramolecular Organic Semiconductors Based on π-Stacked Polymers for Nonvolatile Flash Memory Cell. *J. Am. Chem. Soc.*, 130(7):2120–2121, feb 2008.

[340] M. Kang, D. Khim, W.-T. Park, J. Kim, J. Kim, Y.-Y. Noh, K.-J. Baeg, and D.-Y. Kim. Synergistic High Charge-Storage Capacity for Multi-level Flexible Organic Flash Memory. *Sci. Rep.*, 5(1):12299, dec 2015.

[341] Y.-J. Cheng, S.-H. Yang, and C.-S. Hsu. Synthesis of Conjugated Polymers for Organic Solar Cell Applications. *Chem. Rev.*, 109(11):5868–5923, nov 2009.

[342] J.-T. Chen and C.-S. Hsu. Conjugated polymer nanostructures for organic solar cell applications. *Polym. Chem.*, 2(12):2707, 2011.

[343] B. J. Tremolet de Villers, K. A. O'Hara, D. P. Ostrowski, P. H. Biddle, S. E. Shaheen, M. L. Chabinyc, D. C. Olson, and N. Kopidakis. Removal of Residual Diiodooctane Improves Photostability of High-Performance Organic Solar Cell Polymers. *Chem. Mater.*, 28(3):876–884, feb 2016.

[344] H. Yoo, H. Park, S. Yoo, S. On, H. Seong, S. G. Im, and J.-J. Kim. Highly stacked 3D organic integrated circuits with via-hole-less multilevel metal interconnects. *Nat. Commun.*, 10(1):2424, dec 2019.

[345] B. Reeja-Jayan, P. Moni, and K. K. Gleason. Synthesis of Insulating and Semiconducting Polymer Films via Initiated Chemical Vapor Deposition. *Nanosci. Nanotechnol. Lett.*, 7(1):33–38, jan 2015.

[346] P.J. Linstrom and W.G. Mallard, editors. *NIST Chemistry WebBook, NIST Standard Reference Database Number 69*. National Institute of Standards and Technology, Gaithersburg, USA, 2018.

[347] G. Socrates. Triple Bond Compounds. In *Infrared Raman Charact. Gr. Freq. Tables Charts*, chapter 4, pages 82–87. John Wiley & Sons Ltd, Chichester, England, 3rd edition, 2004.

[348] L. Li and C. Ortiz. Pervasive nanoscale deformation twinning as a catalyst for efficient energy dissipation in bioceramic armour. *Nat. Mater.*, 13: 501–507, 2014.

[349] L. Li and C. Ortiz. Biological design for simultaneous optical transparency and mechanical robustness in the shell of placuna placenta. *Adv. Mater.*, 25:2344–2350, 2013.

[350] E. A. Zimmermann, B. Gludovatz, E. Schaible, N. K. N. Dave, W. Yang, M. A. Meyers, and R. O. Ritchie. Mechanical adaptability of the Bouligand-type structure in natural dermal armour. *Nat. Commun.*, 4:2634, 2013.

[351] R. O. Ritchie. Armoured oyster shells. *Nat. Mater.*, 13:435–437, 2014.

[352] A. Miserez, T. Schneberk, C. Sun, F. W. Zok, and J. H. Waite. The transition from stiff to compliant materials in squid beaks. *Science (80-.).*, 319:1816–1819, 2008.

[353] J. Cai, J. P. Townsend, T. C. Dodson, P. A. Heiney, and A. M. Sweeney. Eye patches: Protein assembly of index-gradient squid lens. *Science (80-.).*, 357:564–569, 2017.

[354] C. E. Jones, D. A. Atchison, R. Meder, and J. M. Pope. Refractive index distribution and optical properties of the isolated human lens measured using magnetic resonance imaging (MRI). *Vis. Res.*, 45:2352–2366, 2005.

[355] M. J. Harrington and J. H. Waite. How nature modulates a fiber's mechanical properties: Mechanically distinct fibers drawn from natural mesogenic block copolymer variants. *Adv. Mater.*, 21:440–444, 2009.

[356] X. Li, J. Xie, J. Lipner, X. Yuan, S. Thomopoulos, and Y. Xia. Nanofiber scaffolds with gradations in mineral content for mimicking the tendon-to-bone insertion site. *Nano Lett.*, 9:2763–2768, 2009.

[357] K. U. Claussen, T. Scheibel, H.-W. Schmidt, and R. Giesa. Polymer gradient materials: Can nature teach us new tricks? *Macromol. Mater. Eng.*, 297: 938–957, 2012.

[358] A. Seidi, M. Ramalingam, E. Elloumi-Hannachi, S. Ostrovidov, and A. Khademhosseini. Gradient biomaterials for soft-to-hard interface tissue engineering. *Acta Biomater.*, 7:1441–1451, 2011.

[359] M. L. K. Tate, M. Detamore, J. R. Capadona, A. Wolley, and U. Knothe. Engineering and commercialization of human-device interfaces, from bone to brain. *Biomaterials*, 95:35–46, 2016.

[360] R. Langer and D. A. Tirrell. Designing materials for biology and medicine. *Nature*, 428:487–492, 2004.

[361] X Luo. Subwavelength artificial structures: Opening a new era for engineering optics. *Adv. Mater.*, page 1804680, 31.

[362] E. Rieger, J. Blankenburg, E. Grune, M. Wagner, K. Landfester, and F. R. Wurm. Controlling the polymer microstructure in anionic polymerization by compartmentalization. *Angew. Chem. Int. Ed.*, 57:2483–2487, 2018.

[363] Y. Ogura, T. Terashima, and M. Sawamoto. Synthesis of fluorinated gradient copolymers via in situ transesterfication with fluoroalcohols in tandem living radical polymerization. *Polym. Chem.*, 8:2299–2308, 2017.

[364] N. Wang, B. Szostek, R. C. Buck, P. W. Folsom, L. M. Sulecki, and J. T. Gannon. 8-2 fluorotelmor alcohol aerobic soil biodegradation: Pathways, metabolites, and metabolite yields. *Cemosphere*, 75:1089–1096, 2009.

List of Publications

M. H. Burk, D. Langbehn, G. Hernández Rodríguez, W. Reichstein, J. Drewes, **S. Schröder**, S. Rehders, T. Strunskus, R. Herges and F. Faupel. Synthesis and Investigation of a Photoswitchable Copolymer Deposited via Initiated Chemical Vapor Deposition for Application in Organic Smart Surfaces. *ACS Appl. Polym. Mater.*, 3:1445-1456, 2021.

S. Schröder, A. M. Hinz, T. Strunskus, and F. Faupel. Molecular insight into real-time reaction kinetics of free radical polymerization from the vapor phase by in-situ mass spectrometry. *J. Phys. Chem. A*, 125:1661-1667, 2021.

W. Reichstein, L. Sommer, S. Veziroglu, S. Sayin, **S. Schröder**, Y. K. Mishra, I. E. Saygili, Y. Acil, J. Wiltfang, A. Gülses, O. C. Aktas, and F. Faupel. Functionalization of polylactic acid-marine algae composite patch by initiated chemical vapor deposition for enhanced osteoblast proliferation. *Polymers*, 13:186 2021.

S. Sayin, T. Kohlhaas, S. Veziroglu, E. Ş. Okudan, M. Naz, **S. Schröder**, E. I. Saygili, Y. Açil, F. Faupel, J. Wiltfang, O. C. Aktas and A. Gülses. Marine Algae-PLA composites as de novo alternative to porcine derived collagen membranes. *Mater. Today Chem.*, 17:100276, 2020.

S. Sayin, T. Kohlhaas, S. Veziroglu, E. Ş. Okudan, M. Naz, **S. Schröder**, E. I. Saygili, Y. Açil, F. Faupel, J. Wiltfang, O. C. Aktas and A. Gülses. Marine Algae-PLA composites as de novo alternative to porcine derived collagen membranes. *Mater. Today Chem.*, 17:100276, 2020.

S. Schröder, O. Polonskyi, T. Strunskus and F. Faupel. Nanoscale gradient copolymer films via single-step deposition from the vapor phase. *Mater. Today*, 37:35-43, 2020.

M. H. Burk, **S. Schröder**, W. Moormann, D. Langbehn, T. Strunskus, R. Herges and F. Faupel. Fabrication of diazocine-based photochromic organic thin films via initiated chemical vapor deposition. *Macromolecules*, 53:1164-1170, 2020.

M. Scharnberg, S. Rehders, Ö. Adiyaman, **S. Schröder**, T. Strunskus and F. Faupel. Evaporated electret films with superior charge stability based on Teflon AF 2400. *Org. Electron.*, 70:167-171, 2019.

S. Schröder, T. Strunskus, S. Rehders, K. K. Gleason, and F. Faupel. Tunable poly(tetrafluoroethylene) electret films with extraordinary charge stability synthesized by initiated chemical vapor deposition for organic electronics applications. *Sci. Rep.*, 9:2237, 2019.

O. C. Aktas, **S. Schröder**, S. Veziroglu, M. Z. Ghori, A. Haidar, O. Polonskyi, T. Strunskus, K. K. Gleason and F. Faupel. Superhydrophobic 3D porous PTFE/TiO_2 hybrid structures. *Adv. Mater. Interfaces*, 6:1801967, 2019.

M. Mintken, M. Schweichel, **S. Schröder**, S. Kaps, J. Carstensen, Y. K. Mishra, T. Strunskus, F. Faupel, and R. Adelung. Nanogenerator and piezotronic inspired concepts for energy efficient magnetic field sensors. *Nano Energy*, 56:420-425, 2019.

M. Wang, A. Liu, **S. Schröder**, J. Zhao and K. K. Gleason. Nanoscale ion-gel films as gate insulator material retaining high capacitance at megahertz switching frequency enabled by initiated chemical vapor deposition (iCVD). In *Abstracts of papers of the american chemical society*, 255, American Chemical Society, 2018.

R. E. Hirschberg, M. Scharnberg, **S. Schröder**, S. Rehders, T. Strunskus and F. Faupel. Electret films with extremely high charge stability prepared by thermal evaporation of Teflon AF. *Org. Electron*, 57:146-150, 2018.

I. Hölken, **S. Schröder** and R. Adelung. Characterisation of silicon nanolayers deposited by plasma enhanced chemical vapor deposition on 3-D ZnO Templates for Hollow Silicon. In *3rd International Conference on Nanotechnologies and Biomedical Engineering*, pages 30-34, Springer, Singapore, 2016.

Currently submitted manuscripts:

S. Schröder, W. Reichstein, T. Strunskus, and F. Faupel. Influence of different end groups on the electret effect in poly(ethylene glycol dimethacrylate) thin films deposited from the vapor phase. *Submitted manuscript*, 2020.

Acknowledgements

First of all I would like to express my deepest gratitude to Prof. Dr. Franz Faupel for giving me the opportunity to work on this interesting topic. I also thank him for all the things he taught me, his friendly personality and the enthusiasm for new ideas he always shared. I would also like to greatly thank Prof. Dr. Rainer Adelung for agreeing to be the second reviewer for this work and all the things I have learned from him over the years. My greatest thanks also include Prof. Dr. Karen K. Gleason for the great three months I was able to spend in her group and all the iCVD related abilities I was able to learn from her. I would also like to thank her entire group for the friendly atmosphere and especially Dr. Andong Liu for all the helpful discussions and conversations. In addition I would like to thank Dr. Thomas Strunskus, Prof. Dr. Klaus Rätzke and Dr. Alexander Vahl for proofreading this thesis and for all the helpful discussions and ideas over the years. Furthermore I thank Prof. Dr. Klaus Rätzke, Dr. Christian Orth and Dr. Maik Butterling for their great help with the PALS measurements and the evaluation of the PALS data. I would also like to express my deepest gratitude to Stefan Rehders for his technical support and all the technical and vacuum related abilities he taught me. In this context, I would also like to express my deepest gratitude to Dr. Alexander M. Hinz for the abilities I learned from him with regard to vacuum systems. Furthermore I owe Peter Sommer a lot of thanks for all the computer based problems he helped me with and all the Linux related tricks he taught me. In addition I thank all members and all former members of the Chair for Multicomponent Materials: Prof. Dr. Cenk Aktas, Igor Barg, Maximilian Heiko Burk, Niko Carstens, Jonas Drewes, Prof. Dr. Mady Elbahri, Frowin Ellermann, Ron-Marco Friedrich, Dr. Muhammad Zubair Ghori, Dr. Björn Gojdka, Benthe Birger Grun, Nicole Gühlke, Simon Hagemann, Torge Hartig, Dr. Alexander Hinz, Sieglinde Kastaun, Katharina Klatt, Kerstin Meurisch, Dr. Christian Ohrt, Dr. Oleksandr Polonskyi, Prof. Dr. Klaus Rätzke, Stefan Rehders, Wiebke Reichstein, Dennis Reimann, Gabriel Hernández Rodriguez, Dr. Viktor Schneider, Josiah Ngenev Shondo, Dr. Brook Shurtleff, Peter Sommer, Benjamin Spetzler,

Dr. Thomas Strunskus, Dr. Alexander Vahl, Dr. Salih Veziroglu, Dr. Jan-Martin Wagner, Dr. Sebastian Zabel, Isabella Zech as well as the people of SFB 1261 and GRK 2154. Furthermore I want to thank Dr. Sören Kaps, Prof. Dr. Jeffrey McCord, Cai Müller, Prof. Dr. Stephan Wulfinghoff and Lukas Zimoch. Last but not least I would like to thank my family and friends who have supported me over the years.

Appendix A

A simplified approach to describe the exponential charge decay in electrets

Assuming a perpendicular geometry the current density ($\vec{j}$) simplifies to

$$j = -\frac{d\sigma}{dt}. \tag{1}$$

The symbol σ represents the surface charge of the electret. Using Ohm's law ($\vec{j} = G\vec{E_i}$) in equation 1 the equation

$$-\frac{d\sigma}{dt} = GE_i \tag{2}$$

is obtained. The symbols G and E_i represent the electrical conductivity and the electric field, respectively. The large air gap approximation $E_i = \frac{\sigma}{\varepsilon_0 \varepsilon_r}$ yields

$$-\frac{d\sigma}{dt} = G\frac{\sigma}{\varepsilon_0 \varepsilon_r}. \tag{3}$$

With $\frac{1}{\tau} = \frac{G}{\varepsilon_0 \varepsilon_r}$

$$-\frac{d\sigma}{dt} = \frac{1}{\tau}\,\sigma \tag{4}$$

The symbol τ represents the time constant. The solution of this differential equation is

$$\sigma = \sigma_0 \exp\left(\frac{-t}{\tau}\right). \tag{5}$$

Appendix B

Response time of butterfly valve

The following figures show the response time of the valve used for different flows and process pressures. Figure 1a and Figure 1b show the time from sending the controller signal to the correct process pressure for 40 Pa (Figure 1a) and for 50 Pa (Figure 1b). Figure 1c and Figure 1d show that in case of a flow interruption during a continuous flow process, the pressure in the reactor is kept constant. The process is then continued as a batch process. Due to the fast response time, switching takes place within a few seconds.

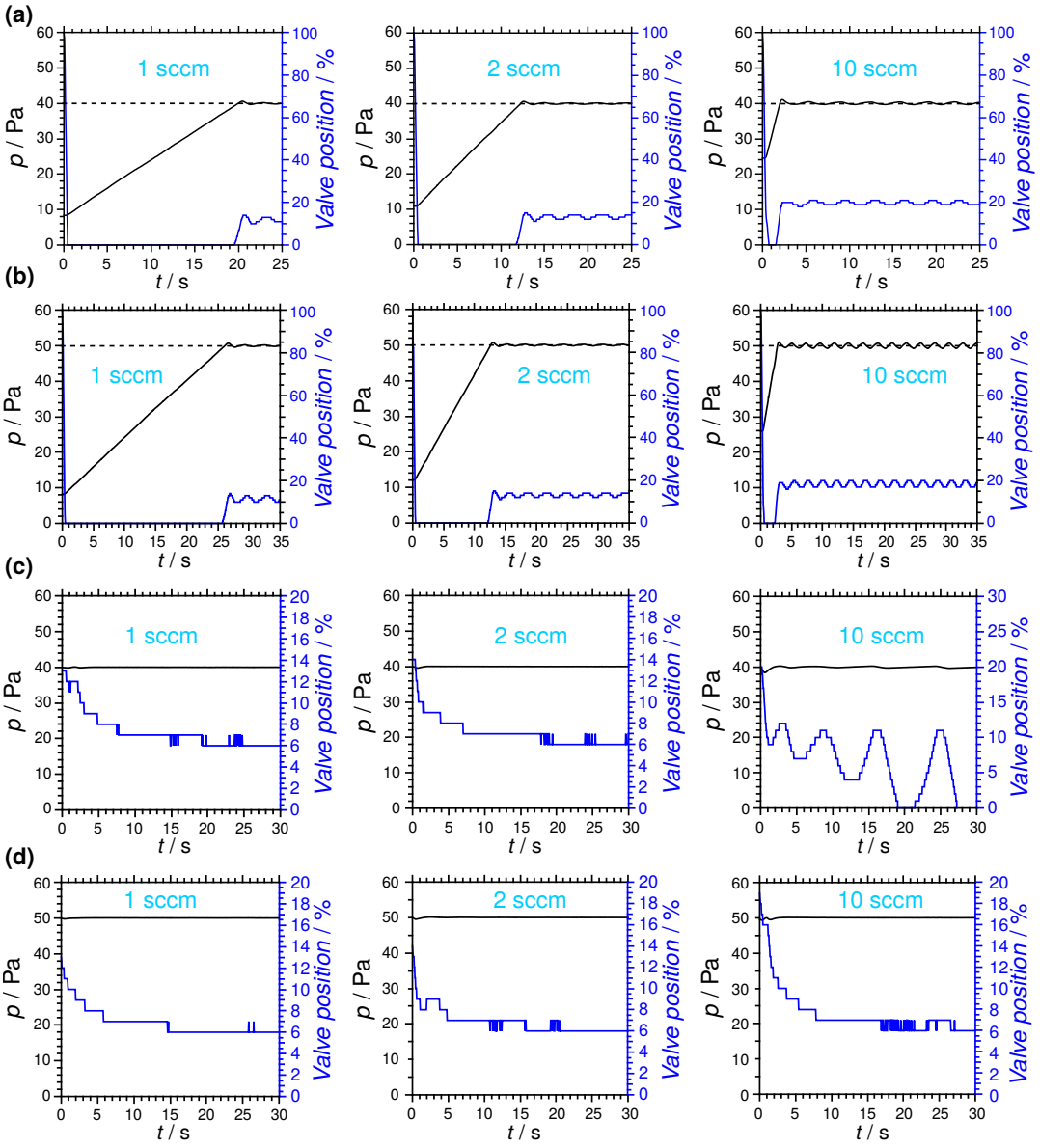

Figure 1: Response time of butterfly valve. (a) Response time of the butterfly valve at 40 Pa for 1 sccm, 2 sccm and 10 sccm process flow. (b) Response time of the butterfly valve at 50 Pa for 1 sccm, 2 sccm and 10 sccm process flow. (c) Response time of the butterfly valve at 40 Pa for 1 sccm, 2 sccm and 10 sccm process flow during flow interruption. (d) Response time of the butterfly valve at 50 Pa for 1 sccm, 2 sccm and 10 sccm process flow during flow interruption.

Appendix C

Chemicals for polymer thin film deposition

The following table shows a detailed list of the chemicals used for the polymer thin film deposition via initiated chemical vapor deposition (iCVD) within the framework of this work.

Table 1: Detailed list of the chemicals used for the polymer thin film synthesis via iCVD within the framework of this work.

Abbr.	Name	Formula	M / g mol^{-1}	Purity	CAS number	Supplier
18N	1,8-Nonadiyne	C_9H_{12}	120.20	97 %	2396-65-8	abcr, DE
1E3F	1-Ethynyl-3-fluorobenzene	C_8H_5F	120.13	98 %	2561-17-3	abcr, DE
1N	1-Nonyne	C_9H_{16}	124.22	98 %	3452-09-3	abcr, DE
C6PFA	1H,1H,2H,2H-perfluorooctyl acrylate	$C_{11}H_7F_{13}O_2$	418.15	95 %	17527-29-6	Fluorochem, GB
EG	Ethylene glycol	$C_2H_6O_2$	62.07	97 %	107-21-1	Sigma-Aldrich, US
EGDMA	Ethylene glycol dimethylacrylate	$C_{10}H_{14}O_4$	198.22	97 %	97-90-5	Sigma-Aldrich, US
HFPO	Hexafluoropropylene oxide	C_3F_6O	166.02	97 %	428-59-1	Fluorochem, GB
PFBSF	Perfluorobutanesulfonyl fluoride	$C_4F_{10}O_2S$	302.09	95 %	375-72-4	Fluorochem, GB
TBPO	Tert-butyl peroxide	$C_8H_{18}O_2$	146.23	97 %	110-05-4	Fluorochem, GB
V3D3	1,3,5-trivinyl-1,3,5-trimethylcyclotrisiloxane	$C_9H_{18}O_3Si_3$	258.50	95 %	3901-77-7	abcr, DE
V4D4	1,3,5,7-tetravinyl-1,3,5,7-tetramethylcyclotetrasiloxane	$C_{12}H_{24}O_4Si_4$	344.67	97 %	428-59-1	Sigma-Aldrich, US

Appendix D

In-situ mass spectrometry reference spectra and fingerprinting

In chapter 4 the extension of the iCVD process by in-situ mass spectrometry is reported. Here the reference spectra are shown (D1) and further information about fingerprinting of the data (D2).

D1: Reference spectra for in-situ mass spectrometry

The reference spectra can be used for fingerprinting in a vapor mixture or for the determination of the reaction kinetics.

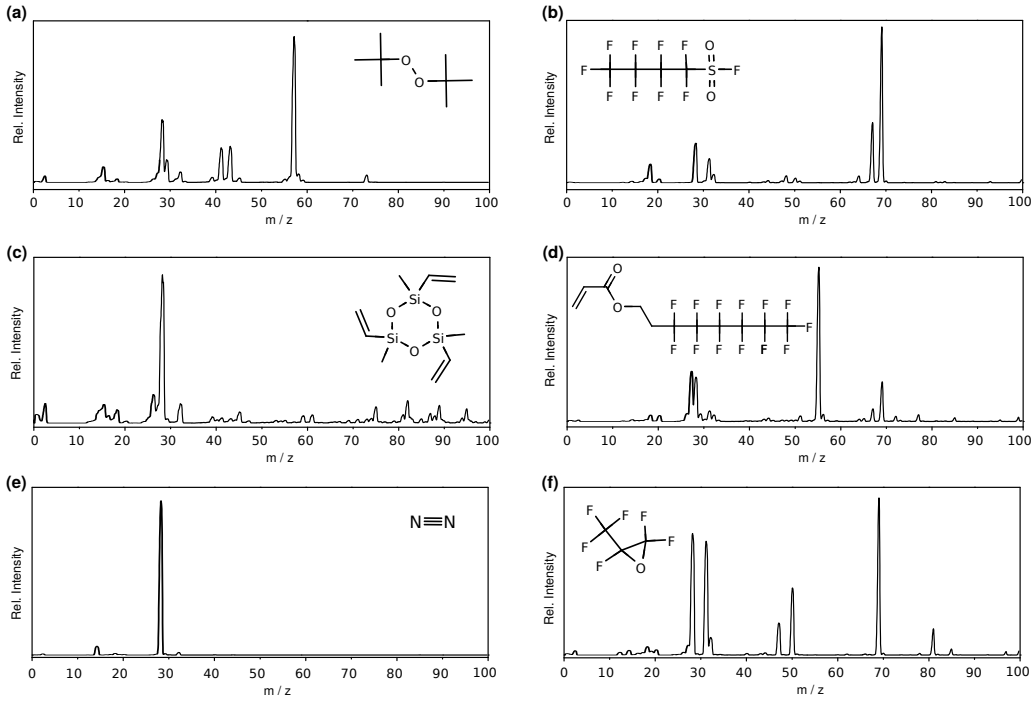

Figure 2: Reference mass spectra of some of the vapors and gases used for iCVD . (a) Tert-butyl peroxide (TBPO). (b) Perfluorobutanesulfonyl fluoride (PFBSF). (c) 1,3,5-trivinyl-1,3,5-trimethylcyclotrisiloxane (V3D3). (d) 1H,1H,2H,2H-perfluorooctyl acrylate (C6PFA). (e) Nitrogen (N_2). (f) Hexafluoropropylene oxide (HFPO).

D2: Outline of the script used for fingerprinting

Prior to the measurement, the individual normalized reference spectra of the respective components (e.g. co-monomer 1, co-monomer 2 and initiator) are loaded from a database (e.g. a matrix). If the chemical is not yet available in the database, it has to be recorded, normalized and then saved in the database prior to the measurement. Some reference lists are also available, e.g. online. The individual normalized reference spectra involved are then loaded into the program. In addition, the currently measured mass spectrum of the reactor atmosphere is transferred to the program or a previously recorded mass spectrum of the reactor atmosphere is loaded as for a post-deposition analysis. This mass spectrum is then also normalized. Next, a mass peak list (p) of the resulting fragments is generated from the vector containing the m/z values (mz) as separation unit and the respective signal intensity (I) of the mass spectrometer. With Matlab this can, e.g. be achieved by using

```
p = mspeaks(mz,I);
```

This is shown for example in Figure 3. After the mass peak list has been generated for the reference spectra and the measured spectra, the individual contributions of the reference spectra are located in the measured spectrum using, e.g. for Matlab

```
C1 = ismember (X,Y);
```

which compares the data in X with the data in Y or by scanning each data entry, e.g. with a for loop. The proportion of the individual components in the overall spectrum can now be written to new variables and a value indicating the respective proportion [Mi] in the vapor phase can then be calculated.

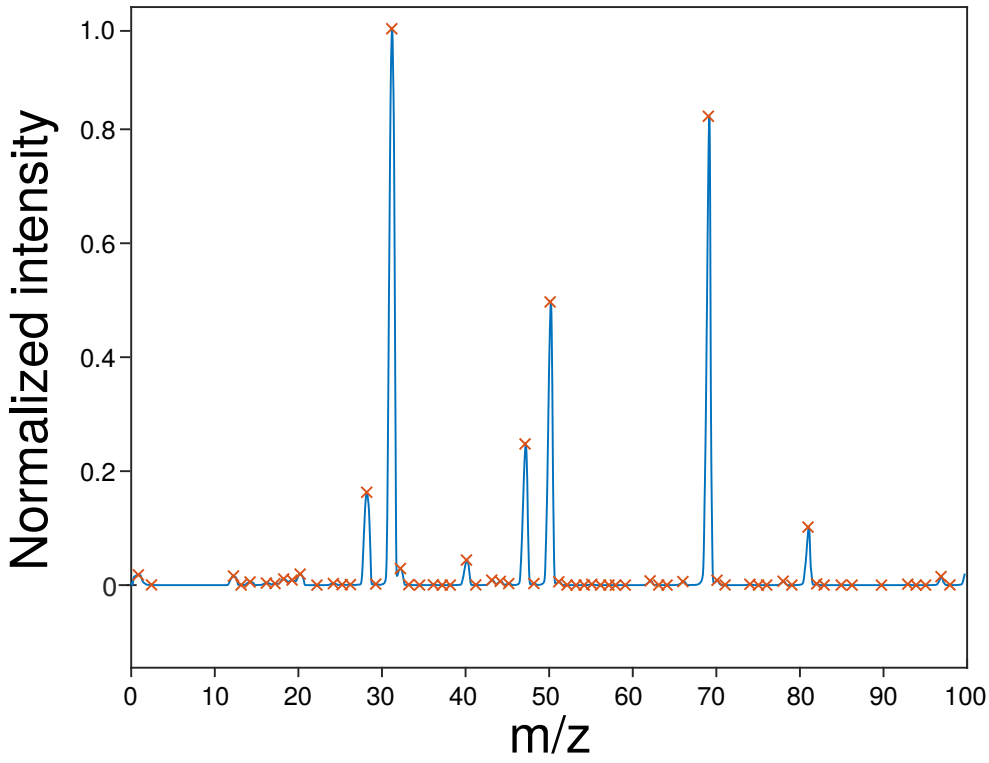

Figure 3: Example of mspeaks applied to the mass spectrometry data in Matlab.

Appendix E

Complex impedance and complex relative permittivity

The relation between complex impedance (Z^*) and complex relative permittivity (ε_r^*) is based on the Maxwell equation

$$\vec{\nabla} \times \vec{H} = \vec{j_f} + \frac{\partial \vec{D}}{\partial \vec{t}}. \tag{6}$$

It is first assumed that a perfect dielectric is considered ($\vec{j_f} = 0$). The symbols $\vec{H}$, $\vec{j_f}$ and $\vec{D}$ represent the magnetic field strength, free current density and displacement field, respectively. With $\vec{D} = \hat{D}\exp(i\omega t)$ the equation

$$\vec{\nabla} \times \vec{H} = i\omega\vec{D} \tag{7}$$

results. $\hat{D}$ and ω are the amplitude and the angular frequency. Now $\vec{D}$ is considered as a secondary calculation. The general relation is

$$\vec{D} = \varepsilon_0\vec{E} + \vec{P}. \tag{8}$$

The symbols ε_0 and $\vec{E_i}$ are the vacuum permittivity and the electric field. The polarization $\vec{P}$ can be replaced by $\vec{P} = \varepsilon_0\chi^*\vec{E}$. The symbol χ^* represents the complex electric susceptibility. This leads to

$$\vec{D} = \varepsilon_0\vec{E}(1 + \chi^*) \tag{9}$$

and thus

$$\vec{D} = \varepsilon_0\varepsilon_r^*\vec{E}_i. \tag{10}$$

The symbol ε_r^* is the complex relative permittivity. Inserting into equation 7 results in

$$\vec{\nabla} \times \vec{H} = i\omega\varepsilon_0\varepsilon_r^*\vec{E}. \tag{11}$$

The expression is equal to the displacement current $\vec{j}_D = \sigma^*\vec{E}$. This yields the equation

$$\sigma^* = i\omega\varepsilon_0\varepsilon_r^*. \tag{12}$$

σ^* represents the complex electrical conductivity. For the material Ohm's law $\vec{j}_D^* = \sigma^*\vec{E}_i^*$ and equation 12 result in

$$\vec{j}_D^* = i\omega\varepsilon_0\varepsilon_r^*\vec{E}_i^*. \tag{13}$$

With $\vec{j}^* = \frac{I^*}{A}$ and $\vec{E}_i^* = \frac{V^*}{x_f}$ the equation

$$\varepsilon_r^* = \frac{I^* x_f}{i\omega\varepsilon_0 A V^*} \tag{14}$$

results after rearranging. The symbols I^*, A, V^* and x_f respresent the complex current, the surface area, the complex voltage and the thickness of the measured sample, respectively. $Z^* = \frac{V^*}{I^*}$ results in

$$\varepsilon_r^* = \frac{x_f}{i\omega\varepsilon_0 A Z^*}. \tag{15}$$

With the introduction of the geometry factor ($C_0 = \frac{A\varepsilon_0}{x_f}$) the equation

$$\varepsilon_r^* = (i\omega C_0 Z^*)^{-1}. \tag{16}$$

results.

Appendix F

Electrets and Entropy

The description of charge storage in electrets or, in general, the electrical charging of polymers often turns out to be difficult from a theoretical point of view. On the one hand, quantum mechanical calculations are necessary, since the electronic structure of the functional groups must be taken into account. On the other hand, periodic boundary conditions, as in the case of crystalline solids, cannot be used because polymers are amorphous or at most partially crystalline systems. However, it has been shown that the macroscopic view must also be taken into account. While in quantum mechanical calculations often only short organic chains can be calculated, it is also the chain arrangement in its "macroscopic" complexity that can have an effect on the charge storage properties. This includes the overall arrangement of the individual chains. This has not been possible to consider in the calculations via quantum mechanical approaches so far. Here a combination of the microscopic and macroscopic properties is suggested in order to consider them in the description. The entropy of the system serves as the starting point. First it is assumed that in the equation for the free energy,

$$F = U - TS, \tag{17}$$

the internal energy (U) can be neglected and therefore F is only determined by temperature (T) and entropy (S). For S the description according to Boltzmann is used, which is

$$S = \mathrm{k_B} \ln(P). \tag{18}$$

This equation links the macroscopic system with the micro states or the possible microscopic configurations. The symbols $\mathrm{k_B}$ and P represent the Boltzmann constant and the probability density, respectively. This results in

$$F = -T\mathrm{k_B} \ln(P). \tag{19}$$

Different models can now be applied. Assuming a Gaussian chain, the expression

$$P = P_0 \exp\left(-\frac{3r^2}{2R_c^2}N\right) \tag{20}$$

results for P. N, R_c and r are the number of segments, the contour length and the end-to-end length. A Langevin chain is characterized by

$$P = P_0 \exp\left(-L_v^{-1}N\frac{r}{R_c} - N\ln\left(\frac{L_v^{-1}}{\sinh(L_v^{-1})}\right)\right). \tag{21}$$

L_v is given by

$$L_v = \coth\left(\frac{r}{R_c}\right) - \frac{R_c}{r}. \tag{22}$$

The Gaussian chain shows a linear relationship between stretch (r/R_c) and force. This deviates from the observed behavior at large (r/R_c). The Langevin chain model describes the behavior at small r/R_c exactly like the Gaussian chain model. It also provides a more accurate description for large r/R_c values. However, only small r/R_c values can be found in the electrostatic approach, which would justify the application of the Gaussian chain model. Choosing the Gaussian chain model, equation 19 becomes equation

$$F = -T\mathrm{k_B}\ln(P_0) + \frac{3\mathrm{k_B}TNr}{2R_c}. \tag{23}$$

Subsequently,

$$\frac{\partial F}{\partial \frac{r}{R_c}} = 3\mathrm{k_B}TN\frac{r}{R_c} \tag{24}$$

provides the force. Assuming that charge carriers have been trapped at the functional groups of the chain, electrostatic repulsion will occur in different segments of the chain. The distribution of the possible microscopic configurations might change and the entropy becomes lower. This can now be used as starting point for further considerations, in which also the different arrangement of the chains is considered.

Appendix G

Equations of motions for electret magnetic field sensor by Lagrangian mechanics

The following is a detailed derivation of the equations of motion for the sensor shown in Chapter 6. The approach is based on the equations reported by Hawley and Romanow [306]. For the new sensor shown, which is again schematically illustrated in Figure 4, the total potential energy (V_P) of the system is first considered.

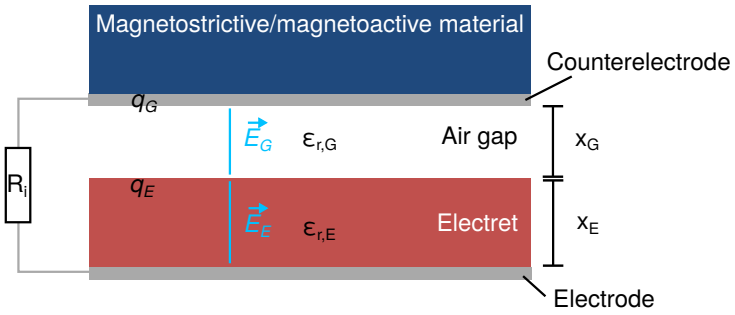

Figure 4: Schematic illustration of the magnetic field sensor as presented in Chapter 6.

It consists of the field energy (V_F) and the energy (V_M) stored in the mechanical components of the system

$$V_p = V_M + V_F. \tag{25}$$

V_M is therefore

$$V_M = \frac{1}{2} k_F x_d^2 \tag{26}$$

where k_F represent the spring constant. V_F is consequently

$$V_F = \frac{1}{2}\varepsilon_0\varepsilon_r A x_i \vec{E_i}^2 \tag{27}$$

with the vacuum permittivity (ε_0), relative permittivity (ε_r), area (A), thickness between the electrodes (x_i) and the electric field ($\vec{E_i}$). Superposition of the two fields in the system ($\vec{E_E}$ for the field in the electret and E_G for the field in the air gap) thus gives with $\varepsilon_0\varepsilon_{r,G} = \varepsilon_{air}$ and $\varepsilon_0\varepsilon_{r,E} = \varepsilon_e$

$$V_F = \frac{1}{2}\varepsilon_{air} A x_{air} \vec{E_G}^2 + \frac{1}{2}\varepsilon_e A x_e \vec{E_E}^2. \tag{28}$$

The electric fields can be determined by the Gaussian law, which is given by

$$q_i = \oint_A \varepsilon_i \vec{E_i}\, d\vec{A}. \tag{29}$$

For the two regions

$$\varepsilon_{air} E_G A + \varepsilon_e E_E A = q_e \tag{30}$$

and

$$\varepsilon_{air} E_G A = q_G \tag{31}$$

result. Solving to E_i provides for the electric fields

$$E_G = \frac{q_G}{A\varepsilon_{air}} \tag{32}$$

and

$$E_E = \frac{q_G + q_E}{A\varepsilon_e}. \tag{33}$$

This can be inserted into 28 and results according to 25 in

$$V_p = \frac{1}{2}k_F(x_0 + x)^2 + \frac{x_{air} q_G^2}{2\varepsilon_{air} A} + \frac{x_e(q_E + q_G)^2}{2\varepsilon_e A} \tag{34}$$

for the potential energy of the system. During operation, the air gap width decreases by $x_0 + x$. In addition, an initial value q_0 is set for q_G, which then varies by q. This results in the equation

$$V_p = \frac{1}{2}k_F(x_0 + x)^2 + \frac{(x_{air} - x_0 - x)(q_0 + q)^2}{2\varepsilon_{air} A} + \frac{x_e(q_E + q_0 + q)^2}{2\varepsilon_e A}. \tag{35}$$

The total kinetic energy of the system (T) can be described by

$$T = \frac{1}{2} m \dot{x}^2 \tag{36}$$

and contains the mass (m). The Lagrangian can be calculated according to

$$L = T - V_p. \tag{37}$$

Thus with 35 and 36 the equation

$$L = \frac{1}{2} m \dot{x}^2 - \frac{1}{2} k_F (x_0 + x)^2 - \frac{(x_{air} - x_0 - x)(q_0 + q)^2}{2 \varepsilon_{air} A} - \frac{x_e (q_E + q_0 + q)^2}{2 \varepsilon_e A} \tag{38}$$

results. To include the damping (D) the Rayleigh function is considered, it is given by

$$D = \frac{1}{2} R \dot{q}^2 + \frac{1}{2} c_D \dot{x}^2. \tag{39}$$

The symbols R and c_d represent the electrical resistance in the system and the damping coefficient in the mechanical part, respectively. For the Lagrange function, which is given by

$$\frac{d}{dt} \left(\frac{\partial L}{\partial \dot{g}_i} \right) - \frac{\partial L}{\partial g_i} + \frac{\partial D_R}{\partial \dot{g}_i} = f, \tag{40}$$

the derivatives are formed in the next step. Deflection (x) and charge (q) are selected as generalized coordinates (g_i). The associated forcing functions are f_M and f_V, which represent the force applied to the system and the force exerted simultaneously by the voltage, respectively. This results in

$$\frac{\partial L}{\partial x} = -k_f (x_0 + x) + \frac{(q_0 + q)^2}{2 \varepsilon_{air} A}, \tag{41}$$

$$\frac{\partial L}{\partial q} = \frac{(q + q_0)(-x_{air} - x_0 - x)}{\varepsilon_{air} A} - \frac{x_e (q_E + 1 + q)}{\varepsilon_e A}, \tag{42}$$

$$\frac{d}{dt} \left(\frac{\partial L}{\partial \dot{x}} \right) = m \ddot{x}, \tag{43}$$

$$\frac{d}{dt} \left(\frac{\partial L}{\partial \dot{q}} \right) = 0, \tag{44}$$

$$\frac{\partial D}{\partial \dot{x}} = c_D \tag{45}$$

and

$$\frac{\partial D}{\partial \dot{q}} = R\dot{q} \tag{46}$$

for the derivatives. Inserting this into equation 40 results in

$$m\ddot{x} + c_D\dot{x} + k_F(x_0 + x) - \frac{(q_0 + q)^2}{2\varepsilon_{air}A} = f_M \tag{47}$$

$$R\dot{q} + \frac{(q + q_0)(x_{air} - x_0 - x)}{\varepsilon_{air}A} + \frac{x_e(q_E + 1 + q)}{\varepsilon_e A} = f_V \tag{48}$$

for the equations of motion. By dividing by m in equation 47 and inserting $\frac{k_F}{m} = \omega_0^2$, $c_d = \zeta c_c$ and $c_c = 2\sqrt{k_F m}$ the undamped angular frequency (ω_0) and damping ratio (ζ) can be introduced. The symbol c_c represents the critical damping coefficient. The equations of motion as presented in Chapter 6 are therefore

$$\ddot{x} + 2\zeta\omega_0\dot{x} + \omega_0^2(x_0 + x) - \frac{(q_0 + q)^2}{2m\varepsilon_{air}A} = \frac{f_M}{m} \tag{49}$$

$$R\dot{q} + \frac{(q + q_0)(x_{air} - x_0 - x)}{\varepsilon_{air}A} + \frac{x_e(q_E + 1 + q)}{\varepsilon_e A} = f_V. \tag{50}$$

Appendix H

The electronic structure of PV3D3

Based on the unexpected fast decay of the surface potential of charged poly(1,3,5-trivinyl-1,3,5-trimethylcyclotrisiloxane) (PV3D3) films observed in Chapter 7, possible causes are discussed here. It was found in Chapter 7 that despite the good insulating properties already reported by many authors, charge carriers introduced into the polymer decay relatively fast. What could be the reason for this? To find an answer, first a look at the orbital levels is provided. This is obtained by second order Møller–Plesset perturbation theory (MP2) using the cc-pVDZ basic set. Hexamethylcyclotrisiloxane (D3) is used as a representative. The results are shown in Figure 5. The distance between HOMO and LUMO band is sufficiently large, which finally results in the well-known insulating properties of the PV3D3. Furthermore, compared to benzene, no conjugated system is present in the cyclotrisiloxane ring, which also does not cause the observed rapid charge decay. The most probable possibility is therefore that the introduced charge carriers are localized in shallow traps. These are located close to the mobility edges and the carriers can be released from these traps by low temperatures and subsequently enter the next shallow trap. By this thermally activated movement of the charge carriers, they can be transported through the polymer relatively easily. The result is the observed fast decay, which leads to a complete discharge of the film after a few days. Slightly higher temperatures increase the decay rate even further. The origin of shallow traps can be attributed, among other things, to disorder in the conformation of the polymer [157].

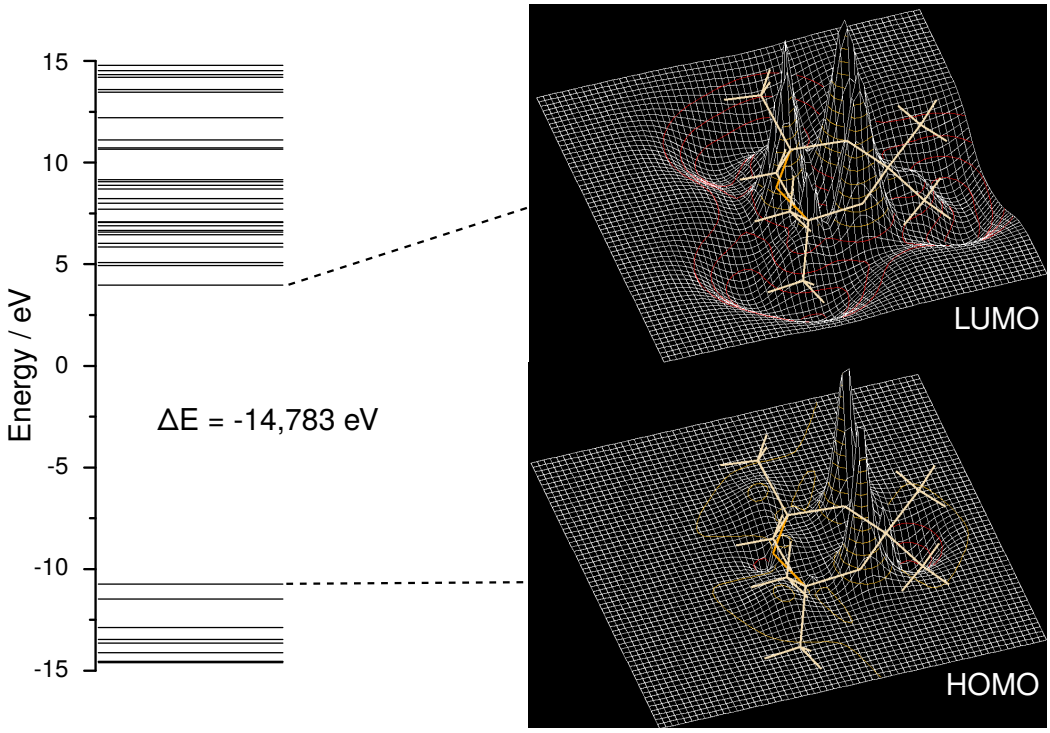

Figure 5: Approximation of the electronic structure of V3D3, represented by hexamethylcyclotrisiloxane (D3). For the calculation second order Møller–Plesset perturbation theory (MP2) with the correlation-consistent basis set cc-pVDZ was applied. The gap between HOMO and LUMO band is 14,783 eV.